Prompt Neutron Polarization Asymmetries in Photofission of Isotopes of Thorium, Uranium, Neptunium, and Plutonium

by

Jonathan M. Mueller

Department of Physics
Duke University

Date: _____

Approved:

_____
Henry R. Weller, Supervisor

_____
Mohammad W. Ahmed

_____
Steffen A. Bass

_____
Mark C. Kruse

_____
Harold U. Baranger

Dissertation submitted in partial fulfillment of the requirements for the degree of
Doctor of Philosophy in the Department of Physics
in the Graduate School of Duke University
2013

Abstract

Prompt Neutron Polarization Asymmetries in Photofission of Isotopes of Thorium, Uranium, Neptunium, and Plutonium

by

Jonathan M. Mueller

Department of Physics
Duke University

Date: _____

Approved:

_____
Henry R. Weller, Supervisor

_____
Mohammad W. Ahmed

_____
Steffen A. Bass

_____
Mark C. Kruse

_____
Harold U. Baranger

An abstract of a dissertation submitted in partial fulfillment of the requirements for the degree of Doctor of Philosophy in the Department of Physics in the Graduate School of Duke University
2013

Abstract

Nearly mono-energetic, high intensity ($\sim 10^7 \gamma/s$), and approximately 100% linearly polarized γ-ray beams at energies between 5.3 and 7.6 MeV were used to induce photofission of ^{232}Th, ^{233,235,238}U, ^{237}Np, and ^{239,240}Pu. Prompt fission neutron yields parallel and perpendicular to the plane of beam polarization were measured using arrays of 12-18 liquid scintillator detectors. Prompt neutron polarization asymmetries close to zero were found for the even-odd actinides (^{233,235}U, ^{237}Np, and ^{239}Pu), while significant asymmetries were found for the even-even actinides (^{232}Th, ^{238}U, and ^{240}Pu). Predictions based on previously measured fission fragment angular distributions combined with a model of prompt neutron emission agree well with our experimental results. Finally, we describe a new method of measuring the enrichment of special nuclear material based on our results.

This dissertation is dedicated to my wonderful wife Sarah, who has read this entire thesis and not once fallen asleep while reading

Contents

List of Tables

List of Figures

List of Abbreviations and Symbols

List of Abbreviations

ADC	Analog-to-Digital Converter
BPM	Beam Position Monitor
BS	Booster Synchrotron
CEBAF	Continuous Electron Beam Accelerator Facility
CERN	European Organization for Nuclear Research
CFD	Constant Fraction Discriminator
CODA	CEBAF Online Data Acquisition
DAQ	Data Acquisition
DFELL	Duke Free Electron Laser Laboratory
DRDY	Data Ready
ESR	Electron Storage Ring
FEL	Free Electron Laser
FWHM	Full Width at Half Maximum
`GEANT4`	GEometry And Tracking, Version 4
HIγS	High Intensity γ-ray Source
HPGe	High Purity Germanium
LINAC	Linear Accelerator
NaI(Tl)	Sodium Iodide (Thallium)
NIM	Nuclear Instrument Module

OK	Optical Klystron
PH	Pulse Height
PMT	PhotoMultiplier Tube
PSD	Pulse Shape Discrimination
RF	Radio Frequency
TAC	Time-to-Amplitude Converter
TDC	Time-to-Digital Converter
TOF	Time Of Flight
TUNL	Triangle Universities Nuclear Laboratory
VME	Versa Module Europa

Acknowledgements

I could not have performed this work and written this thesis without the excellent years of training I have enjoyed. First I would like to thank some of my Math and Science teachers in secondary school: Mr. Hoeman, Mr. McCraith, Ms. Blake, and Mr. Sobkowicz. They instilled in me a passion for math and science and prepared me well for my undergraduate studies at Washington University. At Washington University, I had the pleasure of taking classes with Prof. Bernatowicz, Prof. Dickhoff, Prof. Alford, and Prof. Carl Bender (affectionately called Prof. Crab Lender). These amazing teachers taught me much of what I know now about physics. Here at Duke, I would like to acknowledge all of the professors who have played a role in my formal education.

I would also like to acknowledge those who played a role in my development as a researcher. I became interested in doing physics research during my freshman year at Washington University, and was fortunate to have Prof. Sobotka, a professor in nuclear physics, agree to mentor me despite the fact that I had not yet even taken quantum physics. Working with Prof. Sobotka, Prof. Charity, and Prof. Dickhoff convinced me beyond a shadow of a doubt that I wanted to pursue a doctorate in physics. One of the research opportunities afforded to me by Prof. Sobotka was a 2 week long experiment using the Tandem accelerator here at Duke, and this research experience played a significant role in my decision to come here. I truly would not have been here without the help, mentoring, and training provided by these three

professors.

At Duke, I have had the benefit of working with many outstanding nuclear physicists. I would like to acknowledge fruitful conversations about my research with Prof. Karwowski, Prof. Feldman, Prof. Whisnant, Prof. Prior, Prof. Spraker, Prof. Frances, Prof. Mazumdar, Prof. Johnson, Dr. Myers, Dr. Sikora, Dr. Perdue, Dr. Henshaw, Dr. Zimmerman, Dr. Stave, Dr. Tompkins, and many others with whom I discussed my research. All of you have contributed to this work and I thank you for your help. I would also like to thank our theorists collaborators Prof. Vogt and Dr. Randrup. Our work would not have nearly the same significance without their prompt neutron emission model `FREYA`. We have also had a significant amount of help from our summer REU students, David, Jimmy, Keith, Clarke, and Will, who have helped to set up and operate the neutron detector array.

I would also like to acknowledge the work done by the members of my committee to help me improve this dissertation. In particular, I would like to thank my advisors, Prof. Henry Weller and Prof. Mohammad Ahmed. They have helped me an incredible amount with this project. They have always found time to answer questions or provide guidance, and I have never had to worry about the direction of my project because of their support and experience. I have truly benefited from working with them, as they have taught me so much not only about nuclear physics itself, but also about how to do nuclear physics and what it takes to be a successful physicist. They have been the most influential people to me during my time here at Duke and this work truly is as much theirs as it is mine.

On the topic of support, I would like to acknowledge the sources of funding I have received while working here at Duke. I have been blessed to have somewhat of an unusual funding situation here, as I was supported almost entirely through fellowships. The James B. Duke Fellowship allowed me to get started working with Henry and Mohammad early on, and the DOE Office of Science Fellowship greatly

stimulated my professional development by funding travel to several conferences over my graduate career. I would like to acknowledge our DNDO/ARI grant 2010-DN-077-ARI46-02 for providing support to perform our experiments.

I would also like to acknowledge the support I have received from my friends here at Duke. Sean, Chris, Kevin C., Kevin F., Venkitesh, and Sukrit: I would not have enjoyed this experience nearly as much without you. The same is true for the members of the Basketball Campout Committee; I have thoroughly enjoyed working with you despite any slight graduation delays it may have caused.

Last but certainly not least, I would like to thank my family. My parents have been incredibly supportive and understanding of my sometimes intense focus on my work even over holiday visits. My wife Sarah could not have been more understanding of the time and effort commitment required in graduate school. She constantly rearranged her schedule around our experimental runs, and never complained when I had to bring work home for the night (or sometimes, for the whole weekend). I am forever grateful for the effort you have put in to help me become a better physicist.

1

Introduction

The use of nuclear fission for energy production is one of the most significant advances in the past century. Its importance lies in the tremendous amount of energy released in a fission event. Roughly 200 MeV is released every time a parent nucleus divides into two daughter nuclei, while ordinary chemical processes release energy on the orders of eV or keV per reaction. This large energy release, coupled with the ease with which certain materials can undergo chain reactions, has led to the two most familiar uses of fission in society: nuclear power and nuclear weapons.

The energy released in fission is divided among several different daughter particles. The vast majority of the energy released ($\sim 80\%$) goes to the kinetic energy of the two fission fragments, as they are repelled very quickly from each other by their mutual Coulomb interaction. Some energy ($\sim 6\%$) also goes to prompt neutrons and γ rays; these emissions are called prompt because they occur almost instantaneously with the fission event itself. The remaining energy ($\sim 14\%$) goes to delayed emissions, such as delayed neutrons, γ rays, and other particles emitted during β decay.

From the perspective of applied nuclear physics, the emission of the prompt

neutrons is a key component of the fission process. These neutrons can induce fission of other actinide nuclei (atomic numbers between 89-103), causing even more energy to be released. The average number of prompt neutrons per fission event depends on the specifics of the reaction, such as the energy of the particle inducing fission and the target, but is generally more than two, allowing for a sustained chain reaction.

Given their importance in the fission reaction, prompt neutrons from fission have been extensively studied experimentally. Their energy distribution, multiplicities, and correlation with other fission parameters have been measured for most experimental conditions, in particular for the case of neutron-induced fission. These previous experiments showed that prompt neutrons are correlated in angle with fission fragments, suggesting that prompt neutrons are emitted after the fission fragments have fully accelerated [1]. This fact is of key importance to our work.

In addition to the measurements of prompt neutrons and fission fragments from neutron-induced fission, measurements of fragment mass and angular distributions have been performed for the special case of photofission (γ-ray induced fission). These experiments showed that the fission fragment angular distribution for even-even isotopes can be very anisotropic, while the angular distributions of fission fragments from even-odd parent isotopes are largely isotropic [1].

Our work combines and extends these two types of measurements to test these assumptions, obtain high-precision data sets, and investigate potential applications. We used a polarized γ-ray beam to measure the prompt neutron polarization asymmetries from photofission of seven actinide targets (^{232}Th, ^{233,235,238}U, ^{237}Np, and ^{239,240}Pu). The significant difference in fragment angular distributions between even-even and even-odd actinides manifests as a significant difference in the prompt neutron polarization asymmetries for the even-even and even-odd actinides. We also collaborated with theorists to develop a calculation of prompt neutron polarization asymmetries based on a model of prompt neutron emission, combined with previ-

ously measured photofission fragment angular distributions as experimental inputs. Our experimental results are largely consistent with this photofission calculation.

Despite the long history of experimental studies of the fission reaction, fission theory is not yet capable of predicting many relevant observables. For example, the most successful models of fission cannot be used to predict fragment angular distributions in photofission, nor can this observable be predicted by current models of fission based on first principles. The theory of photofission fragment angular distributions (or prompt neutron angular distributions) is thus composed of phenomenological models that do not provide a solid basis from first principles. This leaves an increased reliance on experimental, rather than theoretical, input. Therefore, we hope our work, which is the first ever measurement of prompt neutron polarization asymmetries in photofission reactions, will improve our overall understanding of the fission process in the absence of predictive models that do not require experimental input.

In addition to these basic science aspects of our work, our results have clear applications in detection of special nuclear materials. The even-even actinides are generally unable to sustain a chain reaction, while the even-odd actinides generally can, depending on the mass and geometry of the material. This is due to the fact that the even-odd actinides generally are fissile, which means that they will undergo fission upon capturing a thermal neutron, while the even-even actinides are generally non-fissile. Typically, special nuclear materials are characterized by their enrichment which is the proportion of fissile to non-fissile content in the material. Because the prompt neutron polarization asymmetries are different for even-odd (fissile) isotopes in comparison with even-even (non-fissile) isotopes, a measurement of the prompt neutron polarization asymmetry of a mixed sample can be used to determine the enrichment of a sample. This new method of measuring the enrichment of special nuclear material could be of great interest to the applied nuclear physics community.

Outline of this Dissertation

Chapter 2 discusses the theoretical basis for our work, including the theory of photonuclear reactions, general aspects of fission, the theory of photofission fragment angular distributions, and some calculations of fragment angular distribution coefficients based on a simplified model of the photofission process. Chapter 3 describes previous measurements relevant to our studies, including previous fragment angular distribution measurements in photofission and previous measurements of prompt neutrons. Chapter 4 discusses the experimental setup, including the γ-ray beams, detectors, targets, and electronics. Chapter 5 describes the analysis of our data, including relevant calibrations and data reduction cuts. Chapter 6 details the calculation of prompt neutron polarization asymmetries, developed in collaboration with nuclear theorists. Finally, the results of the experiments and calculations are presented in Chapter 7, along with some concluding remarks.

2

Photofission Theory

2.1 Introduction

This chapter will describe theoretical models of photofission focusing on understanding angular distributions of fission fragments and prompt neutrons. The goal of understanding the theory of photofission in the context of this dissertation is to predict prompt neutron polarization asymmetries. To make these predictions, it is critical to understand how photons interact with nuclei. This process is described in Section 2.2 with a focus on the dominant modes of interaction between photons and nuclei. To understand photofission, it is important to have a theoretical model of the fission process. Section 2.3 describes the theory behind general aspects of fission, including some early models which lay the foundation for the most recent fission theories. Even the most recent, advanced theoretical models are not yet capable of predicting prompt neutron polarization asymmetries in photofission from first principles. However, a heuristic model that is capable of explaining fission fragment angular distributions is developed in Section 2.4, which combines the results from Section 2.2 and Section 2.3. This model can be used to predict fragment angular distributions,

which can then be used to determine the prompt neutron angular distributions, in conjunction with the theoretical mechanism of prompt neutron emission presented in Section 2.5.

2.2 Photonuclear Reactions

γ rays are useful probes in nuclear physics. In nuclear reactions involving a γ ray, termed photonuclear reactions, the emission or absorption of a γ ray imposes several conditions on the corresponding nuclear transition. Most interesting and relevant to this work is the angular momentum selectivity of the γ ray, which affects the population of excited states in the nucleus and through that the angular distributions and polarization asymmetries of outgoing particles.

The interaction Hamiltonian for a γ ray and a nucleus is given by:

$$H_{int} = -\frac{1}{c}\int \vec{j}\cdot\vec{A}(\vec{r})\mathrm{d}\vec{r} \tag{2.1}$$

where $\vec{j}$ is the total nuclear current, $\vec{r}$ is the integration variable over the nuclear coordinates, and $\vec{A}$ is the electromagnetic vector potential for the photon in the radiation gauge, $\nabla\cdot\vec{A}=0$ [2]. This equation neglects the internal structure of the nucleons, which is a reasonable approximation in our work.

The full expansion of Equation 2.1 to all orders in angular momentum and for electric and magnetic transitions is somewhat complex and provides excessive detail. This detail is not necessary in order to understand the most relevant points about low energy photonuclear reactions in the present context, which are the first and second order effects of the angular momentum and parity selectivity. Therefore, a simpler expansion of Equation 2.1 will be provided here. The results are identical to the full expansion to first and second order. The full expansion is presented in Appendix A.

The transition rate for a photonuclear reaction where the photon is absorbed by the nucleus can be found using Fermi's Golden Rule [2]:

$$\mathrm{d}w_{fi} = (\frac{2\pi}{\hbar})\rho(E_\gamma)|H_{fi}|^2 \tag{2.2}$$

where $\rho(E_\gamma)$ is the density of final states in the nucleus at excitation energy E_γ, i stands for initial state, f stands for final state, and H_{fi} is the matrix element for the transition, given by:

$$H_{fi} = \left\langle f \middle| -\frac{1}{c}\int \vec{j}\cdot\vec{A}(\vec{r})\mathrm{d}\vec{r} \middle| i \right\rangle \tag{2.3}$$

The vector potential $\vec{A}$ is proportional to $\hat{\epsilon}e^{i\vec{k}\cdot\vec{r}}$. Here $\hat{\epsilon}$ is the direction of polarization of the photon and $\vec{k}$ is the wave vector of the photon. Equation 2.2 can be simplified by neglecting the density of final states in the nucleus. In this case, the transition rate is proportional to $|H_{fi}|^2$. H_{fi} can be written as:

$$H_{fi} \propto \left\langle f \middle| \int \vec{j}\cdot\hat{\epsilon}e^{i\vec{k}\cdot\vec{r}}\mathrm{d}\vec{r} \middle| i \right\rangle \tag{2.4}$$

A key approximation is to expand $e^{i\vec{k}\cdot\vec{r}} \approx 1+i\vec{k}\cdot\vec{r}+O((\vec{k}\cdot\vec{r})^2)$. This approximation is valid for $kR << 1$. Because Equation 2.3 integrates over the nuclear current, the relevant radius R is on the order of the size of the nucleus, which is roughly $1.2A^{1/3}$ fm. Using a beam energy of 7 MeV and a nuclear mass of 240 nucleons, which is the heaviest nucleus used in our experiments, and substituting $E = \hbar ck$ yields $kR = 0.26$ which satisfies the requirements for this approximation. The cross section uses the square of H_{fi}, so if interference effects caused by products of two terms are neglected, the cross section for successive orders of kR is lowered by a factor of 0.06.

The remainder of this section will show that the first term will yield the electric dipole interaction (E1). The second term will lead to the magnetic dipole (M1) and electric quadrupole (E2) contributions. Higher order terms, such as the magnetic

quadrupole (M2), electric octupole (E3), and so on have been neglected because they are $O((\vec{k}\cdot\vec{r})^2)$ or higher.

For the moment, consider only the first term of the expansion. Inserting this into Equation 2.4 yields:

$$H_{fi}^{(1)} \propto \left\langle f \left| \int \vec{j}\cdot\hat{\epsilon}\mathrm{d}\vec{r} \right| i \right\rangle \tag{2.5}$$

This can be rewritten as:

$$H_{fi}^{(1)} \propto \left\langle f \left| \int \vec{j}\cdot\nabla(\hat{\epsilon}\cdot\vec{r})\mathrm{d}\vec{r} \right| i \right\rangle \tag{2.6}$$

Using integration by parts and assuming $\vec{j}$ is negligible at the nuclear surface yields:

$$H_{fi}^{(1)} \propto -\left\langle f \left| \int (\nabla\cdot\vec{j})(\hat{\epsilon}\cdot\vec{r})\mathrm{d}\vec{r} \right| i \right\rangle \tag{2.7}$$

Conservation of charge requires:

$$\nabla\cdot\vec{j} = -\frac{\partial\rho(\vec{r})}{\partial t} \tag{2.8}$$

where $\rho(\vec{r})$ is the nuclear charge density. This is a generalization of Siegert's theorem [2]. Substituting this into Equation 2.7 gives:

$$H_{fi}^{(1)} \propto \left\langle f \left| \int (\frac{\partial\rho(\vec{r})}{\partial t})(\hat{\epsilon}\cdot\vec{r})\mathrm{d}\vec{r} \right| i \right\rangle \tag{2.9}$$

Finally, using $\frac{i}{\hbar}[H,\rho(\vec{r})] = \frac{\partial\rho(\vec{r})}{\partial t}$ yields:

$$H_{fi}^{(1)} \propto \omega \left\langle f \left| \int \rho(\vec{r})(\hat{\epsilon}\cdot\vec{r})\mathrm{d}\vec{r} \right| i \right\rangle \tag{2.10}$$

where ω is the difference in energy between the initial and final states, which is the energy of the photon. The dipole moment of the nucleus is:

$$\vec{D} = \int \rho(\vec{r})\vec{r}\mathrm{d}\vec{r} \tag{2.11}$$

so the matrix element of the transition Hamiltonian, to first order in kR, is proportional to

$$H_{fi}^{(1)} \propto \omega\hat{\epsilon} \cdot \vec{D}_{fi} \tag{2.12}$$

This transition matrix element is termed the electric dipole transition (E1) because the principal operator involved is the electric dipole operator. It is clear that the final and initial states must have opposite parities in order for the integral to be non-zero, so E1 transitions must change the parity of the nuclear state. From an angular momentum standpoint, $\vec{r}$ behaves as a rank-1 tensor, so E1 transitions can change the angular momentum of the nucleus by ± 1. This implies the selection rule $|J_i - 1| < J_f < |J_i + 1|$.

The next term in the kR expansion is $i\left\langle f\middle|\int(\vec{j}\cdot\hat{\epsilon})(\vec{k}\cdot\vec{r})\mathrm{d}\vec{r}\middle|i\right\rangle$. This can be rewritten as:

$$H_{fi}^{(2)} \propto \left\langle f\middle|\int \vec{j}\cdot(\nabla((\hat{\epsilon}\cdot\vec{r})(\vec{k}\cdot\vec{r})) - \vec{k}(\hat{\epsilon}\cdot\vec{r}))\mathrm{d}\vec{r}\middle|i\right\rangle \tag{2.13}$$

This can be split into two terms:

$$H_{fi}^{(2a)} \propto \left\langle f\middle|\int \vec{j}\cdot\nabla((\hat{\epsilon}\cdot\vec{r})(\vec{k}\cdot\vec{r}))\mathrm{d}\vec{r}\middle|i\right\rangle \tag{2.14}$$

$$H_{fi}^{(2b)} \propto -\left\langle f\middle|\int(\vec{j}\cdot\vec{k})(\hat{\epsilon}\cdot\vec{r})\mathrm{d}\vec{r}\middle|i\right\rangle \tag{2.15}$$

Integrating by parts and applying Siegert's theorem to $H_{fi}^{(2a)}$ yields:

$$H_{fi}^{(2a)} \propto \omega\hat{\epsilon}\cdot\langle f|\rho(\vec{r})\vec{r}\vec{r}\mathrm{d}\vec{r}\,|i\rangle\cdot\vec{k} \tag{2.16}$$

where $\hat{\epsilon}$ and $\vec{k}$ are dotted to the first and second $\vec{r}$ respectively. Using $\hat{\epsilon}\cdot\hat{k} = 0$ this can be rewritten as:

$$H_{fi}^{(2a)} \propto \omega\hat{\epsilon}\cdot\overleftrightarrow{Q}_{fi}\cdot\hat{k} \tag{2.17}$$

where:

$$\overleftrightarrow{Q}_{fi} = 3\left\langle f\middle|\int\rho(\vec{r})(r_i r_j - \frac{1}{3}\delta_{ij}r^2)\mathrm{d}\vec{r}\middle|i\right\rangle \tag{2.18}$$

is the quadrupole moment tensor. Because the electric quadrupole tensor is used as the transition operator, this is termed an E2 transition. This operator is invariant under a parity transformation, so E2 transitions must connect nuclear states of the same parity. In addition, $\overleftrightarrow{Q}_{fi}$ behaves as a rank-2 tensor, so changes of 2 units of the angular momentum of the nucleus are permitted, yielding the selection rule $|J_i - 2| < J_f < |J_i + 2|$.

The final remaining term is $H_{fi}^{(2b)}$. It can be decomposed into a part which looks like:

$$H_{fi}^{(2b)} \propto (\vec{k} \times \hat{\epsilon}) \cdot \left\langle f \left| \int (\vec{j} \times \vec{r}) \mathrm{d}\vec{r} \right| i \right\rangle \tag{2.19}$$

Using:

$$\vec{\mu_{fi}} = \left\langle f \left| \int (\vec{j} \times \vec{r}) \mathrm{d}\vec{r} \right| i \right\rangle \tag{2.20}$$

where $\vec{\mu_{fi}}$ is the magnetic dipole operator, this part of $H_{fi}^{(2b)}$ can be simplified to:

$$H_{fi}^{(2b)} \propto (\vec{k} \times \hat{\epsilon}) \cdot \vec{\mu_{fi}} \tag{2.21}$$

This transition matrix element is called the magnetic dipole (M1) because it involves the magnetic dipole operator and the B field of the photon (which points in the direction $\vec{k} \times \hat{\epsilon}$). The magnetic dipole operator is invariant under a parity transformation, so M1 can only connect states in a nucleus of the same parity. Also, M1 transitions can connect nuclear states with $|J_i - 1| < J_f < |J_i + 1|$. The remaining terms in $H_{fi}^{(2b)}$ can be decomposed entirely into E2 and M1 components.

In summary, there are only three types of photonuclear transitions relevant to this work: E1, M1, and E2 transitions. E1 transitions connect states of opposite parities and change the angular momentum of the nucleus by 1, M1 transitions connect states of the same parity and transfer 1 unit of angular momentum, and E2 transitions connect states of the same parity and transfer 2 units of angular

momentum. Neglecting final state densities, it is expected that E2 and M1 transitions combined will be less likely than E1 transitions by a factor of approximately $(kR)^2 = 0.06$.

2.3 General Aspects of Fission

Many models have been developed in the long history of the study of the fission process. It is useful to understand some of the early fission models to be able to better understand the more recent, advanced fission models. Section 2.3.1 will discuss the most basic model of the fission process: the liquid drop model. Section 2.3.2 will discuss a major improvement of this model developed by Strutinsky termed the macroscopic-microscopic model. This model is sufficient to explain fission fragment angular distributions, but it cannot make quantitative predictions of fission fragment angular distributions. More advanced fission models based on the macroscopic-microscopic concept are discussed in Section 2.3.3, and an overview of models based on other techniques are described in Section 2.3.4. These models are also unable to quantitatively predict fission fragment angular distributions.

2.3.1 Liquid Drop Model

The liquid drop model is the most fundamental fission model and provides a good introduction to the discussion of fission theories. In the liquid drop model, the nucleus is treated as a uniformly charged liquid drop, and the total energy is expressed as a sum of the following terms:

$$E = E_v + E_s + E_c \tag{2.22}$$

The volume term, E_v, accounts for the binding of the nucleons and depends only on the volume of the nucleus. Since the liquid drop is assumed to be incompressible, the volume of the drop is constant. In the fission process, only the terms which change as a function of deformation of the nucleus are not constant, so the volume term

may be neglected. The surface term, E_s, is a correction to the binding energy of the nucleus to account for lost binding energy near the surface of the drop. As the drop becomes more deformed, the surface area of the drop increases and the surface term correction further reduces the binding energy of the drop. The Coulomb term, E_c, represents the Coulomb repulsion in the uniformly charged drop, which decreases as the drop deforms.

The shape of the drop in this model is given by the radius from the center of the drop to the surface of the drop in the following expansion [3]:

$$R(\theta) = R_0 \left(1 + \sum_{\lambda} \epsilon_\lambda P_\lambda(\cos(\theta)) \right) \tag{2.23}$$

Here P_λ are the Legendre polynomials and ϵ_λ is a set of deformation parameters. R_0 is a constant. Using this parameterization of $R(\theta)$, the deformation energy of the liquid drop (the difference in energy between the deformed nucleus and the ground state nucleus) is:

$$E_{def}(\vec{\epsilon}) = E_s(\vec{\epsilon}) + E_c(\vec{\epsilon}) - E_s(0) - E_c(0) \tag{2.24}$$

where $\vec{\epsilon}$ is the set of deformation parameters.

As the nucleus fissions, it is assumed to pass through various values of $\vec{\epsilon}$ and thus various values of E_{def}. Based on calculations of $E_{def}(\vec{\epsilon})$ for the actinides, the contributions of odd-λ components to fission are negligible [1]. Figure 2.1 shows the $E_{def}(\vec{\epsilon})$ surface as a function of only ϵ_2 and ϵ_4. The fission path passes from the ground state through the saddle point of the surface, after which the nucleus fissions. This path can be parameterized into a generalized coordinate η which follows the dotted path shown in Figure 2.1. Using this generalized coordinate, the multidimensional potential energy surface can be reduced to a one dimensional quantity $E_{def}(\eta)$, shown in Figure 2.2. The saddle point is located at the maximum of the single fission barrier in η.

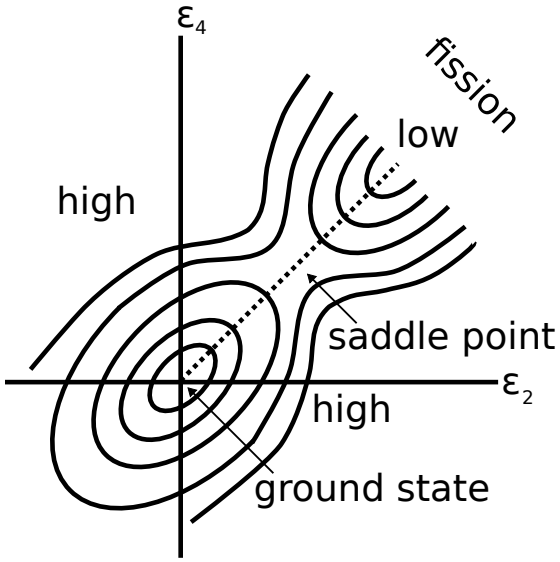

FIGURE 2.1: The potential energy surface for E_{def} is shown as a function of ϵ_2 and ϵ_4. The dotted line indicates the path of fission. Figure taken from [3].

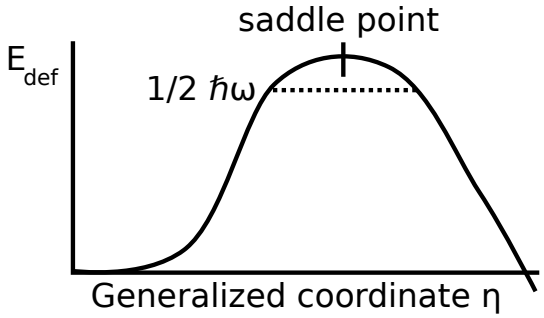

FIGURE 2.2: The fission barrier resulting from the potential energy surface in Figure 2.1 is shown. The saddle point is located at the maximum of the barrier. The curvature of the barrier is parameterized by $\hbar\omega/2$ as shown in Equation 2.25

This "single humped" fission barrier can be parameterized by a parabolic potential. There are two parameters in this model: the height and curvature of the barrier. The height of the barrier is given by E_f, and the curvature is described by the zero-point energy of the potential, $\hbar\omega_f/2$. The probability for tunneling through a parabolic potential barrier can be found using the WKB approximation and is given by [4]:

$$P(E) = \left(1 + e^{\frac{2\pi(E_f - E)}{\hbar\omega_f}}\right)^{-1} \tag{2.25}$$

The simplicity of the liquid drop model is useful for understanding the basics of the fission process, but there are several shortcomings of this model [3]. The primary shortcoming is that the odd-λ components are negligible. The odd-λ components correspond to mass-asymmetric shapes. Experimentally, there is typically a heavy fission fragment (A $\sim$ 140) and a light fission fragment (A $\sim$ 95). Therefore, the nucleus must be reflection-asymmetric during fission. An additional shortcoming is that the liquid drop model predicts that the ground state nucleus should have no deformation. However, ground state quadrupole deformations in actinide nuclei are known to exist and have been experimentally measured [5].

Experimental evidence suggests that shell effects cause the mass asymmetry in the fission fragments. As the mass of the fissioning nucleus increases, the extra nucleons are given preferentially to the light fragment instead of the heavy fragment. This suggests the influence of a shell closure which makes the heavy fragment particularly stable. A major improvement to the understanding of fission was made by including these shell effects, as described in the next section.

2.3.2 Strutinsky's Macroscopic-Microscopic Model

Generally, in a simple nuclear shell model, the average interaction between the nucleons is represented by a central potential ($V(r)$) and a spin-orbit potential

($V_{so}(r) \propto \vec{l} \cdot \vec{s}$). Single particle states can be calculated using this potential and the Schrödinger equation. The energy of the ground state of a nucleus is given by the energies of the single particle states multiplied by the occupancies of each state:

$$U = \sum_{\nu} n_\nu E_\nu \tag{2.26}$$

where ν indexes the states, including spin degrees of freedom, and n is the occupation number of each state. The nuclear shell model explains the existence of "magic numbers", which are nuclei that are especially stable due to the low level densities near the ground state.

Nilsson extended the spherical nuclear shell model to shapes with oblate and prolate deformations. In this updated model, the single particle energies were found to vary dramatically as a function of deformation. This led to new "magic numbers" for deformed nuclei. However, there was significant difficulty in applying the deformed shell-model calculations to fission [3]. This was due to the accumulation of small errors due to approximations in the shell model potential and neglected residual interactions. As a result, the shell model was considered to be less accurate than the liquid drop model for describing fission.

Strutinsky developed a model that combined both the shell model and the liquid drop model into a hybrid model, termed the macroscopic-microscopic model or the shell correction method. In this model, the energy of a particular configuration in single particle states and deformation $\vec{\epsilon}$ is given by [3]:

$$E = U - \widetilde{U} + E_{LDM} \tag{2.27}$$

where E_{LDM} is the liquid drop model energy given by Equation 2.22 and U is the shell model energy as in Equation 2.26. $\widetilde{U}$ is an "average" shell model energy calculated using a uniform distribution of states matched to an average density of true shell model single particle levels. The average density of states $\widetilde{g}(E)$ is given by smearing

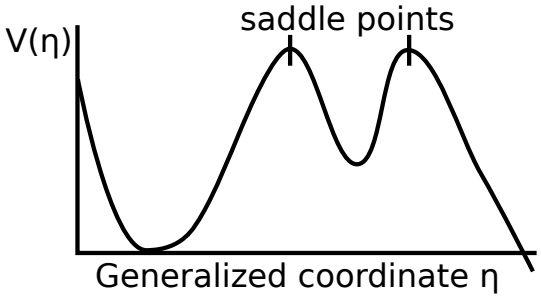

FIGURE 2.3: The fission barrier resulting from the macroscopic-microscopic model is shown.

the true density of states with a Gaussian:

$$\widetilde{g}(E) = \frac{1}{\sqrt{\pi}\sigma} \sum_{\nu} e^{(E-E_\nu)^2/\sigma^2} \tag{2.28}$$

The width of the smearing is given by σ. The average shell model energy $\widetilde{U}$ is given by:

$$\widetilde{U} = \int_{-\infty}^{\tilde{\lambda}} E\widetilde{g}(E)dE \tag{2.29}$$

The chemical potential $\widetilde{\lambda}$ is given by constraining the total number of nucleons N:

$$N = \int_{-\infty}^{\tilde{\lambda}} \widetilde{g}(E)dE \tag{2.30}$$

Through this procedure, the shell effects relevant for a particular deformation can be singled out, and the approximations used in the shell model (which previously led to inaccuracies) will be canceled out by $\widetilde{U}$. In regions where the density of single particle states is lower than average, the correction $\delta U = U - \widetilde{U}$ will be negative, corresponding to a tighter bound nucleus around these magic numbers. If the density of states is higher than average, the correction δU will be positive, reducing the binding energy of the nucleus.

Incorporating this shell correction leads to dramatic changes in the energy surface as a function of ϵ_2 and ϵ_4. The fission process can again be parameterized by the progress along the fission path by using the coordinate η. An example of the fission barrier ($V(\eta)$) for the macroscopic-microscopic model using the generalized deformation coordinate η is shown in Figure 2.3. First, it is clear that the ground state well has a nonzero deformation, leading to a nonzero quadrupole moment for the ground state. This corrects one of the problems with the liquid drop model. In addition, the barrier is now "double humped" with a potential well between the inner barrier and outer barrier [3].

The probability of penetrating a double humped barrier is different from that of a single humped barrier. The presence of internal structure in the nucleus modifies the penetration formalism. For the liquid drop model, it is assumed that the nucleus adiabatically passes through the multidimensional energy surface, and that there is no internal structure of the nucleus. In reality, internal configurations are possible, leading to excited states on top of the fission barrier [3]. These excited states are characterized by quantum numbers J^π and K, which are the angular momentum (J), parity (π), and projection of J on the symmetry axis of the nucleus (K). The transition states act as fission channels, and the total transmission coefficient for each J^π and K is given by [1]:

$$T^{J^\pi,K}(E) = \sum_i \frac{1}{1 + e^{\frac{2\pi(E_f + E_i - E)}{\hbar\omega_f}}} \tag{2.31}$$

where i indexes the fission channels with quantum numbers J^π and K and E_i is the excitation energy of a particular fission channel with respect to the height of the barrier, E_f. The transmission coefficients give the probability of tunneling through the barrier. For high densities of excited states, the sum may be replaced by an integral and the density of excited states with J^π and K may be included.

For two barriers, the WKB approximation can be used again to calculate the overall transmission coefficient through both barriers. Transmission resonances arise from the internal structure in the nucleus and appear in the potential well between the two barriers. These resonance can greatly increase the probability of tunneling through the first barrier, and thus increase the overall probability of barrier penetration. Only including the lowest fission channel for each J^π and K, the WKB approximation gives the total probability of barrier penetration as [3]:

$$P_F = \frac{P_A P_B}{4} \left(\left(\frac{P_A + P_B}{4} \right)^2 \sin^2 \phi + \cos^2 \phi \right)^{-1} \tag{2.32}$$

where $P_{A,B}$ is the probability of penetrating the first or second barrier using Equation 2.25. The phase ϕ is given by:

$$\phi = \int_{\eta_1}^{\eta_2} \left(\frac{2\mu}{\hbar^2} (E - V(\eta)) \right)^{1/2} \mathrm{d}\eta \tag{2.33}$$

Here $V(\eta)$ is the potential energy, η_1 is the point where $E = V(\eta)$ on the left side of the barrier, and η_2 is the point where $E = V(\eta)$ on the right side of the barrier. μ is the reduced mass. $V(\eta)$ is typically parameterized by three parabolas, one each for barrier A and B and another parabola for the well between the two barriers. The fission resonances are typically at lower energies than those used in our experiments, so it is appropriate to neglect these resonances by averaging over the phase ϕ in the above expressions. The average penetrability $\widetilde{P_F}$ is given by:

$$\widetilde{P_F} = \frac{1}{2\pi} \int_0^{2\pi} P_F(\phi) \mathrm{d}\phi \tag{2.34}$$

The averaging procedure yields:

$$\widetilde{P_F} = \frac{P_A P_B}{P_A + P_B} \tag{2.35}$$

In summary, the macroscopic-microscopic model includes shell corrections in an average way allowing it to model the fission process much more accurately. The next section will discuss some modern advancements based on this technique.

2.3.3 Modern Macroscopic-Microscopic Models

Modern macroscopic-microscopic models improve on Strutinsky's model by employing a significantly larger phase-space for shape deformations and including more accurate macroscopic and microscopic potentials. A recently developed macroscopic-microscopic model is presented in [6]. In this model, 2.6 million phase space points were explored in 5 deformation parameters: the quadrupole moment, mass asymmetry, left fragment deformation, right fragment deformation, and the neck size. The macroscopic model used was a finite range liquid drop model, and the microscopic model used was a folded Yukawa potential with spin-orbit, Coulomb, and pairing interactions [7]. The folded Yukawa potential consisted of an integral of a Yukawa potential over the nuclear volume. The potential energy of each point in the 5 dimensional lattice was calculated. Fragment masses were calculated by simulating water flows from the ground state location on the surface of the potential [6] or by assuming Brownian motion from the ground state position on the potential energy surface [8]. The barrier shapes are qualitatively similar to Figure 2.3. The outer barrier was calculated to be reflection-asymmetric, leading to a heavy fission fragment and a light fission fragment. The resulting fragment mass distributions agree well with experimental data. Specifically, they show previously observed experimental features of fission termed fission "modes".

Experimental measurements have shown the existence of fission modes. The three modes relevant for low energy fission of the actinides are the standard-I, standard-II, and superlong modes. Each mode is associated with different average fragment masses, average total kinetic energies, and average prompt neutron multiplicities

[9]. The standard-I and standard-II modes both yield asymmetric fragment masses, while the superlong mode yields symmetric fission masses. The standard-I mode has an average heavy fragment mass of ~ 134 and is associated with the spherical shell closure at $N = 82$, and the standard-II mode has an average heavy fragment mass of ~ 141 and is associated with the deformed shell closure at $N = 88$ [9] [10].

These different fission modes appear as valleys in the multidimensional potential energy surface. These valleys are separated by ridges, which typically prevent the fissioning nucleus from transferring between modes. The ability of these models to reproduce the different fission modes demonstrates the accuracy to which they can describe the multidimensional fission landscape.

2.3.4 Other Fission Models

The models considered so far have been static fission models, meaning that the multidimensional potential energy surface is constructed and the calculated observables are simply the result of passing through this precalculated surface. There are two other general types of fission models: statistical models and dynamical models. A brief overview of these classes of models will be provided here, but more detailed descriptions can be found in [11].

Statistical models assume that the fission system is in statistical equilibrium for almost all of its degrees of freedom. For these models, the deformation energy and level density at the equilibrium point must be given. Generally, these models are most applicable at the saddle point and at scission.

The scission point is defined to be the point along the fission path where the two nascent fragments have only one point in contact with each other. At the scission point, the "neck" connecting the two fission fragments ruptures, separating them. The fragment masses depend on the size of each fragment and the location of the rupture along the neck, while the kinetic energies depend on the distance between

the fragments when the neck ruptures. Models based on rupturing this neck agree well with experimental measurements of mass and total kinetic energy distributions (with some phenomenological parameters fit to the data) [11, 12]. These models can also be used to calculate the rate of fission at the saddle point after parameterization of the fission barrier. At the saddle point, the internal angular momentum of each fragment can be modeled, but the sharing of the total angular momentum between internal angular momentum and orbital angular momentum cannot be understood without a fully dynamical model [11].

Truly dynamical models attempt to calculate the entire path from the ground state to scission from a more *ab initio* standpoint. Currently, these models can be applied for two cases: to calculate spontaneous fission lifetimes, and when the excitation energies are high enough that quantum effects can be neglected [11]. Spontaneous fission lifetimes have been modeled using microscopic equations of motion from the time-dependent Hill-Wheeler theory. The primary difficulty in this theory, which uses an adiabatic collective Hamiltonian, lies in modeling the inertia tensor. Phenomenological models have been used with fit parameters to varying levels of success, sometimes achieving agreement with spontaneous fission lifetimes within one order of magnitude. Mass distributions from spontaneous fission have not been modeled well due to difficulty obtaining a consistent, dynamical description of fission from the saddle point to scission. A canonical model has been used to model fission at high excitation energies. Here both an inertia tensor and a friction tensor are required, increasing the difficulty to model accurately. Typical excitation energies for applicability of this model are $E > 50\,\mathrm{MeV}$ [11], which is much higher than the energies used in our experiments. Finally, current dynamical models are not able to predict fragment angular distributions, making the heuristic model developed in the following section more useful in the context of our work.

2.4 Photofission

This section will combine the theoretical models discussed in Section 2.2 and Section 2.3 into a consistent theoretical description of the photofission process. The Strutinsky approach and the double-humped fission barrier will be used as the primary fission theory from Section 2.3. This model will be used in Section 2.4.1 to visualize the fragment angular distributions in terms of the fission barrier. The main result from Section 2.2 is that, in photonuclear reactions, E1 absorption dominates over E2 and M1 absorption if final state densities in J^π are neglected. This result will also be used in Section 2.3 to constrain the angular momentum involved in the photofission process and to discuss the influence of fission channels on the angular distribution. The angular distributions from specific fission channels will be presented in Section 2.4.2 using the Bohr formalism [13]. The angular distributions from specific fission channels from the Kadmensky formalism [14, 15, 16], which uses different assumptions but yields similar results, are presented in Section 2.4.3. Finally, angular distribution calculations using assumed barrier shapes and the Bohr formalism are given in Section 2.4.4. These calculations serve as a qualitative prediction of fission fragment angular distributions for four different cases: ^{232}Th, ^{238}U, ^{240}Pu, and ^{239}Pu.

2.4.1 Fission Barrier Interpretation

Let us first consider the case of photofission of an even-even nucleus. In this case, E1 absorption of a photon will make a 1^- compound nuclear state, E2 absorption leads to 2^+ states, and M1 absorption leads to 1^+ states. After the nucleus absorbs the γ ray, it deforms and passes through the fission barrier.

A. Bohr postulated that at the maximum of the fission barrier, most of the excitation energy of the nucleus is in deformation energy rather than internal excitation

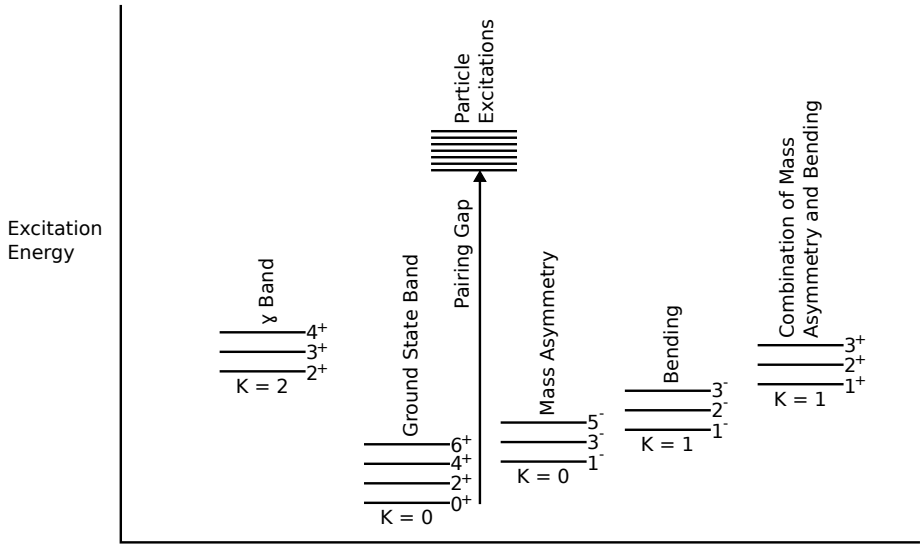

FIGURE 2.4: Expected excited states, or channels, for a prolate deformed even-even nucleus are shown. The differences in energies between the bands can vary for different deformations. Figure taken from [1].

energy [13]. Therefore, within a fission barrier, the nucleus is expected to be thermodynamically cold and in a low-lying excited state termed a fission "channel". Hereafter the terms channel and state will be used interchangeably. Because the nucleus is highly deformed within the fission barrier, the different possible channels are characterized by J^π and K. Calculations have revealed that the inner fission barrier in the Strutinsky model has only a small mass asymmetry but a large quadrupole deformation, while the outer barrier has a larger mass asymmetry and quadrupole deformation [3]. The spectrum of fission channels for such a deformed nucleus is shown in Figure 2.4.

The lowest energy fission channel at the top of the inner barrier is the $(J, K) = (2^+, 0)$ state, which belongs to the rotational band built on the ground state. The next excited state with low angular momentum is expected to be a mass-asymmetric state corresponding to a sloshing vibration [1]. The vibration inverts the slight mass-asymmetric pear shape of the nucleus, and so is expected to have quantum numbers

$J^\pi = 1^-$ and $K = 0$. The next state corresponds to a bending mode with $J^\pi = 1^-$ and $K = \pm 1$. γ vibrational states with $J^\pi = 2^+$ and $K = \pm 2$, which correspond to ellipsoidal shapes that break the axial symmetry of the prolate deformed nucleus, are also expected. Finally, combinations of mass asymmetric and bending modes leading to $J^\pi = 1^+$ and $K = \pm 1$ are expected.

Each of these different fission channels has a different angular distribution. The total photofission angular distribution depends on the relative contributions of each of these channels. The $J^\pi = 1^+$ channels are high in energy and must be populated by M1 absorption, so the contribution from these channels are assumed to be negligible. Note that from this point on in the text, the parity of the channel will be dropped, since it is no longer needed to distinguish M1 from E1 transitions. Because E2 photoabsorption is also less likely than E1, the only quadrupole channel which must be included is the $(2, 0)$ channel. The $(2, 0)$ channel is expected to have the lowest excitation energy of any channel at the top of the inner barrier.

It is expected that the nucleus can readjust its value of K between the inner and outer barriers. The quantum numbers J and M must be conserved due to conservation of angular momentum, but K may or may not be conserved [17]. K may change between the two barriers as the nucleus redistributes its internal energy. At the outer barrier, the mass asymmetry in the nucleus is expected to be much larger. This reduces the energy of the mass asymmetric band to roughly coincide with the ground state rotational band.

In the barrier model, these different fission channels at the top of the fission barrier are modeled by different barrier shapes. The barrier heights and curvatures govern the relative populations of the different channels and thus the angular distribution of the fission fragments. Knowledge of the barrier heights and curvatures for these different channels could be used to predict the fragment angular distribution. For example, because the $(2, 0)$ channel is lower than the $(1, 0)$ channel at the

inner barrier, the inner barrier height for the $(2,0)$ barrier should be lower than the $(1,0)$ inner barrier. At the outer barrier where these two states should be closer in excitation energy, their corresponding barrier heights should be closer as well.

Unfortunately, no calculation of the multidimensional fission landscape has been performed for channels of different J and K. Therefore, the macroscopic-microscopic models cannot provide a quantitative prediction of fission fragment angular distributions or prompt neutron angular polarization asymmetries. However, heuristic assumptions about the excitation energy of each channel, as made above, can provide estimates of fission fragment angular distributions.

For photofission of even-odd actinides, the pairing gap which pushes the single-particle excitations to high energies in Figure 2.4 is zero, so the single-particle excitations overlap with the ground state rotational band. It is assumed that some of the single-particle excitations have quantum numbers corresponding to dipole absorption, so the E2 channels are neglected for the even-odd actinides.

The angular distributions resulting from population of each of these fission channels will be calculated in Section 2.4.2 and Section 2.4.3. After these angular distributions are calculated, some calculations using this barrier model will be shown in Section 2.4.4.

2.4.2 Photofission Angular Distributions: Bohr Formalism

A. Bohr developed the first theory of photofission that was able to explain experimentally observed fission fragment angular distributions [13]. His theory revolves around the use of the fission channels labeled by (J,K) introduced in the previous section. There are two key assumptions in his model that are necessary to obtain fragment angular distributions: the fission process must proceed along the symmetry axis of the deformed nucleus, and the quantum number K must be well defined and conserved from the saddle point to scission [3]. The first assumption is based on

the fact that the fragment angular distribution is governed by their mutual Coulomb repulsion, which is directed primarily along the symmetry axis. The second assumption is more difficult to justify. It is assumed that the transition from saddle point to scission happens quickly, so there is not time for vibrations or shape changes to alter K, even though these changes would be physically allowed. The overall success of the model suggests that K is indeed conserved in the fission process, which implies physically that the descent from saddle to scission happens faster than nuclear rotations [17].

Under these two assumptions, the symmetry axis of the nucleus is equivalent to the momentum direction of the fission fragments, and can be found by using the Wigner rotation function $d^J_{M,K}(\theta)$. This function represents the probability of starting in a state (J, M) and ending up in a state (J, K) after rotation through an angle of θ relative to the z-axis, which is taken to be the beam axis. The Wigner functions are well-known quantum mechanical rotation functions given by [18]:

$$d^J_{M,K}(\theta) = \sum_n (-1)^{n-K+M} \frac{\sqrt{(J+K)!(J-K)!(J+M)!(J-M)!}}{(J+K-n)!n!(J-n-M)!(n-K+M)!} \tag{2.36}$$

$$\times \left(\cos\frac{\theta}{2}\right)^{2J-2n+K-M} \left(\sin\frac{\theta}{2}\right)^{2n-K+M} \tag{2.37}$$

The fragment angular distribution for photofission through a channel (J, M, K) using unpolarized photons is given by [17]:

$$W^J_{M,K}(\theta) = \frac{2J+1}{2} |d^J_{M,K}(\theta)|^2 \tag{2.38}$$

The contributions from (J, M, K) are given weights equal to those for $(J, M, -K)$, so:

$$W^J_{M,K}(\theta) = \frac{2J+1}{2} \left(\frac{|d^J_{M,K}(\theta)|^2}{2} + \frac{|d^J_{M,-K}(\theta)|^2}{2} \right) \tag{2.39}$$

Hereafter K will refer to $|K|$ and the $\pm K$ states will be given equal weights. To obtain contributions from individual channels (J, K), M is summed over:

$$W_K^J(\theta) = \sum_M P(J, M) W_{M,K}^J(\theta) \tag{2.40}$$

where $P(J, M)$ is the probability of forming the compound nucleus (J, M) from a nucleus with ground state spin and projection (I_0, μ) after absorbing a photon of multipolarity L and helicity ± 1. For fixed J, I_0, and L this is simply a squared Clebsch-Gordan coefficient.

Finally, the W_K^J functions can be adjusted to include the effects of polarized photons as used in our γ-ray beam. This procedure is detailed in [19]. First, the angular distribution must be decomposed into Legendre polynomials. Then, the effect of a linearly polarized photon is included by adjusting:

$$P_\nu(\cos\theta) \rightarrow P_\nu(\cos\theta) + \omega P_\gamma f_\nu(L, L) \cos 2\phi P_\nu^2(\cos\theta) \tag{2.41}$$

where ν is the order of the Legendre polynomial, ω is $+1$ for electric transitions and -1 for magnetic transitions, $f_\nu(L, L)$ are coupling coefficients which depend on the photon multipolarity [19], ϕ is the azimuthal coordinate, and P_ν^2 is an associated Legendre polynomial. Incorporating this procedure gives $W_K^J(\theta, \phi)$.

The differential photofission cross section is given by [3]:

$$\frac{d\sigma_{\gamma,f}}{d\Omega}(E_\gamma, \theta, \phi) = \sum_J \sum_K \frac{1}{2\pi} \Phi_{\gamma,f}(J, K, E_\gamma) W_K^J(\theta, \phi) \tag{2.42}$$

$\Phi_{\gamma,f}(J, K, E_\gamma)$ is the probability for the nucleus to fission for given quantum numbers J and K and an excitation energy E_γ. Fragment angular distribution measurements in photofission typically attempt to learn about the fission barrier structure for specific fission channels by measuring $\frac{d\sigma_{\gamma,f}}{d\Omega}(E_\gamma, \theta, \phi)$ and deducing $\Phi_{\gamma,f}(J, K, E_\gamma)$ based on the known functions $W_K^J(\theta, \phi)$ for polarized beams or $W_K^J(\theta)$ for unpolarized beams.

Table 2.1: Fragment angular distributions for even-even photofission in the Bohr formalism

J	K	$W_K^J(\theta,\phi)$	$\Sigma_K^J(90^\circ)$
1	0	$\frac{3}{4}\sin^2\theta + \cos 2\phi(\frac{3}{4}\sin^2\theta)$	1
1	1	$\frac{3}{4} - \frac{3}{8}\sin^2\theta + \cos 2\phi(-\frac{3}{8}\sin^2\theta)$	−1
2	0	$\frac{15}{16}\sin^2 2\theta + \cos 2\phi(\frac{15}{16}\sin^2 2\theta)$	-
2	1	$\frac{5}{4} - \frac{5}{8}\sin^2\theta - \frac{5}{8}\sin^2 2\theta + \cos 2\phi(\frac{5}{8}\sin^2\theta - \frac{5}{8}\sin^2 2\theta)$	1
2	2	$\frac{5}{8}\sin^2\theta + \frac{5}{32}\sin^2 2\theta + \cos 2\phi(-\frac{5}{8}\sin^2\theta + \frac{5}{32}\sin^2 2\theta)$	−1

The $W_K^J(\theta,\phi)$ functions also depend on the target spin. Here we will divide the discussion into two cases: even-even targets with zero target spin and even-odd targets with non-zero target spin. The introduction of target spin decreases the influence of the photon angular momentum on the angular distribution and thus decreases fragment anisotropies.

2.4.2.1 Even-Even Fragment Angular Distributions

For even-even targets, the form of $W_K^J(\theta,\phi)$ becomes much simpler. As discussed in Section 2.4.1, the dominant channels in even-even photofission are expected to be $(1,0)$, $(1,1)$, and $(2,0)$. The $(2,1)$ and $(2,2)$ channels are at high excitation energies (Figure 2.4) and are unlikely to contribute to the angular distribution.

$W_K^J(\theta,\phi)$ for these channels are given in Table 2.1. The polarization asymmetries from photofission of any of these channels except for $(2,0)$ are large. The combined angular distribution from the contribution of all the channels given in Table 2.1 can be written in the form:

$$W(\theta,\phi) = a + b\sin^2\theta + c\sin^2 2\theta + \cos 2\phi\left(d\sin^2\theta + c\sin^2 2\theta\right), \tag{2.43}$$

where c corresponds to pure quadrupole excitations and b is a mixed coefficient which contains dipole and quadrupole contributions. If the contributions from the $(2,1)$

and $(2,2)$ channels are neglected, this simplifies to:

$$W(\theta,\phi) = a + b\sin^2\theta + c\sin^2 2\theta + \cos 2\phi\left(b\sin^2\theta + c\sin^2 2\theta\right) \tag{2.44}$$

where b now is a pure dipole coefficient. $\Sigma_K^J(\theta)$ is called the polarization asymmetry and defined to be:

$$\Sigma_K^J(\theta) = \frac{W(\theta,0) - W(\theta,\pi/2)}{W(\theta,0) + W(\theta,\pi/2)} \tag{2.45}$$

and, using Equation 2.44,

$$\Sigma_K^J(\theta) = \frac{2b\sin^2\theta + 2c\sin^2 2\theta}{2a + 2b\sin^2\theta + 2c\sin^2 2\theta} \tag{2.46}$$

If the $W_K^J(\theta,\phi)$ are weighted by the number of K-states and summed together for a particular J, the result is an isotropic angular distribution. At higher energies, the density of states increases and there are expected to be equal numbers of states with different K. Assuming equal populations of these different K-projections for a given J, the result is an isotropic angular distribution. In the barrier model of fission channels, at high energies the barrier penetrability is independent of small differences in barrier heights or curvatures, so the channels would each have equal contributions to the angular distribution. This also would result in an isotropic angular distribution. In summary, isotropic angular distributions are expected in the presence of many states or at large excitation energies.

2.4.2.2 Even-Odd Fragment Angular Distributions

Even-odd fragment angular distributions are typically more isotropic because of the additional angular momentum given by the ground state spin of the target. In addition, in even-odd targets, the level density at the saddle point is expected to be much larger because there is no pairing gap. The dense region of particle excitations shown in Figure 2.4 is coincident with the ground state band, as mentioned in Section 2.4.1.

Table 2.2: Fragment angular distributions for spin-1/2 photofission in the Bohr formalism

J	K	$W_K^J(\theta,\phi)$	$\Sigma_K^J(90^\circ)$
$\frac{3}{2}$	$\frac{3}{2}$	$\frac{1}{2}-\frac{1}{4}\sin^2\theta+\cos 2\phi(-\frac{1}{4}\sin^2\theta)$	-1
$\frac{3}{2}$	$\frac{1}{2}$	$\frac{1}{6}+\frac{1}{4}\sin^2\theta+\cos 2\phi(\frac{1}{4}\sin^2\theta)$	$\frac{3}{5}$
$\frac{1}{2}$	$\frac{1}{2}$	$\frac{1}{6}$	0

The $(2,0)$, $(2,1)$, and $(2,2)$ states will be neglected, leaving only the electric dipole transition states $(1,0)$ and $(1,1)$, because the probability for quadrupole photoabsorption is small and there are dipole states available.

The ground state of ^{239}Pu has the smallest angular momentum ($1/2^+$) of the even-odd targets. Upon dipole absorption of a photon, the channels $(3/2,3/2)$, $(3/2,1/2)$, and $(1/2,1/2)$ can be formed. The angular distributions from those channels are listed in Table 2.2. Again, summing all of the $W_K^J(\theta,\phi)$ together yields an isotropic distribution. Generally, the polarization asymmetries are smaller than what was shown in Table 2.1. Note that one polarization asymmetry is positive, another is negative, and the third is 0.

The calculations for ^{233}U and ^{237}Np can be grouped because both of these nuclei have ground state spin $5/2^+$. A total of 9 fission channels can be made in electric dipole photofission from these nuclei. The angular distributions from these channels are shown Table 2.3. As before, the angular distributions are isotropic if all of the states are populated with equal probabilities, and the polarization asymmetries from any given state are, on average, smaller than for even-even or spin-1/2 actinides.

Finally, the calculation of expected channels for ^{235}U ($7/2^-$) is shown in Table 2.4. 12 fission channels can be made from electric dipole photoabsorption. Again, the polarization asymmetries are on average smaller and the angular distribution is isotropic

Table 2.3: Fragment angular distributions for spin-5/2 photofission in the Bohr formalism

J	K	$W_K^J(\theta,\phi)$	$\Sigma_K^J(90^\circ)$
$\frac{7}{2}$	$\frac{7}{2}$	$\frac{1}{3}-\frac{1}{6}\sin^2\theta+\cos 2\phi(-\frac{1}{6}\sin^2\theta)$	-1
$\frac{7}{2}$	$\frac{5}{2}$	$\frac{5}{21}-\frac{5}{210}\sin^2\theta+\cos 2\phi(-\frac{5}{210}\sin^2\theta)$	$\frac{1}{9}$
$\frac{7}{2}$	$\frac{3}{2}$	$\frac{11}{63}+\frac{1}{14}\sin^2\theta+\cos 2\phi(\frac{1}{14}\sin^2\theta)$	$\frac{9}{31}$
$\frac{7}{2}$	$\frac{1}{2}$	$\frac{1}{7}+\frac{5}{42}\sin^2\theta+\cos 2\phi(\frac{5}{42}\sin^2\theta)$	$\frac{5}{11}$
$\frac{5}{2}$	$\frac{5}{2}$	$\frac{1}{14}+\frac{1}{7}\sin^2\theta+\cos 2\phi(\frac{1}{7}\sin^2\theta)$	$\frac{2}{3}$
$\frac{5}{2}$	$\frac{3}{2}$	$\frac{13}{70}-\frac{1}{35}\sin^2\theta+\cos 2\phi(-\frac{1}{35}\sin^2\theta)$	$-\frac{2}{11}$
$\frac{5}{2}$	$\frac{1}{2}$	$\frac{17}{70}-\frac{4}{35}\sin^2\theta+\cos 2\phi(-\frac{4}{35}\sin^2\theta)$	$-\frac{8}{9}$
$\frac{3}{2}$	$\frac{3}{2}$	$\frac{11}{90}-\frac{1}{60}\sin^2\theta+\cos 2\phi(-\frac{1}{60}\sin^2\theta)$	$-\frac{3}{19}$
$\frac{3}{2}$	$\frac{1}{2}$	$\frac{1}{10}+\frac{1}{60}\sin^2\theta+\cos 2\phi(\frac{1}{60}\sin^2\theta)$	$-\frac{1}{7}$

for an equal population of the states.

2.4.3 Photofission Angular Distributions: Kadmensky Formalism

Kadmensky [14, 15, 16] discovered a potential flaw of the Bohr formalism presented above. Specifically one of the key assumptions of the Bohr formalism - that the fragments are emitted along the symmetry axis of the parent nucleus - is not accurate. In reality, the uncertainty relation imposes a strict connection between the angle of emission of the fragments and the orbital angular momentum of the parent nucleus. If the orbital angular momentum of the nucleus is completely unknown ($0 < l_m < \infty$), then the angle of emission of the fission fragments can be known completely. However, if some information about l_m is known, then the angle of emission of the fragments relative to the symmetry axis of the nucleus cannot be completely specified and must have some uncertainty. This means that the fragments are not always emitted exactly along the symmetry axis of the nucleus.

Table 2.4: Fragment angular distributions for spin-7/2 photofission in the Bohr formalism

J	K	$W_K^J(\theta,\phi)$	$\Sigma_K^J(90^\circ)$
$\frac{9}{2}$	$\frac{9}{2}$	$\frac{5}{16} - \frac{5}{32}\sin^2\theta + \cos 2\phi(-\frac{5}{32}\sin^2\theta)$	-1
$\frac{9}{2}$	$\frac{7}{2}$	$\frac{35}{144} - \frac{5}{96}\sin^2\theta + \cos 2\phi(-\frac{5}{96}\sin^2\theta)$	$-\frac{3}{11}$
$\frac{9}{2}$	$\frac{5}{2}$	$\frac{55}{288} + \frac{5}{192}\sin^2\theta + \cos 2\phi(\frac{5}{192}\sin^2\theta)$	$\frac{3}{25}$
$\frac{9}{2}$	$\frac{3}{2}$	$\frac{5}{32} + \frac{5}{64}\sin^2\theta + \cos 2\phi(\frac{5}{64}\sin^2\theta)$	$\frac{1}{3}$
$\frac{9}{2}$	$\frac{1}{2}$	$\frac{5}{36} + \frac{5}{48}\sin^2\theta + \cos 2\phi(\frac{5}{48}\sin^2\theta)$	$\frac{3}{7}$
$\frac{7}{2}$	$\frac{7}{2}$	$\frac{1}{18} + \frac{1}{6}\sin^2\theta + \cos 2\phi(\frac{1}{6}\sin^2\theta)$	$\frac{3}{4}$
$\frac{7}{2}$	$\frac{5}{2}$	$\frac{19}{126} + \frac{1}{42}\sin^2\theta + \cos 2\phi(\frac{1}{42}\sin^2\theta)$	$\frac{3}{22}$
$\frac{7}{2}$	$\frac{3}{2}$	$\frac{3}{14} - \frac{1}{14}\sin^2\theta + \cos 2\phi(-\frac{1}{14}\sin^2\theta)$	$-\frac{1}{2}$
$\frac{7}{2}$	$\frac{1}{2}$	$\frac{31}{126} - \frac{5}{42}\sin^2\theta + \cos 2\phi(-\frac{5}{42}\sin^2\theta)$	$-\frac{15}{16}$
$\frac{5}{2}$	$\frac{5}{2}$	$\frac{33}{224} - \frac{15}{448}\sin^2\theta + \cos 2\phi(-\frac{15}{448}\sin^2\theta)$	$-\frac{5}{17}$
$\frac{5}{2}$	$\frac{3}{2}$	$\frac{27}{224} + \frac{3}{448}\sin^2\theta + \cos 2\phi(\frac{3}{448}\sin^2\theta)$	$\frac{1}{19}$
$\frac{5}{2}$	$\frac{1}{2}$	$\frac{3}{28} + \frac{3}{112}\sin^2\theta + \cos 2\phi(\frac{3}{112}\sin^2\theta)$	$\frac{1}{5}$

The notation of Equation 2.42 will be used for consistency, even though it is different from [14, 15]. The unpolarized differential cross section is given by:

$$\frac{d\sigma_{\gamma,f}}{d\Omega}(E_\gamma,\theta) = \sum_J \sum_K \frac{1}{2\pi}\Phi_{\gamma,f}(J,K,E_\gamma)T_K^J(\theta) \tag{2.47}$$

using

$$T_K^J(\theta) = \sum_M P(J,M)T_{M,K}^J(\theta) \tag{2.48}$$

and

$$T_{M,K}^J(\theta) = \frac{2J+1}{2}\left(\frac{|d_{M,K}^J(\theta)|^2}{2} + \frac{|d_{M,-K}^J(\theta)|^2}{2}\right) \tag{2.49}$$

At this point in the derivation, the Kadmensky angular distribution $T_{M,K}^J$ is still

equivalent to the Bohr angular distribution. It can be rewritten as:

$$T^J_{M,K}(\theta) = \frac{2J+1}{4} \int \left(|d^J_{M,K}(\theta - \theta')|^2 + |d^J_{M,-K}(\theta - \theta')|^2 \right) \times \left(\delta(\cos\theta' - 1) + \delta(\cos\theta' + 1) \right) \frac{\mathrm{d}\Omega'}{4\pi} \tag{2.50}$$

where θ' is the angle between the direction of emission of the fragments and the symmetry axis of the nucleus. In the Bohr formalism, θ' must be fixed to be $0\,^\circ$ or $180\,^\circ$, which is ensured by the δ functions. These δ functions can be expanded into spherical harmonics using:

$$\delta(\cos\theta' \mp 1) = \sum_{l=0}^{l_m} 2\pi Y_{l0}(\cos\theta') Y_{l0}(\pm 1) \tag{2.51}$$

taking $l_m \to \infty$. This expansion directly connects the maximum angular momentum involved in the process (l_m) with the δ function which defines the emission angle of the fragments relative to the symmetry axis. Using this δ function means that all values of l_m are possible.

However, in the fission process, infinite values for l_m are not possible. The maximum orbital angular momentum possible in the system can be estimated based on the final spins of the fragments, the spins carried off by prompt γ rays emitted by the fragments, the spins carried off by prompt neutrons emitted by the fragments, and the spin of the parent nucleus. Kadmensky estimates l_m to be roughly 25 in [15] and approximately 30 in [16]. Therefore, l_m should not be allowed to tend to infinity and it should be constrained by this maximum value.

The constraint on l_m is imposed by modifying $T^J_{M,K}$:

$$T^J_{M,K}(\theta) = \frac{2J+1}{4} \int \left(|d^J_{M,K}(\theta - \theta')|^2 + |d^J_{M,-K}(\theta - \theta')|^2 \right) F^2_{l_m}(\theta') \mathrm{d}\Omega' \tag{2.52}$$

where $F^2_{l_m}(\theta')$ is a smeared δ function given by:

$$F_{l_m}(\theta') = b(l_m)\sum_{l=0}^{l_m} Y_{l0}(\cos\theta')Y_{l0}(1)\left(1+\pi\pi_1\pi_2(-1)^l\right) \tag{2.53}$$

Here π is the parity of the parent nucleus, π_1 is the parity of the first fission fragment, and π_2 is the parity of the second fission fragment. $b(l_m)$ is a normalization factor to ensure $\int F^2_{l_m}(\theta')\mathrm{d}\Omega' = 1$.

After significant algebraic manipulation, this can be simplified to:

$$T^J_{M,K}(\theta) = \sum_L B_{JMKL}P_L(\cos\theta) \tag{2.54}$$

with

$$\begin{aligned} B_{JKML} = {} & \frac{2J+1}{4}|b(l_m)|^2 \sum_{l=0}^{l_m}\sum_{l'=0}^{l_m}\sum_{jL} C^{jK}_{Jl'K0}C^{jK}_{JlK0}C^{L0}_{ll'00}C^{JM}_{JLM0} \\ & \times \begin{Bmatrix} l & j & J \\ J & L & l' \end{Bmatrix} (2l+1)(2l'+1)\sqrt{\frac{2L+1}{2J+1}}(-1)^{j+J} \\ & \times (1+\pi\pi_1\pi_2(-1)^l)(1+\pi\pi_1\pi_2(-1)^{l'}) \end{aligned} \tag{2.55}$$

C is a Clebsch-Gordan coefficient and $\begin{Bmatrix} a & b & c \\ d & e & f \end{Bmatrix}$ is a 6-j symbol. The effects of a linearly polarized beam can be included using Equation 2.41 or the equivalent formalism presented in [16].

Table 2.5 shows the angular distributions resulting from the Kadmensky formalism. They are presented as a function of l_m with two cases shown: $l_m \to \infty$ and $l_m = 30$. As expected, the $l_m \to \infty$ case reproduces the Bohr formalism angular distributions from Table 2.1. The $l_m = 30$ angular distributions are different from the Bohr case, but these discrepancies are found to be small. Kadmensky presents results

Table 2.5: Fragment angular distributions for even-even photofission in the Kadmensky formalism

l_m	J	K	$W_K^J(\theta,\phi)$
∞	1	0	$0.75\sin^2\theta + \cos 2\phi(0.75\sin^2\theta)$
30	1	0	$0.02 + 0.71\sin^2\theta + \cos 2\phi(0.71\sin^2\theta)$
∞	1	1	$0.75 - 0.38\sin^2\theta + \cos 2\phi(-0.38\sin^2\theta)$
30	1	1	$0.74 - 0.36\sin^2\theta + \cos 2\phi(-0.36\sin^2\theta)$
∞	2	0	$0.94\sin^2 2\theta + \cos 2\phi(0.94\sin^2 2\theta)$
30	2	0	$0.06 - 0.02\sin^2\theta + 0.85\sin^2 2\theta + \cos 2\phi(0.01\sin^2\theta + 0.85\sin^2 2\theta)$
∞	2	1	$1.25 - 0.63\sin^2\theta - 0.63\sin^2 2\theta + \cos 2\phi(0.63\sin^2\theta - 0.63\sin^2 2\theta)$
30	2	1	$1.20 - 0.58\sin^2\theta - 0.57\sin^2 2\theta + \cos 2\phi(0.59\sin^2\theta - 0.57\sin^2 2\theta)$
∞	2	2	$0.63\sin^2\theta + 0.16\sin^2 2\theta + \cos 2\phi(-0.63\sin^2\theta + 0.16\sin^2 2\theta)$
30	2	2	$0.03 + 0.59\sin^2\theta + 0.14\sin^2 2\theta + \cos 2\phi(-0.59\sin^2\theta + 0.14\sin^2 2\theta)$

for even smaller values of l_m down to $l_m = 4$ in [15], which differ significantly from the Bohr formalism, but an l_m of 4 is too low to be physically reasonable. Despite the advances in Kadmensky's formalism, the good agreement between Kadmensky and Bohr for reasonable l_m suggests that the Bohr formalism is adequate. Kadmensky does not extend these calculations to even-odd nuclei. Because of the relatively good agreement between the two formalisms for reasonable l_m, good agreement is assumed in the case of even-odd nuclei for the two formalisms.

2.4.4 Fragment Angular Distribution Predictions

Calculations using the formalism developed earlier in the chapter will be presented to illustrate the differences in behavior between the even-even and even-odd actinides studied in this work. These calculations are not meant to precisely reproduce observed fragment angular distributions, but rather to illustrate how the fission barriers

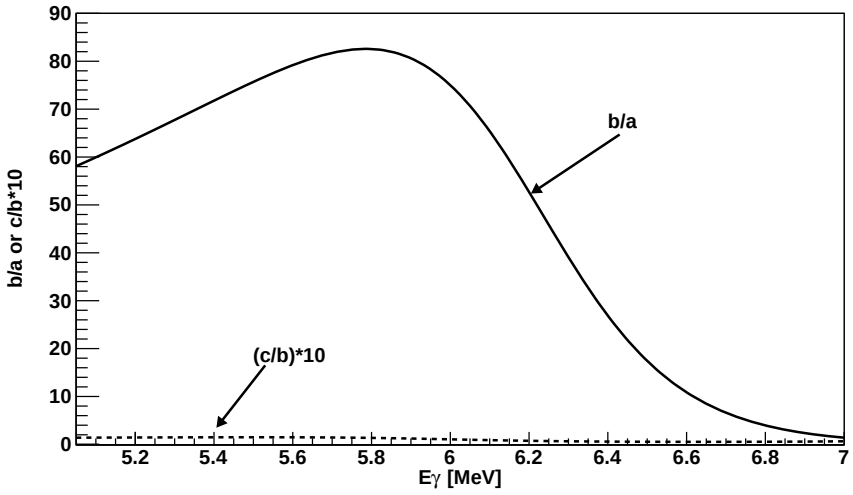

FIGURE 2.5: A calculation of fragment angular distribution coefficients for ^{232}Th based on a simplified model is shown. b/a is shown by the solid line, and c/b is the dashed line. The c/b value has been scaled up by a factor of 10.

Table 2.6: Barrier parameters for a fragment angular distribution calculation for ^{232}Th

J	K	E_{B1} (MeV)	$\hbar\omega_1$ (MeV)$^{-1}$	E_{B2} (MeV)	$\hbar\omega_2$ (MeV)$^{-1}$
1	0	5.47	0.94	6.30	1.05
1	1	5.80	1.12	7.31	1.18
2	0	3.60	1.20	6.06	1.00
2	1	3.60	1.06	7.60	0.70
2	2	3.42	1.17	6.08	1.05

for different channels can impact the fragment angular distribution. Equation 2.25 is used as the penetrability for a single barrier of height E_B and curvature $\hbar\omega$, and Equation 2.35 is used to calculate the penetrability of a double humped barrier. The angular distributions for each fission channel are taken from Section 2.4.2. Different angular distributions from different fission modes, as discussed in Section 3.5, are ne-

glected in this relatively simple calculation. A constant ratio of electric quadrupole absorption to electric dipole absorption of 0.03 was assumed over all calculated γ-ray energies.

In ^{232}Th, the inner barrier is expected to be lower than the outer barrier. Section 2.4.1 discusses the expected ordering of fission channels at the inner and outer barrier. At the inner barrier the $(2,0)$ state should be lowest in energy, followed by the $(1,0)$ and $(1,1)$ states. If, as discussed in that section, K is forgotten between the inner and outer barrier, the inner barrier should have the same barrier heights and curvatures for different values of K but the same values of J. At the outer barrier, states with different (J,K) can have different barrier heights and curvatures, but the $(2,0)$ and $(1,0)$ states should have approximately the same barrier height. These assumptions based on Section 2.4.1 are used in generating a barrier parameterization for ^{232}Th shown in Table 2.6. The angular distribution coefficients are shown in Figure 2.5. As the beam energy decreases from 7 MeV, selective population of the $(1,0)$ state over the $(1,1)$ state leads to a nonzero b coefficient. The height of the highest barrier, the outer barrier, is the same for the $(2,0)$ and $(1,0)$ states and the probability of quadrupole photoabsorption is low, so there is no significant quadrupole contribution to fission. Figure 2.5 agrees well with measured angular distribution coefficients presented in Section 3.2 (Figure 3.1).

The calculations for ^{238}U and ^{240}Pu differ from the ^{232}Th case in that the second barrier is expected to be lower than the first barrier. Again, at the inner barrier the $(2,0)$ state should be lower in energy than the $(1,0)$ state, while at the outer barrier they should be roughly degenerate. Based on these assumptions, the barrier parameters used to calculate the angular distribution for photofission of ^{238}U are given in Table 2.7. The calculations yield angular distributions coefficients shown as a function of energy in Figure 2.6. As the beam energy decreases from 7 MeV, first the dipole coefficient increases due to selective population of the $(1,0)$ channel

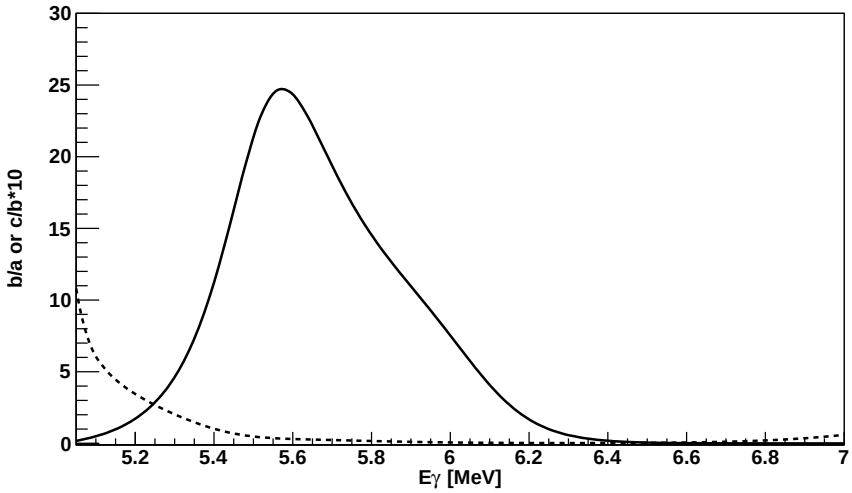

FIGURE 2.6: A calculation of fragment angular distribution coefficients for ^{238}U based on a simplified model is shown. b/a is shown by the solid line, and c/b is the dashed line. The c/b value has been scaled up by a factor of 10.

Table 2.7: Barrier parameters for a fragment angular distribution calculation for ^{238}U

J	K	E_{B1} (MeV)	$\hbar\omega_1$ (MeV)$^{-1}$	E_{B2} (MeV)	$\hbar\omega_2$ (MeV)$^{-1}$
1	0	5.56	0.37	5.34	0.41
1	1	5.71	0.51	6.38	0.53
2	0	4.99	0.61	5.49	0.51
2	1	5.64	0.64	5.78	1.11
2	2	5.60	0.31	5.55	0.40

over the $(1,1)$ channel. As the beam energy decreases further, the contribution of the quadrupole channels increases because of their lower inner barrier heights, and selective population of the $(2,0)$ state leads to a significant quadrupole fission component. Figure 2.6 is in good agreement with data presented in Section 3.2 (Figure 3.2).

The calculations for ^{240}Pu are qualitatively similar to those presented for ^{238}U.

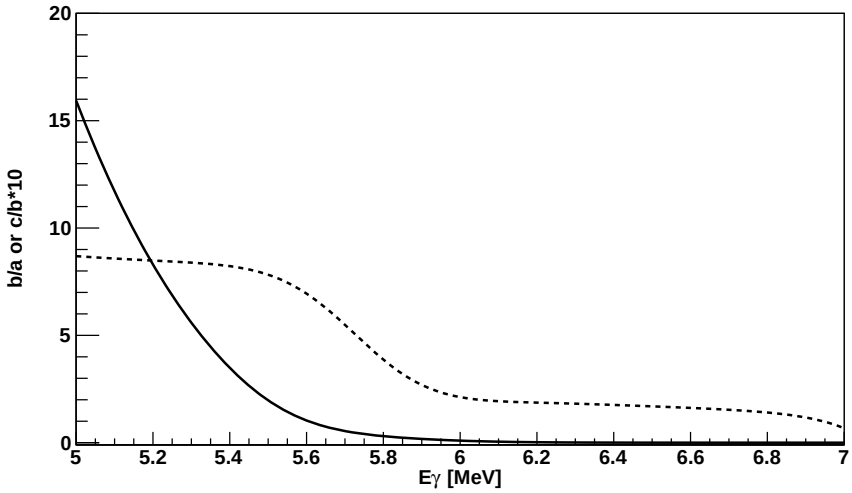

FIGURE 2.7: A calculation of fragment angular distribution coefficients for ^{240}Pu based on a simplified model is shown. b/a is shown by the solid line, and c/b is the dashed line. The c/b value has been scaled up by a factor of 10.

Table 2.8: Barrier parameters for a fragment angular distribution calculation for ^{240}Pu

J	K	E_{B1} (MeV)	$\hbar\omega_1$ (MeV)$^{-1}$	E_{B2} (MeV)	$\hbar\omega_2$ (MeV)$^{-1}$
1	0	5.99	0.62	4.97	0.52
1	1	6.00	0.70	5.92	0.50
2	0	5.59	0.75	5.06	0.67
2	1	6.09	0.72	3.43	1.15
2	2	5.57	0.74	5.28	1.16

The barrier parameters used to calculate the angular distribution from photofission of ^{240}Pu are given in Table 2.8. The calculations yield angular distributions coefficients shown as a function of energy in Figure 2.7. Figure 2.7 is in good agreement with data presented in Section 3.2 (Figure 3.3).

Finally, a calculation for ^{239}Pu is shown in Figure 2.8. The barrier parameters

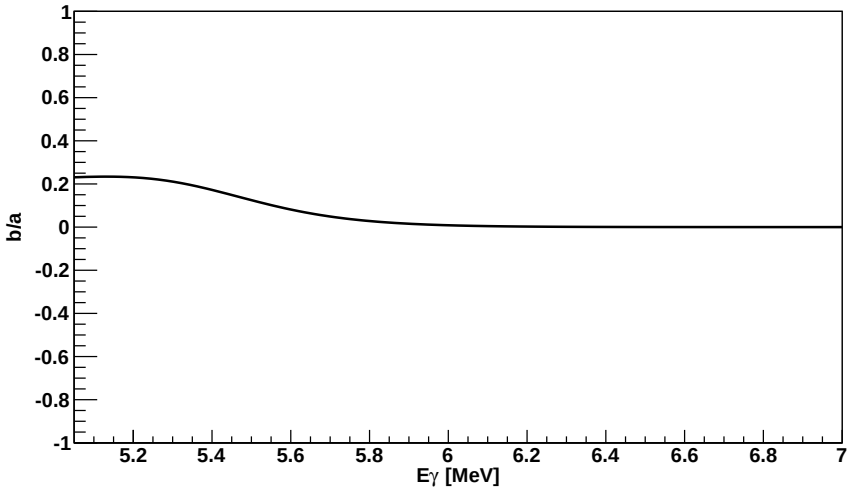

FIGURE 2.8: A calculation of fragment angular distribution coefficients for ^{239}Pu based on a simplified model is shown. The b/a value is indicated by the solid line.

Table 2.9: Barrier parameters for a fragment angular distribution calculation for ^{239}Pu

J	K	E_{B1} (MeV)	$\hbar\omega_1$ (MeV)$^{-1}$	E_{B2} (MeV)	$\hbar\omega_2$ (MeV)$^{-1}$
$\frac{1}{2}$	$\frac{1}{2}$	5.20	1.00	4.80	1.00
$\frac{3}{2}$	$\frac{1}{2}$	5.40	1.00	4.80	1.00
$\frac{3}{2}$	$\frac{3}{2}$	5.60	1.00	4.80	1.00

used to calculate this barrier are shown in Table 2.9. There is no heuristic argument for the relative order or spacing between the different states, so one possible set of barrier parameters was chosen simply to illustrate the relative lack of anisotropy for the case of an even-odd nucleus. The angular distribution resulting from this barrier parameterization is much more isotropic than those for ^{232}Th, ^{238}U, or ^{240}Pu. The fact that the angular distribution is more isotropic is in good agreement with data presented in Section 3.2, though the shape of the angular distribution is not in agreement with previous measurements on ^{239}Pu. This may be due to a potential

fission resonance in ^{239}Pu (Section 3.6).

2.5 Prompt Neutron Emission in Fission

In addition to the fission fragments, prompt neutrons can be emitted in a fission event. These neutrons are called prompt because they are emitted at approximately the same time as the fission event. Other neutrons may be emitted on the order of μs or ms after the fission event; these are called delayed neutrons. The number of prompt neutrons varies with the mass of the fission nucleus, the incident particle, the excitation energy of the nucleus, the fission mode, and other dynamical aspects of the fission event. The average number of prompt neutrons emitted for the nuclei studied over our energy range is approximately $2-4$ per fission event.

The prompt neutrons are expected to be emitted by nearly fully accelerated fragments based on the timescales associated with the acceleration of the fission fragments and prompt neutron emission. It is estimated that the nucleus passes from the saddle point to scission within $\sim 10^{-20}$ s [3]. The acceleration of the fission fragments can be modeled based on the masses and charges of the nascent fission fragments. Calculations by the author and in [3] show that the fragments achieve $\sim 95\%$ of their terminal kinetic energies within $\sim 10^{-20}$ s after scission.

The other relevant timescale is the time it takes for the prompt neutrons to be emitted from the fragments. Prompt neutron emission from the excited fission fragments is modeled as an evaporation process analogous to the evaporation of electrons from the surface of a heated solid. This is modeled using the Richardson equation [3]:

$$j = \frac{2\pi m}{h^3}(kT)^2 e^{\frac{-E_B}{kT}} \tag{2.56}$$

where j is the current (number) density for electrons (neutrons), m is the mass of the evaporated particle, T is the temperature of the heated material, and E_B is

the binding energy of the evaporated particle. The temperature is related to the excitation energy of the fission fragment. The number of neutrons emitted per unit time is then [3]:

$$1/\tau_n = 4\pi R^2 j \tag{2.57}$$

where R is the nuclear radius. To model evaporation neutrons, kT is taken to be approximately 1 MeV, E_B is roughly 6 MeV, and $R \sim 6$ fm. This yields a neutron evaporation time τ_n of $\sim 10^{-18}$ s. This timescale can also be approximated using the uncertainty principle, $\tau_n \sim \hbar/\Lambda_n$. Λ_n is the neutron width of states in the excited fragments and is estimated to be $1-100$ eV. This leads to a minimum of $\tau_n \sim 10^{-18}$ s.

Based on these estimates of the neutron emission timescale and the fragment acceleration timescale, it is generally assumed that the prompt neutrons are emitted from nearly or fully accelerated fission fragments. The neutron energy in the lab frame is given by its energy in the rest frame of the fragment and the fragment kinetic energy. The neutron spectrum in the rest frame of the fragment in the evaporation model is given by [20]:

$$P(\epsilon) \propto \epsilon e^{-\epsilon/T_f^{max}} \tag{2.58}$$

where T_f^{max} is the maximum possible temperature of the daughter nucleus and ϵ is the energy of the neutron in the rest frame of the fragment. This can be understood as the product of the normal Maxwell-Boltzmann distribution of particle energies at a given temperature ($\sqrt{(}\epsilon)e^{-\epsilon/T}$) and the velocity of the particles ($\sqrt{(}\epsilon)$) which biases evaporation to the faster moving neutrons. The maximum temperature in the daughter is used instead of the temperature of the parent nucleus for two reasons: first, the level densities of the parent and daughter nuclei are different, and second the separation energy of the neutron must be taken into account. Details of the derivation are given in [20].

It is also assumed that the prompt neutrons are emitted with no preferred direc-

tion in the rest frame of the fragments because they are considered to be evaporation neutrons. If it is assumed that all fission fragments have the same kinetic energy per nucleon, then the neutron energy spectrum in the laboratory frame is given by a Watt spectrum:

$$N(E) = \frac{2A^{3/2}}{\pi B^{1/2}} e^{-\frac{B}{4A}} e^{-AE} (\sinh(BE))^{1/2} \tag{2.59}$$

where A and B are adjustable parameters. This functional form describes the prompt neutron energy spectrum well [3].

Experiments have confirmed that the vast majority of prompt neutrons are emitted after the fragments have nearly fully accelerated and the neutrons are emitted with no preferred direction in the rest frame of the fragment. Many experiments have been performed to measure the prompt neutron energy spectrum and neutron-fragment angular correlations. They are all largely consistent with models based on the preceding assumptions, with small differences (generally $< 5\%$) attributed to scission neutrons, which are discussed further in Section 3.8. [1] and [3] contain a more complete discussion of these experiments. However, the important point is that these experiments confirm the assumptions used in our model.

3

Previous Photofission Measurements

3.1 Introduction

Many fission measurements have been performed in the long history of the study of the fission process. Here, several measurements specifically relevant to the study of prompt neutron polarization asymmetries will be highlighted and discussed, though prompt neutron polarization asymmetries have not been previously measured. Section 2.5 discussed that the prompt neutrons are expected to be emitted with no preferred direction in the rest frame of the fragments after the fragments have fully accelerated. As a result of the kinematics, the prompt neutron angular distribution should be correlated with the fragment angular distribution, making previous measurements of fragment angular distributions relevant to our work. Section 3.2 provides an overview of previous photofission fragment angular distribution measurements on the targets used in our experiments, with specific attention given to experiments that either 1) used a bremsstrahlung beam and tried to unfold the beam energy distribution from the measured angular distribution or 2) used a quasi-monoenergetic beam. Our experiments used a quasi-monoenergetic beam, and it

is difficult to directly compare our results with those taken with a beam with a broad energy spread, such as a bremsstrahlung beam without unfolding. The implications of the angular distribution measurements on the fission barrier structure are described in Section 3.3. These angular distributions are also compared to the calculations in Section 2.4.4 and good agreement is found.

Several experiments are described in greater detail because of their relevance to our work. Section 3.4 discusses an experiment that measured both the unpolarized photofission prompt neutron angular distribution and the fission fragment angular distribution, showing that they are correlated. Section 3.5 describes an experiment that demonstrated a correlation between the mass of the fragments and the fragment angular distributions. Section 3.6 describes a measured photofission resonance in ^{239}Pu that could potentially be detected in our experiments. Our results relevant to the potential existence of this resonance will be discussed further in Section 7.5. Section 3.7 highlights fragment polarization asymmetry measurements performed with polarized γ-ray beams.

Finally, previous measurements of scission neutrons, which are emitted during fission through a different process than prompt neutrons, are described in Section 3.8. These neutrons are a potential background to the prompt neutrons, but are typically negligible due to their very small yield and lower energies than the prompt neutrons.

3.2 Photofission Fragment Angular Distribution Measurements

Thirty six different papers reporting results of photofission fragment angular distributions from ^{232}Th, ^{233}U, ^{235}U, ^{238}U, ^{237}Np, ^{239}Pu, or ^{240}Pu for beam energies between 5-7 MeV are available in the literature. These papers are presented in Table 3.1. The tables list the reference for the work, the first author of the publication, the targets measured, and the type of γ-ray beam used.

Table 3.1: Previous measurements of photofission fragment angular distributions

Ref.	First Author	Publication Year	Targets	γ-ray Beam Type
[21]	A. P. Baerg	1959	^{232}Th, ^{233}U, ^{235}U, ^{238}U, ^{237}Np, ^{239}Pu, ^{240}Pu	Brem. not unfolded
[22]	A. I. Baz	1958	^{238}U	Brem. not unfolded
[23]	I. E. Bocharova	1966	^{238}U	Brem. not unfolded
[24]	I. E. Bocharova	1987	^{238}U	Brem. not unfolded
[25]	H. G. de Carvalho	1961	^{238}U	Brem. not unfolded
[26]	E. J. Dowdy	1971	^{238}U	(n, γ)
[27]	B. Forkman	1960	^{238}U	Brem. not unfolded and (p, γ)
[28]	L. P. Geraldo	1986	^{237}Np	(n, γ)
[29]	A. V. Ignatyuk	1971	^{232}Th, ^{238}U	Brem. not unfolded
[30]	K. N. Ivanov	1973	^{235}U	Brem. not unfolded
[31]	S. P. Kapitza	1969	^{232}Th, ^{238}U, ^{240}Pu	Brem. not unfolded
[32]	L. Katz	1958	^{232}Th, ^{233}U, ^{238}U, ^{237}Np, ^{239}Pu	Brem. not unfolded
[33]	V. M. Khvastunov	1994	^{232}Th	Polarized Brem. not unfolded
[34]	V. M. Khvastunov	2001	^{238}U	Polarized Brem. not unfolded
[35]	L. J. Lindgren	1978	^{238}U	Brem. not unfolded
[36]	A. Manfredini	1969	^{238}U	(n, γ)
[37]	S. Nair	1977	^{232}Th, ^{238}U	Brem. not unfolded
[38]	N. S. Rabotnov	1965	^{232}Th, ^{238}U, ^{239}Pu, ^{240}Pu	Brem. not unfolded

Continued on Next Page...

Table 3.1 – Continued

Ref.	First Author	Publication Year	Targets	γ-ray Beam Type
[39]	N. S. Rabotnov	1966	^{239}Pu	Brem. not unfolded
[40]	N. S. Rabotnov	1968	^{232}Th, ^{238}U, ^{239}Pu, ^{240}Pu	Brem. not unfolded
[41]	N. S. Rabotnov	1970	^{232}Th, ^{238}U, ^{240}Pu	Brem. unfolded
[42]	H. J. Raj Prakash	2011	^{232}Th	Brem. not unfolded
[43]	H. J. Rajaprakash	2011	^{237}Np	Brem. not unfolded
[44]	R. Ratzek	1982	^{232}Th, ^{238}U	Polarized Brem. not unfolded
[45]	V. E. Rudnikov	1988	^{232}Th, ^{238}U	Brem. unfolded
[46]	A. S. Soldatov	1965	^{232}Th, ^{238}U	(p, γ)
[47]	A. S. Soldatov	1965	^{238}U	Brem. not unfolded
[48]	A. S. Soldatov	1970	^{239}Pu	Brem. unfolded
[49]	F. Steiper	1993	^{232}Th	Polarized Brem. not unfolded
[50]	J. R. Tompkins	2012	^{232}Th, ^{238}U	HIγS beam
[51]	E. J. Winhold	1952	^{232}Th	Brem. not unfolded
[52]	E. J. Winhold	1956	^{232}Th, ^{235}U, ^{238}U	Brem. not unfolded
[53]	V. E. Zhuchko	1976	^{238}U	Brem. not unfolded
[54]	V. E. Zhuchko	1977	^{238}U	Brem. not unfolded
[55]	V. E. Zhuchko	1978	^{235}U	Brem. not unfolded
[56]	V. E. Zhuchko	1979	^{232}Th, ^{238}U	Brem. not unfolded

The most common beams used are unpolarized bremsstrahlung γ-ray beams. These beams have continuous energy distributions that extend to low energies. Mod-

ern techniques such as tagging the bremsstrahlung photon by measuring the recoiling electron were not used in any of these experiments, so contributions from particular γ-ray energies could not be directly measured. In most cases, the measurements are characterized by the endpoint energy of the beam, which is the energy of the electron beam used to generate the γ-ray beam and which also corresponds to the maximum γ-ray energy in the distribution. Most of these works did not try to unfold the contribution of this continuous beam energy spectrum from their measured angular distribution data. Therefore, those works are not suitable for direct comparison to measurements with a quasi-monoenergetic beam, such as ours. However, they can still give qualitative information about the fission barrier for different channels.

The bremsstrahlung beam measurements revealed significantly anisotropic angular distributions for the even-even actinides, with the largest dipole anisotropies being observed in ^{232}Th at beam energies near 5 MeV. As the beam energy increased, the dipole term from ^{232}Th decreased. ^{232}Th also displayed negligible quadrupole contributions to photofission at all beam energies. ^{238}U had smaller dipole contributions which decreased faster than ^{232}Th as the beam energy increased, and a quadrupole contribution to ^{238}U was measured at the lowest energies ($\sim$ 5 MeV). For ^{240}Pu, the dipole contributions were smaller and fell faster than ^{238}U with increasing beam energy, and the quadrupole contributions were larger than ^{238}U at beam energies near 5 MeV.

References [41], [45], and [48] did unfold their beam energy distribution from their raw bremsstrahlung angular distribution measurement. While this allows us to compare these results to our quasi-monoenergetic beam results, the unfolding procedure introduces additional uncertainties. Unfolding the true angular distribution parameters from the measured bremsstrahlung data is an ill-posed problem and is subject to "swinging" solutions, where the angular distribution parameters oscillate as a function of energy. Solutions were found which did not exhibit these oscilla-

tions, but the resulting solutions do not contain any real fine structure and can only be considered as averages of the true angular distribution parameters over a finite energy range. This is similar to a quasi-monoenergetic beam which averages over angular distribution parameters in a finite energy range. In these previous measurements, the uncertainties in the unfolded angular distribution parameters were not calculated. Therefore, the unfolded results of [41], [45], and [48] are presented without any experimental uncertainties. Despite these additional difficulties, the unfolded results are still useful as inputs to a simulation to predict prompt neutron polarization asymmetries as described in Section 6.6.

Finally, [26], [27], [28], [36], and [46] generated γ-ray beams by particle-induced reactions on nuclei. Reference [46] used the $^{19}F(p,\alpha\gamma)^{16}O$ reaction at $E_p = 1.5\,\mathrm{MeV}$ to generate γ rays of energies 6.1, 6.9, and 7.1 MeV in a $1.00 : 0.15 : 0.17$ ratio of intensities. The measured angular distribution is the ratio of these intensities folded with the photofission cross section at each γ-ray energy. Reference [46] does not unfold the contribution from each of the γ-ray lines from each other, so it cannot be directly compared to a quasi-monoenergetic beam. Reference [27] also used this reaction, but at different proton energies and fluorine thicknesses, which changed the relative intensities of the three γ-ray lines. This allowed [27] to measure the contribution of each γ-ray line independently. Alternatively, [26], [28], and [36] used (n,γ) reactions on various targets to generate mono-energetic γ rays. The lists of different targets used, and their respective γ-ray lines, can be found in [36].

Figures 3.1, 3.2, and 3.3 show the results from the unfolded bremsstrahlung measurements and monoenergetic beam measurements of photofission of ^{232}Th, ^{238}U, and ^{240}Pu respectively. Similar to the results from the bremsstrahlung beam studies, ^{232}Th shows a very large dipole anisotropic fission contribution (b) and a small quadrupole anisotropic contribution (c). ^{240}Pu, on the other hand, shows a smaller dipole contribution and a very large quadrupole contribution.

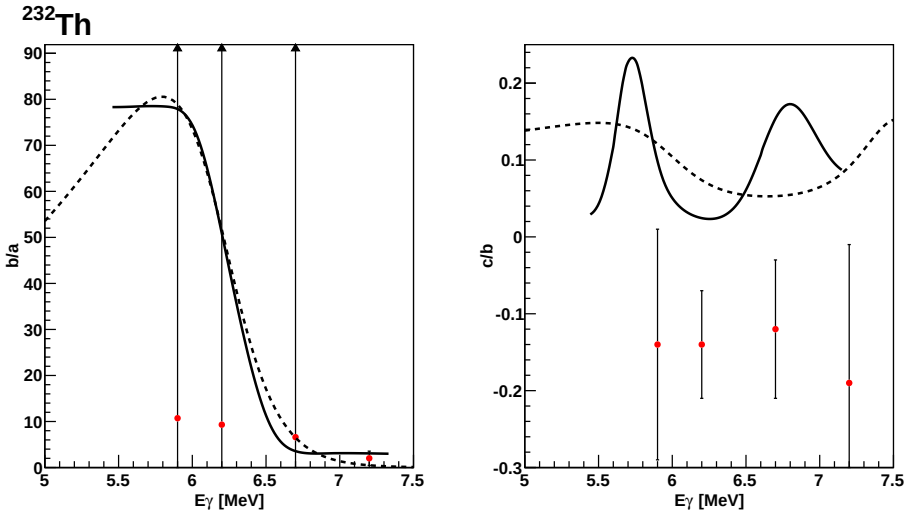

FIGURE 3.1: Previously measured ratios of the fragment angular distribution coefficients a, b, and c as a function of incident γ-ray energy for ^{232}Th. The black line is the unfolded bremsstrahlung angular distribution from [41]. The red points are from [50]. The dashed line is the calculated angular distribution based on assumed barrier shapes in Section 2.4.4 (Figure 2.5).

Much more data has been taken on ^{238}U than the other targets in our study. Of the works with mono-energetic beams, [26], [27], [36], and [46] focused on ^{238}U. These works largely agree on the size of the dipole anisotropic term (b), but they disagree on the size of the quadrupole anisotropic term (c). Reference [27] found significant contributions of the quadrupole term above a γ-ray energy of 6 MeV, which at the time disagreed with most experiments using bremsstrahlung beams. Reference [46] attempted to reproduce the data from [27], but found a quadrupole contribution of less than a few percent. Later, [36] again found a significant quadrupole contribution above 6 MeV with large experimental uncertainties using (n, γ) reactions, but when [26] repeated their experiment, only a small quadrupole contribution was found, in agreement with [46]. Most experiments agree that the quadrupole contribution is negligible above 6 MeV.

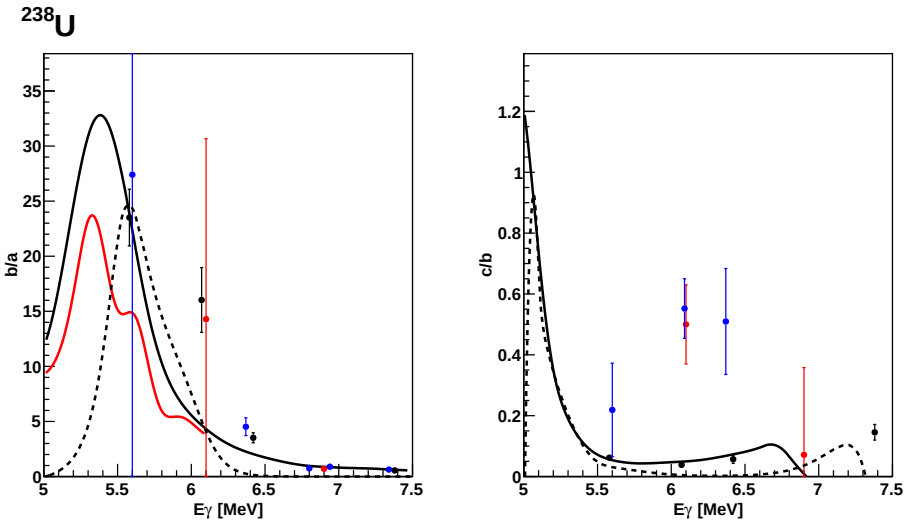

FIGURE 3.2: Previously measured ratios of the fragment angular distribution coefficients a, b, and c as a function of incident γ-ray energy for ^{238}U. The black line is the unfolded bremsstrahlung angular distribution from [41], and the red line is the unfolded bremsstrahlung from [45]. The black points are from monoenergetic beams in [26], red points from [27], and blue points from [36]. The dashed line is the calculated angular distribution based on assumed barrier shapes in Section 2.4.4 (Figure 2.6).

Angular distributions of the even-odd actinides were found to be much more isotropic than for the even-even actinides. For the even-odd actinides, only the dipole anisotropic term (b) was typically measured because it is expected to dominate over the quadrupole anisotropic term (c). Figures 3.4 and 3.5 show the angular distributions taken with monoenergetic beams or unfolded bremsstrahlung beams for ^{239}Pu and ^{237}Np respectively. For ^{237}Np, small but statistically significant values of the dipole term were found with a quasi-monoenergetic beam. It was expected that if any even-odd nucleus would show an anisotropic angular distribution, it would be ^{239}Pu because its spin is only 1/2 instead of the other larger spin even-odd nuclei. Indeed, the dipole term in the angular distribution from photofission of ^{239}Pu is approximately a factor of $2-3$ larger than that of ^{237}Np, but it is still much smaller than that of ^{232}Th. For the case of ^{233}U, no data were taken with a quasi-monoenergetic

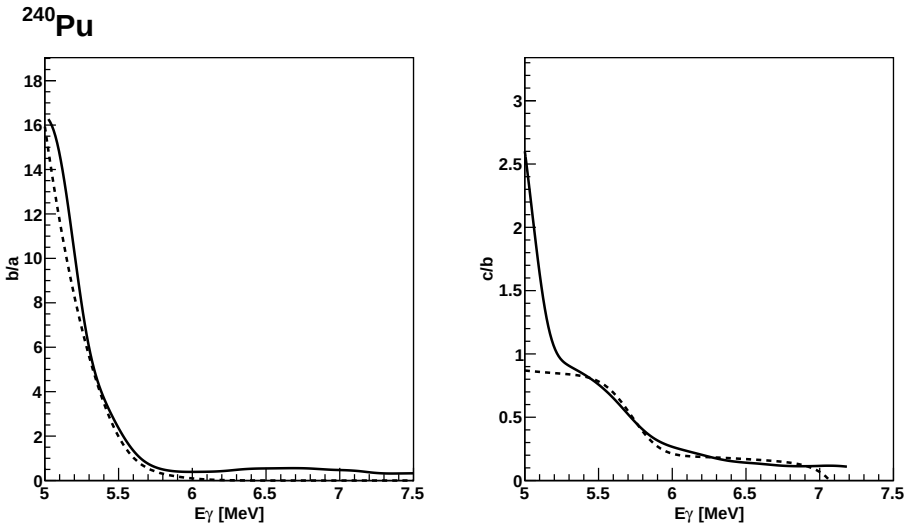

FIGURE 3.3: Previously measured ratios of the fragment angular distribution coefficients a, b, and c as a function of incident γ-ray energy for ^{240}Pu. The black line is the unfolded bremsstrahlung angular distribution from [41]. The dashed line is the calculated angular distribution based on assumed barrier shapes in Section 2.4.4 (Figure 2.7).

beam, but data taken using a bremsstrahlung beam at an endpoint energy of 8 MeV resulted in an angular distribution that was consistent with being isotropic within errors. Bremsstrahlung measurements on ^{235}U also indicated an isotropic angular distribution. Neither of the measurements on ^{233}U or ^{235}U were unfolded.

3.3 Photofission Barrier Implications

Many of the experiments which measured fragment angular distributions in photofission used either a single-hump or double-hump model to interpret their results in terms of fission barrier characteristics. Neglecting the different fission modes, such as standard-I and standard-II, and the complex multi-dimensional fission barrier landscape, the fission barrier can be reasonably modeled as having two humps at different points along a generalized deformation parameter. This is analogous to the Strutinsky model described in Section 2.3.2 and used in the angular distribution

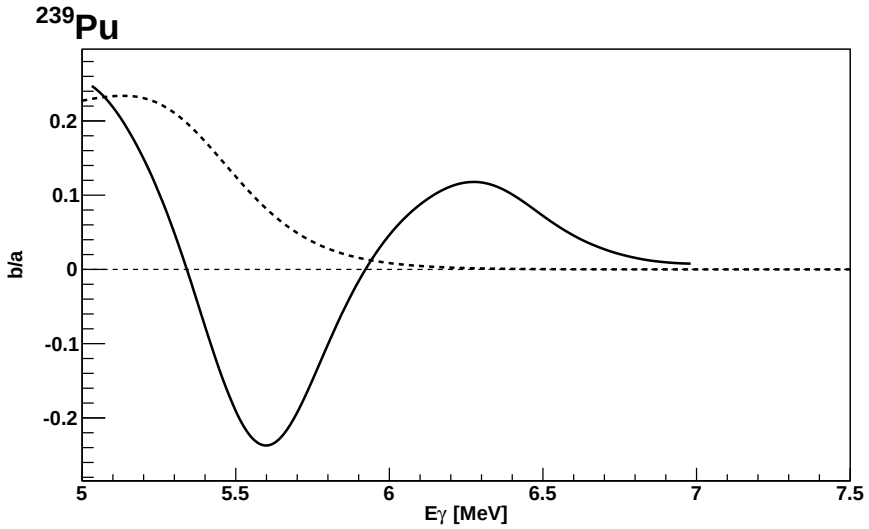

FIGURE 3.4: Previously measured ratios of the fragment angular distribution coefficients a and b as a function of incident γ-ray energy for ^{239}Pu. The black line is the unfolded bremsstrahlung angular distribution from [48]. The dashed line is the calculated angular distribution based on assumed barrier shapes in Section 2.4.4 (Figure 2.8).

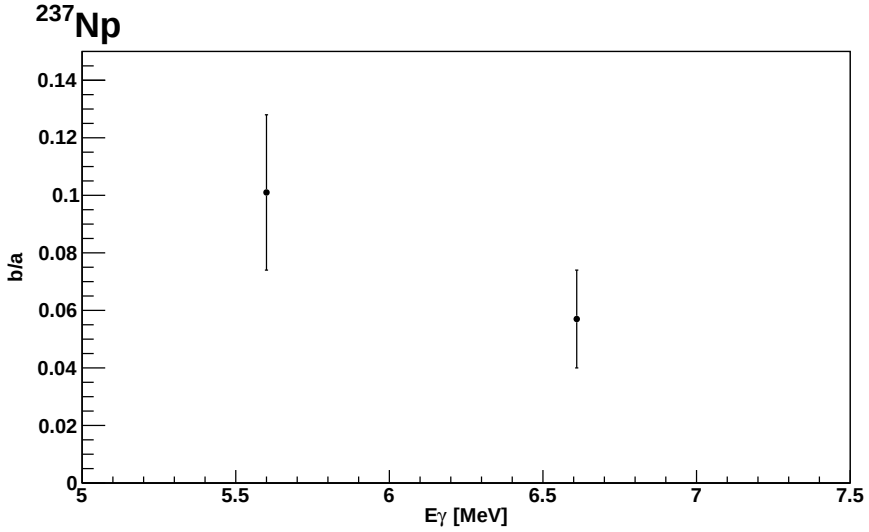

FIGURE 3.5: Previously measured ratios of the fragment angular distribution coefficients a and b as a function of incident γ-ray energy for ^{237}Np with monoenergetic beams. The black points are from [28].

calculations presented in Section 2.4.4.

The angular distributions presented in Section 2.4.4 for ^{232}Th, ^{238}U, and ^{240}Pu, and shown by the dashed lines in Figures 3.1, 3.2, and 3.3, qualitatively reproduce the behavior of b/a and c/b for those isotopes as measured by [41]. This suggests that the heuristic model to translate the fission channels into barriers, along with the phenomenological ordering of the different fission barrier heights, is a reasonable model for the photofission process.

For ^{233}U, ^{235}U, and ^{237}Np, the angular distributions were too isotropic to learn much about the barrier heights of the different fission channels. A fission resonance was observed for ^{239}Pu (Section 3.6), obscuring the contributions from the different barriers and preventing the measurement of the barrier parameters of the different states. Note that the measurements on ^{239}Pu in Figure 3.4 do not agree with the simplified calculation because of this resonance.

3.4 Measured Photofission Neutron Angular Distributions

One of the experiments most relevant to our work is described in [37]. In this experiment, a bremsstrahlung photon beam was used to induce photofission of ^{238}U and ^{232}Th targets. Prompt neutron angular distributions were measured using multiple detector assemblies composed of sandwiches of Markrofol foils and ^{238}U. The Markrofol foils used were solid state track detectors which show damage tracks after bombardment by fission fragments and subsequent chemical etching. These detector assemblies were located at different scattering angles relative to the beam direction. The prompt neutrons emitted from the target induced fission of ^{238}U nuclei in a given assembly, and the recoiling fission fragments left damage tracks in the Markrofol foil. The prompt neutron angular distribution was measured by counting the number of damage tracks per assembly. In addition to this measurement, they also measured the fragment angular distribution directly using Markrofol foils. These measurements

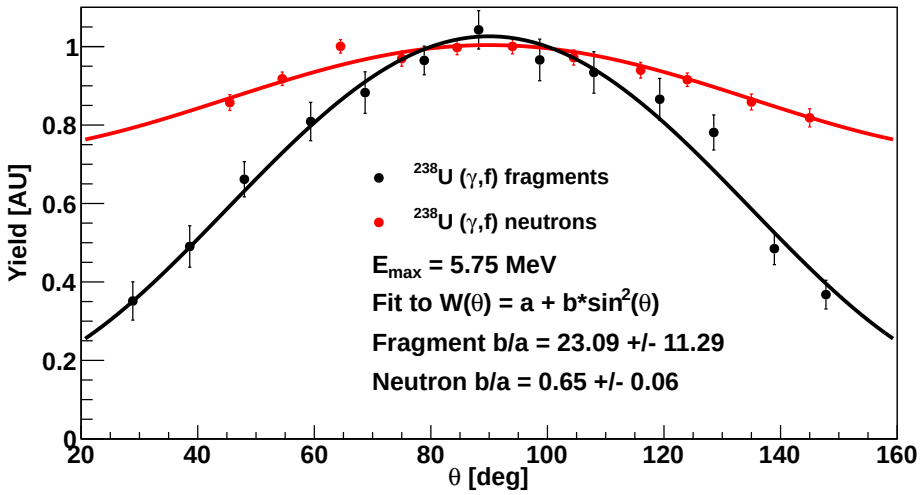

FIGURE 3.6: Measured angular distributions for fission fragments (black) and prompt neutrons (red) in photofission of ^{238}U at a bremsstrahlung endpoint energy of 5.75 MeV. θ is in the lab frame, and the uncertainties are statistical only. Data taken from [37].

were done consecutively and two bremsstrahlung beam endpoint energies were used for each target.

A direct comparison between these measurements and our angular distribution measurements with a quasi-monoenergetic γ-ray beam is not feasible because they did not unfold the bremsstrahlung γ-ray beam energy distribution from their measured data. However, they demonstrate that the prompt neutron angular distribution is correlated with the fragment angular distribution. As noted in Section 2.3, the prompt neutrons are emitted by fully accelerated fission fragments, so there is an angular correlation between the fission fragments and the prompt neutrons. This angular correlation is directly observed in the photofission measurements of [37].

Figure 3.6 shows the measured fragment and neutron angular distributions for photofission of ^{238}U at a bremsstrahlung endpoint energy of 5.75 MeV, which includes the entire bremsstrahlung energy spectrum down to 0 MeV. The fragment angular distribution is measured to be highly anisotropic with a value of $b/a = 23$. For the

neutrons, the angular distribution had a b/a value of 0.65.

Several previous experiments had measured angular correlations between fragments and prompt neutrons [1], but [37] measured it for the first time in photofission. Because fission is a compound reaction, it was expected that the neutron-fragment angular correlations would be the same for neutron-induced fission, photofission, or spontaneous fission. Reference [37] was the first to experimentally demonstrate this correlation in photofission and verify this assumption.

3.5 Photofission Mass-Angle Correlation Measurements

It is well known that the average prompt neutron multiplicity and energy is sensitive to the mode (standard-I, II, or superlong) of the fission process [3]. Reference [49] measured that the fission fragment angular distribution also depends on the fission mode. This could be explained by the existence of different barrier heights for the different fission channels in the different fission modes. Fragment angular distributions and masses from photofission were directly measured and the data were separated into contributions from standard-I fission and standard-II fission based on the fragment mass. At a bremsstrahlung beam endpoint energy of 8.5 MeV for photofission of ^{232}Th, $(b/a)_{STII}$ was larger than $(b/a)_{STI}$ by approximately 10%. As they increased the endpoint beam energy, the difference became more dramatic. For beam endpoint energies between 10.5 and 12 MeV, $(b/a)_{STII}$ hovered around 1.0 while $(b/a)_{STI}$ ranged from 0.0 to -0.4.

The significant difference between the fragment angular distributions of the two modes could affect the prompt neutron angular distribution because the different modes have different average neutron multiplicities. However, there is no precise measurement of fragment angular distributions and masses taken with a quasi-monoenergetic beam on our targets. Therefore, this correlation will be neglected when modeling the fission fragment angular distributions.

3.6 ^{239}Pu Photofission Resonance Measurement

A previous measurement of photofission fragment angular distributions from ^{239}Pu indicated the existence of a photofission resonance [48]. The existence of the resonance was determined by structure in the behavior of b/a as a function of γ-ray energy. The excitation energy of the resonance was approximately 5.6 MeV and its width was measured to be $\sim$ 200 keV. However, [48] found no increase in the photofission cross section, which would be expected if there were a resonance. Also, the width of the resonance is wider than expected from neutron-induced fission studies [3]. The existence of the photofission resonance is unexpected and has not been thoroughly tested, but our experiments may be useful in searching for this resonance because we determine the value of b/a for the prompt neutrons, which is correlated to b/a for the fragments.

In [48], the Strutinsky model (Section 2.3.2) was used to generate barriers for each of the channels excited by dipole absorption of the photon $(J, K) = (3/2, 3/2)$, $(3/2, 1/2)$, $(1/2, 1/2)$. Their experiment used an unpolarized γ-ray beam, so the angular distributions for these states can be taken from Table 2.2 with $\phi = \pi/4$. The b/a values for the different channels are: -0.5 for $(3/2, 3/2)$, 1.5 for $(3/2, 1/2)$, and 0 for $(1/2, 1/2)$. If each (J, K) channel can be modeled by only one double-humped fission barrier, then at most the value of b/a could change sign only once with increasing beam energy, since the penetration of the barrier should increase monotonically with increasing beam energy. However, in their measurement of b/a, two sign changes were observed: one at approximately 5.3 MeV and another at approximately 5.9 MeV. This structure could be explained by several different effects:

- A resonance in the fission barrier for the $(3/2, 3/2)$ state at approximately 5.6 MeV with a width of approximately 200 keV.

- Contributions at low beam energies from a ^{240}Pu contaminant in the target. This cannot be determined because the target enrichment is not noted in the paper.

- Contributions from quadrupole effects that alter the angular distribution. This explanation seems unlikely due to the high density of dipole states at low excitation energies in ^{239}Pu.

- Differences in the fission barriers for standard-I and standard-II modes which combine in a way to recreate the observed angular distributions.

The possible existence of this resonance can be investigated by measuring the prompt neutron polarization asymmetries in our experiments. The existence of the resonance would be confirmed if the polarization asymmetry changes sign twice and the prompt neutron counting rate increases on the resonance. If the polarization asymmetry does not change sign twice and there is no resonance-like behavior in the prompt neutron counting rate, then the existence of the resonance could be refuted. Our results for ^{239}Pu are investigated for this resonance in Section 7.5, and while we are not able to definitively prove or disprove the existence of the resonance, we can certainly put its existence into question.

3.7 Measured Photofission Fragment Polarization Asymmetries

References [33], [34], [44], and [49] used polarized bremsstrahlung beams to induce photofission. These beams were generated by using a crystal radiator and a γ-ray beam generated off the axis of the incident electron beam. These off-axis γ-ray beams can be highly polarized depending on the alignment of the crystal and the scattering angle. These measurements discovered significant positive polarization asymmetries in the fission fragments from ^{232}Th and ^{238}U. However, they did not unfold the beam

energy distribution from the measured data, so their polarization asymmetries are not comparable to those measured with a quasi-monoenergetic beam.

Reference [50] measured photofission fragment polarization asymmetries at HIγS from ^{232}Th and ^{238}U. This would seem like the ideal experiment to obtain fragment polarization asymmetries since the beam profile is the same as our experiment. However, their experiment was complicated by the use of thick targets of the two isotopes. The fission fragments straggled on their way out of the thick target, affecting the angular distribution. Reference [50] attempted to unfold this straggling effect from the true angular distribution of the fragments, but the resulting true fragment polarization asymmetries had very large uncertainties. For beam energies near 6 MeV, the value of b/a deduced from their work had an uncertainty of several orders of magnitude. This large uncertainty makes it difficult to directly compare to the results of our experiments.

3.8 Scission Neutron Measurements

Unfortunately, there are other neutrons that are emitted at approximately the same time as the prompt neutrons, but from a different mechanism. These neutrons are termed "scission neutrons", and it is believed that they are emitted at the instant of scission, rather than from the excited, accelerated fission fragments. These scission neutrons are assumed to be isotropic in the lab frame [57], and measurements which claim their existence also indicate they are lower in energy than the prompt fission neutrons [58].

The existence and average yield of scission neutrons is still an open question in the nuclear physics community. Reference [57] initially postulated the existence of scission neutrons in order to explain anomalous neutron yields that appeared to be isotropic in the lab frame and not emitted from accelerated fragments. They directly measured prompt neutron and fragment angular correlations from spontaneous fis-

sion of ^{252}Cf and used a model of prompt neutrons based on evaporation from the excited fission fragments to predict the angular correlations between the neutrons and fragments. Based on the disagreement between the model and experimental measurements, they claimed that 10-20% of the total prompt neutron yield came from neutrons emitted isotropically in the lab frame, which they termed scission neutrons. That experiment was repeated by [59] and [60], who used a different model and found the scission neutron yield to be under 5%. More recently, [61] claimed to have found an error in the models used in these measurements, and reported a scission neutron yield of 10%. As recently as a few years ago, another experiment [62] was performed measuring prompt neutrons emitted from ^{235}U (n_{th},f). Those authors used a different approach to model the expected angular correlation between the fragments and the neutrons. One of the main difficulties in modeling this quantity is that the neutron energy spectrum in the rest frame of the fragment is unknown. By combining neutron energy measurements taken parallel and anti-parallel to the fragment momentum direction, the authors of [62] claim to have directly measured the neutron energy spectrum in the rest frame of the fragment. They then used this spectrum in their model to calculate the expected neutron-fragment angular correlations, and they reported a scission neutron yield of approximately 5%.

Using the spectrum information from [58], approximately 20% of the total scission neutron yield is above the neutron energy threshold used for the detectors in the present experiment. If the total scission neutron yield is less than 5% as reported in the most recent study by [62], then less than 1% of the neutrons observed by our detectors would be scission neutrons instead of neutrons emitted from accelerated fragments. Therefore, any contribution of scission neutrons to the prompt neutron yield will be neglected.

4

Description of the Experiment

4.1 Introduction

Prompt neutron yields from polarized photofission of ^{232}Th, ^{233}U, ^{235}U, ^{238}U, ^{237}Np, ^{239}Pu, and ^{240}Pu were studied as a function of beam energy (E_γ), neutron energy (E_n), polar angle (θ), and azimuthal angle (ϕ). This chapter will present a detailed description of the γ-ray beams and how they were monitored, the targets, and the neutron detectors and associated electronics. Section 4.2 describes how the nearly 100% linearly-polarized and circularly-polarized γ-ray beams with mean energies between 5.3 and 7.6 MeV and Full Width at Half Maxima (FWHM) of approximately 250 keV were generated using the High Intensity γ-ray Source (HIγS). Three detectors were used to monitor the γ-ray beam as mentioned in Section 4.3: an HPGe detector to measure the beam energy, a set of 5 plastic scintillators to measure the relative intensity, and a large NaI(Tl) detector to measure the absolute intensity. The γ-ray beams were incident on a D_2O target or one of 7 actinide targets, which are detailed in Section 4.4. The experiments on these targets spanned three years and included contributions from multiple experimental groups, as discussed in Sec-

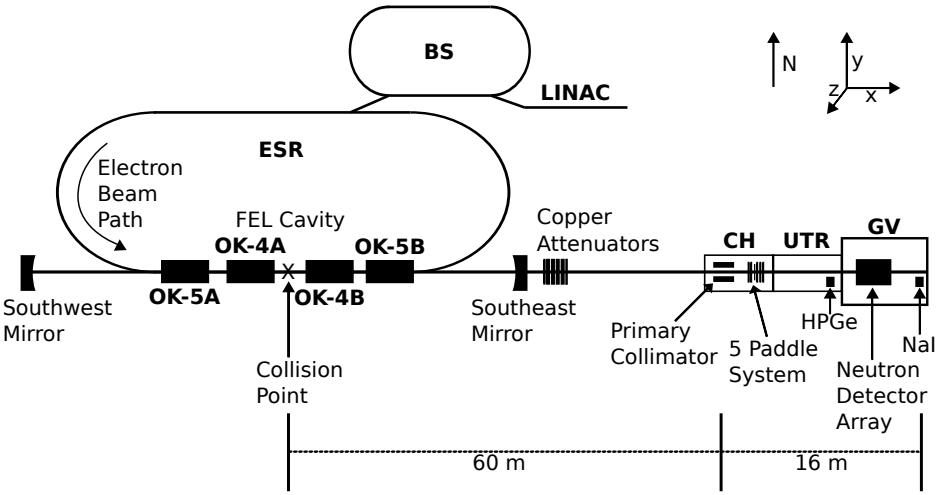

FIGURE 4.1: A schematic of the HIγS facility. The principle accelerator components are the linear accelerator (LINAC), booster synchrotron (BS), and electron storage ring (ESR). Photons are generated by the optical klystrons (OKs). γ rays travel down the beam line to the collimator hut (CH), upstream target room (UTR), and γ vault (GV). This schematic is not to scale.

tion 4.5. Section 4.6 describes the array of $12-18$ liquid scintillator neutron detectors which was used to detect neutrons emitted from these targets. Detector signals were processed using analog electronics and converted to digital signals, then stored in an event-by-event basis on a computer, as discussed in Section 4.7.

4.2 The High Intensity γ-ray Source (HIγS)

The High Intensity γ-ray Source (HIγS), located at Duke University and operated by Triangle Universities Nuclear Laboratory (TUNL), is capable of producing high on-target intensity ($\leqslant 5\text{x}10^8\gamma/s$), nearly 100% linearly or circularly polarized, quasi-monoenergetic γ-ray beams of between $1-100\,\text{MeV}$ [63]. The γ-ray beams are produced by backscattering laser light off of high energy electrons, boosting the laser light to γ-ray energies. At the HIγS facility, the laser light is produced by wiggling these electrons in a Free Electron Laser (FEL) cavity located inside the Electron Storage Ring (ESR), shown in a schematic of the HIγS facility in Figure 4.1. A

description of the electron beam is given in Section 4.2.1, while the FEL is discussed in Section 4.2.2 and the γ-ray beam is described in Section 4.2.3.

4.2.1 Electron Beam Production

The HIγS facility operates using electron beam energies between 0.24 and 1.2 GeV [63]. Electrons are freed from a photocathode using a pulsed high power nitrogen laser. These electrons are then sent through a linear accelerator (LINAC) consisting of eleven Radio Frequency (RF) segments operating at 2.856 GHz. Because the nitrogen laser pulse duration is approximately 0.5 ns, one central LINAC bucket is filled while two other buckets contain relatively few electrons. The eleven RF segments accelerate the electrons to $0.18 - 0.28$ GeV and then inject them into the Booster Synchrotron (BS) for further acceleration. The repetition rate of the LINAC is approximately 1 Hz.

The BS fully accelerates the electrons to the energies used in FEL operation with an RF cavity operating at 178.55 Hz. The circumference of the BS is 31.902 m, which allows for 19 RF buckets in the BS. Electrons accelerated using the LINAC are injected into these buckets, and the energy of the BS is ramped up to the ESR energy ranging from $0.24 - 1.2$ GeV. After ramping, electrons from any one of the BS RF buckets are injected into any one of the RF buckets in the ESR. Typical charges injected into the ESR range from $35 - 50$ pC/s. The entire BS operates between $0.4 - 0.8$ Hz.

The ESR is a continuous track with two straight sections, each 34.21 m long, and two curved sections 19.52 m long, as shown in Figure 4.1. An RF cavity in the straight section on the north side of the ESR replaces energy lost due to synchrotron radiation. The RF cavity frequency is 178.547 MHz, allowing for 64 RF buckets in the ESR. After the electrons leave the BS, they are injected into the ESR. Because the electron pulse length after the injector is less than 11 ns, and each bucket in

the ESR is 5.6 ns wide, only one main bucket in the ESR is filled for each bucket injected from the BS. This injection scheme allows for individual buckets in the ESR to be filled as needed from any bucket in the BS. Because the vacuum in the ESR is imperfect, some of the electrons in the main bucket in the ESR will be lost over time due to collisions with particles in the beam pipe as well as with photons. The BS injector can fill particular buckets of the ESR, so the lost electrons can be replaced as needed to prevent losses in γ-ray beam intensity. This "top-off" operation allows for continuous, stable beam current in the ESR.

Because the γ-ray beam is produced by colliding FEL light with the electrons in the ESR, the energy spread of the electron beam will contribute to the energy spread of the γ-ray beam. The relative RMS energy spread of the electrons ranges from $1\text{x}10^{-3} - 7\text{x}10^{-3}$ depending on the energy of the electron beam [64]. For the electron beams used in this experiment, the electron beam RMS relative energy spread was expected to be $6\text{x}10^{-3}$ [64].

4.2.2 Free Electron Laser (FEL) Production

The FEL photons are produced by one of two Optical Klystrons (OKs) located on the south straight section of the ESR. The purpose of the OKs are to generate and amplify Free Electron Laser light. The OK-4, one of the OKs, consists of four arrays of magnets. One array above the beam pipe and another below the beam pipe comprise the OK-4A wiggler as shown in Figure 4.1, and another pair of arrays combines to form the OK-4B wiggler. Each OK-4 wiggler is composed of 66 dipole magnets each separated by 2.5 cm with a period of $\lambda_w = 10$ cm, and these magnets force the electron to oscillate in the horizontal direction. The maximum magnetic field in these wigglers is 0.536 T at 3 kA of current. The OK-4 is used to produce linearly polarized FEL photons, which can be backscattered off of electrons to make linearly polarized γ-ray beams. The other OK used at HIγS is the OK-5, which

consists of two wigglers (OK-5A and OK-5B) that cause helical trajectories of the electron beam, generating circularly polarized FEL photons and circularly polarized γ-ray beams. Each OK-5 wiggler consists of 60 magnets each separated by 4.0 cm with a 12 cm period and a field of 0.286 T between each magnet. As shown in Figure 4.1, one each of the OK-4 wigglers and OK-5 wigglers is located upstream of the electron-photon collision point, while the other OK-4 and OK-5 wigglers are located after the collision point. Not indicated in the figure is the buncher magnet, which is an additional wiggler composed of 6 dipole magnets [65]. The buncher is located next to the collision point and can be used to add FEL gain, though it is only used sparingly during γ-ray beam operation [64].

The physics of generating linearly polarized FEL photons using the OK-4 is qualitatively similar to the physics involved in making circularly polarized photons using the OK-5. Because the generation of linearly polarized FEL photons is easier to visualize than circularly polarized photons, a detailed discussion of the FEL operation will be provided only for the OK-4.

Let the x-direction point east, the y-direction point north, and the z-direction point out of the page as shown in Figure 4.1. In the ideal case, electrons traveling east in the ESR along the south straight section enter the first OK-4 wiggler. The electrons encounter an oscillating magnetic field in the z-direction denoted by B_z. Using $\gamma_x = 1/\sqrt{1-\beta_x^2}$, in the rest frame of the electrons the wiggler field appears as a magnetic field $\gamma_x B_z$ in the z-direction. Because the electrons are highly relativistic, the wiggler field also transforms to an electric field $\sim c\gamma_x B_z$ in the y-direction. This combination of perpendicular electric and magnetic fields moving at nearly the speed of light closely approximates a 100% linearly polarized virtual photon field, so the interaction between the electron beam and the OK-4 wiggler can be interpreted in the rest frame of the electron as a simple electron-photon collision [66]. The wavelength of the virtual photon, λ_v, is determined by the relativistic length contraction of the

OK-4 wiggler period λ_w: $\lambda_v = \lambda_w/\gamma_x$. Typical values of γ_x for the electron beams range from $470 - 2350$, yielding $\lambda_v \approx 40 - 200\,\mu$m or $E_v \approx 6 - 31\,$meV. Because the energy of the virtual photon is much less than the electron rest mass, recoil effects are negligible and the scattered photon will have approximately the same energy as the incident virtual photon. The 100% linear polarization of the virtual photon is maintained so the scattered photons are also 100% linearly polarized.

After the collision, the real photon will be Doppler shifted back into the lab frame and has a wavelength $\lambda_f = \lambda_v/(\gamma_x(1+\beta_x))$. Assuming highly relativistic electrons and $\gamma \approx \gamma_x$, this reduces to $\lambda_f \approx \lambda_w/(2\gamma^2)$. This approximation fails because the magnetic field of the wiggler accelerates the electron in the y-direction, reducing the longitudinal velocity of the electron and making γ_x slightly smaller than γ. Accounting for this effect gives the FEL equation: $\lambda_f = \lambda_w/(2\gamma^2)(1 + K_w^2/2)$ [67], where $K_w = eB_w\lambda_w/(2\pi m_0 c^2)$ is called the wiggler parameter and can vary from $0 - 5.42$ for the OK-4[65]. This implies a range of possible FEL photon wavelengths of $\lambda_f \approx 120 - 3000\,$nm, but practical considerations such as mirror reflectivity limit this range to $\lambda_f = 190 - 1064\,$nm [63].

The photons emitted by the electrons are trapped inside an optical cavity which is the same round-trip length as the circumference of the ESR. They rejoin with the electron bunch that had emitted them at the west OK-4 wiggler magnet with the same phase with which they were emitted. Due to non-ideal effects such as the finite length of the wiggler, the photons are not all monoenergetic with the FEL photon wavelength. However, after many passes through the OK-4 wigglers, part of the incoherent radiation spectrum emitted from the electrons will be amplified faster than other frequencies. The line width of this primary FEL wavelength becomes very small, $\delta\lambda/\lambda \sim 1 - 3\text{x}10^{-4}$, so the photons can be well-approximated by a single wavelength [65].

After many passes through the wiggler magnets, the amplitude of the photons will

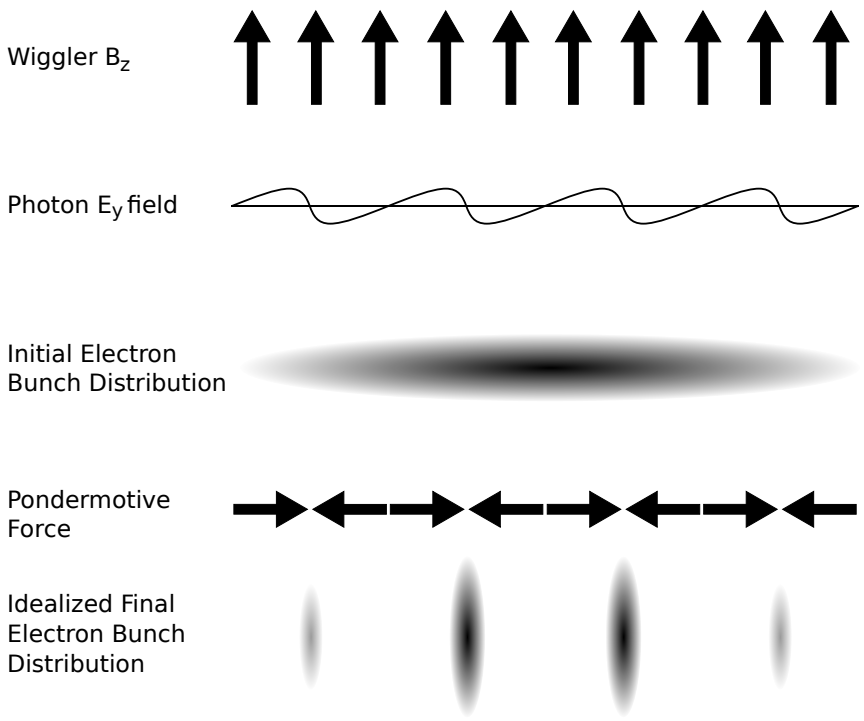

FIGURE 4.2: An illustration of microbunching in an OK-4. The electron bunch is inside a dipole magnet in the OK-4 and experiences a magnetic field from the wiggler. The magnetic field from the photons co-propagating with the electrons leads to the pondermotive force. The final idealized electron distribution is microbunched exactly one photon wavelength apart.

become large enough to influence the electron motion inside the first OK-4 wiggler magnet. This effect gives rise to coherent photon emission in the second OK-4 wiggler magnet and greatly enhances the gain of the FEL. In the first OK-4 wiggler magnet, the electrons initially traveling in the x-direction encounter an electric field from the photons in the y-direction E_y. This electric field will accelerate the electrons in the y-direction, giving them a nonzero v_y. Then, the magnetic field of the wiggler magnet B_z will accelerate the electrons in the x-direction, as shown in Figure 4.2. The acceleration in the x-direction depends on v_y, which depends on the phase between the electrons and the photon field. This force which accelerates the electrons in

the x-direction is called the pondermotive force. In the ideal situation, this force causes the electrons to separate into well-defined microbunches at the nodes of the photons' magnetic field, with each microbunch exactly one FEL photon wavelength apart. These microbunches propagate to the second OK-4 wiggler where they radiate photons coherently, greatly amplifying the existing photon field and generating an FEL consisting of 100% linearly polarized photons. The polarization of the FEL photons has been measured experimentally to be $> 98\%$, which was limited by the precision of the measurement device [64].

4.2.3 γ-Ray Production

The FEL can operate with only one of the 64 RF buckets in the ESR filled. FEL photons co-propagate with this electron bunch, termed the lasing bunch, when it is in the optical cavity. When the electron bunch is in the north straight section of the ESR, the photons are traveling west in the cavity towards the southwest mirror. To make the γ-ray beam, the RF bucket exactly opposite to the lasing bunch is filled with electrons. This scattering bucket passes east through the FEL photons traveling west at the midpoint of the optical cavity in a field-free region. Electrons in this scattering bunch can collide head-to-head with FEL photons, boosting them into MeV energies. In the actual operation of HIγS, both electron bunches lase and scatter each other's FEL photons.

Assume an electron with 4-momentum $(E_e, p_e, 0, 0)$ collides with a photon with 4-momentum $(E_\gamma, -E_\gamma, 0, 0)$ as illustrated in Figure 4.3. Using conservation of 4-momentum, the energy of the scattered photon is given by:

$$E_{\gamma'} = \frac{E_\gamma(1+\beta)}{1-\beta\cos(\theta_{\gamma'}) + \frac{E_\gamma}{E_e}(1+\cos(\theta_{\gamma'}))} \tag{4.1}$$

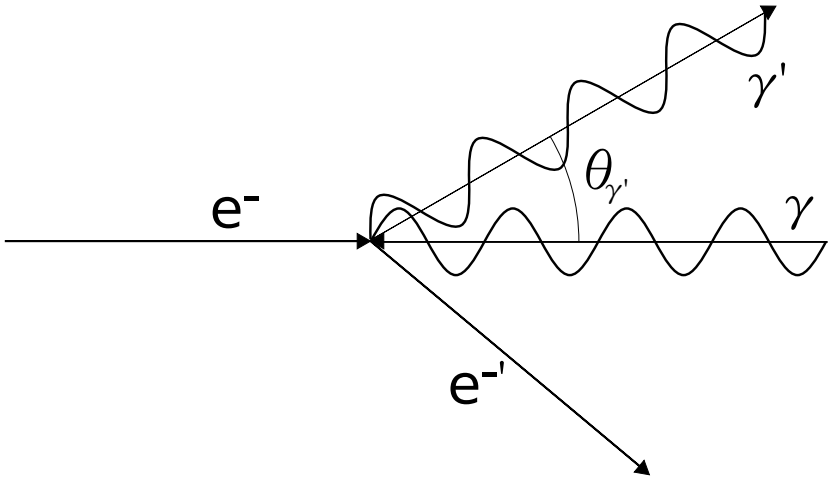

FIGURE 4.3: An illustration of an electron-photon collision.

In the limits that $\theta_{\gamma'} \ll 1$ and $\gamma \gg 1$ this equation reduces to:

$$E_{\gamma'} \approx \frac{4\gamma^2 E_\gamma}{1 + (\theta_{\gamma'}\gamma)^2 + 4\gamma\frac{E_\gamma}{m_e c^2}} \tag{4.2}$$

Neglecting the electron recoil term in the denominator, as $\theta_{\gamma'}$ approaches zero this equation becomes $E_{\gamma'} \approx 4\gamma^2 E_\gamma$. FEL photons with wavelengths of 1064 nm would be boosted to approximately 1 MeV, using a γ-factor for the electron beam of 470 ($E_e \sim 0.24$ GeV). For a γ-factor of 2350 ($E_e \sim 1.2$ GeV) and FEL photons with wavelengths of 190 nm, the final γ-ray energies would be approximately 140 MeV. For the present experiment, γ-ray beams of $5.3 - 7.6$ MeV were generated by colliding FEL photons with wavelengths of 540 nm with electron beams of energies between $380 - 460$ MeV.

The calculation of the γ-ray beam polarization is more involved and requires QED [68]. The cross section for electron-photon scattering, referred to as the Klein-Nishina formula, can be expressed in terms of kinematic variables x and y, where

$x = (s - m^2)/m^2$ and $y = (m^2 - u)/m^2$. Here s and u are the usual kinematic variables: $s = (p + k)^2$ and $u = (p - k')^2$, where p is the initial 4-momentum of the electron, k is the initial 4-momentum of the photon, and k' is the final 4-momentum of the photon. m is the rest mass of the electron. Using this notation, the cross section for scattering a polarized photon off of an unpolarized electron is [68]:

$$d\sigma \propto F_0 + F_3(\xi_3 + \xi_3') + F_{11}\xi_1\xi_1' + F_{22}\xi_2\xi_2' + F_{33}\xi_3\xi_3' \tag{4.3a}$$

$$F_0 = (\frac{1}{x} + \frac{1}{y})^2 + (\frac{1}{x} + \frac{1}{y}) - \frac{1}{4}(\frac{x}{y} + \frac{y}{x}) \tag{4.3b}$$

$$F_{11} = \frac{1}{x} - \frac{1}{y} + \frac{1}{2} \tag{4.3c}$$

$$F_{22} = \frac{1}{4}(\frac{x}{y} + \frac{y}{x})(1 + \frac{2}{x} - \frac{2}{y}) \tag{4.3d}$$

$$F_3 = -(\frac{1}{x} - \frac{1}{y})^2 - (\frac{1}{x} - \frac{1}{y}) \tag{4.3e}$$

$$F_{33} = (\frac{1}{x} - \frac{1}{y})^2 + (\frac{1}{x} - \frac{1}{y}) + \frac{1}{2} \tag{4.3f}$$

Here $\vec{\xi}$ are the Stokes parameters for the incoming photon and $\vec{\xi'}$ are for the outgoing photon. ξ_3 characterizes the linear polarization of the photon in the y or z axes: $\xi_3 = 1$ is complete polarization along the y-axis and $\xi_3 = -1$ is complete polarization along the z-axis. In a similar way, ξ_1 characterizes the linear polarization of the photon 45° from the y or z axes, and ξ_2 characterizes the degree of circular polarization of the photon. For simplicity, only linear polarization along the y-axis will be considered, so only ξ_3 is non-zero. The total cross section averaged over ξ' is given by:

$$d\sigma \propto F_0 + \xi_3 F_3 \tag{4.4}$$

Let $F = F_0 + \xi_3 F_3$. The polarization of the emitted photon is given by the ratio of the coefficient of ξ' to F [68], so the linear polarization of the emitted photon is:

$$\xi_3^f = \frac{F_3 + F_{33}\xi_3}{F} \tag{4.5}$$

Because the FEL photons are 100% linearly polarized, $\xi_3 = 1$. This allows significant simplification of Equation 4.5, leading to:

$$\xi_3^f = \frac{2xy}{x^2 + y^2} \tag{4.6}$$

Assuming the photon and electron collide head-on, x and y are given by:

$$x = \frac{2E_\gamma\gamma(1+\beta)}{mc^2} \tag{4.7a}$$

$$y = \frac{2E_{\gamma'}\gamma(1-\beta\cos(\theta_{\gamma'}))}{mc^2} \tag{4.7b}$$

Inserting these into Equation 4.6 and assuming $\theta_{\gamma'} \ll 1$, $\gamma \gg 1$, $\theta_{\gamma'}\gamma \ll 1$, using Equation 4.1 yields:

$$\xi_3^f = 1 - \frac{8\gamma^2 E_\gamma^2}{(mc^2)^2}(1 - 2\gamma^2\beta\theta_{\gamma'}^2) \tag{4.8}$$

For this experiment, $E_\gamma = 2.3\,\text{eV}$ and $\gamma \sim 820$ yielding:

$$\xi_3^f = 1 - .000047(1 - 2\gamma^2\beta\theta_{\gamma'}^2) \tag{4.9}$$

For $\theta_{\gamma'}$ equal to 0, $\xi_3^f = 0.999953$, so the ideal linear polarization of the beam is 99.990%.

There is another effect which alters the polarization of the γ-ray beam. In the rest frame of the electron beam, for a γ ray emitted at an angle $\theta_{\gamma'}$, the polarization of the γ ray is in the direction of $\hat{\theta_{\gamma'}}$ [69]. The polarization does not change in the Lorentz transformation into the laboratory frame, so this effect causes a $\cos(\theta_{\gamma'})$ dependence of the polarization on the direction of the γ ray. Using an angle of $100\,\mu$rad, which is the maximum possible $\theta_{\gamma'}$ in our experiment (Section 4.2.4), the ideal polarization at the outer edge of the γ-ray beam based on this effect is expected to be better than 99.990%, so this effect can be neglected. Because the calculated polarization from these two effects (the recoil term in the Klein-Nishina formula and

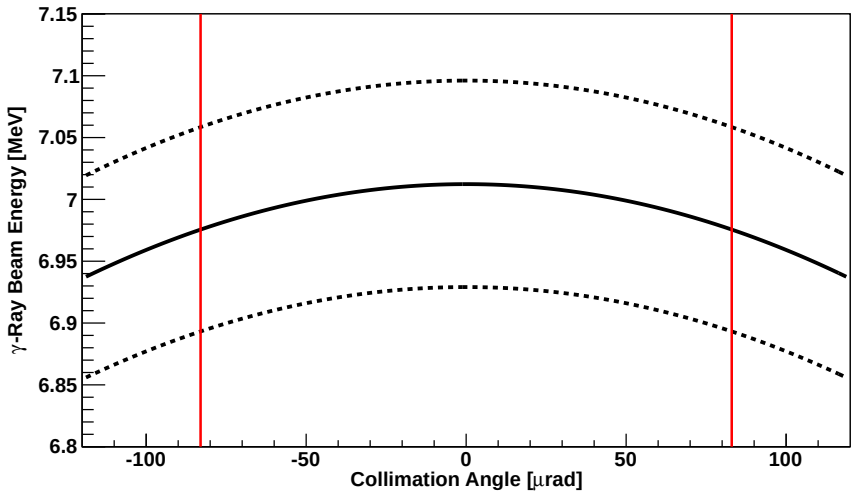

FIGURE 4.4: The solid black line shows the γ-ray beam energy as a function of collimation angle for a nominal beam energy of 7 MeV. Equation 4.1 was used with $\gamma = 881.4$ and $\lambda = 540$ nm. The dashed black lines show the γ-ray beam energy spread due to the electron beam energy spread, which was assumed to be $6\text{x}10^{-3}$. The red lines show $\pm 83\,\mu$rad from the center position.

the emittance effect of the γ-ray beam) is very close to 100%, for this dissertation the beam will be assumed to be 100% polarized with no systematic uncertainty. Previous measurements are consistent with a beam polarization of 100% [70].

Because the γ rays are made by colliding bunched electrons with photons, the γ-ray beam is pulsed. Each electron bunch travels in the ESR with a repetition rate of 2.79 MHz, and because each bunch lases photons and scatters the other bunch's photons, the repetition rate of the beam is 5.58 MHz, leading to a pulse of γ rays every 179 ns.

4.2.4 γ-Ray Collimation

As can be seen from Equations 4.2 and 4.9, the beam energy spread increases and the beam polarization increases as $\theta_{\gamma'}$ increases. To keep the energy spread of the beam low and ensure that all of the γ rays produced encounter the target, $\theta_{\gamma'}$ must be constrained to small values around $\theta_{\gamma'} = 0$. This is achieved by collimating the beam

in the collimator hut (CH). The CH is the first room that the γ-ray beam passes through after exiting the optical cavity and evacuated beam pipe. Lead collimators are inserted into the beam line roughly 60 m downstream of the electron-photon collision point, as shown in Figure 4.1 [63]. For these experiments, collimators of either 10 mm or 12 mm diameter were used depending on the target dimensions. This restricted $\theta_{\gamma'}$ to 83 or 100 μrad, respectively. Figure 4.4 shows the dependence of beam energy on θ, indicating the collimation angle of 83 μrad, and the dependence of beam energy on the electron beam energy spread, which was assumed to be 0.6% as discussed in Section 4.2.1.

4.3 γ-Ray Beam Monitoring

4.3.1 The Beam Position Monitor

The Beam Position Monitor (BPM) is a set of 4 button style electrodes made of aluminum located in the ESR [71]. The BPM signal was used to correlate particular events in the neutron detectors with either the γ-ray beam or with room backgrounds. After an electron bunch passes by the BPM, a charge is induced on the electrodes which is read off using a capacitive pickoff circuit. The electrons passing the BPM and the γ rays traveling into the target room both occur at 5.59 MHz and have a constant phase difference. The BPM circuit is described in Section 4.7.1 and the use of the BPM signal in the data analysis is described in Section 5.5.

4.3.2 The 5-Paddle System to Monitor γ-Ray Beam Intensity

The purpose of the 5-paddle system is to continuously monitor the γ-ray beam intensity during production runs [72]. The thin plastic scintillating paddles are labeled $0-4$ as shown in Figure 4.5. Paddles 0 and 1 are upstream of an aluminum radiator, while paddles 2 through 4 are downstream of the radiator. The paddles are approximately 2.1 mm thick and composed mainly of hydrogen and carbon, so it is unlikely

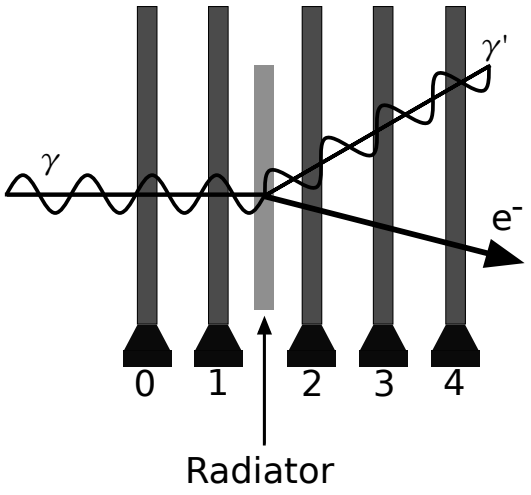

FIGURE 4.5: An illustration of the 5-paddle system. A γ ray can Compton scatter or pair produce in an aluminum radiator between paddles 1 and 2, generating a free electron. The electron can then cause paddles 2-4 to trigger in coincidence without triggering paddle 1.

that a γ ray in the beam will directly deposit energy through Compton scattering or pair production in one of the paddles. It is more likely that a γ ray traveling down the beam will either Compton scatter off of an atomic electron in the radiator or pair produce in the radiator. Either of these interactions will generate an electron that will likely travel through paddles 2 through 4 but not hit paddle 1, as can be seen in Figure 4.5. On the other hand, an electron or proton traveling in the beam will intersect paddle 1 in addition to paddles 2 through 4. By requiring a coincidence between paddles 2 through 4 and an anti-coincidence with paddle 1, the γ-ray beam intensity can be monitored without including contributions from any charged particles in the beam. Charged particles in the beam, including those generated by the 5-paddle system, are later removed using a sweeper magnet. Advantages to requiring a coincidence between paddles 2 through 4 include a reduction in background triggers and a lower efficiency than requiring a single trigger. This reduction in efficiency allows the 5 paddle system to count at a reasonable rate ($\sim 200\,\text{kHz}$) even at large

beam intensities ($\sim 10^7\gamma/s$). The overall efficiency of the 5 paddle system for these experiments was approximately 1/60.

The paddles are made of the plastic scintillator BC-400. This material was chosen because it provides a prompt pulse of short duration when struck by an electron. Because the beam is pulsed every 179 ns, a detector with prompt, short duration pulses was required. Electrons produced by the radiator that travel through the scintillator will be minimum ionizing, so the overall system is relatively insensitive to gain drifts in the PMTs attached to the scintillators. Because the efficiency is low and the electrons do not deposit much energy in the scintillators, the paddles can be left in the full intensity of the beam during production runs to continuously monitor the relative intensity of the beam. The 5-paddle system begins to saturate at very high beam intensities ($\geqslant 10^7\gamma$/s), but the beam intensities for our experiments were all below this saturation threshold.

4.3.3 The Copper Attenuator System

The purpose of the copper attenuator system is to reduce the beam intensity. Sensitive detectors inserted directly into the γ-ray beam, such as the NaI(Tl) detector to measure the beam intensity or the HPGe detector to measure the beam energy, may not operate properly when the counting rate exceeds 2x10^3 Hz. High beam intensity could potentially damage the detector, in addition to causing significant dead time in signal processing and storage.

To reduce the beam intensity, any of 6 copper attenuators can be inserted remotely into the beam by the experimenter. Attenuator 1 has a length of 2.45 cm, attenuator 6 has a length of 4.90 cm, and attenuators 2 through 5 are 8.00 cm long. The lengths were chosen to attenuate a 5 MeV γ-ray beam by factors of 2, 4, and 10 for attenuators 1, 6, and $2-5$ respectively. The copper attenuators are located just downstream of the southeast mirror in the lasing cavity, which is well upstream of

the 5 paddle system and the GV, as shown in Figure 4.1. Therefore, any scattered photons, neutrons, or charged particles freed from the attenuators are unlikely to make it down the beam and reach the target. For these experiments, beams ranging from approximately $3\text{x}10^6 - 10^7\gamma/s$ were attenuated to reduce the beam intensity to approximately $10^3\gamma/s$ when the NaI(Tl) or HPGe detectors were used.

4.3.4 The NaI(Tl) Detector to Measure Beam Intensity

A large NaI(Tl) detector is used to perform a measurement of the absolute value of the γ-ray beam intensity and to calibrate the 5-paddle system. When both the NaI(Tl) detector and the 5-paddle system are in the γ-ray beam, the efficiency of the 5-paddle system can be directly measured. The NaI(Tl) detector is located next to the downstream wall in the GV (Figure 4.1) and can be moved in or out of the beam remotely using a Labview controller and a stepper motor. The detector is cylindrical in shape with a diameter of 10 in and a length of 14 in [73]. The NaI(Tl) detector cannot be used as a real-time beam monitor during production runs because the beam must be attenuated in order to obtain quality spectra, reduce dead time, and prevent damage to the detector. However, by using the NaI(Tl) detector and the 5-paddle system together during a short ($\sim$ 10 minute) run with an attenuated beam of known attenuation, the efficiency of the 5-paddle system can be measured relative to the NaI(Tl) detector. That efficiency can then be used to calculate the actual beam intensity when the beam is not attenuated during production runs.

At the γ-ray energies used in these experiments, the NaI(Tl) detector is nearly 100% efficient, so a direct integration of the measured detector spectrum above room backgrounds gives a reasonable estimate of the total number of γ rays incident on the detector. This estimate is then corrected for dead time (typically 5%) and attenuation in the air between the 5 paddle system and the detector (typically $4-5\%$) to obtain an estimate of the total number of γ rays incident on the 5 paddle system

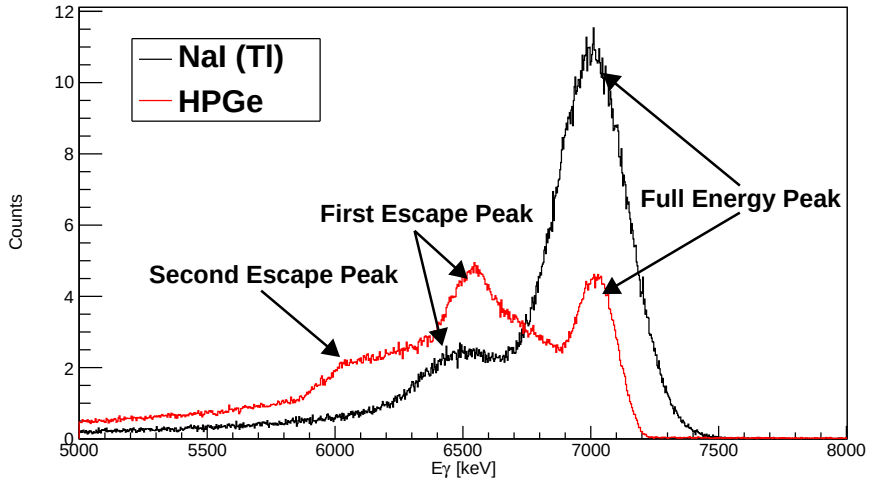

FIGURE 4.6: Spectra from the NaI(Tl) and the HPGe detectors for a beam energy of 7 MeV. The first escape peak occurs when an electron-positron annihilation photon of energy 511 keV escapes the detector. Two escapes of 511 keV generate the second escape peak. In the HPGe detector, the energy resolution of the full energy peak is dominated by the energy spread of the beam. The energy resolution in the NaI(Tl) detector is worse than the HPGe, but the peak efficiency of the NaI(Tl) detector is much greater than that of the HPGe.

during the intensity measurement. Because the 5-paddle system has a very low background counting rate, the efficiency of the 5-paddle system can be directly measured by comparing the total number of 5 paddle counts and projected 5 paddle counts from the NaI(Tl) detector. Typically this efficiency is approximately 1/60 for γ-ray beams between $5 - 7.5$ MeV.

4.3.5 The HPGe Detector to Measure Beam Energy

A High Purity Germanium (HPGe) detector, located next to the downstream wall in the UTR, is used to measure the beam energy spectrum. Beam energy measurements were taken before or after most production runs to measure the beam energy spectrum. The energy resolution of the HPGe is much better than the NaI(Tl) at the beam energies used in this experiment, as can be seen from Figure 4.6. To use the HPGe to measure the beam energy, the beam intensity was attenuated to ap-

proximately $10^3\gamma/s$ and the detector was remotely moved into the beam. The beam energy spread is much larger than the HPGe resolution at these energies [74], so the HPGe measurements give a direct estimate of the beam energy spectrum. The beam energy spread shown in Figure 4.6, as measured by the HPGe, is in agreement with the expected beam energy spread from Figure 4.4.

4.4 Targets

4.4.1 The D_2O Target

A liquid D_2O target was used to calibrate the neutron detectors. The target was a 4.7 cm long cylinder with a diameter of 4.1 cm. For a given γ-ray energy and detector angle, the $d(\gamma, n)$ reaction emits mono-energetic neutrons. These neutrons serve as a test of the neutron energy determination algorithm for each neutron detector. Measurements using the D_2O target were performed at the start of each experiment. More details on how the $d(\gamma, n)$ reaction was used in the analysis are provided in Section 5.5.3.

4.4.2 Fissionable Targets

Measurements on seven different fissionable targets were taken for this dissertation. The target isotope, mass, enrichment, and main impurity in each target are listed in Table 4.1. The ^{238}U and ^{232}Th targets were natural uranium and natural thorium. The enrichment of the ^{233}U target was measured by Pacific Northwest National Laboratory (PNNL) using passive γ ray counting. This assay yielded an unknown amount of ^{232}Th in the ^{233}U target, which could create a significant background to the ^{233}U measurements. The assay was only able to set an upper limit on the amount of ^{232}Th in the target. Unfortunately due to the long half-life of ^{232}Th, this upper limit was well above the actual mass of the target. The scientist who conducted the assay estimated the ^{232}Th mass to be less than 0.1 g based on the measured mass

Table 4.1: Masses and enrichments of the fissionable targets.

Target	Mass (g)	Enrichment (%)	Main Impurity
^{232}Th	17.36	99.9	-
^{233}U	4.08	>97.5	^{232}Th (<2.5%)
^{235}U	4.620	93.7	^{238}U (6.3%)
^{238}U	6.884	99.3	^{235}U (.7%)
^{237}Np	4.40	99.9	-
^{239}Pu	3.808	94.0	^{240}Pu (5.8%)
^{240}Pu	4.71	98.7	^{239}Pu (.5%)

of the target and the mass of the ^{233}U oxide based on the radioactive decay assay [75]. An analysis of photofission data in an attempt to extract the enrichment of this target was performed and yielded an enrichment of $94.6 \pm 3.0\%$, as described in Section 5.9.5. The estimate from the assay scientist is close to the results from the analysis of the photofission data and did not require any underlying assumptions, so the enrichment of the target is assumed to be 97.5%.

In addition to having different masses and enrichments, the targets also had different geometries. The ^{239}Pu, ^{233}U, and ^{237}Np targets were all in a lollipop configuration, as shown in Figures 4.7 and 4.8. The ^{237}Np target was identical to the ^{233}U target. In this configuration, the fissionable material was enclosed in a disk with thin entrance and exit windows on the sides and a holder rod coming out of the edge of the disk. The thin windows did not significantly attenuate the beam or scatter neutrons as they exited the target. To mount the target in the beam, the holder rod was screwed into a target holder.

The ^{235}U, ^{238}U, and ^{232}Th targets were foil targets, as shown in Figures 4.9, 4.10, and 4.11. For the ^{235}U and ^{238}U targets, the fissionable powders were sealed in plastic

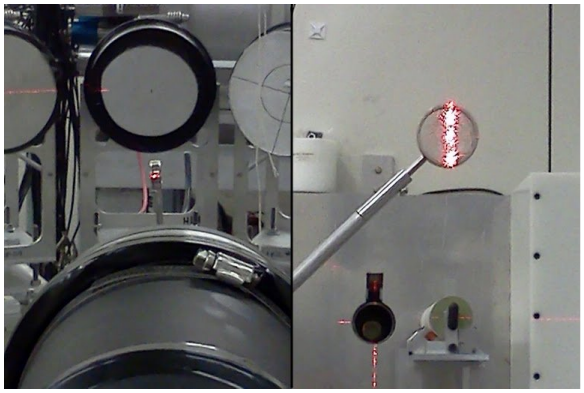

FIGURE 4.7: A picture of the ^{239}Pu target mounted in the neutron detector array. The lasers indicate the position of the beam. The diameter and thickness of the ^{239}Pu in the target are 14 mm and approximately 1.3 mm respectively. The diameter and thickness of the target, including the steel casing, are 25 mm and 6.5 mm respectively.

FIGURE 4.8: A picture of the ^{233}U target. A chamber of diameter 25.4 mm holding the ^{233}U is located in the center of the casing. The thickness of this chamber is 5.0 mm, and the thickness of the entrance and exit windows total 1.5 mm. Other dimensions of the casing are indicated. The ^{237}Np target is identical to this target.

wrap and a ziplock bag. The ^{232}Th target was a piece of natural thorium metal. The targets were mounted using a clamp screwed into the target rod holder.

As seen from Figure 4.12, the ^{240}Pu target had a much more complicated geometry than the other targets. The fissionable powder was suspended at the bottom of a metal cylinder capped by a large bolt. In this configuration, the ^{240}Pu powder was

FIGURE 4.9: A picture of the ^{235}U target. All three foils were taped together and rotated by 45° in θ and 45° in ϕ when mounted in the beam. Each square foil is 25.4 mm per side and approximately 0.3 mm thick.

FIGURE 4.10: A picture of the ^{238}U target. The target has dimensions 36.5 mm x 52.0 mm x 0.2 mm. It was rotated by 45° in θ and 45° in ϕ when it was mounted in the beam.

surrounded by a significant amount of aluminum. ^{240}Pu emits α particles which can induce neutrons to be emitted from the target casing through the $^{27}Al(\alpha, n)$ reaction. Even though these neutrons were emitted out of time with the pulsed γ-ray beam, they generated a significant background for the prompt fission neutron measurements which primarily affected the low beam energies ($E_\gamma \sim 5.6$ MeV) where the fission cross section decreased quickly. This background will be discussed further

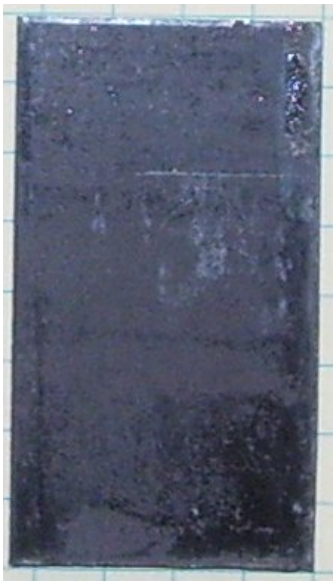

FIGURE 4.11: A picture of the ^{232}Th target. The target is 28 mm wide, 53 mm long, and 1 mm thick.

FIGURE 4.12: A picture of the ^{240}Pu target. A technical drawing of the target is not available, so all measurements are only approximate. The length of the target is 88 mm and the outer diameter of the tube is 23 mm. The diameter of the bolt is 35 mm.

in Section 5.7.

Table 4.2: Summary of linearly-polarized beam energy and target combinations

Letter	Targets	Energy Range (MeV)	Primary Group	Date
A	^{238}U	5.7 - 6.5	LLNL	March, 2010
B	^{235}U	5.6 - 7.0	LLNL	July, 2010
C	^{235}U, ^{238}U, ^{239}Pu, ^{232}Th	5.6 - 7.3	TUNL	September, 2010
D	^{239}Pu	5.3 - 7.0	TUNL	July, 2011
E	^{233}U	5.6 - 7.0	TUNL	October, 2011
F	^{240}Pu	5.9 - 7.6	TUNL	November, 2011
G	^{240}Pu, ^{238}U, ^{239}Pu	5.5 - 7.0	TUNL	December, 2011
H	^{232}Th, ^{237}Np	5.4 - 7.0	TUNL	July, 2013

4.5 Beam Usage Summary

Table 4.2 shows a summary of the linearly polarized γ-ray beam energies used for each target. Experiments **A** and **B** were performed as a collaboration between the Capture group at TUNL, of which the author is a member, and scientists from Lawrence Livermore National Laboratory (LLNL). The Capture group set up and operated the detectors, while the personnel from LLNL made decisions on beam energies and the run plan. Experiments **C** through **H** were performed primarily by the Capture group. The author aided in setting up and operating the detectors for experiment **C** but did not make decisions regarding the run plan. The author was the primary experimenter for experiments **D**, **E**, **G**, and **H**, and made decisions regarding the run plan in addition to setting up and operating the detectors. In experiment **F**, the primary experiment took place in the UTR and our data were collected parasitically downstream in the GV. Each experiment used approximately 48 hours of beam time. All data taken in these experiments and shown in this thesis

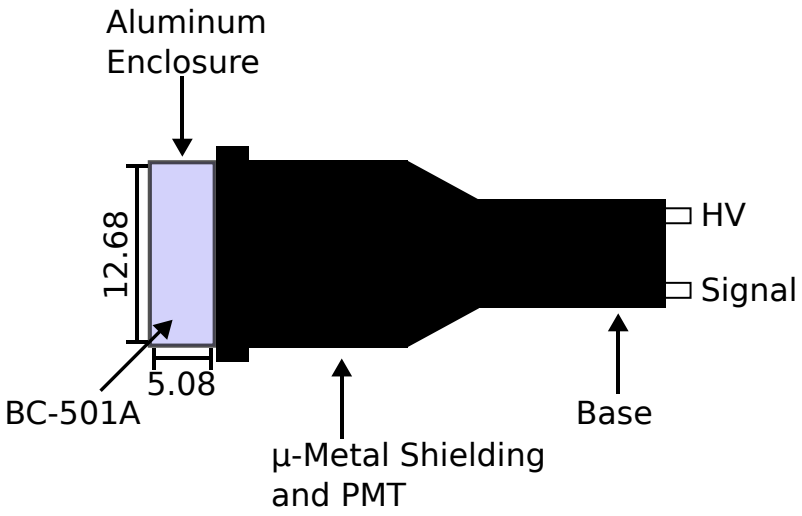

FIGURE 4.13: An illustration of a neutron detector. All dimensions are given in cm. This drawing is not to scale.

have been analyzed by the author and have not been published elsewhere except for a previous publication on some of the early results by the author [76].

4.6 Neutron Detectors

4.6.1 Physical Construction

The detector is composed of three main pieces: the active volume, the PMT, and the base. An illustration of the detector is shown in Figure 4.13. The active volume is cylindrical in shape with a diameter of 12.68 cm and thickness of 5.08 cm and is filled with the organic liquid scintillator BC-501A [73]. One face of the cylinder is glass while the other sides are aluminum coated with a reflective paint to increase the amount of scintillation light that exits the volume through the glass.

The glass face of the scintillating volume is coupled to a PMT using optical grease. The PMT is encased in μ-metal which shields it from magnetic fields. The base attached to the back of the PMT has a high voltage connection to supply

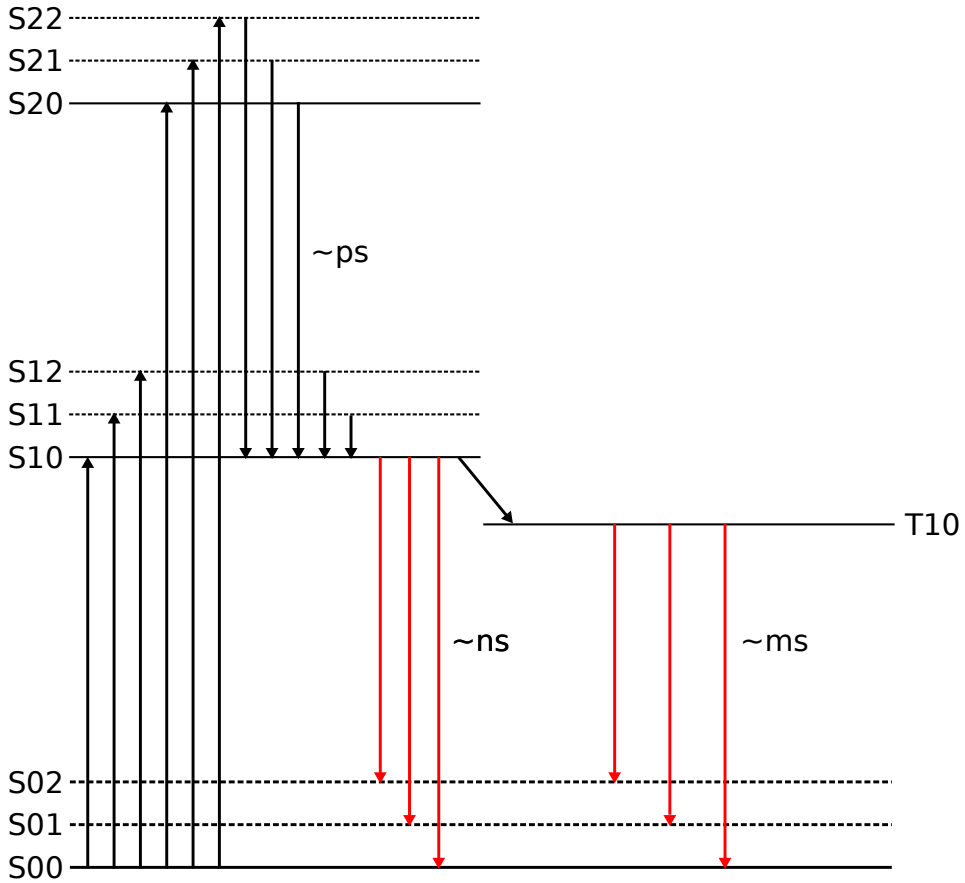

FIGURE 4.14: An approximate energy level diagram of a scintillating organic molecule [74]. Not to scale. Radiative transitions are indicated in red, and approximate timescales are shown next to the relevant transitions.

negative voltage to the different stages of the PMT, keeping the anode at ground in the absence of a signal. The base also has a connection to the anode of the PMT so that the electrical signal can be read.

4.6.2 Characteristics of BC-501A

BC-501A is a commercially available organic liquid scintillator developed for applications involving fast neutron detection in high γ-ray background environments. As is true for scintillator detectors in general, BC-501A converts a small fraction of de-

posited energy into scintillation light. BC-501A and other organic scintillators take advantage of the π-electron structure of certain organic molecules to generate scintillation light [74]. Neutrons and γ rays can scatter off of charged particles in the detector, and as charged particles travel through the active volume, they deposit energy by exciting electrons in molecular orbitals. The ground state of these electrons is a singlet state called S00, as indicated in Figure 4.14. Vibrational states based off of this ground state are labeled by S0I, where I is an index, and the typical spacing of these states is 0.15 eV. Excited singlet (SI) and triplet (TI) states exist with energy spacings of approximately $3 - 4$ eV. The molecular electrons excited by the charged particle will generally be excited to a singlet state SIJ which will decay on the order of picoseconds to the S10 state through radiationless internal conversion. The S10 state can then decay to either the S00 state, an S0I state, or the T10 state. The lifetime of the decay from the S10 state to the S00 or S0I state is on the order of nanoseconds, while the lifetime of the decay from the T10 state to the S00 or S0I state is on the order of milliseconds. All of the decays to the S0I state produce a photon of scintillation light, as shown in red in Figure 4.14.

4.6.2.1 Pulse Shape Discrimination (PSD)

BC-501A was developed to have a useful property where the shape of the pulse depends on the type of recoiling charged particle. The pulse from the detector is typically well characterized by the sum of two exponentials: a fast exponential with a decay time of a few nanoseconds and a slow exponential with a decay time of a few hundred nanoseconds. Particles with large stopping powers leave a higher density of excited T10 states along their path. Two T10 states can undergo a bimolecular interaction converting them to one excited S10 state and another S00 state [74]. The S10 state can then decay and emit a photon. Because the T10 states are long lived and the recombination probability depends on the square of the density of T10 states,

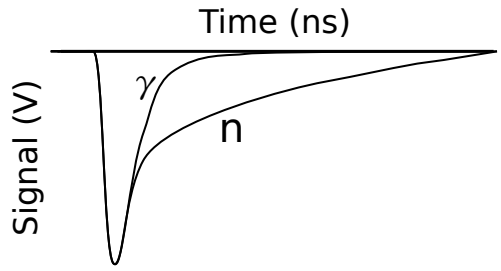

FIGURE 4.15: An example of pulses from the neutron detector for incident γ rays and neutrons. These pulses can be distinguished using Pulse Shape Discrimination, as discussed in Section 4.6.2.1.

particles with larger stopping powers will have a higher proportion of emitted light in the slow component relative to particles with smaller stopping powers. By measuring the ratio of the slow component to the fast component, the stopping power of the recoiling charged particle can be measured.

γ rays will typically interact in the detector by Compton scattering off of molecular electrons. The electron will then recoil in the detector and deposit energy. On the other hand, neutrons will scatter off of protons and ^{12}C nuclei, and those heavier particles will recoil and deposit the energy in the detector. Because the stopping power of electrons is very different from that of protons or ^{12}C nuclei, events originating from γ rays can be distinguished from events originating from neutrons, as can be seen in Figure 4.15. Because a γ-ray beam was used in this experiment, it was critical to eliminate γ ray backgrounds using PSD cuts, as described in Section 5.6.3.

4.6.2.2 Light Output Response

The light output response of the detector is the distribution of pulse heights generated by the detector from a mono-energetic source of particles. Neutrons entering the

detector can elastically scatter off of protons and ^{12}C nuclei, and those recoiling nuclei can generate scintillation light by exciting molecular electrons. Assuming a nonrelativistic neutron has an elastic collision with a proton or ^{12}C nucleus, the energy of the recoiling nucleus, and thus the energy deposited in the detector, is given by [74]:

$$E_R = \frac{4AE_n}{(1+A)^2}\cos^2\theta \tag{4.10}$$

where θ is the lab angle between the initial direction of the neutron and the momentum direction of the recoiling nucleus, A is the mass of the recoiling nucleus and E_n is the energy of the neutron. The probability of depositing a given energy E_R in the detector for a mono-energetic source gives the ideal light output response. For the case of neutrons elastically scattering in the detector, this probability is given by [74]:

$$P(E_R) = \frac{(1+A)^2}{A}\frac{\sigma(\Theta)}{\sigma_s}\frac{\pi}{E_n} \tag{4.11}$$

where Θ is the center-of-mass scattering angle, σ_s is the total elastic scattering cross section, and $\sigma(\Theta)$ is the differential elastic scattering cross section. If the differential cross section is isotropic as is the case for scattering off of protons at low energies, and the scintillator light output scales linearly with energy deposited in the detector, then the ideal light output response is given by a simple rectangle:

$$\frac{dN}{dH} = \frac{(1+A)^2}{A}\frac{1}{4E_n} \tag{4.12}$$

where N is the number of counts observed with pulse height H.

Several effects distort the ideal light output response of the detector. One important effect is the non-linearity inherent in the detector. In reality, the light generated by the scintillator does not depend linearly on the energy deposited in the detector.

The light generated per unit length is well described by Birk's Law [74]:

$$\frac{dL}{dx} = \frac{S\frac{dE}{dx}}{1 + kB\frac{dE}{dx}} \tag{4.13}$$

where S and kB are adjustable parameters that depend on the type of scintillator. For charged particles with low stopping powers ($\frac{dE}{dx}$), the light generated per unit length is proportional to the energy deposited per unit length. Therefore the total light collected is proportional to the energy deposited and the detector has a linear response. kB takes into account the quenching effect of the detector for particles with large stopping powers. For large stopping powers, quenching effects reduce the amount of light generated per unit length. In this experiment, recoiling electrons, protons, and ^{12}C nuclei generated the majority of the scintillation light. For electrons the detector was expected to behave linearly, and for protons only a small non-linearity was expected [74]. For ^{12}C nuclei, the quenching effects were expected to be significant, so much less light was generated from elastic scattering off of ^{12}C nuclei.

Other effects that impact the light output response include:

- The finite size of the scintillating volume makes it possible for recoiling protons to escape the active volume without depositing their full energy
- Multiple scattering of neutrons off of protons in the scintillator would increase the observed pulse height
- The finite resolution of the detector, due to nonuniform light collection, photoelectron statistics, or electronic noise, smears the light output response function

The combination of these non-ideal effects yields a light output response function as shown in Figure 4.16. A neutron entering the detector with a different amount of kinetic energy than that shown in Figure 4.16 will have a similar light output response, but it will be shifted or stretched. It is clear that the energy of the incident neutron

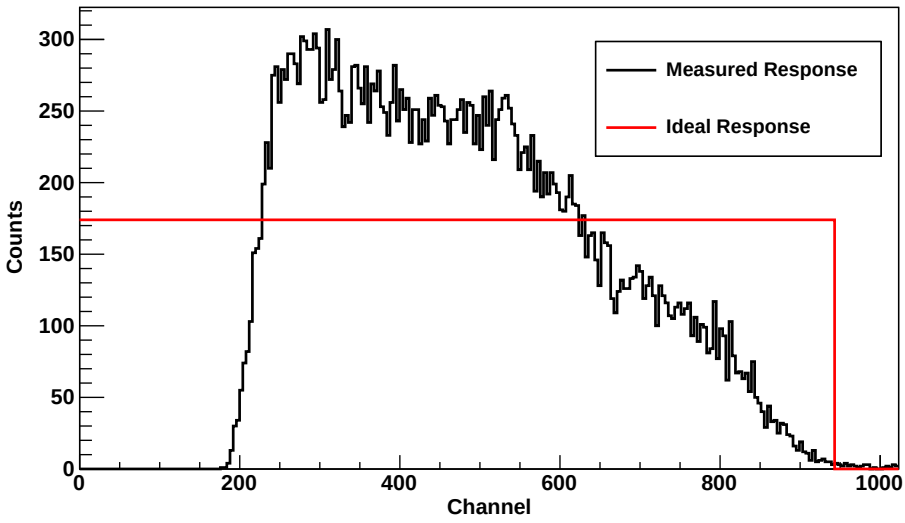

FIGURE 4.16: The measured detector response for incident neutrons of 2.4 ± 0.1 MeV. The detector threshold is near channel 200.

cannot be recovered on an event-by-event basis from the pulse height measured by the detector. However, using time-of-flight techniques as described in Section 5.5, the neutron energy can be accurately determined on an event-by-event basis.

4.6.2.3 Additional advantages of using BC-501A

There are several additional characteristics of BC-501A scintillation detectors that are useful for neutron detection [74]:

Transparency to its own emissions Ideally, the scintillator should be transparent to its own scintillation light to allow for efficient light collection. BC-501A achieves this property through the population of vibrational states S0I in the radiative decay from S10, as shown in Figure 4.14. The photon emitted from the decay of S10 to S0I will not have enough energy to excite another molecular electron from the S00 state to the S10 state, so another molecular electron will not reabsorb this photon and the scintillator is transparent to its own emissions.

Fast decay time The decay time of BC-501A is on the order of nanoseconds which allows for fast signal pulses to be generated. This fast decay time also permits the use of time-of-flight techniques to measure detected neutron energies, as will be shown in Section 5.5.

Large hydrogen content The ratio of ^{1}H to ^{12}C in the scintillator is 1.212 [74]. The majority of the light generated is from recoiling protons, while recoiling carbon nuclei produce less scintillation light. A larger hydrogen content gives a larger light output, which improves the energy resolution of the detector.

4.6.3 Detector Calibration

Two sources were used to calibrate the detectors. A ^{137}Cs source was used to measure the gain of the detector and calibrate the pulse height spectrum. The calibration of the pulse height spectrum is important in setting the detector threshold, which determines the detector efficiency. The calibration relies on the 662 keV γ ray emitted when ^{137}Cs beta-decays to an excited state of ^{137}Ba. This γ ray can enter the detector and Compton scatter off of a molecular electron. The midpoint of the edge of the light output response function for this γ ray corresponds to a deposited energy of 517 keV [73]. This gives a calibration between the deposited energy and the light output. To distinguish the light output from deposited energy, the units of keVee or MeVee are used for the light output, where the ee stands for *e*lectron *e*quivalent light output. A recoiling electron with an energy of 517 keV would generate a light output of 517 keVee. However, because protons generate a different amount of light per keV deposited, as is clear from Birk's Law in Equation 4.13, a recoiling proton with 517 keV would generate less than 517 keVee of light output. The ^{137}Cs source is used to calibrate the pulse height spectrum in units of keVee or MeVee. The light output response function from a ^{137}Cs source is shown in Figure 5.1.

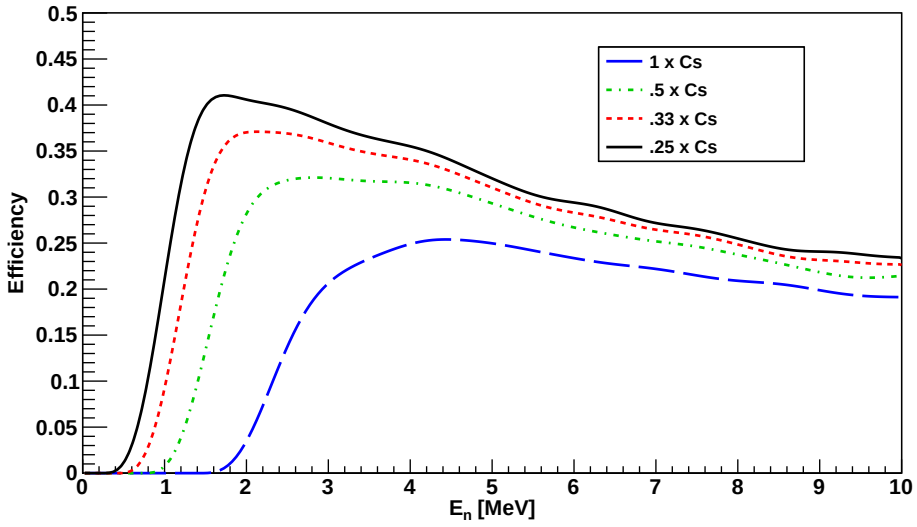

FIGURE 4.17: The simulated neutron detector efficiency as a function of detector threshold and neutron energy [77].

Any changes in the detector gain would affect the detector threshold, and these changes could be detected as a shift of the midpoint of the ^{137}Cs edge. Measurements of the detector gain with a ^{137}Cs source were performed two or three times a day during every experiment to ensure that the gains of the detectors were stable.

The other source used for calibration in these experiments was an ^{241}Am/^{9}Be source. ^{241}Am is an α-particle emitter, and a ^{9}Be nucleus can capture an α-particle to form ^{13}C and then emit a neutron. 4.4 MeV γ rays are emitted when the resulting ^{12}C nucleus decays to its ground state. The ^{241}Am/^{9}Be source can be used to test the PSD properties of the neutron detectors because both neutrons and γ rays are generated by this source. A measurement with the ^{241}Am/^{9}Be source was taken daily to ensure that the PSD properties of the detectors were functioning normally. An ^{241}Am/^{9}Be source spectrum is shown in Figure 5.4.

4.6.4 Detector Efficiency

Because the light output response function has a significant component at low pulse heights, the detector efficiency has a strong dependence on the detector threshold. By increasing the detector threshold, the efficiency of the detector is reduced. Experimental measurements of neutron detector efficiencies have been performed and shown to agree well with a simulation developed by Physikalisch-Technische Bundesanstalt [77]. The detector threshold is typically referenced in terms of multiples of the midpoint of the ^{137}Cs edge. For example, 1xCs refers to 517 keVee, while 0.25xCs is 129 keVee. Figure 4.17 shows the simulated efficiency of a detector as a function of neutron energy and detector threshold.

4.6.5 Construction and Alignment of the Detector Array

The eighteen neutron detectors used in these experiments were attached to support structures made of an 80/20 aluminum alloy. Two support structures were constructed, one with a nominal neutron flight path of 1 m and another with a flight path of 0.5 m. Experiment **A** (Table 4.2) was performed using the 1 m flight-path detector array, while the other experiments were performed with the 0.5 m flight path array.

A schematic of the 0.5 m flight path neutron detector array is shown in Figure 4.18. Nine neutron detectors are in the horizontal plane and the other nine detectors are in the vertical plane. The front faces of the detectors are approximately 57 cm from the target position, which is located above the center of the horizontal ring. To precisely measure asymmetries originating from the polarization of the beam, the horizontal and vertical detectors are paired in scattering angle relative to the beam direction. The size of the detector mounts constrained the possible angles of the detectors. Using the letter designations in Table 4.2, the locations of

FIGURE 4.18: A schematic of the half-meter neutron detector array

the centers of detectors for the different experiments were:

A Only twelve detectors were used. Three sets of four neutron detectors, two in the horizontal plane and two in the vertical plane, were located at scattering angles of 75°, 90°, and 126°.

B and C Three sets of four detectors, two in the horizontal plane and two in the vertical plane, were located at scattering angles of 55°, 90°, and 125°. Three sets of two detectors, one in the horizontal plane and one in the vertical plane, were located at scattering angles of 72°, 107°, and 142°. In this arrangement, the detector mounts spanned 17°, so detectors could not be placed within 17° of each other.

D through H Three sets of four detectors, two in the horizontal plane and two in the vertical plane, were located at scattering angles of 53°, 90°, and 126°. Three sets of two detectors, one in the horizontal plane and one in the vertical plane, were located at scattering angles of 71°, 107°, and 144°. In this arrangement, the detector mounts were pushed as close as possible on the 0.5 m array to the target, which slightly increased the angles between the detectors. In experiment **H** the detectors at 144° were not used.

The uncertainty on the measured angles is approximately 0.5°. Due to the finite size of the active volume, each detector spanned approximately ±6.4° in scattering angle. After the detectors were mounted, a survey was performed to measure the detector angles, and the detectors were adjusted as needed to ensure the horizontal and vertical detectors were matched in angle.

The alignment of the detector array was performed using multiple alignment lasers. The lasers are calibrated to the position of the beam spot on the east wall of the GV and the beam pipe on the west wall of the GV (Figure 4.1). The target is mounted with the aid of a beam spot laser, which begins in the CS and travels downstream through the beam pipe and onto the beam spot on the east wall of the GV.

4.7 Signal Processing and Storage

Analog signals originating in the detectors were carried to the counting room from the GV or UTR using low-loss coaxial cables. Many different electronic circuits were used to process the different detector signals. In general, Nuclear Instrument Module (NIM) based electronic modules processed signals and generated triggers, and the processed signals were sent to Versa Module Europa (VME) based digitizers and then sent to a computer for storage.

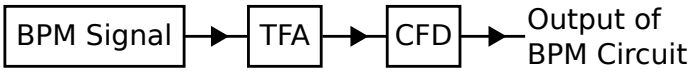

FIGURE 4.19: The BPM circuit.

4.7.1 BPM Circuit

The Beam Position Monitor (BPM) circuit is shown in Figure 4.19. The signal from the BPM, as described in Section 4.3.1, is sent first to a Timing Filter Amplifier (TFA) to shape the pulse for better timing information. The shaped pulse then passes to a Constant Fraction Discriminator (CFD), and the output of this CFD is used in the neutron detector circuit as a stop in the Time to Digital Converter (TDC), as shown in Figure 4.22. The CFD outputs a NIM logic true pulse, defined to be -800 mV, whenever a signal exceeds a threshold set on the CFD. The NIM logic false is defined to be 0V.

4.7.2 NaI(Tl) and HPGe Circuits

Similar circuits were used to process signals from the NaI(Tl) and HPGe detector. A representative circuit is shown in Figure 4.20. The signal from the NaI(Tl) or HPGe travels to a Magic Tee, which is a set of resistors that splits the signal into two branches having matched impedances. One branch is sent to a Spectroscopic Amplifier, where the signal is amplified and shaped, then sent as an input to the Analog to Digital Converter (ADC). The other branch from the Magic Tee goes to a TFA and a CFD. A logic unit prevents triggers while the ADC and DAQ are busy by vetoing the signal before it goes to a Gate & Delay Generator, which forms a gate for the ADC.

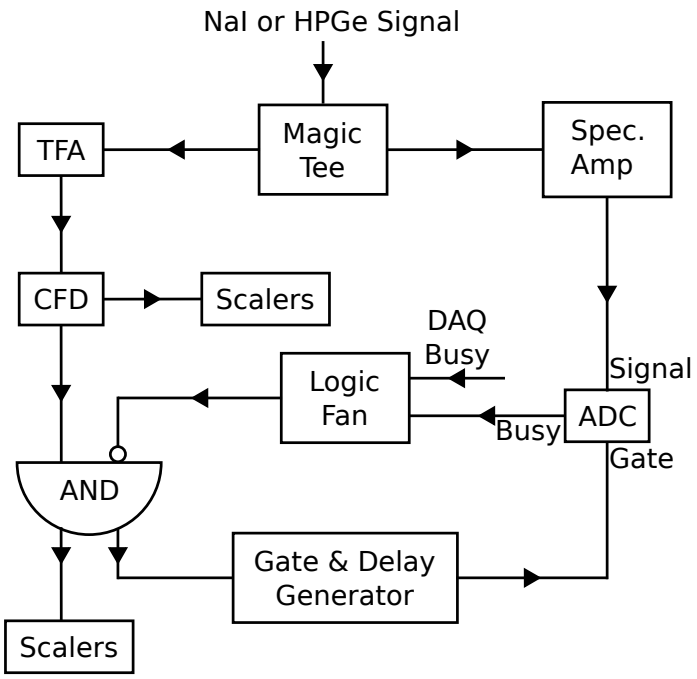

FIGURE 4.20: The NaI(Tl) and HPGe circuits. Both the NaI(Tl) and the HPGe use similar circuits, so only one is shown.

4.7.3 Veto Circuit

Pulses from the neutron detectors were processed using analog electronics and stored digitally using two Analog to Digital Converters (ADCs), a Time to Digital Converter (TDC), and a trigger module. Some time is required by the ADCs and TDC to digitize the analog signal, and during this time the ADCs and TDC are unable to process additional events. Also, the trigger module requires some time to send the digitized information to the computer during which it cannot process events. To accommodate these requirements, a veto circuit was designed to prevent the electronics from triggering when an event is being processed by the ADCs, the TDC, or the trigger module.

The veto circuit is shown in Figure 4.21. The ADCs and TDC output a NIM

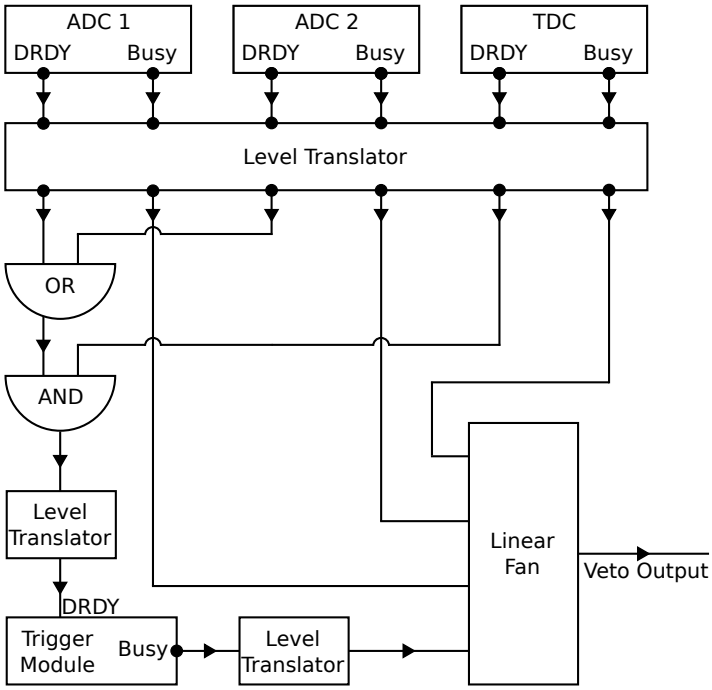

FIGURE 4.21: The neutron detector veto circuit. It prevents multiple triggers when the ADCs, TDC, or trigger module is busy.

logic signal when they are busy processing an event, and these signals are referred to as the ADC busy or TDC busy signals. The control module also outputs a NIM logic signal, called the DAQ busy, when it is sending the data to the computer. These four busy signals are sent to a level translator and then a logic fan, which outputs the logic overlap of the four signals. The output of the logic fan is sent to the neutron detector circuit as shown in Figure 4.22.

In addition to sending out a busy signal, the ADCs and TDC also send out a NIM logic pulse when they have finished digitizing the input pulse and the data is ready to be read out. This pulse is called the data-ready, or DRDY for short. The DRDY outputs from the ADCs were ORed together and then ANDed with the DRDY from the TDC to form the readout trigger for the trigger module. When the trigger module received a NIM logic pulse in the readout trigger channel, it sent the

digitized data to the computer. This circuit is also shown in Figure 4.21.

4.7.4 Neutron Detector Circuit

The circuit for the neutron detectors is designed to store the height, time information, and shape information about every pulse that exceeds a height and shape threshold. The height threshold is to prevent electronic noise from triggering the electronics, and the shape threshold is to reduce the trigger rate from γ rays without affecting neutron events.

The neutron detector circuit is built around *mesytec* MPD-4 modules [78]. The MPD-4 modules are optimized for use with organic liquid scintillator detectors, such as BC-501A, and experiments utilizing neutron time-of-flight methods with γ ray backgrounds. Inside the MPD-4 modules are an input amplifier, a CFD, and a Time to Analog Converter (TAC) to measure the length of the pulse for use in PSD. The module was operated in neutron detection mode, which enabled the TAC threshold in the module to reduce the trigger rate from γ rays. The MPD-4 module processes the pulse from a neutron detector and generates four outputs:

Ampl This output is the amplified integrated charge from the detector, and is proportional to the energy deposited in the detector as discussed in Section 4.6.2.2.

TAC The TAC output is the ratio of the fast to slow component of the detector pulse. A larger TAC value corresponds to a larger slow component, which indicates an event caused by a neutron, as described in Section 4.6.2.1.

n/g-Trig This outputs a NIM logic pulse if the input signal passes both the pulse height threshold and the TAC threshold.

Gate The **Gate** output generates a gate for the **Ampl** and **TAC** outputs for use in the ADC or TDC. For these experiments, ADC and TDC gates were generated using the **n/g-Trig**, and the **Gate** output was only used as a scaler.

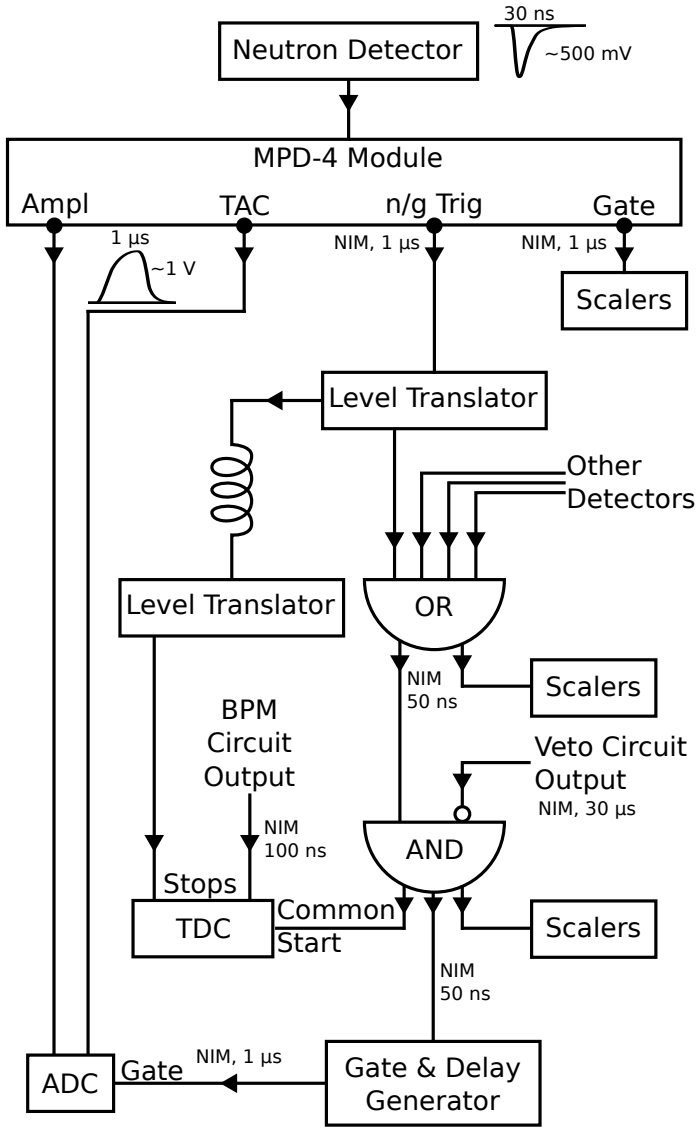

FIGURE 4.22: The circuit used to process signals from the neutron detectors.

Figure 4.22 shows the complete neutron detector circuit. Each MPD-4 module can process signals from four neutron detectors. For most experiments 18 detectors were used, so 5 different MPD-4 modules were implemented in the circuit. The **n/g-Trig** outputs of each channel of each MPD-4 module were ORed together using a logic module to make an overall trigger for the circuit. This overall trigger was sent to

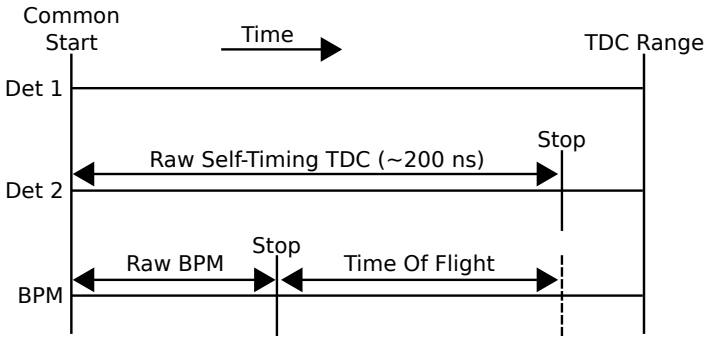

FIGURE 4.23: An illustration of the relative timings of the neutron detectors and the BPM in the TDC. Detector 1 saw no signal, while detector 2 caused a trigger in the circuit. The channel corresponding to detector 2 in the TDC shows a self-timing stop, and the channel corresponding to the BPM also shows a stop.

another logic module, which was vetoed by the veto circuit to prevent simultaneous triggers. This output was copied and one copy was used as a start for the TDC while the other copy was sent to a Gate and Delay module to generate gates for the ADCs and the TDC. The **Ampl** and **TAC** outputs were sent directly to the ADCs. Two 32-channel ADCs were used in these experiments to digitize up to 36 signals from up to 18 detectors. Copies of the **n/g-Trigs** were delayed and used as the individual stops in the TDC. The BPM circuit, as described in Section 4.7.1, was sent to another individual stop in the TDC.

An example illustrating the timing structure seen in the TDC is shown in Figure 4.23. In this example, detector 2 caused the trigger and detector 1 recorded no signals exceeding the MPD-4 thresholds. The channel corresponding to detector 2 shows a self-timing stop, allowing one to determine that detector 2 caused the trigger. Because the BPM triggers every 179 ns and the full range of the TDC was 200 ns, the BPM was guaranteed to give a stop for every trigger. The Time Of Flight (TOF) is the difference between the stop caused by detector 2 and the BPM stop.

4.7.5 Data Acquisition (DAQ)

The purpose of the Data AcQuisition (DAQ) system is to store the processed detector signals onto a computer for future analysis. The DAQ system utilized at TUNL and HIγS is the "`CODA` at TUNL " package, where `CODA` stands for CEBAF Online Data Acquisition [73]. `CODA` was developed at the Thomas Jefferson National Accelerator Facility as a novel and scalable method of storing digital signals using preexisting protocols such as TCP/IP.

Four components comprise the `CODA` at TUNL package: the mSQL database, the Single Board Computer (SBC) terminal, the Event Builder (EB), and the Run Control application. The mSQL database maintains a database of filepaths to where the runs, scaler data, and other information is in the computer. The SBC terminal manages communication between the host computer and the SBC in the VME crate. The EB parses the data into the `CODA` format for storage. The final component, Run Control, manages the acquisition as a whole.

Run Control has several different stages that can be configured to perform specific actions. The first stage at the beginning of an experiment is the Configure stage, which reads in the mSQL database and sets path variables. The next step is the Download step. In this step, drivers for communication between the SBC and the ADCs and TDC are sent to the SBC, and the precompiled code used to control the SBC is transmitted to the SBC. This code, called the CRL code, governs the actions of the SBC for each step of the Run Control, and tells the SBC what to do when the trigger module receives a trigger. After a successful Download step, the Prestart step is enabled. In the Prestart step, the ADCs and TDC are cleared of any data they may have, the time range of the TDC is set, and the ADCs and TDC are enabled. The next step available to the experimenter is the Go step, which activates the ADCs and TDC for use. When sufficient data is collected, the experimenter may start the

End Run step. All the data recorded by the ADCs and TDC are stored after the ADCs and TDC are disabled from taking new events. Scaler data are read out every second and a final scaler read is performed at the End Run transition.

There are three VME-based modules in addition to the ADCs and TDC which are important for the DAQ system: the scaler module, the SBC, and the Trigger Module. The scaler module has 32 different logic inputs and a counter for each input. Whenever the scaler module receives a logic true NIM pulse on an input, it increments the counter for that particular input. This allows the experimenter to keep track of scaler data, such as the 5 paddle count rate or a clock to record the run time. The Trigger Module receives triggers from the ADCs and TDC, and informs the SBC to read out those modules. The SBC then transmits the digitized data to the host computer.

Once the data is stored on the computer, it can be analyzed at a later time by the experimenter. `CODA` does not provide an analysis component. `ROOT`, a software package developed by CERN for particle physics analysis, was used to analyze the raw experimental data. Two programs are available to convert the `CODA` formatted file to a `ROOT` tree: TRAP and CODA2ROOT. The author has used both of these programs and verified that they produce the same resulting `ROOT` tree. The analysis of the `ROOT` tree will be discussed in the next chapter.

5

Data Reduction and Analysis

5.1 Introduction

The previous chapter detailed the experimental setup of the detectors and the electronics system used to process and store measured data. As discussed in Section 4.7, the data were stored on an event by event basis in a `ROOT` tree, and each event contained the Amplitude, Time to Amplitude Converter (TAC), and Time to Digital Converter (TDC) information for all neutron detectors (Figure 4.22) in addition to the Beam Pickoff Monitor (BPM) TDC timing (Figure 4.23). The Amplitude output of the MPD module contained information regarding the size of the pulse, so it will be referred to as the Analog to Digital Converter (ADC) output in this chapter. The TAC output contained the n/γ discrimination information based on the shape of the pulse, so it will be called the Pulse Shape Discrimination (PSD) output here.

This chapter will cover the analysis of the measured data used to calculate the polarization asymmetries and angular distribution coefficients of the prompt fission neutrons for the actinide targets studied. The first step of the analysis was to calibrate the detectors and electronics. The calibration of the ADC output in Section 5.2

was performed using a ^{137}Cs source, while the PSD adjustments in Section 5.3 required an ^{241}Am/^{9}Be source. The TDC was calibrated in Section 5.4 using cables of known delays. The neutron energy calibration in Section 5.5 required an accurate measurement of the γ-ray beam timing and fine-tuning the recorded detector distances to $\sim 1\,\mathrm{mm}$ using the monoenergetic neutrons from the $\mathrm{d}(\gamma,\mathrm{n})$ reaction. After all calibrations were performed, multiple cuts were placed on the prompt fission neutron data to remove contributions from background neutrons and γ rays, as described in Section 5.6. Estimates of remaining backgrounds were subtracted using out-of-time cuts in Section 5.7. Neutron detector efficiency corrections were then applied to the background-subtracted yields in Section 5.8. After extracting the efficiency-corrected prompt neutron yields, the prompt neutron polarization asymmetries and angular distribution coefficients were calculated in Section 5.9. Systematic uncertainties, as calculated in Section 5.10, were reduced by calculating the polarization asymmetries of the prompt neutrons as opposed to absolute quantities such as cross sections.

5.2 ADC Calibration

Calibration of the ADC using an intense ^{137}Cs source was required to accurately set detector thresholds and determine the detector efficiencies. Upon β-decay, ^{137}Cs emits a 662 keV γ ray, which can scatter off of an electron in the neutron detector and deposit energy as outlined in Section 4.6. ^{137}Cs sources are commonly used to calibrate neutron detector ADC spectra [74].

The response of a detector to the 662 keV γ rays generated by the ^{137}Cs source is shown in Figure 5.1. A key feature of the detector response is the cesium edge, which is defined to be the midpoint of the right side of the "peak" near channel 700. The cesium edge is one of two points used to calibrate the ADC spectrum. The cesium edge is calculated by finding the maximal counts per bin in the peak and finding

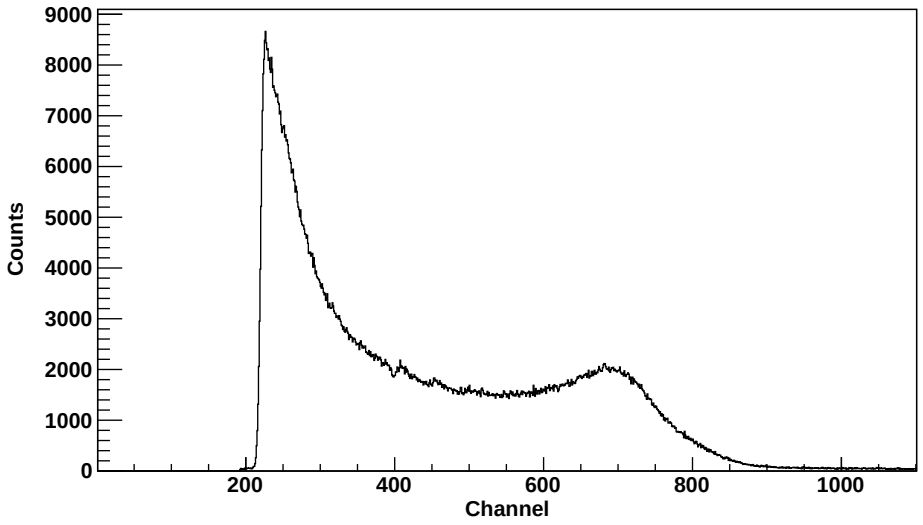

FIGURE 5.1: The response of the detector to the 662 keV γ rays emitted by the ^{137}Cs source. In this figure, the sharp drop in counts near channel 200 is the ADC hardware threshold, and the cesium edge is located near channel 760.

the channel number which has exactly half those counts per bin. In Figure 5.1, the cesium edge would be located at approximately channel 760.

A `GEANT4` simulation was performed by B. Perdue to calculate the energy deposited in the detector for events occurring at the cesium edge and found the edge location to correspond to 517 keV [73]. However, different types of recoiling particles can generate different amounts of scintillation light while depositing the same amount of energy in the detector, as is clear from Birk's Law in Section 4.6.2.2. To account for this effect, the units of electron-equivalent energy deposited (keVee) are used for the light output of the scintillator. In the case of the ^{137}Cs source, the recoiling particles in the scintillator are electrons, so the energy deposited is equal to the electron-equivalent energy deposited. Therefore, the cesium edge yields a calibration point of 517 keVee for the ADC spectrum.

Denoting the calibrated ADC value in keVee as the Pulse Height (PH) and as-

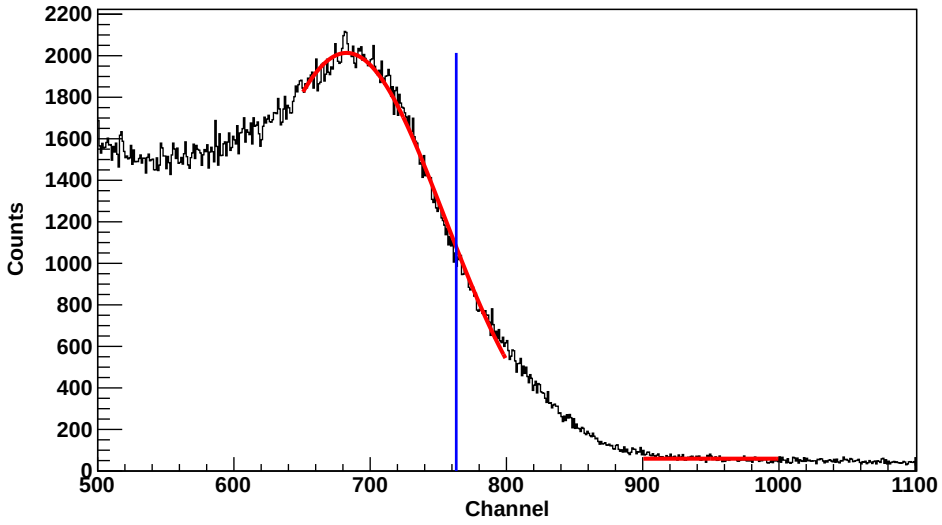

FIGURE 5.2: The fit to locate the cesium edge. The Gaussian fit to the "peak" and the constant background fit are shown in red, while the recorded location of the cesium edge is shown in blue.

suming the ADC is linear, the PH calibration is given by:

$$\mathrm{PH} = \frac{\mathrm{ADC} - \mathrm{ADC_{ped}}}{\mathrm{ADC_{edge}} - \mathrm{ADC_{ped}}} \times 517\,\mathrm{keVee} \tag{5.1}$$

where ADC is the ADC value, ADC_{edge} is the cesium edge, and ADC_{ped} is the location of the pedestal on that ADC input. The ADC leaked a very small signal into each input, so when the ADC saw no real signal in an input, it read out a pedestal value which was typically around channel 80-100 instead of reading out a value corresponding to the channel 0. Therefore 0 keVee deposited in the detector appeared at the pedestal channel, and this pedestal is used as the other calibration point in the ADC spectrum.

A fitting routine was written to quickly and reproducibly locate the cesium edge in a ^{137}Cs source spectrum. The routine fit a Gaussian to the cesium "peak" and assumed a flat background below this peak. This background was determined by fitting a region well above the cesium edge. It subtracted the flat background from

beneath the "peak" and found the channel number corresponding to half of the background-subtracted "peak" height. This channel number corresponded to the cesium edge. The result from performing this procedure on Figure 5.1 is shown in Figure 5.2. As can be seen from this figure, the statistics on the source runs were very good, so small statistical fluctuations would not affect the calculated value of the cesium edge.

Analysis cuts on the PH value were applied (Section 5.6.2) to reduce γ-ray contributions and to make the detector efficiencies approximately equal between detectors. Typically the PH threshold was placed at 0.25xCs, where 1xCs refers to the location of the cesium edge (517 keVee). The hardware thresholds on the ADCs were always lowered beyond 0.25xCs, or 129 keVee, to ensure that a software cut could be placed at that energy.

5.3 Pulse Shape Discrimination

As discussed in Section 4.7, the TAC output of the MPD module contained information about the shape of the pulse from the detector, which was used to discriminate neutrons from γ rays. To avoid confusion with other elements of the circuit and analysis, this value will be referred to as the PSD value.

Neutrons and γ rays were generated through the ^{9}Be(α,n)^{12}C* reaction with an ^{241}Am/^{9}Be source to ensure that the PSD properties of the detector and electronics were functioning properly. Runs with the ^{241}Am/^{9}Be source were taken twice daily to ensure the stability of the PSD functionality. For this analysis, the PSD value was not calibrated and was left in the units of "Channel". Figure 5.3 shows the raw PSD value using the ^{241}Am/^{9}Be source. Figure 5.4 shows the PSD value versus the PH value.

High background rates of γ rays made it necessary to eliminate some γ-ray events in hardware. The MPD module was set to automatically reject events with PSD

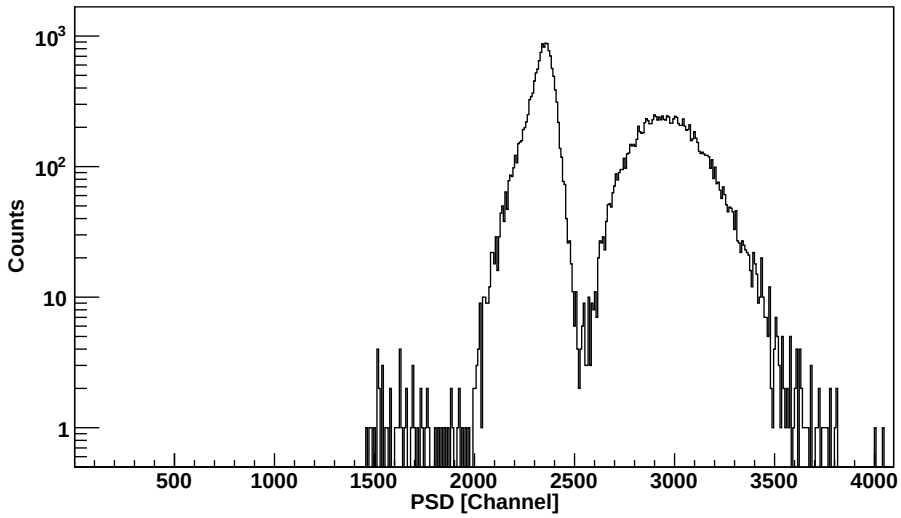

FIGURE 5.3: The PSD response of the detector and electronics to an ^{241}Am/^{9}Be source. The peak on the right is from neutrons and the peak on the left is from γ rays. A PH threshold of 0.25xCs has been applied in the analysis.

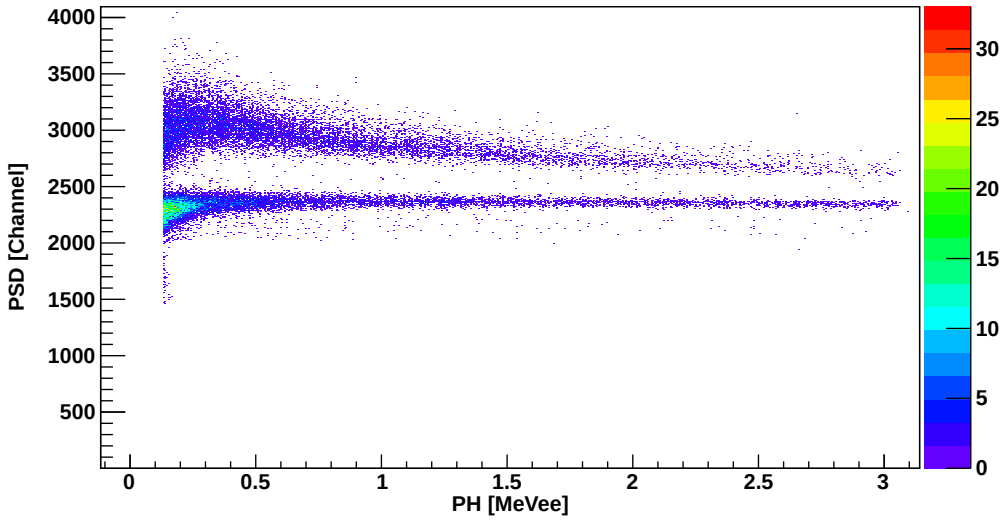

FIGURE 5.4: The PH versus PSD response of the detector and electronics to an ^{241}Am/^{9}Be source. The band on the top is from neutrons and the band on the bottom is from γ rays. A PH threshold of 0.25xCs has been applied in the analysis.

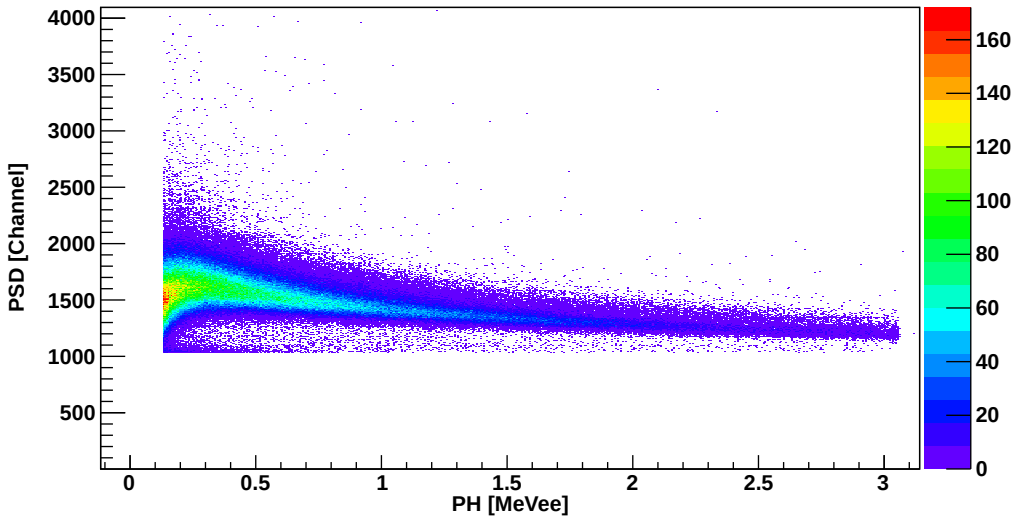

FIGURE 5.5: The PH versus PSD response of the detector and electronics to an ^{241}Am/^{9}Be source. The DC voltage offset in the PSD output of the MPD module has been reduced, increasing the effective hardware PSD threshold and eliminating many of the γ rays seen in Figure 5.4. A PH threshold of 0.25xCs has been applied in the analysis.

values below a fixed PSD threshold. This mode of operation is called the "neutron mode". The PSD threshold of the MPD module can be effectively adjusted by adding a DC offset to the PSD outputs at each channel. The DC offset to each channel was controlled using the "ndis" parameter, which is short for neutron/γ discrimination and adjusted in the MPD module. By adjusting the "ndis" parameter, the effective PSD threshold to discriminate γ rays from neutrons is adjusted. Figures 5.3 and 5.4 both show the PSD functionality with this adjustable threshold set to the maximum, effectively disabling the hardware PSD threshold. Figure 5.5 shows the PSD versus PH spectrum with this threshold set as for typical production runs. Note that all the neutrons passed this threshold while only some of the γ rays remained.

Table 5.1: Delays used for the TDC Calibration for the BPM input channel. Δt_1 and Δt_2 represent cable lengths that were not changed between the calibrations.

Delay (ns)	Peak Channel in TDC
Δt_1	2055
$\Delta t_1 + 32.0$	2757
$\Delta t_1 + 64.0$	3458
Δt_2	1321
$\Delta t_2 + 32.0$	2019
$\Delta t_2 + 64.0$	2720

5.4 TDC Calibration

The TDC used in these experiments recorded the time difference between the start and stop signals, and digitized this difference into a channel ranging from 0 to 4095. To accurately determine the detected neutron energy by using its detection time, the channel number in the TDC must be converted into absolute time units such as nanoseconds. Two identical signals were taken from a clock module and used to measure the calibration from the TDC channel number into nanoseconds. One signal was sent to the start of the TDC, while another was sent through some delay. The delay was varied between 0, 32, and 64 ns while using the same cables and a coaxial delay cable box. The added delays were verified using an oscilloscope. The procedure was repeated twice to map the full range of the TDC, which was set to approximately 200 ns. The results of both calibrations are shown in Table 5.1.

Calibration 1 yielded 0.04561 ns per channel, while calibration 2 resulted in 0.04575 ns per channel. The average value of the two calibrations, 0.04568 ns, was used in the analysis to reconstruct detected neutron energies. The uncertainty on this calibration was taken to be the difference between the two calibrations, which

was approximately 0.2%. This uncertainty was primarily due to uncertainties in the cable lengths.

5.5 Neutron Energy Calibration

The calibration of the TDC from channel values to nanoseconds was on its own insufficient to determine detected neutron energies. Recall from Figure 4.22 that the start signal to the TDC was a trigger from a detector, and the stop signals to the TDC were delayed copies of the start signal. These starts and stops contained no information about the timing of the event relative to the beam. To obtain that information, the BPM discussed in Section 4.3.1 was used. An example of relative timings of the BPM and the neutron detectors is shown in Figure 4.23.

The timing value for each event is defined to be the difference between the detector stop in the TDC and the BPM stop in the TDC for that event. Because the channel for the BPM stop was calibrated in the TDC, this timing value was known in nanoseconds. The detector stops in the TDC were given by self-timing peaks, and were the same for every event in a particular detector. The timing of the BPM signal relative to the γ-ray beam passing through the GV was unknown, so the timing values may be offset by a constant amount. Therefore, the timing value alone does not provide time of flight information which was needed to reconstruct the detected neutron energies.

The final piece of information used to reconstruct detected neutron energies was the γ flash. γ rays from the beam scattered off of the target and entered the detector causing a peak in the TDC called the γ flash. Because the γ rays traveled at a fixed velocity (c) and the distance between the detector and the target was known, the time of flight for the γ rays can be calculated. The timing value for when the γ rays from the beam strike the target can be calculated using their time of flight and the measured timing value for the γ rays (which is when γ rays from the beam strike

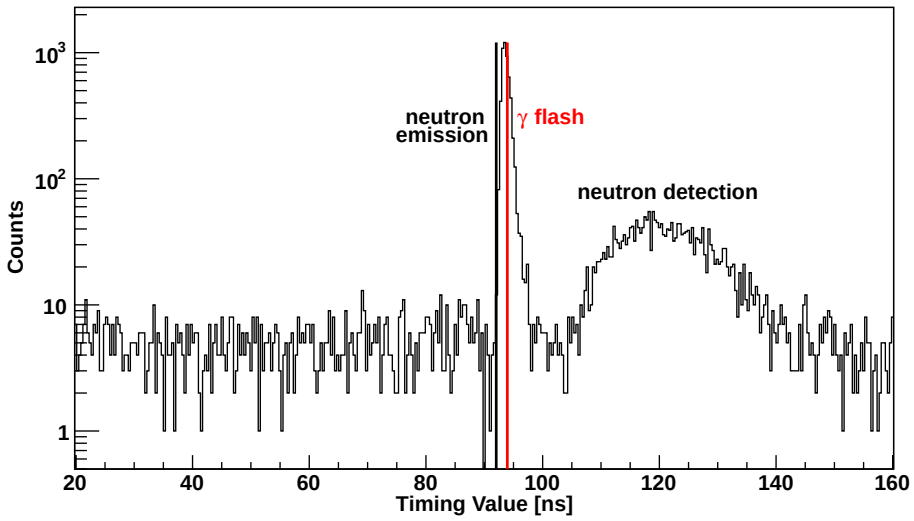

FIGURE 5.6: The timing values for neutrons and γ rays. The γ flash is indicated by the red line, and the effective neutron emission timing value is shown by the black line.

the detector). The photofission reaction and prompt neutron emission occur on a much shorter timescale than nanoseconds as discussed in Section 2.5, so the timing value for when the γ rays strike the target was effectively the timing value of the prompt neutron emission. The distance from the target to the detector was known and the timing values of the prompt neutrons were known for each event, so the absolute time of flight for the neutrons (and thus detected neutron energies) can be calculated using the timing value of the prompt neutron emission. Figure 5.6 shows the timing values of the γ flash, effective neutron emission, and neutron detection.

The prompt neutrons detected from photofission ranged in energy from $1.5 - 9.5\,\mathrm{MeV}$, so effects from special relativity must be used when reconstructing the

neutron energies, as follows:

$$TOF_n = TV_n - TV_{\gamma flash} + \frac{d}{c} * 10^9 \tag{5.2a}$$

$$\beta_n = \frac{d}{TOF_n * c} * 10^9 \tag{5.2b}$$

$$E_n = \frac{M_n}{\sqrt{1-\beta^2}} - M_n \tag{5.2c}$$

where TV_n is the neutron timing value, $TV_{\gamma flash}$ is the γ-flash timing value, d is the distance from the target to the detector, and TOF_n is the neutron time of flight. Both timing values and the time of flight are given in nanoseconds.

5.5.1 γ-Flash Calibration

As is clear from Equation 5.2, an accurate timing value for the γ flash was critical in reconstructing detected neutron energies. The γ flash timing value was measured during designated γ-flash runs. For these runs, the hardware discrimination as discussed in Section 5.3 between neutrons and γ rays in the MPD modules was disabled. This allowed all γ rays entering the detector to cause triggers. The majority of the γ rays that caused triggers in the electronics had low pulse heights, and the CFD in the MPD module exhibited a small timing walk which affected the timing of the low pulse height γ-ray triggers. This walk can be seen in Figure 5.7. A cut was placed to eliminate these low pulse height events, and the remaining events were projected onto the timing axis and fit to determine the γ flash, as shown in Figure 5.8.

In principle, the γ flash depended on the exact target location and geometry. Therefore, a new γ-flash run was taken every time a target was put into the beam. Once the target was mounted, care was taken to not move the target at all to ensure its location remained the same.

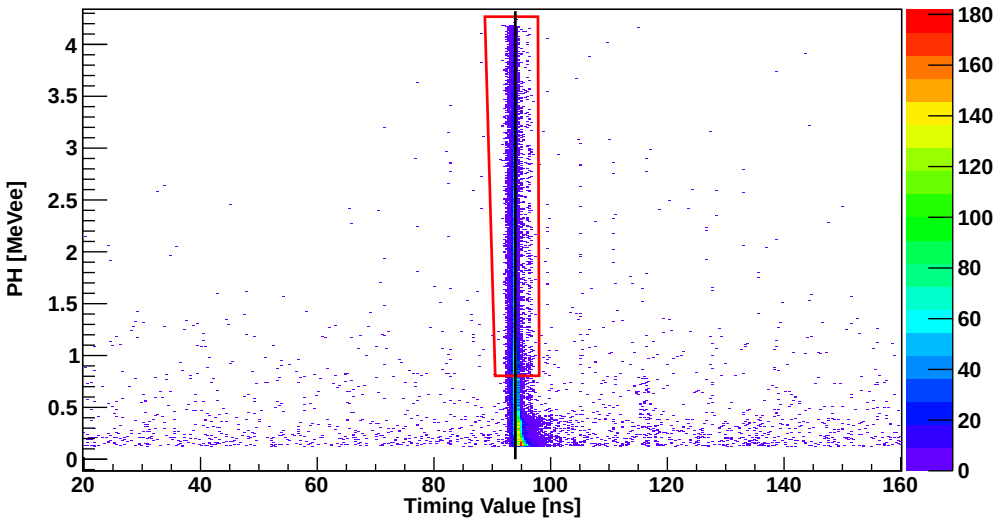

FIGURE 5.7: The PH versus timing value for a γ-flash run. The walk in the CFD in the MPD module can be seen at low pulse heights. The red cut removed the low pulse height values. The bottom edge of the red cut was ensured to be parallel to the x-axis. The black line shows the location of the γ flash.

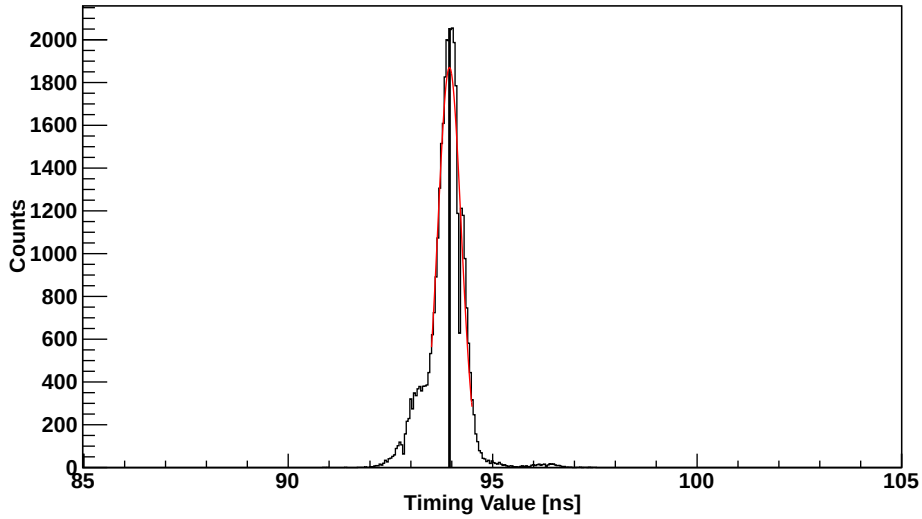

FIGURE 5.8: A fit to a γ flash. The histogram is the projection of the events inside of the red cut in Figure 5.7 onto the x-axis. The γ flash is fit to a Gaussian, shown in red, and the centroid is defined to be the γ flash, shown in black.

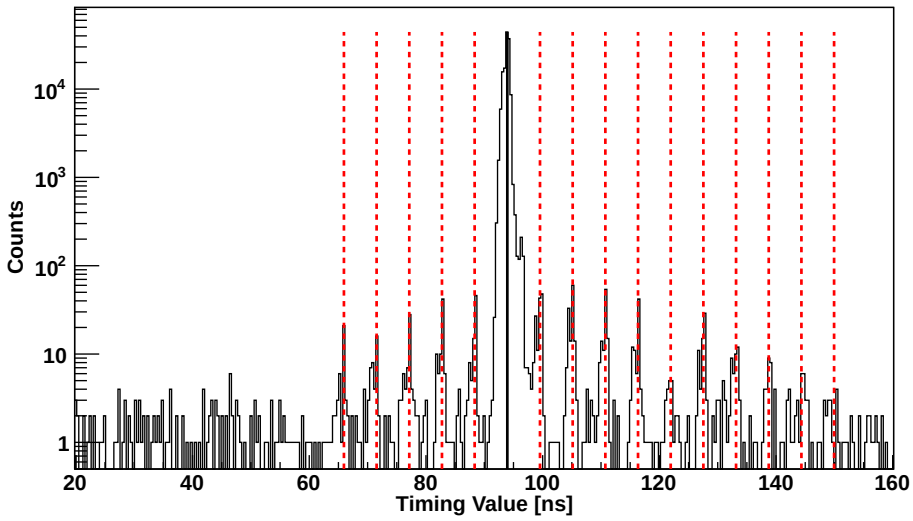

FIGURE 5.9: A measurement of the relative contributions from the spillover buckets. The black line is the location of the γ flash and the red dashed lines are ± 5.6 ns from the black line and each other. The spillover buckets can be easily identified. This histogram was subject to a 3xCs PH cut in the analysis.

5.5.2 Other Important Uses for γ-Flash Measurements

In addition to its use in reconstructing neutron energies, the γ-flash runs were also useful for beam diagnostics and background γ ray measurements. Figure 5.9 shows a γ-flash measurement in a forward detector after the γ-ray beam had been operating for several hours. Additional γ-ray events can be seen besides the γ flash. These events had a separation of approximately 5.6 ns, and came from beam γ rays scattering off of the target. These mistimed beam γ rays came from minor RF buckets rather than the two main buckets in the ESR (see Section 4.2.3 for a discussion of the main ESR buckets). These spillover buckets can become partially filled after several hours of operation. The γ-flash run directly measured the contribution of the spillover buckets to the total γ-ray beam intensity. Typically this contribution was below 0.5%.

Figure 5.10 shows a different γ-flash measurement at a backward angle detector.

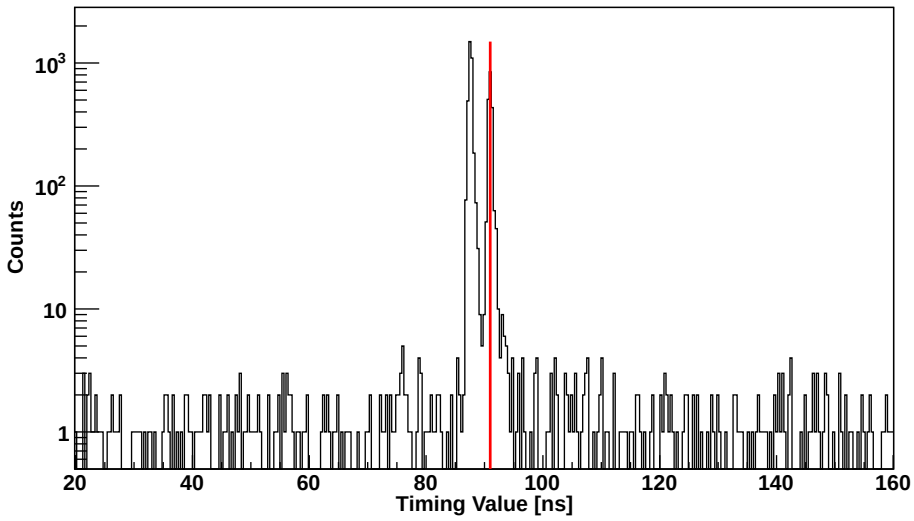

FIGURE 5.10: A measurement of beam γ rays scattering off of the upstream wall of the GV. The γ flash is indicated by the red line. The timing value difference between the peaks is approximately 3.5 ns, which corresponds to a difference of flight path of approximately 1 m. This histogram was subject to a 3xCs PH cut in the analysis.

Two γ-flash peaks can be seen. The peak earlier in time came from γ rays scattering off of material upstream of the target, such as the collimator or upstream wall of the GV, and entering the detector. This was another useful diagnostic for other experiments, as it gave an estimate of the total intensity of background γ rays scattering off of material upstream of the target.

5.5.3 D_2O Calibration

Photodisintegration of the deuteron was used to check the accuracy of the neutron energy reconstruction method, and to provide a more accurate measurement of the detector distances. The $d(\gamma, n)$ reaction emits mono-energetic neutrons for a fixed γ-ray energy and detector angle because it is a two-body reaction and energy and momentum must be conserved. Assuming a fixed angle and γ-ray energy, the only parameters needed to reconstruct neutron energies for the $d(\gamma, n)$ reaction are the γ flash timing value, detector distance, and the TDC calibration factor. The relative

uncertainty in β_n is approximately equal to the relative uncertainties of these parameters added in quadrature. Of these parameters, the one with the largest relative uncertainty was the detector distance, which was known to ± 1 cm in approximately 57 cm, or 1.8%. The TDC calibration was known to 0.2% and the γ flash timing value was known to approximately 0.5%. Therefore the detector distances were modified within ± 1 cm if any discrepancies were found between the predicted neutron energies from the D_2O runs and the measured neutron energies. Note that in Equation 5.2 the distance is not the distance from the target to the front of the detector, but rather the distance from the target to the effective center of the scintillating volume. The effective center of the detector is defined to be the mean distance before a neutron interacts with the scintillating volume. Because the probability of a neutron interacting in the volume is relatively low, the effective center of the detector is approximately 2 cm behind the front face of the detector, which is close to the geometric midpoint of the 5.08 cm thick detector. Therefore the distances used in the analysis routine are generally ~ 2 cm longer than the measured detector distances.

A computer program known as `RKIN`, which is short for Relativistic KINematics, was used to calculate the neutron energies from $d(\gamma, n)$ as a function of γ-ray energy and detector angle. Figure 5.11 shows the calculated neutron energy from the $d(\gamma, n)$ reaction at a beam energy of 7.0 MeV compared to the measured spectrum from the D_2O target. The correction to the detector distance was calculated by fitting the measured spectrum to a Gaussian and altering the detector distance in the calculation until good agreement was found between the `RKIN` calculation and the Gaussian centroid. This particular detector was located at 90°, and its measured detector distance from the target to the front face of the detector was 54.5 cm while the corrected detector distance for the analysis was 57.3 cm. Assuming an effective detector center which is 2 cm behind the front face of the detector, based on the $d(\gamma, n)$ measurement, the detector was placed 55.3 cm from the target, which is within the 1 cm

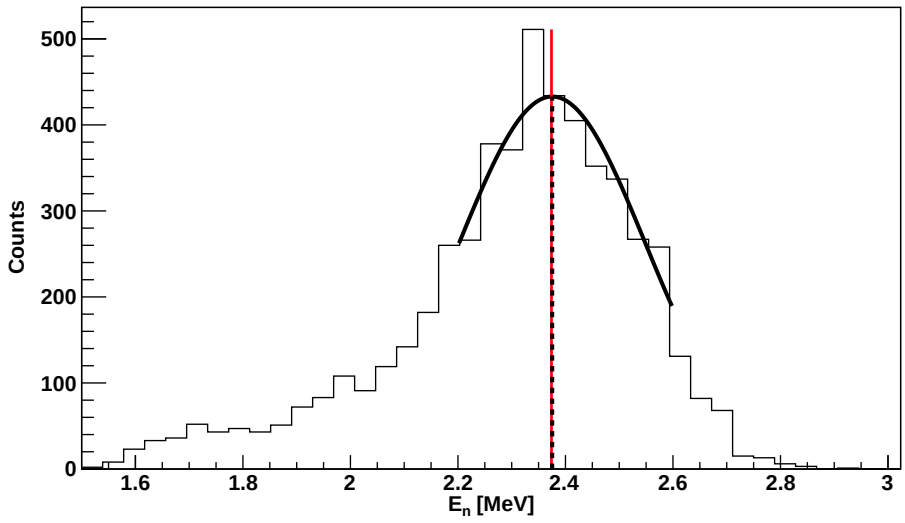

FIGURE 5.11: The measured spectrum from photodisintegration of D_2O compared to the predicted $d(\gamma, n)$ energy using `RKIN`. The solid black line is a Gaussian fit to the spectrum, and the dashed black line shows the centroid of the Gaussian. The red line is the predicted $d(\gamma, n)$ energy for a 7.0 MeV γ-ray beam.

uncertainty on the measured distance of 54.5 cm.

In order to ensure accurate neutron energy reconstruction calculations, calibrations using the D_2O target were performed at the start of every experiment. Generally detector distances were modified by only a few centimeters, indicating that the γ-flash placement and TDC calibrations were accurate.

5.6 Analysis Cuts

After the calibration of the ADC, TDC, and neutron energies, cuts were placed on the data to remove γ-ray events and neutrons out of time with the beam. The first cuts placed were the self-timing TDC cut in Section 5.6.1 and the PH threshold cut in Section 5.6.2. Next, a two dimensional cut was placed on the PH-PSD spectrum in Section 5.6.3 to remove the majority of the γ-ray events. Finally, a two dimensional cut was placed on the TOF-PSD spectrum in Section 5.6.4 to remove the remaining

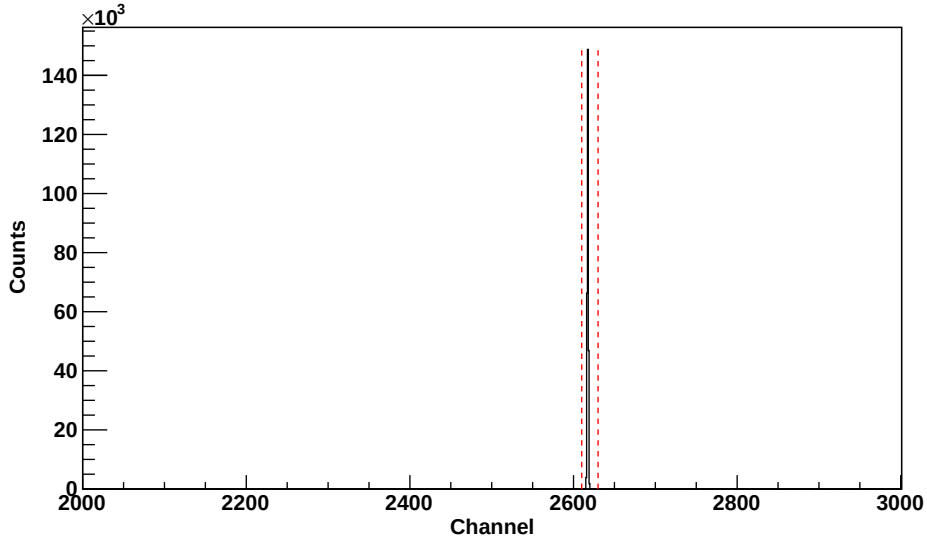

FIGURE 5.12: The self-timing TDC peak is shown in black. The self-timing cut for this detector is shown in red. Events excluded using this cut are located at channel zero and therefore are not shown above.

γ-ray events and those neutrons arriving out of time with the beam.

5.6.1 Self-Timing TDC Cut

The first analysis cut was a cut on the TDC spectrum of each detector. Figure 4.23 shows the relative timing of the TDC start and stop for two detectors, one which had an event that caused the TDC to start and another that did not. The detector that had the event and triggered the TDC has a TDC stop after a fixed delay, while the detector that did not cause the trigger has no stop in the TDC. The self-timing TDC cut was used to identify which detector caused the trigger, so that detector can be analyzed in detail. The gates for the ADC were based on the timing from the detector that caused the trigger, so other detectors that also had events but did not cause the trigger may have signals that are out of time with the ADC gate. If the signal is out of time with the ADC gate, the information stored may be inaccurate. Therefore, the TDC self-timing cut ensures that only the detector with accurate data

(the detector that caused the trigger) was analyzed. Figure 5.12 shows a self-timing peak with the self-timing cut.

5.6.2 PH Threshold Cut

The next cut placed on the data was the PH threshold cut. As previously mentioned in Section 4.6.4, the detection efficiency varies as a function of PH threshold. As the PH threshold is raised from 0.25 to 1xCs, the detection efficiency decreases significantly. The hardware threshold of the MPD module varied from channel to channel, but all hardware thresholds were kept below 0.25xCs. This allowed for software thresholds to be placed at 0.25xCs on all detectors. Common thresholds on the detectors ensured that the efficiencies for each detector are similar.

Because corrections using the circularly polarized beam were used in every polarization asymmetry calculation (Section 5.9.1), the resulting asymmetry measurement is insensitive to changes in the PH threshold cut. In some cases, such as for targets with low neutron yields and high γ-ray background rates, the PH threshold was raised up to 0.5xCs in some detectors to help eliminate γ-ray backgrounds. The circular corrections, discussed in Section 5.9.1, compensated for this change in efficiency.

5.6.3 PH-PSD Cut

After the self-timing cut and the PH threshold cut were applied, the next cut used was on the PH-PSD spectrum. Figure 5.13 shows the location of the PH-PSD cut on an ^{241}Am/^{9}Be spectrum (5.13a) and on measured data from photofission of ^{240}Pu at 7 MeV (5.13b). The cut, shown in red, was set using the ^{241}Am/^{9}Be spectrum and then applied to the measured photofission data. This cut eliminated a significant fraction of the γ-ray backgrounds present in the measurement. This cut was kept fairly wide since an additional cut will be placed on the PSD spectrum in Section 5.6.4. By keeping this cut wide, systematic uncertainties due to the placement

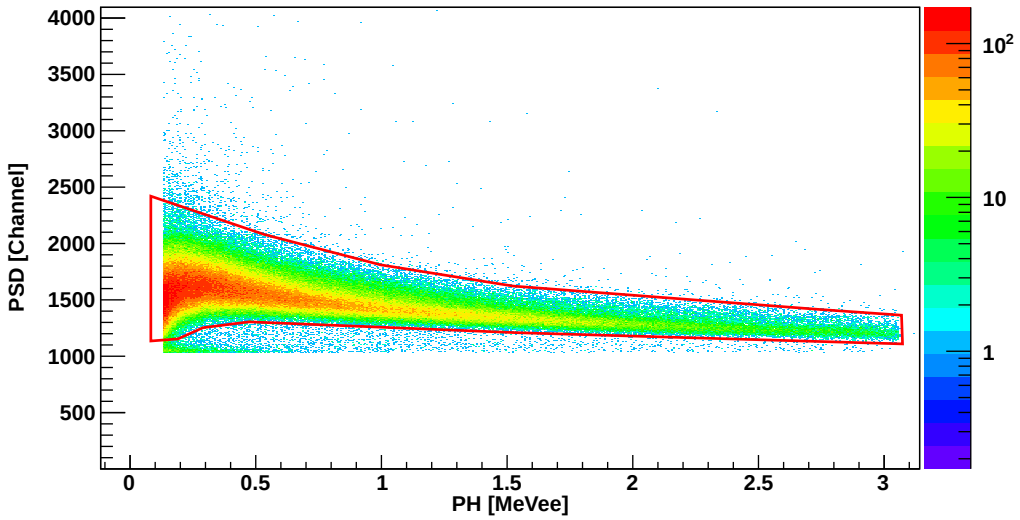

(a) The ^{241}Am/^{9}Be response

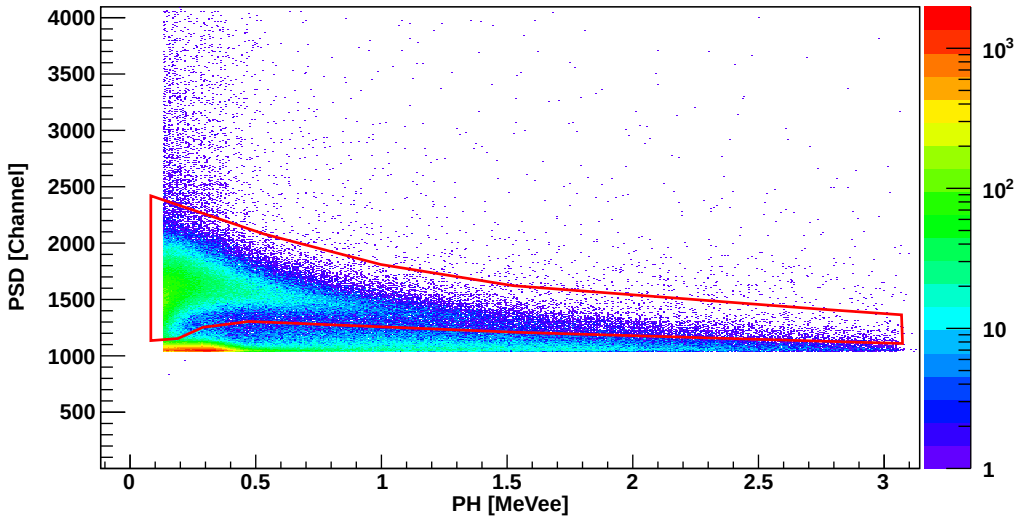

(b) Data from photofission of ^{240}Pu at $E_\gamma = 7\,\text{MeV}$

FIGURE 5.13: The PH-PSD spectrum is shown for an ^{241}Am/^{9}Be source measurement and measured ^{240}Pu data taken at 7 MeV. The red line shows the placement of the PH-PSD cut. The cut placement is the same in both plots. The spectrum from photofission of ^{240}Pu appears different from the ^{241}Am/^{9}Be spectrum due to the much higher background γ-ray rate during the photofission measurement.

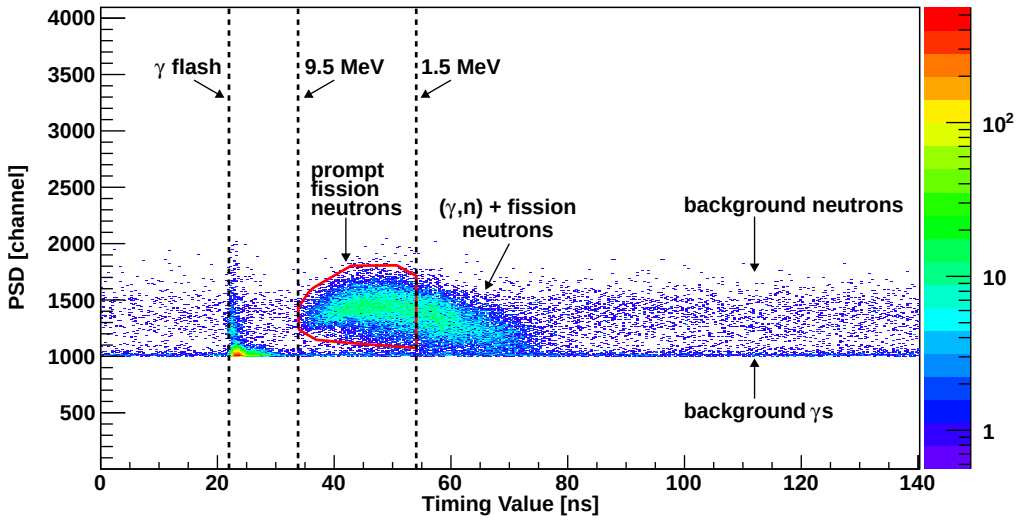

FIGURE 5.14: The TOF-PSD cut is shown in red. The data are from photofission of ^{239}Pu at 7 MeV and a scattering angle of 90°. Arrows point to interesting features of the spectrum, including the upper and lower energies for prompt neutron integration, the γ flash, and backgrounds.

of this cut can be neglected.

5.6.4 TOF-PSD Cut

The final cut applied to the measured data was the TOF-PSD cut, as shown in Figure 5.14. This cut removed the majority of the remaining backgrounds and selected only those neutrons above an energy threshold of 1.5 MeV and below an energy cut of 9.5 MeV. This was a graphical cut, drawn by hand, which will be optimized later in Section 5.7.3. The γ-ray backgrounds were easily eliminated using this cut. The background neutrons, which were a combination of delayed fission neutrons and ^{27}Al(α,n) neutrons, could not be fully eliminated using this cut. The calculation of the contribution of background neutrons to the measured prompt neutron yield will be described in Section 5.7. The systematic uncertainty in using this TOF-PSD cut to reduce backgrounds will be discussed in Section 5.10.4.

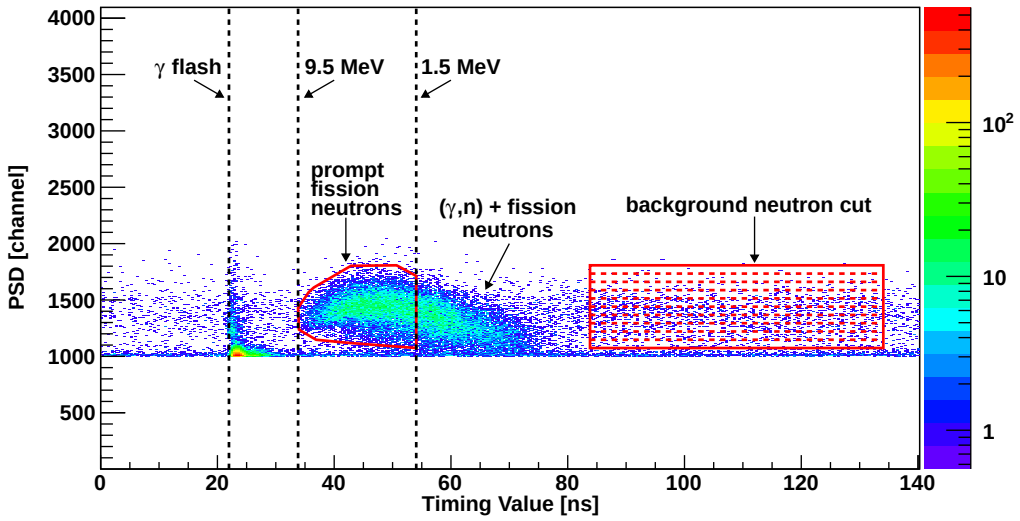

FIGURE 5.15: The TOF-PSD prompt neutron cut and out of time background neutron cut are shown in red. The red dashed lines in the background neutron cut indicate the different background slices used in the background subtraction.

5.7 Background Subtraction

As can be seen in Figure 5.14, some neutron events occurred significantly out of time with the prompt neutrons from photofission and the (γ,n) neutrons. The spectra are consistent with the assumption that the out of time neutrons are emitted without any time dependence, so it is assumed the background neutron yield was the same out of time and in time with the prompt neutrons. By calculating the background neutron yield per bin of the histogram and the size of the prompt neutron cut, the total number of background neutrons that were misidentified as prompt neutrons can be estimated. Then, these misidentified background neutrons can be subtracted from the prompt neutron yield.

5.7.1 Placement of Out-of-Time Cut

To calculate the background neutron yield per bin, a cut was placed out of time with the prompt neutrons and (γ,n) neutrons. This cut is shown in Figure 5.15. The

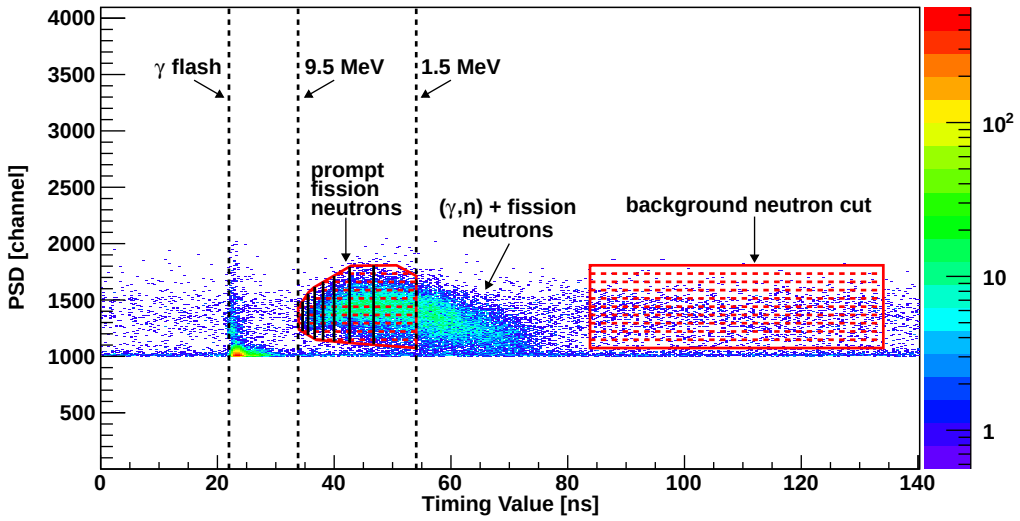

FIGURE 5.16: The TOF-PSD prompt neutron cut and out of time background neutron cut are shown in red. The red dashed lines in the background neutron cut indicate the different background slices used in the background subtraction, and the red dashed lines in the prompt neutron cut show these slices projected onto the prompt neutrons. The black solid lines within the prompt neutron cut indicate neutron energies ranging from 1.5 MeV to 9.5 MeV in 1 MeV steps.

height of this cut was matched to the prompt neutron cut, and the time position of this cut was ensured to be out of time with prompt fission neutrons and (γ,n) neutrons. It is clear from the spectrum that the background neutron yield depended on the PSD value in the cut. At high and low PSD values within the cut, the background neutron yield was smaller than at PSD values near the middle of the cut. To account for this effect, the background neutron cut was subdivided into ten horizontal slices. The background neutron yield was calculated for each slice individually.

5.7.2 Background Subtraction Calculation

The number of counts per bin in each background cut slice was measured in order to estimate the number of background neutrons within the prompt neutron cut. This was achieved by integrating the yield within each horizontal slice in the background

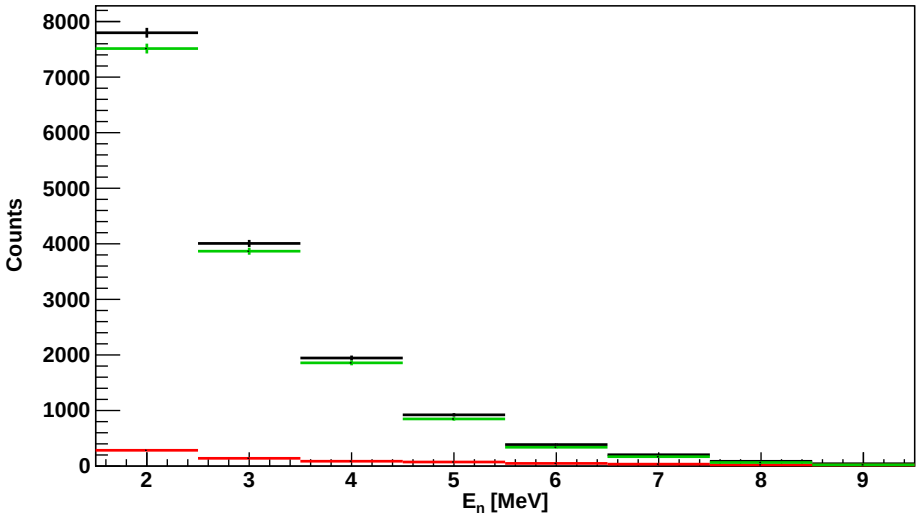

FIGURE 5.17: The binned prompt neutron spectrum before the background subtraction (black), the estimated background spectrum (red), and the spectrum after the background subtraction (green) are compared. Error bars are statistical only. Data shown are from photofission of ^{239}Pu at 7 MeV at a scattering angle of 90°.

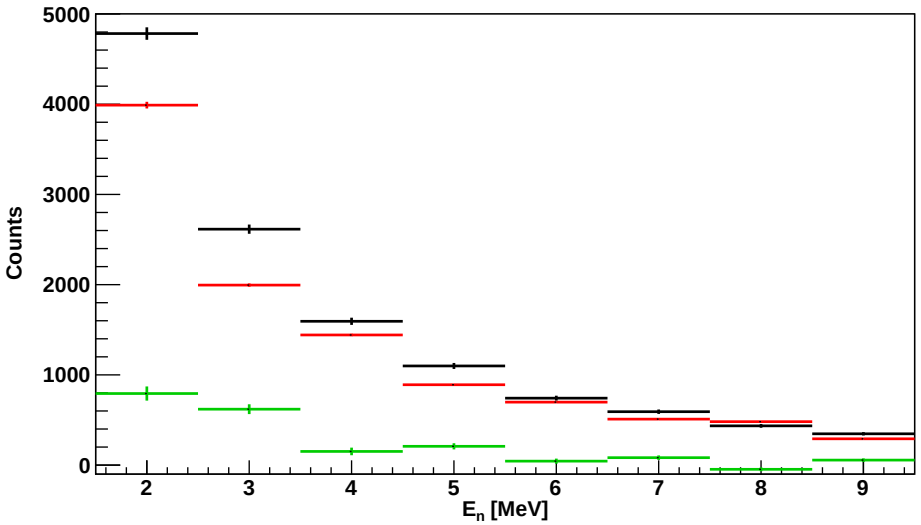

FIGURE 5.18: The binned prompt neutron spectrum before the background subtraction (black), the estimated background spectrum (red), and the spectrum after the background subtraction (green) are compared. Error bars are statistical only. Data shown are from photofission of ^{240}Pu at 5.8 MeV at a scattering angle of 90°.

neutron cut and dividing by the number of bins in each slice. Then, the slices were projected onto the prompt neutron cut. This is shown in Figure 5.16. The estimated background was then calculated for each energy bin of the prompt neutron spectrum. There were eight energy bins, each 1 MeV wide, ranging from 1.5 MeV up to 9.5 MeV. Figure 5.17 shows the binned prompt neutron spectrum before the subtraction is applied (black), the estimated spectrum from the background (red), and the subtracted prompt neutron yield (blue). For these data, which were taken from photofission of ^{239}Pu at 7 MeV at a scattering angle of 90°, the background contribution to the prompt neutrons was small. Figure 5.18 shows prompt neutron spectra from photofission of ^{240}Pu at 5.8 MeV at a scattering angle of 90°. Here the backgrounds were much more significant and the subtracted yield was much smaller than the raw yield.

5.7.3 TOF-PSD Cut Optimization

Because the TOF-PSD cut was drawn by hand on the spectrum, it may not be the optimal cut to separate the prompt neutrons from background γ rays and neutrons. To try to improve the effectiveness of this cut, the cut was adjusted in order to minimize the relative uncertainty in the background-subtracted prompt neutron yield. If the cut were too tight vertically around the prompt neutrons, increasing the vertical size of the cut would add more prompt neutrons than background neutrons, which would decrease the relative uncertainty of the background-subtracted prompt neutron yield. If the cut were too loose vertically, by reducing the vertical size of the cut, excess backgrounds would be removed from the background-subtracted prompt neutron yield which would reduce its relative uncertainty.

This concept was implemented in the analysis of the photofission data. First, all of the data taken on a specific target during a particular experiment were added together. The prompt neutron spectrum did not depend strongly on the γ-ray beam

energy, so the same cut was applied for all of the γ-ray beam energies used in each experiment. Then, a cut was drawn by hand around the prompt fission neutrons. The background cut was defined, the backgrounds were subtracted, and the relative uncertainty of the energy-integrated background-subtracted prompt neutron yield was calculated. Then, the cut is adjusted slightly. The analysis routine adjusted the cut by either moving it up or down or by scaling it smaller or larger in the vertical direction. If the relative uncertainty in the energy-integrated background-subtracted yield decreased, then the adjustment was repeated. If the uncertainty increased, then the adjustment to the cut was undone and a different adjustment was tried. After all adjustments were tried (moving up, moving down, scaling larger vertically, shrinking vertically) and the cut was optimized for a given adjustment size, the adjustment size was reduced and the process was repeated. The adjustment size was reduced until the cut adjustments were negligible.

5.8 Efficiency Correction

After calculating the background-subtracted prompt neutron yields, an efficiency correction was applied. Each neutron energy bin was corrected for the average detection efficiency in that bin. The efficiencies shown in Figure 4.17 were used. This correction depended on the software PH threshold used for each detector, as discussed in Section 5.6.2.

5.9 Asymmetry Calculations and Corrections

After the efficiency-corrected, background-subtracted prompt neutron yields were extracted, the polarization asymmetries were calculated as described in Section 5.9.1. Section 5.9.2 describes the fitting procedure used to calculate the angular distribution coefficients from the measured polarization asymmetries. The angular distribution coefficients were then corrected for the finite size of the detectors in Section 5.9.3.

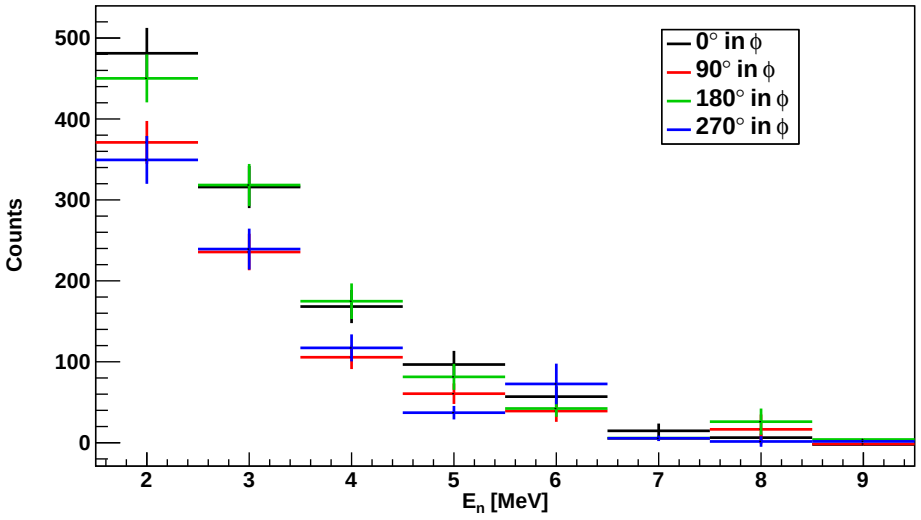

FIGURE 5.19: Background-subtracted prompt neutron spectra for four different detectors at scattering angles of 90°. The data are from photofission of ^{238}U at a beam energy of 6.7 MeV. The correction factors from using a circularly polarized beam have been applied.

Section 5.9.4 details the corrections to the angular distribution coefficients due to contaminant isotopes in each target. Finally, the analysis to extract the enrichment of the ^{233}U target is described in Section 5.9.5.

5.9.1 Calculation of Target Polarization Asymmetry

Using the background-subtracted prompt neutron yields, the polarization asymmetries can be calculated by comparing the yields in the plane of the linear γ-ray beam polarization to the yields perpendicular to the plane of linear γ-ray beam polarization. Figure 5.19 shows the yields of the four detectors at a scattering angle of 90° and azimuthal angles of 0°, 90°, 180°, and 270°. The data shown are from photofission of ^{238}U at 6.7 MeV. A significant polarization asymmetry between $\phi = 0, 180°$ and $\phi = 90, 270°$ is clear in the spectra.

In principle, the prompt neutron yields in the plane of beam polarization can differ from the yields perpendicular to the plane of beam polarization even for a

true polarization asymmetry of zero. This can occur because each detector was at a slightly different distance from the target, and the measured yields depended on the solid angle subtended by the detector. Another effect which may lead to false polarization asymmetries is that the efficiency of each detector may be slightly different. This could be due to small changes in the scintillating liquid from detector to detector, such as the oxygen content and the amount of bubbles in the liquid. False asymmetries caused by small differences in efficiencies or solid angles can be corrected by using a circular polarized beam. With a circularly polarized beam, the true polarization asymmetry must be equal to zero, so any observed asymmetries were instrumental.

The true polarization asymmetry for a specific target, prompt neutron energy bin E_n, scattering angle θ, and beam energy E_γ is given by:

$$\Sigma(E_\gamma,\theta,E_n) = \frac{\sum\limits_{\phi=0,180^\circ} \frac{Y^L(E_\gamma,\theta,E_n,\phi)}{Y^C(E_{\gamma circ},\theta,E_n,\phi)} - \sum\limits_{\phi=90,270^\circ} \frac{Y^L(E_\gamma,\theta,E_n,\phi)}{Y^C(E_{\gamma circ},\theta,E_n,\phi)}}{\sum\limits_{\phi=0,180^\circ} \frac{Y^L(E_\gamma,\theta,E_n,\phi)}{Y^C(E_{\gamma circ},\theta,E_n,\phi)} + \sum\limits_{\phi=90,270^\circ} \frac{Y^L(E_\gamma,\theta,E_n,\phi)}{Y^C(E_{\gamma circ},\theta,E_n,\phi)}} \tag{5.3}$$

where $\Sigma(E_\gamma,\theta,E_n)$ is the polarization asymmetry, Y^L is the background-subtracted yield using a linearly-polarized beam, Y^C is the background-subtracted yield using a circularly-polarized beam, and $E_{\gamma circ}$ is the beam energy of the circularly-polarized beam measurement. For most experiments, there was only one circularly-polarized beam measurement per target. In cases where only two detectors are used at a given scattering angle θ, the formula is the same except only $\phi = 0, 90^\circ$ are used. It is clear that this equation accurately incorporates the corrections by using a circularly-polarized beam; if the linearly-polarized beam yields Y^L are replaced by Y^C, the polarization asymmetry is automatically zero.

In addition to measuring the polarization asymmetries for different targets and beam energies as a function of neutron energy, the polarization asymmetries when

integrated over neutron energy were also calculated. These integrated polarization asymmetries were calculated by using the neutron-energy-integrated yields in place of $Y^L(.., E_n, ..)$ and $Y^C(.., E_n, ..)$. Summing the yields over neutron energy increased the statistical accuracy of the asymmetry measurements. Unless specifically denoted by $\Sigma(.., E_n, ..)$, the polarization asymmetry has been integrated over neutron energy.

5.9.2 Calculation of Angular Distribution Coefficients Using the Polarization Asymmetries

As previously discussed in Section 2.4.2, the polarized angular distribution of the prompt fission neutrons is given by:

$$W(\theta, \phi) = a + b\sin^2(\theta) + c\sin^2(2\theta) + \cos(2\phi)(b\sin^2(\theta) + c\sin^2(2\theta)) \tag{5.4}$$

The coefficients of the angular distribution, a, b, and c were determined at each beam energy by fitting the angular dependence of the polarization asymmetry. In terms of the coefficients a, b, and c, the polarization asymmetry is given by:

$$\Sigma(\theta) = \frac{b\sin^2(\theta) + c\sin^2(2\theta)}{a + b\sin^2(\theta) + c\sin^2(2\theta)} \tag{5.5}$$

Rearranging terms in Equation 5.5 yields:

$$\Sigma(\theta) = \frac{\frac{b}{a}\sin^2(\theta) + \frac{c}{a}\sin^2(2\theta)}{1 + \frac{b}{a}\sin^2(\theta) + \frac{c}{a}\sin^2(2\theta)} \tag{5.6}$$

Equation 5.6 shows that there are only two fitting parameters for $\Sigma(\theta)$: $\frac{b}{a}$ and $\frac{c}{a}$. In previous works on fragment angular distributions, the parameter space was reduced by simply fixing $a = 1 - b$ to normalize the angular distribution [41]. The same normalization was also chosen in this work. For the fitting procedure, an uncertainty of 0.5° in θ was assumed for each data point of the polarization asymmetry. An example fit is shown in Figure 5.20.

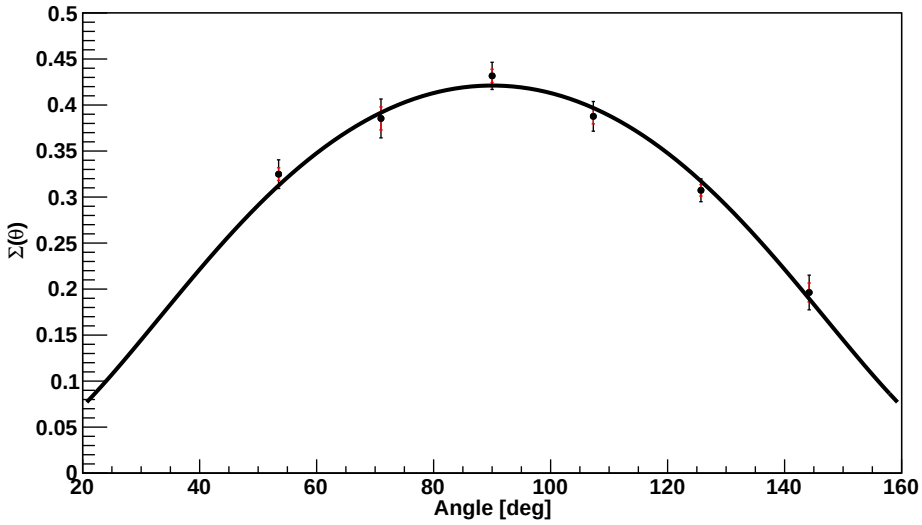

FIGURE 5.20: Polarization asymmetries as a function of θ. The data shown are from photofission of ^{238}U at 5.8 MeV. The black error bars show the statistical uncertainties and the red error bars show the systematic uncertainties. The best fit parameters are $b = 0.433 \pm 0.011 \pm 0.006$ and $c = -0.012 \pm .017 \pm 0.009$, where the first uncertainties are statistical and the second are systematic.

One advantage of fitting the polarization asymmetries is that it incorporated all prompt neutron data from all detectors into only two parameters: b and c. This allowed for easy comparisons of different γ-ray beam energies and different targets.

5.9.3 Correction for Finite Size of the Detectors

The measured angular distribution coefficients using the fitting procedure outlined in Section 5.9.2 depended on the specific detector locations. Because the detectors were of finite size, they subtended a finite range of angles outside of the central angles used in Figure 5.20. The angular span of the detectors was approximately $\pm 6.4^\circ$.

The corrections to the angular distribution coefficients b and c due to the angular span of the detectors were calculated using a `GEANT4` simulation. In this simulation, 10^7 neutrons were thrown from the target position according to a specific angular distribution $W(\theta, \phi)$ using coefficients b_{pl} and c_{pl}, where $_{pl}$ denotes a "point-like"

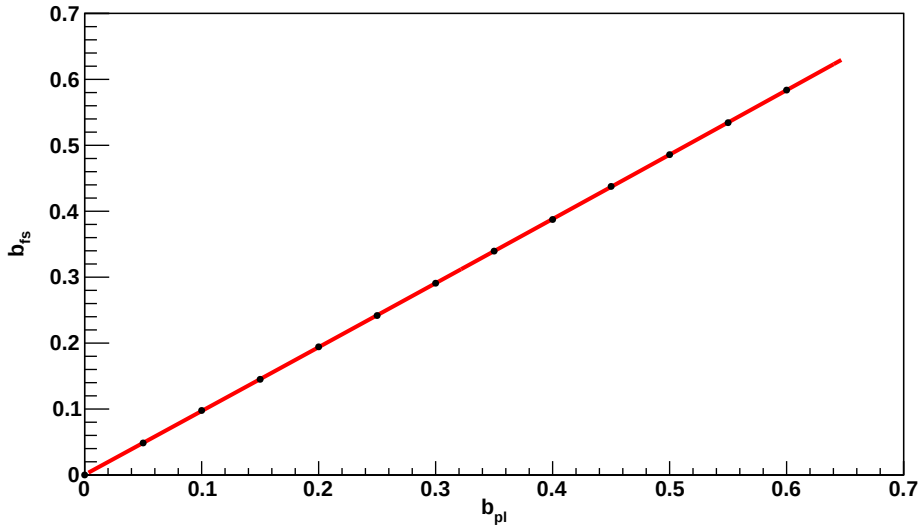

FIGURE 5.21: The points show the results of a GEANT4 simulation to calculate b_{fs} for a given b_{pl}. The simulation points were fit to a $O(b_{pl}^2)$ polynomial to interpolate between the points. The fit result is $b_{fs} = 0.00 + 0.96 * b_{pl} + 0.01 * b_{pl}^2$.

distribution. Detectors were placed at the same angles and distances as used in the experiments, and the polarization asymmetries were calculated and fit to obtain new angular distribution coefficients b_{fs} and c_{fs}, where $_{fs}$ denotes a "finite-size" distribution. If the detectors spanned no angular range, then b_{fs} and c_{fs} would be equal to b_{pl} and c_{pl}. Because of the finite angular span of the detectors, b_{fs} and c_{fs} are slightly smaller than b_{pl} and c_{pl}.

The points in Figure 5.21 show the result of the simulation to calculate b_{fs} using b_{pl}. These points were fit using a $O(b_{pl}^2)$ polynomial. The polynomial was inverted to allow for a calculation of b_{pl} from the measured b_{fs}. The results for correcting c are very similar and are not shown. The potential uncertainty introduced through this correction is discussed in Section 5.10.3.

5.9.4 Correction for Contaminants in the Target

After b_{pl} was calculated for each target, the final step in the analysis was to correct for the impurities in each target. Table 4.1 lists the targets used, their enrichments, and their impurities. The correction for the contaminants in each target depended on the cross sections, prompt neutron multiplicities, and angular distribution coefficients for each isotope in the target. To avoid reliance on other measurements, results from these experiments were used when possible. The efficiency-corrected yields, normalized to the average detector solid angle and normalized to the 5-paddle counts, and finally divided by the target mass in the γ-ray beam, were proportional to the product of the prompt neutron multiplicity (ν) and the photofission cross section (σ). Let the proportionality constant between these quantities be α, so:

$$\alpha(\sigma\nu)_{tA} = \alpha(\sigma\nu)_{i1}x_{tA} + \alpha(\sigma\nu)_{i2}(1 - x_{tA}) \tag{5.7a}$$

$$\alpha(\sigma\nu)_{tB} = \alpha(\sigma\nu)_{i1}x_{tB} + \alpha(\sigma\nu)_{i2}(1 - x_{tB}) \tag{5.7b}$$

where $(\sigma\nu)_{tA}$ is the product of the photofission cross section times the prompt neutron multiplicity for the measured target A, $(\sigma\nu)_{i1}$ is the expected cross section times multiplicity for isotope 1, and x_{tA} is the enrichment of isotope 1 in the given target A. For example, target 1 could be the ^{238}U target and target 2 could be the ^{235}U target. In this case, isotope 1 would be ^{238}U, isotope 2 would be ^{235}U, x_1 would be 0.993, and x_2 would be 0.063. Through using Equation 5.7, $(\sigma\nu)_{^{238}U}$ and $(\sigma\nu)_{^{235}U}$ could be calculated independent of α.

After $(\sigma\nu)_i$ is calculated for all the pairs of isotopes, the angular distribution coefficients can be corrected using:

$$\alpha(\sigma\nu)_{tA}b_{tA} = \alpha(\sigma\nu)_{i1}b_{i1}x_{tA} + \alpha(\sigma\nu)_{i2}b_{i2}(1 - x_{tA}) \tag{5.8a}$$

$$\alpha(\sigma\nu)_{tB}b_{tB} = \alpha(\sigma\nu)_{i1}b_{i1}x_{tB} + \alpha(\sigma\nu)_{i2}b_{i2}(1 - x_{tB}) \tag{5.8b}$$

where b_i is the point-like angular distribution coefficient for the given isotope. These

Table 5.2: References of other measurements used to correct for the contribution of contaminant isotopes in each target

Target (measured)	Contaminant Isotope (not measured)	Energies Needed (MeV)	σ	ν	b_f
^{235}U	^{238}U	5.6	[79]	[79]	[41]
^{239}Pu	^{240}Pu	5.3, 5.4, 5.5, 5.6	[41]	-	[41]
^{240}Pu	^{239}Pu	7.2, 7.6	[80]	-	0

equations were solved for b_i yielding the corrected values for the angular distribution coefficients b. The c coefficients were corrected in the same way.

The quantities $(\sigma\nu)$, b, and c all depend on the γ-ray beam energy. Therefore, the corrections were applied at each beam energy studied. In several cases, only one of the two principal isotopes in a target was measured at a given beam energy. These cases are listed in Table 5.2. In these situations, previously measured cross sections and prompt neutron multiplicities were used to correct for the unmeasured isotope in the target. These quantities were normalized to our measured data at the closest beam energy measured. Previously measured fragment angular distribution coefficients b_f and c_f were normalized to the prompt neutron angular distribution coefficients at the same energies as the cross sections and prompt neutron multiplicities. The prompt neutron multiplicities for ^{239}Pu and ^{240}Pu have not been measured over the required energy ranges and were assumed constant between the normalization point and extrapolated data points. The angular distribution for ^{239}Pu above 7.0 MeV was assumed to be isotropic.

5.9.5 ^{233}U Enrichment Calculation

Section 4.4 discussed the fissionable targets used in this experiment and the uncertainty regarding the enrichment of the ^{233}U target. Based on photofission angular

distribution theory in Section 2.4.2.2 and other measurements of even-odd isotopes with large ground state spins discussed in Section 3.2, the prompt neutron polarization asymmetry expected from this isotope (^{233}U) is 0. If it were exactly 0, then the enrichment of the target could be deduced from the asymmetry measurement, as the asymmetry from ^{232}Th is significant as shown in Figure 7.1. The enrichment calculation was performed by varying x_{tA} for the ^{233}U target and calculating the difference between the b coefficient for ^{233}U and 0. The x_{tA} that yielded the minimum difference between the b coefficient for ^{233}U and 0 was considered to be a possible enrichment of the sample.

5.10 Systematic Uncertainties

Typical systematic uncertainties in a reaction cross section measurement include uncertainties in the detector solid angle and efficiency, uncertainty in the beam flux, and uncertainty in the target thickness. However, because the observable of interest here is the polarization asymmetry, which was formed by taking ratios of detector yields, the dependence on the beam flux and target thickness canceled. Additionally, because circularly-polarized beams were used to directly correct for differences in detector solid angle and efficiency, the systematic uncertainty from those effects were eliminated. The polarization asymmetry was sensitive to the γ-ray beam polarization, which was assumed to be 100% with no systematic uncertainty.

For these measurements of polarization asymmetries, four remaining potential sources of systematic uncertainties were identified: the statistical uncertainty in the corrections using a circularly-polarized γ-ray beam, potential gain shifts in the detectors during the experiment, the correction for the finite size of the detectors, and the placement of the analysis cuts.

5.10.1 Statistical Uncertainty on Circular Correction

The measurements using a circularly-polarized beam to correct for differences in detector solid angles and efficiencies were only performed at one γ-ray beam energy and only performed once per target. It is clear from Equation 5.3 that the yields from this circularly-polarized beam measurement enter into the calculations of the polarization asymmetry for all linearly-polarized beam runs on that target. Therefore, the statistical uncertainty of the circularly-polarized beam measurement entered as a systematic uncertainty for the polarization asymmetry measurements at different γ-ray beam energies. This is the dominant source of systematic uncertainty.

However, it is important to note that the corrections from the circularly-polarized beam are uncorrelated systematic uncertainties for detectors at different scattering angles at the same beam energy. In addition, the systematic uncertainties in the polarization asymmetries were also uncorrelated for different neutron energies at the same beam energy.

The use of the same circular correction at different beam energies implies that the angular distribution coefficients are systematically correlated at different beam energies. The extent of this correlation was determined by a Monte Carlo technique. Each polarization asymmetry at each beam energy and each angle was varied by a value sampled from a Gaussian with a standard deviation of the systematic uncertainty of that polarization asymmetry. Then, new fits of the polarization asymmetry as a function of θ (Section 5.9.2) were performed at each beam energy using only the statistical uncertainties, and new values of b and c were extracted for each beam energy. This procedure was repeated 1000 times for each beam energy and the standard deviation of the values of b and c was taken as the systematic uncertainty. The statistical uncertainty in b and c was given by the uncertainty in the parameters using only the statistical uncertainties in the fit.

5.10.2 Uncertainty from Gain Shifts in the Detectors

Possible gain shifts in the detectors during the experiment generated other potential sources of systematic uncertainty. If a gain shift occurred between the circularly-polarized beam measurement and the linearly-polarized beam measurement, or during the linearly-polarized beam measurement, the effective threshold would change which would affect the efficiency of the detector as discussed in Section 4.6.3. This effect would not be compensated for by the circular correction. Therefore, the gains of the detectors were checked twice during each day of the experiment using a ^{137}Cs source. The procedure detailed in Section 5.2 to fit the ^{137}Cs edge was performed for each run with a ^{137}Cs source, and gain shifts were not detected above $\sim 1\%$. A gain shift of 1% would translate into a change of efficiency integrated over the prompt neutron energy spectrum of approximately 0.3%. Most of this change in efficiency would affect the lowest neutron energy bin. Typical uncertainties on Σ, b, and c were on the order of a few percent, so this small additional uncertainty can be safely neglected.

5.10.3 Uncertainty From the Correction for the Finite Size of the Detectors

One additional potential source of uncertainty is from the correction for the finite size of the detectors. This correction was performed using a `GEANT4` simulation and is discussed in Section 5.9.3. The statistics on each simulation point are very good, and the polynomial fits the points well, so the resulting uncertainties on the fit parameters are small. For the correction to b, the resulting polynomial with uncertainties is:

$$b_{pl} = (-0.0004 \pm 0.0005) + (1.037 \pm 0.003) b_{fs} + (-0.013 \pm 0.006) b_{fs}^2 \qquad (5.9)$$

The values of b_{pl} were calculated using this fit from the measured values of b_{fs}.

The uncertainty on the resulting value for b_{pl} due to this fit is estimated to be 0.1%, which is much less than the uncertainty of b_{fs} so it can be safely neglected.

5.10.4 Uncertainty From the Placement of the Analysis Cuts

The final potential source of systematic uncertainties was the placement of the analysis cuts. Because the cuts were drawn by hand, even though they were later optimized, they were a potential source of systematic uncertainty and bias. To estimate the uncertainty due to the particular analysis cuts used, the cuts were adjusted and the polarization asymmetries were recalculated. The three cuts potentially subject to systematic uncertainty were the PH threshold cut, the PH-PSD cut, and the TOF-PSD cut.

The systematic uncertainties due to the PH threshold cut and the PH-PSD cut were not calculated. The PH threshold cut was not adjusted because of the relative certainty in setting the PH threshold as shown in Section 5.10.2. The PH-PSD cut was intentionally set relatively loosely around the prompt neutrons to minimize the uncertainty regarding this cut.

Therefore, the only cut for which the systematic uncertainty was calculated was the TOF-PSD cut. This cut was manipulated in the same way as outlined in Section 5.7.3. The cut was moved up until the background-subtracted yield was two standard deviations above or below the yield using the optimal cut position, and then the circular corrections and polarization asymmetries were recalculated using this adjusted cut. Next, the cut was moved down until the yield changed by two standard deviations, and the process was repeated. This entire process was also repeated by scaling the cut larger vertically or smaller vertically until the yield changed by two standard deviations.

After the cuts were adjusted, the differences between the optimal and adjusted polarization asymmetries were calculated for each neutron energy bin and for the

total prompt neutron yield at a given scattering angle θ. The differences between the asymmetries for different adjusted cuts were added in quadrature and divided by 4. This took into account the square root of the number of adjustments made ($\sqrt{4}$) and the 2 standard deviations by which the cuts were adjusted.

In general, the resulting systematic uncertainty due to the cut placement was small. It is clear from Figure 5.14 that many different TOF-PSD cuts would result in the same neutron yield as long as the γ-ray backgrounds are avoided. In cases of significant neutron backgrounds and low prompt neutron yields, the systematic uncertainty of the cut placement was larger, but even in these extreme cases it was generally less than the systematic uncertainty from the circularly polarized beam measurements.

6

Photofission Calculation

6.1 Introduction

Chapter 2 discussed the theory behind photofission fragment angular distributions and the prompt neutron emission mechanism from the excited fission fragments. This chapter discusses a fission calculation (`FREYA`) developed by nuclear theorists at Lawrence Livermore National Laboratory (LLNL) and Lawrence Berkeley National Laboratory (LBNL) which models the prompt neutron emission mechanism. The results of `FREYA` are used in a simplified model of the photofission process to predict prompt neutron polarization asymmetries. Calculations of ^{238}U and ^{240}Pu were performed, because experimental information needed for the calculation exist for these nuclei and they exhibit highly anisotropic fragment angular distributions.

Section 6.2 discusses several prompt fission neutron calculations and how they work in general terms. Section 6.3 gives details of the fragment mass, charge, and energy calculations in `FREYA`. Section 6.4 details the generation of prompt neutrons from the fission fragments in `FREYA`. Section 6.5 discusses the data sets obtained through `FREYA` and gives an example of the `FREYA` output. As previously mentioned

in Section 2.3, there is no theory capable of quantitatively predicting the fragment angular distributions from photofission. Therefore, previously measured photofission fragment angular distributions were used as inputs to the photofission model, as discussed further in Section 6.6. Section 6.7 illustrates how the calculated prompt neutron angular distribution coefficients and polarization asymmetries were determined.

6.2 General Aspects of Prompt Neutron Calculations

There are several calculations of prompt neutron observables (multiplicity, energy, etc.) which rely on modeling the excited fission fragment properties (mass, charge, etc.): one developed primarily at Los Alamos National Laboratory [81, 82, 83], another developed primarily at Commissariat a lEnergie Atomique Cadarache in France [84], and a third, `FREYA`, developed primarily at LLNL and LBNL [10, 85, 86, 87, 88]. All of the calculations except for [83] are conceptually similar. They select the fragment masses from experimentally measured fragment mass distributions, and then choose the fragment charge based on experimental measurements. Then, the calculations find the Q-value for the reaction based on the masses of the nuclei involved and distribute excitation energy and kinetic energy to the fragments. The distribution of excitation energy depends on the particular calculation, while the distribution of kinetic energy is determined by the kinematics. After the fragments have repelled each other based on their mutual Coulomb repulsion and fully accelerated to their final kinetic energies, they are assumed to decay by emitting prompt neutrons. The neutron energies in the rest frame of the fission fragment are taken from a Weisskopf evaporation spectrum [20], and the neutrons are emitted with no preferred direction in the rest frame of the fragment. Finally, the neutrons are boosted into the lab frame by the fragment. Once the Q-value of neutron emission is below the neutron separation energy, neutron emission stops as it is no longer energetically possible.

After this point, it is assumed that the fragment decays by emitting γ rays. This is an approximation; in reality, there is a small probability that the nucleus will decay by γ-ray emission even when neutron emission is possible. Calculation [83] differs only in that it uses a Hauser-Feshbach statistical approach to more accurately describe the competition between neutron emission and γ-ray emission during the fragment decay.

The calculations described above are generally benchmarked to experimental measurements of spontaneous fission of ^{238}U, ^{240}Pu, ^{244}Cm, and ^{252}Cf and neutron-induced fission of ^{235}U, ^{239}Pu, ^{240}Pu. The experimental measurements typically used as benchmarks are:

- the average kinetic energy of the fission fragments as a function of fragment mass
- the average prompt neutron multiplicity
- the average prompt neutron multiplicity as a function of fragment mass
- the prompt neutron multiplicity distribution integrated over fragment mass
- the prompt neutron energy spectrum
- the average neutron kinetic energy as a function of fragment mass

The fragment-neutron angular correlation is the key observable that is expected to influence the prompt neutron angular distribution. This observable is not used as a benchmark for any of the current calculations. The predicted fragment-neutron angular correlations can be tested by comparing the current measurements to the calculated results.

6.2.1 Adapting Calculations for Photofission

The calculations described above have been designed for use in both neutron-induced fission and spontaneous fission. None of these calculations are specifically intended for modeling photofission. However, because fission is a compound reaction, photofission and neutron-induced fission should be equivalent if they create the same compound nucleus. Neglecting angular momentum effects, photofission of ^{A}X is considered to be equivalent to neutron-induced fission of $^{A-1}$X with a neutron energy of $E_n = E_\gamma - S_n$, where E_γ is the γ-ray energy and S_n is the neutron separation energy in the parent nucleus.

However, as shown in Section 2.4, angular momentum effects from the photon give rise to the polarization asymmetry of the fission fragments, which in turn is expected to give rise to the polarization asymmetries of the prompt neutrons. Neutron-induced fission will create compound nuclei with different angular momenta and thus the fission fragments will have different angular distributions. To adapt a calculation designed for neutron-induced fission to model photofission, several steps must be taken:

- it must be assumed that the angular distribution of the fragments is independent of other characteristics of the fission reaction, such as the mass division, charge division, and energy division between the fragments
- experimentally measured photofission fragment angular distributions must be used as inputs to the calculation
- the neutron-induced fission calculation must be used at the appropriate excitation energy to model photofission at a given γ-ray beam energy

The assumptions above have been found to be violated to some extent by a previous experiment [49], which found a correlation between the mass division and

fragment angular distribution in photofission. If the average prompt neutron multiplicities for the different fragment masses are similar, then this violation of our assumptions is negligible. This is discussed in more detail when the fragment angular distributions are implemented in the calculation in Section 6.6.

6.3 FREYA Fragment Calculation

6.3.1 Fragment Masses and Charges

The first step in the calculation is to determine the masses, charges, and energies of the fission fragments [10, 85, 86, 87]. FREYA begins with a fissioning nucleus of mass A_0, charge Z_0, and excitation energy E_0^*, which in the case of photofission is approximately equal to E_γ.

The first quantities calculated are the fragment masses. Because there is no computationally fast and accurate quantitative model for fragment masses, experimentally measured masses are used as inputs. There are two methods to use the experimental masses as inputs: to interpolate between the masses directly, or to model the dependence of the fragment masses as a function of excitation energy. The FREYA developers used the latter method for neutron-induced fission of ^{239}Pu as follows.

Modeling the energy dependence of the fragment masses requires unfolding the contributions of the different fission modes. As discussed in Section 2.3.3, there are three principle components to low-energy fission: standard-I and standard-II asymmetric fission and superlong symmetric fission [12]. Symmetric or asymmetric in this case refers to the mass division between the fragments. For the standard-I and standard-II asymmetric modes, both the heavy fragment and the light fragment masses can be well-modeled using separate Gaussians, while the superlong symmetric mode masses can be well modeled by a single Gaussian. Therefore, a five-Gaussian

fit to the experimental data is performed to interpolate the measured fragment mass distribution. The four standard asymmetric mode Gaussians are parameterized by:

$$S_i(A_f) = \frac{N_i}{\sqrt{2\pi}\sigma_i}(e^{-(A_f - A_0/2 - D_i)^2/2\sigma_i^2} + e^{-(A_f - A_0/2 + D_i)^2/2\sigma_i^2}) \tag{6.1}$$

where $i = 1, 2$ indicates standard-I or standard-II, A_f is the fragment mass, N_i is the relative normalization of the mode, D_i is the displacement from symmetric fission, and σ_i is the width. The symmetric mode is modeled by a single Gaussian:

$$S_{sym}(A_f) = \frac{N_{sym}}{\sqrt{2\pi}\sigma_{sym}} e^{-(A_f - A_0/2)^2/2\sigma_{sym}^2} \tag{6.2}$$

where *sym* denotes the symmetric mode. The normalization is given by:

$$2N_1 + 2N_2 + N_{sym} = 2 \tag{6.3}$$

where 2 is chosen for the normalization because two fragments are emitted for each binary fission. A fission fragment mass is chosen from this five-Gaussian fit and the mass of the complementary fragment is then determined by using the mass of the parent nucleus.

The range of γ-ray energies used in our experiments was relatively narrow ($\sim 5 - 7\,\mathrm{MeV}$), so the changes in the Gaussian parameters D_i, σ_i, N_i, N_{sym}, and σ_{sym} as a function of E_0^* are expected to be small. D_i is governed by the spherical and deformed shell closures, so it is expected to be energy independent. σ_i changes slowly with energy, while σ_{sym} is energy independent. The normalizations change slowly until the symmetric mode begins to dominate, occurring near $E_0^* \approx 25\,\mathrm{MeV}$.

The five-Gaussian fitting procedure was performed using the data of [89] for neutron-induced fission of ^{239}Pu, which creates a compound nucleus of ^{240}Pu before fissioning. This ^{239}Pu fitting procedure was performed to model the energy dependence of the fission fragment masses over a wide neutron energy range ($\sim 1 - 20\,\mathrm{MeV}$),

as described in [87]. For photofission of ^{240}Pu over our relatively narrow energy range, this procedure did not significantly differ from interpolating the masses directly. Therefore, for ^{238}U, experimental fragment mass distributions from neutron induced fission at 500 keV were used and interpolated directly [89].

The fission fragment masses A_H and A_L also depend on the "chance" of the fission reaction. First chance fission is defined to be when the compound nucleus directly fissions, whereas multichance fission occurs if the nucleus emits one or several neutrons before fissioning. At our γ-ray beam energies, first chance fission dominates over multichance fission. In the case of multichance fission, after the compound nucleus emits a neutron and loses the binding energy S_n, which is typically around 6 MeV, the compound nucleus would be left with at most only ~ 1 MeV of excitation energy. This is insufficient energy to overcome the fission barrier. Assuming only first chance fission implies $A_0 = A_H + A_L$.

After determining the fragment masses, the fragment charges are selected. A Gaussian is used to select the heavy fragment charge:

$$P_{A_f}(Z_f) \propto e^{-(Z_f - \widetilde{Z_f(A_f)})^2/2\sigma_{Z_f}^2} \tag{6.4}$$

where Z_f is the fragment charge, $\widetilde{Z_f(A_f)}$ is the average charge based on fixing the charge-to-mass ratio of the fragments and the parent nucleus ($\widetilde{Z_f(A_f)} = A_f Z_0/A_0$), and $\sigma_{Z_f} = 0.5$ is the experimentally measured charge width [90]. The `FREYA` developers limited possible charges to $|Z_f - \widetilde{Z_f(A_f)}| \leqslant 5\sigma_{Z_f}$. The charge of the complementary fragment is given by $Z_L + Z_H = Z_0$.

6.3.2 Fragment Energies

After the fragment masses and charges are determined, the kinetic and excitation energies of the fragments are calculated. The Q-value of the reaction gives the total

energy released in the fission:

$$Q_f = M_0^* - M_L - M_H \tag{6.5}$$

where M_0^* is the total mass of the excited parent nucleus and M_L, M_H are the ground-state fragment masses. When possible, fragment masses are taken from on experimentally measured masses [91]. If the fragment masses have not been measured, masses calculated from [7] are used.

Next, the average total kinetic energy, $\overline{TKE}$, is calculated. $\overline{TKE}$ is a function of the fragment mass and excitation energy of the parent. $\overline{TKE}(A_H, E_0^*)$ is assumed to have the form:

$$\overline{TKE}(A_H, E_0^*) = \overline{TKE}(A_H) + dTKE(E_0^*) \tag{6.6}$$

where $\overline{TKE}(A_H)$ is an experimentally measured $\overline{TKE}$ distribution as a function of fragment mass, and $dTKE(E_0^*)$ is an adjustable parameter. The parameter is changed so that the calculated average prompt neutron multiplicity matches the experimentally measured average prompt neutron multiplicity. As $dTKE(E_0^*)$ is increased, more energy on average is given to the kinetic energy of the fragments, which for a fixed Q-value means that less energy is available as excitation energy. As the excitation energy is reduced, the average prompt neutron multiplicity decreases. $dTKE(E_0^*)$ impacts the average prompt neutron multiplicity through this effect.

The $\overline{TKE}(A_H)$ distributions were taken from an average of [92, 93, 94] for thermal neutron induced fission of ^{239}Pu to calculate photofission of ^{240}Pu. Since a stable target of ^{237}U is not available, neutron induced fission of ^{238}U (measured in [95]) was used as the $\overline{TKE}(A_H)$ distribution for the ^{238}U calculation. The average prompt neutron multiplicities were taken from [96] to calculate $dTKE(E_0^*)$.

After $\overline{TKE}$ is calculated, the average total excitation energy $\overline{TXE}$ is calculated using conservation of energy: $\overline{TXE} = Q_f - \overline{TKE}$. $\overline{TXE}$ must be partitioned to the

light and heavy fragments to calculate their average excitation energies $\overline{E^*_{L,H}}$. The energy is partitioned by assuming that, on average, the two fragments are in mutual thermal equilibrium: $T_L = T_H$, where T is the temperature of the fragment.

A relationship between temperature and excitation energy must be derived to calculate the average excitation energy of the fission fragments: $\overline{E^*_{L,H}}$. Generally, the nuclear level density is approximated as $\rho(E^*_i) \propto e^{2\sqrt{a_i E^*_i}}$, where a_i is the level density parameter and $i = L, H$ indexes the fragments [97]. The level density parameter a_i is parameterized by [98]:

$$a_i(E^*_i) = \frac{A_i}{e_0}(1 + \frac{\delta W_i}{E^*_i}(1 - e^{-\gamma E^*_i})) \tag{6.7}$$

where A_i is the fragment mass, e_0 is the asymptotic level density, δW is the shell correction energy, and γ is a damping coefficient. δW is given by [99] and the other parameters are given in [98]. The entropy is given by $S_i = 2\sqrt{a_i E^*_i}$, and using $\frac{\mathrm{d}S}{\mathrm{d}E} = \frac{1}{T}$ yields $E^*_i = a_i T_i^2$. Since the fragments share a common temperature, $T_i = T_{LH}$ is a constant. Using the above equations yields:

$$\overline{E^*_i} = a_i \frac{\overline{TXE}}{a_L + a_H} \tag{6.8}$$

The average excitation energy of each fragment was then adjusted slightly to give more energy to the light fragment. Without this adjustment, `FREYA` underpredicts the average prompt neutron multiplicity of the light fragment [87]. The average excitation energy of the light fragment was increased by a factor of 1.1 for ^{240}Pu and 1.2 for ^{238}U. The average excitation energy of the heavy fragment was reduced by a corresponding amount.

Finally, after the average kinetic energy $\overline{TKE}$ and average excitation energies $\overline{E^*_{L,H}}$ are calculated, `FREYA` includes the effect of thermal fluctuations on the calculated TKE and $E^*_{L,H}$. The variances in the excitation energy are given by $\sigma_i^2 =$

$T^2 \frac{d\overline{E_i^*}}{dT} = 2\overline{E_i^*} T_{LH}$, and the distribution of real energies about $\overline{E_i^*}$ is expected to be Gaussian. Two adjustments δE_L and δE_H are chosen from Gaussian distributions centered about 0 with variances σ_L^2 and σ_H^2 respectively. The calculated fragment excitation energies are then given by $E_i^* = \overline{E_i^*} + \delta E_i$. To conserve energy, the kinetic energy released in the calculated event is adjusted by $TKE = \overline{TKE} - \delta E_L - \delta E_H$. The individual kinetic energy of each fragment can be determined by conservation of energy, conservation of momentum, and the fragment masses.

6.3.3 FREYA Fragment Angular Distribution

FREYA is not capable of quantitatively predicting fragment angular distributions. In principle, FREYA could interpolate from experimentally measured photofission fragment angular distributions. However, it was not designed specifically for photofission so this feature was not implemented by the developers. In the general version of FREYA, the fragments are emitted with no preferred direction. However, in the FREYA data sets that the developers provided to the author, the fragment direction was fixed to be along the z-axis. This allowed for an easier incorporation of the previously measured fragment angular distribution, as discussed further in Section 6.6.

6.4 FREYA Prompt Neutron Emission

After the fragment kinetic energies, excitation energies, masses, and charges are calculated, FREYA assumes each fragment decays by neutron evaporation as long as it is energetically feasible. FREYA assumes that the fragments have fully accelerated to their terminal velocities before any neutrons are evaporated, which is consistent with the timescale discussed in Section 2.5. The Q-value for neutron emission from each fragment is given by $Q_n = M_i^{gs} + E_i^* - M_f^{gs} - m_n$ where M_i^{gs} is the fragment ground state mass and M_f^{gs} is the ground state mass of the daughter nucleus. Masses are taken from [91] and supplemented with [7] when needed.

The Q-value is equal to the maximum possible excitation energy in the daughter nucleus, E_f^{max}, which occurs if the neutron is evaporated with no kinetic energy. E_f^{max} leads to a maximum possible daughter temperature $T_f^{max} = \sqrt{\frac{E_f^{max}}{a_f}}$. This temperature is used in equation 2.58 to obtain the probability of evaporating a neutron of energy ϵ in the rest frame of the fragment. After a neutron is emitted, the daughter nucleus retains an excitation energy of $Q_n - \epsilon$. The process of neutron evaporation is repeated sequentially until it is no longer energetically feasible, at which point `FREYA` assumes the fragment de-excites through γ-ray emission.

In the `FREYA` calculation, ϵ represents the total kinetic energy released in the decay. The neutron kinetic energy is actually slightly below ϵ due to energy lost from the small recoil of the daughter nucleus.

`FREYA` assumes the neutrons are emitted in no preferred direction in the rest frame of the fragment. Finally, the neutrons are boosted into the lab frame by the fragments.

6.5 `FREYA` Calculated Datasets

The LLNL and LBNL group supplied the author with 1 million calculated events for photofission of ^{240}Pu at 5 MeV and 7 MeV and photofission of ^{238}U at 5 MeV, 6 MeV, and 7 MeV. These nuclei were chosen because they both exhibit highly anisotropic fragment angular distributions and the experimental data required by `FREYA` is known. Below is one example fission event from the `FREYA` calculation:

```
1:  event
42 110 -44.643 -35.242 4383.477
52 130 4.260 -57.124 -4458.289
3 neutrons:
45.678 31.063 31.076
```

```
-1.035 4.178 48.643
-6.450 57.010 -4.146
```

The first line of the output contains the event number. The next two lines give information on the fragments in the following order: Z, A, p_x, p_y, and p_z. The units of momentum here are MeV/c. In the data set provided to the author, the fragments' initial direction was fixed along the z-direction, which is consistent with the sample event provided above. The number of prompt fission neutrons followed by their momenta is given after the fragment information.

6.6 Incorporation of Previously Measured Fragment Angular Distributions

As shown in Section 6.5, the fragments' initial direction was fixed to be along the z-axis to simplify incorporating an underlying fragment angular distribution. In reality, the fragment direction should not be fixed, but rather the fragments should travel according to their angular distribution $W(\theta, \phi)$. If according to this angular distribution, the fragment should have traveled at an angle (θ, ϕ) instead of along the z-direction, the momenta were rotated as follows:

$$\begin{bmatrix} p_x^f \\ p_y^f \\ p_z^f \end{bmatrix} = \begin{bmatrix} \cos\theta\cos\phi & -\sin\phi & \sin\theta\cos\phi \\ \cos\theta\sin\phi & \cos\phi & \sin\theta\sin\phi \\ -\sin\theta & 0 & \cos\theta \end{bmatrix} \times \begin{bmatrix} p_x^i \\ p_y^i \\ p_z^i \end{bmatrix} \tag{6.9}$$

where $p^i_{x,y,z}$ is the initial momentum and $p^f_{x,y,z}$ is the final momentum. To perform this rotation, the underlying fragment angular distribution $W(\theta, \phi)$ is required. Previously measured fragment angular distributions from photofission of ^{238}U and ^{240}Pu from [41] are used as inputs. The results of [41] were chosen because the authors performed measurements on many different isotopes using a consistent setup, and their angular distribution parameters largely agreed with other available data taken

on ^{238}U as shown in Figure 3.2 of this dissertation.

These fragment angular distribution measurements were performed with unpolarized γ-ray beams. Recall from Section 2.4.2.1 that if the unpolarized angular distribution is:

$$W(\theta) = a + b\sin^2(\theta) + c\sin^2(2\theta) \tag{6.10}$$

a polarized angular distribution of the form:

$$W(\theta,\phi) = a + b\sin^2(\theta) + c\sin^2(2\theta) + \cos(2\phi)(b\sin^2(\theta) + c\sin^2(2\theta)) \tag{6.11}$$

can be used.

Each event in the `FREYA` calculated data set is rotated by a random (θ,ϕ) sampled from Equation 6.11 to reflect the underlying $W(\theta,\phi)$. For simplicity, it is assumed that the rotation angles are independent of the fragment mass, fragment charge, fragment momenta, neutron multiplicity, and neutron momenta. As discussed in Section 3.5, a previous photofission experiment on ^{232}Th has found a correlation between the fragment mass and the angular distribution coefficient b [49]. This correlation partially violates one of the assumptions in our photofission simulation. However, due to the lack of high-precision data taken with ^{238}U and ^{240}Pu, this correlation between the fission mode and fragment angular distribution was not included in the current calculation.

6.7 Determination of Prompt Neutron Angular Distribution Coefficients

The final step of the calculation is to determine the calculated prompt neutron angular distribution coefficients. A two-dimensional histogram in (θ,ϕ) is filled by each prompt neutron generated by the calculation that is above 1.5 MeV (the detector threshold used in our experiments). After the (θ,ϕ) histogram is filled, it is fit to

the angular distribution shown in Equation 6.11. The fitting procedure was tested against known angular distributions to ensure its accuracy.

Prompt neutron angular distribution coefficients are calculated in 10 keV steps in E_γ to try to predict the neutron coefficients as a function of E_γ. This requires calculating the fragment angular distribution in 10 keV steps and rotating the `FREYA` events at each energy step by the corresponding fragment angular distribution. The `FREYA` data set used at each energy is a weighted average of the different data samples available. For example, in the 6.5 MeV calculation of ^{240}Pu, the 7 MeV ^{240}Pu data sample is used and weighted by 0.75 and the 5 MeV ^{240}Pu data sample is used and weighted by 0.25.

A systematic uncertainty is introduced by using the same `FREYA` data samples at different beam energies. Because the statistical power of each data sample is good (1 million events per sample), these uncertainties should be small. In addition to these uncertainties, there are also statistical and systematic uncertainties arising from the fragment angular distributions themselves. The fragment angular distributions in [41] are presented without statistical uncertainties or systematic uncertainties, so no uncertainties are assumed.

7

Results and Conclusions

7.1 Introduction

This chapter will present the experimental results and discuss the implications of our results for basic science and potential applications. The χ^2 distribution will be used for hypothesis testing and parameter estimation throughout this chapter. Before the results are presented, some aspects of the χ^2 distribution will be discussed in Section 7.2. Section 7.3 shows the results of our experimental measurements of prompt neutron polarization asymmetries $\Sigma(E_\gamma, \theta, E_n)$ along with the prompt neutron angular distribution coefficients b and c for the 7 actinides studied. Section 7.4 presents the results of a calculation of prompt neutron polarization asymmetries for ^{238}U and ^{240}Pu (as developed in Chapter 6) and compares them to our experimental results; good agreement is found. This calculation is extended to model ^{232}Th, ^{239}Pu, and ^{237}Np, and good agreement is found for these isotopes as well. Section 7.5 investigates the existence of the hypothesized resonance in ^{239}Pu that was described in Section 3.6.

One potential application of our work is a new method of measuring the enrich-

ment of special nuclear material. That potential application is discussed in Section 7.6, and it is used to investigate the enrichment of the ^{233}U target used in our studies in Section 7.6.3. Finally, concluding remarks are presented in Section 7.7.

7.2 The χ^2 Distribution

The χ^2 distribution is used in hypothesis testing (including tests of goodness-of-fit) and parameter estimation [100]. The χ^2 distribution is given by the sum of standard normal distributions and has a probability density of:

$$P(x) = \frac{(x/2)^{\nu/2-1}e^{-x/2}}{2\Gamma(\nu/2)} \tag{7.1}$$

where ν is the degrees of freedom, which is a parameter of the distribution and is given by the difference between the number of data points and the number of constraints in a model or fit.

For the purposes of hypothesis testing, the χ^2 test statistic can be found from:

$$\chi^2 = (\vec{y} - \vec{\mu})^T V^{-1} (\vec{y} - \vec{\mu}) \tag{7.2}$$

where $\vec{y}$ is the vector of data points $(y_1, ..., y_i, ...y_N)$, $\vec{\mu}$ is the vector of predictions based on the null hypothesis $(\mu_1, ..., \mu_i, ...\mu_N)$, and V is the covariance matrix, defined as:

$$V_{i,j} = \sigma_i^{sys}\sigma_j^{sys} + \delta_{i,j}(\sigma_i^{stat})^2 \tag{7.3}$$

with σ_i^{sys} as the systematic (correlated) uncertainty at point i, and σ_i^{stat} as the statistical (uncorrelated) uncertainty at point i [101]. If the null hypothesis is true, the χ^2 statistic should follow a χ^2 distribution with N degrees of freedom, where N is the number of data points. The p-value is defined to be the integral of the χ^2 distribution from the χ^2 test statistic to infinity. The p-value represents the probability of falsely rejecting the null hypothesis. If the p-value is less than a

critical value, here taken to be 0.05, then we reject the null hypothesis. The p-value will also be reported along with each null hypothesis test.

The goodness-of-fit was determined by calculating the average χ^2 per degree of freedom ν. A good fit has a value of $\chi^2/\nu \approx 1$ [100]. Fits with small values of χ^2/ν indicate that the error bars on the points are generally too large, while fits with large values of χ^2/ν generally indicate possible problems with either the data or the choice of the fitting function.

Finally, the χ^2 distribution was also used to estimate fit parameters. The values of the parameters were found by minimizing the overall χ^2 statistic. The uncertainties on the parameters were found by adjusting the parameters until the χ^2 increased by 1. These uncertainties yield the 1σ confidence interval; given our data, it is expected that 68% of the time the true parameter value would fall within this range.

7.3 Experimental Results

7.3.1 Polarization Asymmetry Results

The primary results extracted from our experimental measurements are the prompt neutron polarization asymmetries (Σ) for each target, as discussed in Section 5.9. These asymmetries depend on the beam energy E_γ, the detected neutron energy E_n, and the scattering angle θ. The neutron energies are binned into eight 1 MeV wide bins starting at our detector threshold of 1.5 MeV. Only some of the polarization asymmetry data are shown here, however all of these data are presented in tabular form in Appendix B for all detector angles, beam energies, and neutron energy bins.

The dependence of $\Sigma(\theta = 90^\circ)$ on E_γ is shown in Figure 7.1. To create this plot, the yields were integrated over the detected neutron energies. $\Sigma(90^\circ)$ is shown because it maximizes the dipole contribution to the polarization asymmetry, as can be seen from Equation 5.6. These asymmetry data are for the targets themselves and

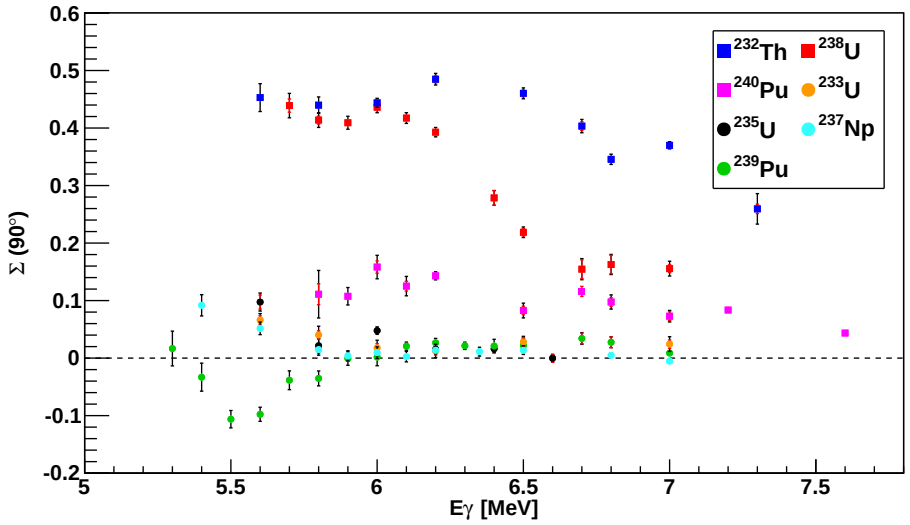

FIGURE 7.1: The polarization asymmetry at 90° is shown as a function of the beam energy. Prompt neutrons of all energies above our 1.5 MeV detector threshold have been summed. The black error bars indicate the statistical uncertainties and the red error bars show the systematic uncertainties. Uncertainties not shown are smaller than the size of the data points.

include the contributions from any contaminant isotopes. For example the results from ^{235}U contain a 6% contribution from ^{238}U as noted in Section 4.4. These contributions must be removed in order to thoroughly examine the results, but a short description of these asymmetries is still useful.

There are several interesting features of these results. First, the polarization asymmetries from ^{232}Th and ^{238}U are large at low beam energies. These asymmetries roughly correspond to 3 neutrons emitted in the plane of beam polarization for every 1 emitted perpendicular to that plane. Second, the polarization asymmetries from the other even-even actinide, ^{240}Pu, are significantly larger than 0 at low beam energies but not as large as ^{232}Th or ^{238}U. Third, as the beam energy increases, the polarization asymmetries decrease. Fourth, the polarization asymmetries of the even-odd actinides show a very different behavior. For ^{239}Pu, an interesting structure is seen; the polarization asymmetry is negative at 5.6 MeV and positive at 6.3 MeV.

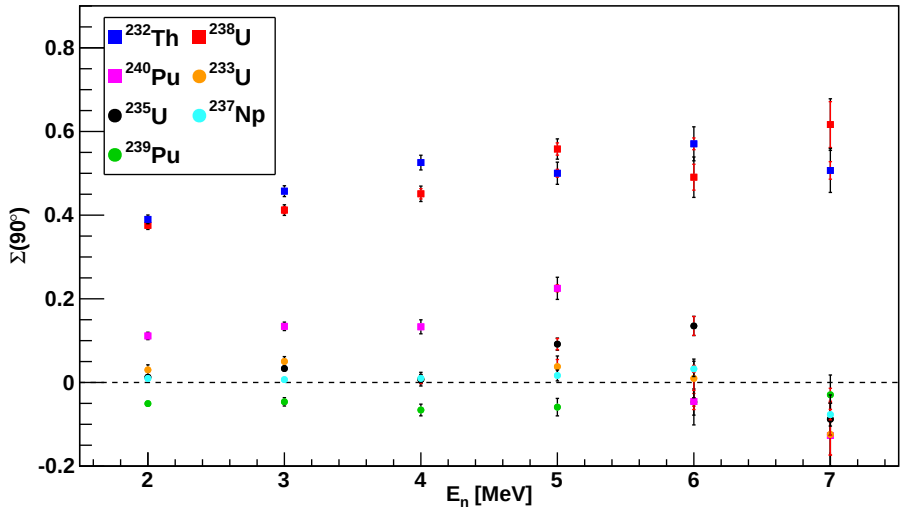

FIGURE 7.2: The polarization asymmetry at 90° is shown as a function of neutron energy. Yields from all beam energies below 6.2 MeV were integrated. The black error bars indicate the statistical uncertainties and the red error bars show the systematic uncertainties. Uncertainties not shown are smaller than the size of the data points.

For ^{233}U, ^{235}U, and ^{237}Np the polarization asymmetry is close to 0 at all energies other than the lowest beam energies studied.

The dependence of $\Sigma(90°)$ on E_n is shown in Figure 7.2. To create this plot, only the beam energies in the region below 6.2 MeV were used. These beam energies were chosen because the polarization asymmetries for the even-even actinides are large here. As expected, there is almost no polarization asymmetry in the even-odd actinides. Two of the even-even actinides, ^{232}Th and ^{238}U, show an interesting effect: the polarization asymmetry increases as the energy of the detected neutron increases. Let us use the null hypothesis that the asymmetry was a constant value as a function of E_n. We can reject this null hypothesis for ^{238}U (p-value: 4.0e-11) and ^{232}Th (p-value: 1.8e-12). In the case of ^{240}Pu, the polarization asymmetries increase until the 6 MeV bin where they drop to 0. However, the highest energy bins have large uncertainties. The null hypothesis of a constant asymmetry as a function of

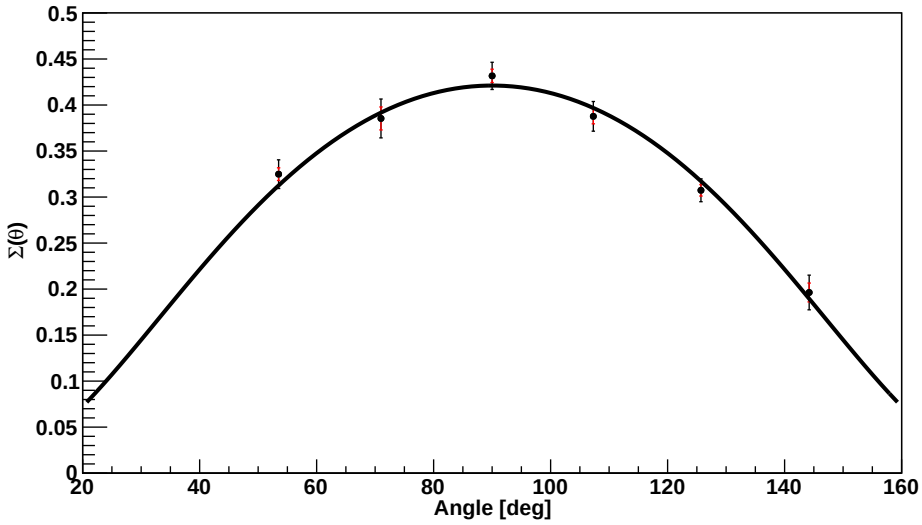

FIGURE 7.3: The polarization asymmetry as a function of θ. The data shown are from photofission of ^{238}U at 5.8 MeV. The black error bars show the statistical uncertainties and the red error bars show the systematic uncertainties. The best fit parameters are $b = 0.433 \pm 0.011 \pm 0.006$ and $c = -0.012 \pm .017 \pm 0.009$, where the first uncertainties are statistical and the second are systematic. This figure is identical to Figure 5.20.

neutron energy is again rejected (p-value: 1.0e-5).

This correlation between Σ and E_n is physically intuitive. Recall that the neutrons are assumed to be emitted with no preferred direction in the rest frame of the fragment. The neutrons which happen to be emitted along the direction of motion of the fragment will gain more energy when they are boosted into the lab frame, while the neutrons emitted perpendicular to the fragments will gain less energy when boosted into the lab frame. The even-even fission fragment polarization asymmetries are expected to be large, as discussed in Section 3.2. Therefore, the higher-energy prompt neutrons (which preferentially travel along the fragment direction) will have correspondingly larger polarization asymmetries.

Finally, the dependence of Σ on θ is shown in Figure 7.3 for the ^{238}U target at a beam energy of 5.8 MeV. To create this plot, the yields were integrated over the

detected neutron energies. This figure is identical to Figure 5.20. These data are presented in tabular form in Appendix C for all targets, beam energies, and scattering angles. These data were fit using Equation 5.5 to calculate the anisotropic dipole angular distribution coefficient b and quadrupole angular distribution coefficient c. This plot is one example of the fits performed to the data. Every angular distribution for every target at every γ-ray beam energy studied was fit to Equation 5.5 to calculate the angular distribution coefficients b and c.

The appropriateness of the fits was determined using χ^2 tests. Let us assume the null hypothesis that Equation 5.5 is the true form of the angular distribution. The χ^2 test statistic was calculated using the value of the data point, the value of the fit, and the statistical and systematic errors added in quadrature. It was possible in this case to combine the statistical and systematic uncertainties because the systematic errors were not correlated for the different angles. One fit was performed for each beam energy and target combination. Because many fits are performed, it is expected that some of the fits will have abnormally high χ^2 values leading to a false rejection of the null hypothesis. In total, 86 fits were performed, and of those, 81 could not reject the null hypothesis and 5 did reject the null hypothesis at a confidence level of 0.05. There is no pattern of the rejections of the null hypothesis. We would expect $86 \times 0.05 \approx 4.3$ to reject the null hypothesis at this confidence level, so we cannot reject the null hypothesis that the true form of the angular distribution is as given in Equation 5.5. The average χ^2 per degree of freedom for the fits was 1.15, which indicates good agreement between the fitted distribution and the data. The resulting values of b and c along with the χ^2 values are reported in Appendix D.

7.3.2 Corrected Angular Distribution Coefficients

The values of b and c extracted from the fits were then corrected for finite-size effects and the contributions from contaminant isotopes in the target as discussed

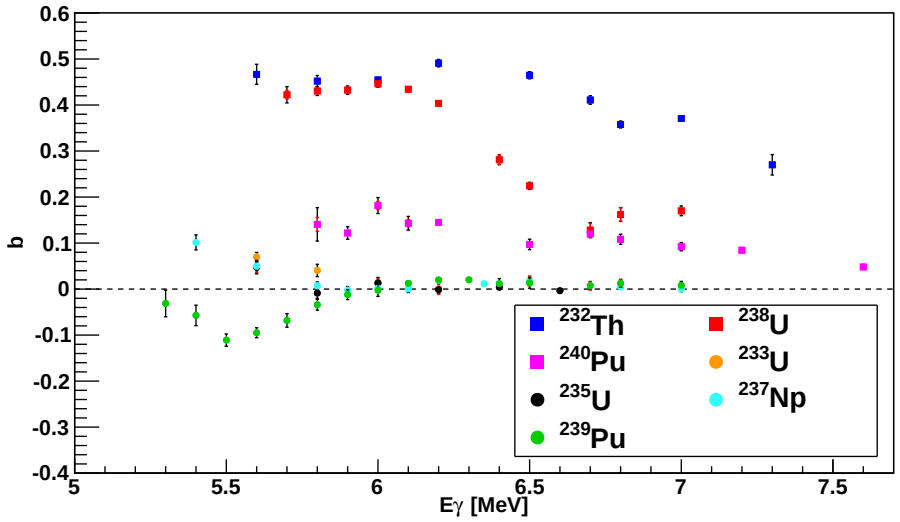

FIGURE 7.4: The values for b are shown as a function of the beam energy. Yields were integrated over all neutron energies above 1.5 MeV. The black error bars show the statistical uncertainties and the red error bars show the systematic uncertainties. Uncertainties not shown are smaller than the size of the data points.

in Section 5.9.3 and Section 5.9.4, respectively. A 5% systematic uncertainty was assumed for the mass of the target in the correction for the contaminant isotopes in each target. For the extrapolated points as discussed in Section 5.9.4, this systematic uncertainty was increased to 10%. The angular distribution coefficients and their uncertainties are presented in tabular form in Appendix D. Figure 7.4 shows the extracted and corrected value of b as a function of E_γ. This plot largely agrees with Figure 7.1 in that the b values are largest for the even-even actinides and smaller for the even-odd actinides.

Of the even-even actinides, ^{232}Th shows the largest values of b, and the b values do not begin to decrease until approximately 6.5 MeV. ^{238}U has similarly large b values at low beam energies, but they begin to decrease at a lower energy of approximately 6.2 MeV. Recall from Section 2.4.1 that the difference in the $(1, 0)$ and $(1, 1)$ barrier heights leads to a large value of b. The point where the b value starts to decrease

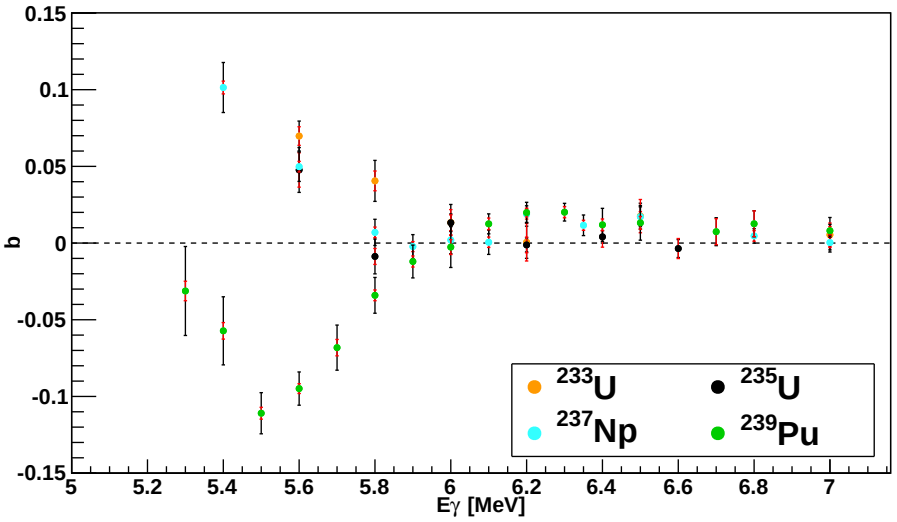

FIGURE 7.5: The values for b are shown as a function of the beam energy for the even-odd actinides only. Yields were integrated over all neutron energies above 1.5 MeV. The black error bars show the statistical uncertainties and the red error bars show the systematic uncertainties. Uncertainties not shown are smaller than the size of the data points. This is the same as Figure 7.4 but the range of the vertical axis is reduced.

is where the $(1,1)$ channel begins to influence the angular distribution, which in the barrier model is approximately the barrier height for this channel. Therefore, we can interpret this as indicating that ^{232}Th has a higher outer barrier height for the $(1,1)$ channel than ^{238}U. For ^{240}Pu, b is not as large as in ^{232}Th or ^{238}U. Therefore, from this we can conclude that the $(1,1)$ channel has an even lower barrier height in ^{240}Pu than in ^{238}U. Also, note that all of the b values remain significantly larger than 0 through the highest energies that we have studied.

The b values are much smaller for the even-odd actinides. Figure 7.5 shows the values for b with a narrower range on the vertical axis to make the smaller b values more visible. As previously found in [48], there is interesting structure in the b value for ^{239}Pu. At the lowest beam energy studied (5.3 MeV) the sign of the b value cannot be conclusively determined. However, the value for b is negative at beam energies around 5.5 MeV, and as the beam energy increases the b value becomes more positive.

Between 6.1 and 6.5 MeV, the value for b is significantly greater than 0 based on a χ^2 test; we can reject the null hypothesis that $b = 0$ at a critical value of 0.05 (p-value: 0.016). At 6.7 MeV and above, the value for b decreases and is consistent with 0 (p-value: 0.400).

The other three even-odd actinides show a different behavior than ^{239}Pu. Below 6.0 MeV, ^{233}U, ^{235}U, and ^{237}Np all have values of b larger than 0. These results conflict with the isotropic fragment angular distribution measurements on ^{233}U and ^{235}U reported in [21], [32], [52], and [55]. Our measurement is more precise and sensitive to small values of b, so it is possible that we are within the uncertainties listed for those measurements. However, we cannot directly compare these experiments to ours because the other works did not use quasi-monoenergetic beams. Above 6.0 MeV, the values of b for ^{233}U and ^{235}U are not statistically different from 0; we cannot reject a null hypothesis that these isotopes have a b of 0 (p-value: 0.330). Reference [28] measured positive values of b for the fragments from photofission of ^{237}Np, so our measurement may be within the uncertainties for that result. The values of b for ^{237}Np are small but statistically larger than 0 above 6.0 MeV; we can reject a null hypothesis that $b = 0$ (p-value: 0.039). The values of b for ^{237}Np also agree with the sign of the previously measured value in [28].

The values of the c coefficients are shown in Figure 7.6. Overall, values close to 0 are seen for all of the isotopes studied. Only one of the isotopes, ^{240}Pu, has a c value statistically different from 0; we can reject a null hypothesis that $c = 0$ for ^{240}Pu (p-value: 0.007). The other six isotopes have values of c consistent with 0. Based on the previous measurements of fragment angular distributions (Section 3.2), we would expect ^{240}Pu to have the largest values of c, while the other actinides should have values of c close to 0.

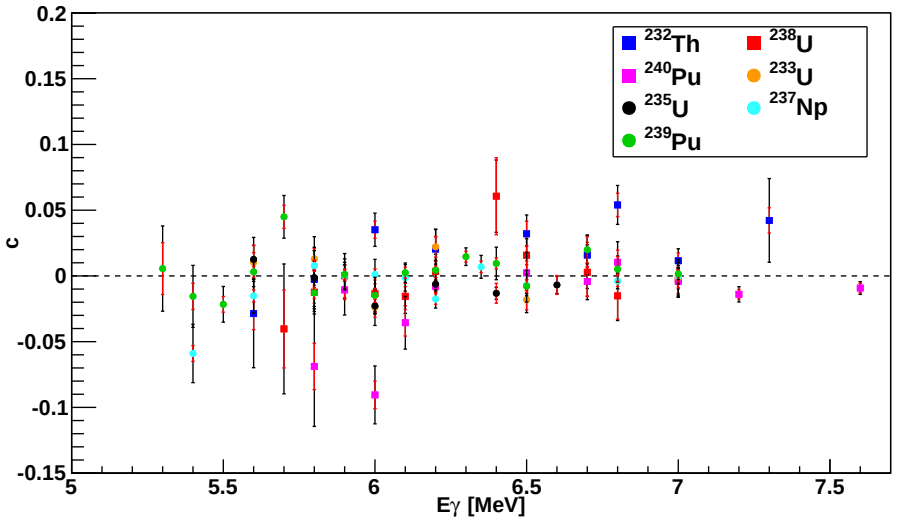

FIGURE 7.6: The values for c are shown as a function of the beam energy. Yields were integrated over all neutron energies above 1.5 MeV. The black error bars show the statistical uncertainties and the red error bars show the systematic uncertainties. Uncertainties not shown are smaller than the size of the data points.

7.4 Comparison with the Fission Calculation

7.4.1 Predictions for ^{238}U and ^{240}Pu

The calculation described in Chapter 6 was used to predict the prompt neutron polarization asymmetries and angular distribution coefficients for photofission of ^{238}U and ^{240}Pu. Recall that previously measured fragment angular distributions were used as experimental inputs into the calculation, and that these angular distributions were experimentally measured using bremsstrahlung beams and then an analysis procedure was performed to unfold the continuous energy spectrum of the bremsstrahlung beam from the measured results. While this procedure makes these fragment angular distributions suitable for comparison with quasi-monoenergetic beams, such as those used in our experiments, it may introduce significant uncertainties in the resulting fragment angular distribution coefficients. The fragment angular distribution coefficients were taken from a hand-drawn graph in [41], which could also be a source

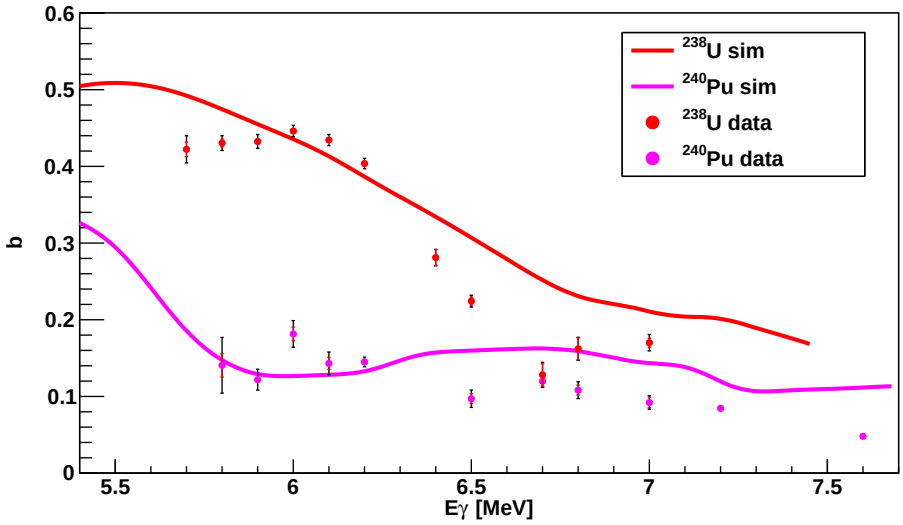

FIGURE 7.7: The measured b values for ^{238}U and ^{240}Pu as a function of beam energy are compared to the results of the calculation. The black error bars show the statistical uncertainties and the red error bars show the systematic uncertainties. Uncertainties not shown are smaller than the size of the data points.

of potential errors. In addition, recall that the model we have used, `FREYA`, was designed for neutron-induced fission and spontaneous fission, but not specifically for photofission. Based on all of these reasons, we would not expect our calculation to be in perfect agreement with the experimental results. Rather, we hope to reproduce the trends present in the experimental results along with the relative scale of the polarization asymmetries and angular distribution coefficients.

Figure 7.7 shows the b values from the calculation compared to the experimental results as a function of beam energy. Overall, relatively good agreement is found. The calculation reproduces both the trend and the scale of the measured b values. It does not perfectly reproduce the experimental data, but that is somewhat expected based on the above arguments.

Figure 7.8 shows the c values of the calculation compared to the experimental results. The calculation is in good agreement with the experimental measurements, as they both have c values close to 0 at high beam energies.

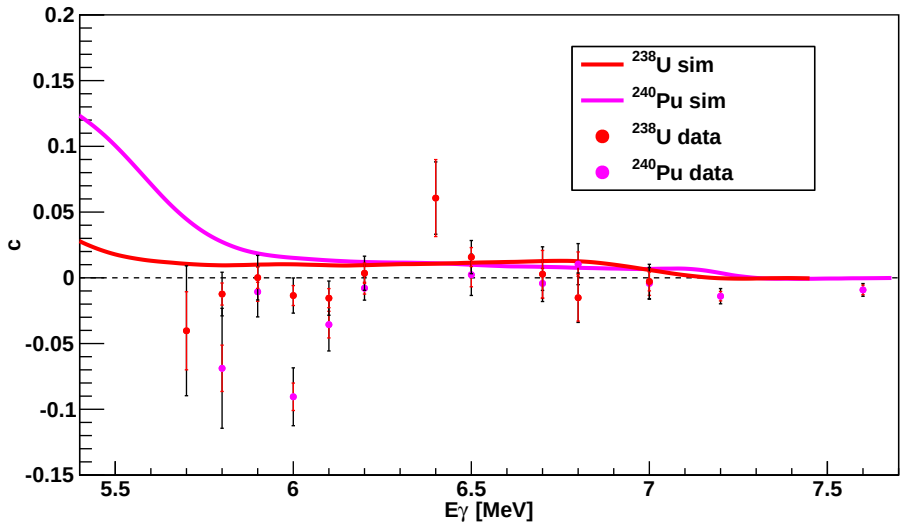

FIGURE 7.8: The measured c values for ^{238}U and ^{240}Pu as a function of beam energy are compared to the results of the calculation. The black error bars show the statistical uncertainties and the red error bars show the systematic uncertainties. Uncertainties not shown are smaller than the size of the data points.

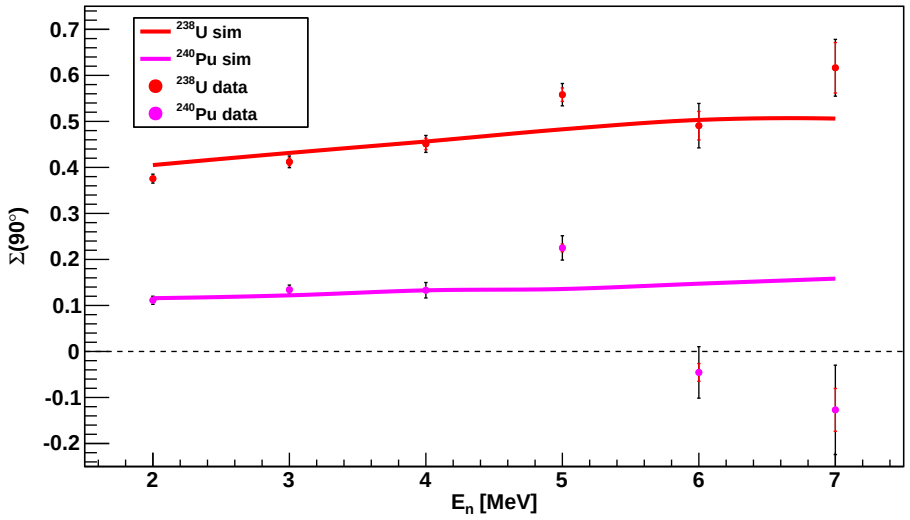

FIGURE 7.9: The polarization asymmetries at 90° are shown compared to the results of a calculation for ^{238}U and ^{240}Pu.

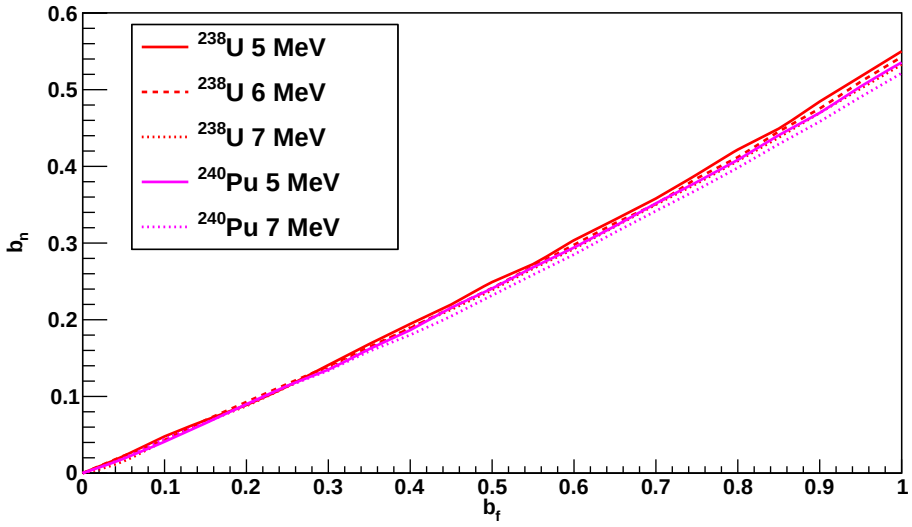

FIGURE 7.10: The value of b for the prompt neutrons (b_n) for a given b of the fragments (b_f) is shown for the two different isotopes at different excitation energies.

Figure 7.9 shows the predictions of the polarization asymmetry compared to the experimental results at 90°. The calculation reproduces the trend that $\Sigma(90°)$ increases slightly with increasing neutron energy, and is in agreement with the overall scale of the experimental measurements.

7.4.2 Sensitivity of the Calculation to the Target and Excitation Energy

In addition to investigating the agreement between the calculation and the data for ^{238}U and ^{240}Pu, we also investigated the sensitivity of the calculation to the different excitation energies that were simulated. Figure 7.10 shows a comparison between the five different calculated data sets: ^{240}Pu at 5 and 7 MeV and ^{238}U at 5, 6, and 7 MeV. The value of the neutron coefficient b_n was calculated as a function of the fragment angular distribution coefficient b_f. It is clear from this comparison that the prompt neutron angular distribution is not very sensitive to the change in target between ^{238}U and ^{240}Pu or the differences in excitation energies in the different calculations.

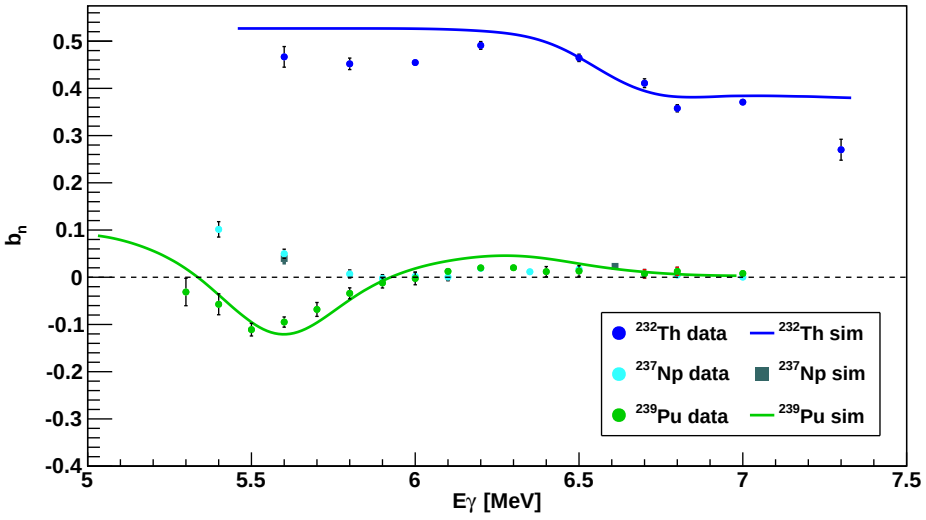

FIGURE 7.11: Calculations of neutron angular distribution b coefficients for ^{232}Th, ^{239}Pu, and ^{237}Np are shown as a function of beam energy.

The best fit quadratic is:

$$b_n = 0.000 + (0.422 \pm 0.003)b_f + (0.113 \pm 0.002)b_f^2 \tag{7.4}$$

7.4.3 Extension of the Calculation to ^{232}Th, ^{239}Pu, and ^{237}Np

Figure 7.11 shows a comparison between predicted neutron b values and measured neutron b values for ^{232}Th, ^{237}Np, and ^{239}Pu. Equation 7.4 was used to predict the neutron b value given a fragment b value. The fragment b values were taken from [41] for ^{232}Th, [28] for ^{237}Np, and [48] for ^{239}Pu. Very good agreement is found for ^{239}Pu and ^{237}Np. The calculation predicts b values for ^{232}Th that are too high at low beam energies. The disagreement may occur because Equation 7.4 is inaccurate for modeling ^{232}Th or it could be due to errors in the fragment angular distribution.

7.5 ^{239}Pu Resonance

Our results were also used to investigate a potential photofission resonance in ^{239}Pu. A previous photofission measurement which claimed the existence of this resonance [48] was described in Section 3.6. Reference [48] bases their claim on the fact that the sign of the fragment b value changes twice as a function of energy, which cannot be explained by the current theory of photofission angular distributions. If the fragment b value changes sign twice, then the prompt neutron value of b must also change sign twice. Our results for the neutron b value are shown in Figure 7.11 compared to the calculation discussed in Section 7.4.3. Our results show a positive b value at 6.2 MeV and a negative b value at 5.6 MeV, but we cannot prove that the sign changes again below 5.3 MeV as the previous fragment measurement would suggest. Therefore, we cannot prove or disprove that the sign of b does change twice and cannot prove or disprove the existence of the resonance on the basis of our present data.

If there were a resonance in ^{239}Pu, we would expect the cross section for photofission to increase in the region of the resonance. Unfortunately, we do not measure the photofission cross section alone, but rather the cross section σ multiplied by the average prompt neutron multiplicity $\overline{\nu}$. However, if $\overline{\nu}$ is either constant or smooth over the region of the photofission resonance, then any resonance-like behavior in $\sigma\overline{\nu}$ could be attributed to a resonance in σ. The only measurement of $\overline{\nu}$ is given in [102] and it used beam energies above 7 MeV, which is well above the energy of the previously measured resonance (5.6 MeV). No resonant structure was found in $\overline{\nu}$ above 7 MeV in [102]. To investigate our neutron yields for the existence of the previously measured resonance at 5.6 MeV, we must assume that there is no resonant-like behavior in $\overline{\nu}$ around 5.6 MeV.

Figure 7.12 shows the relative prompt neutron yield as a function of beam energy. A small shoulder can be seen at a beam energy of 5.6 MeV. This corresponds to

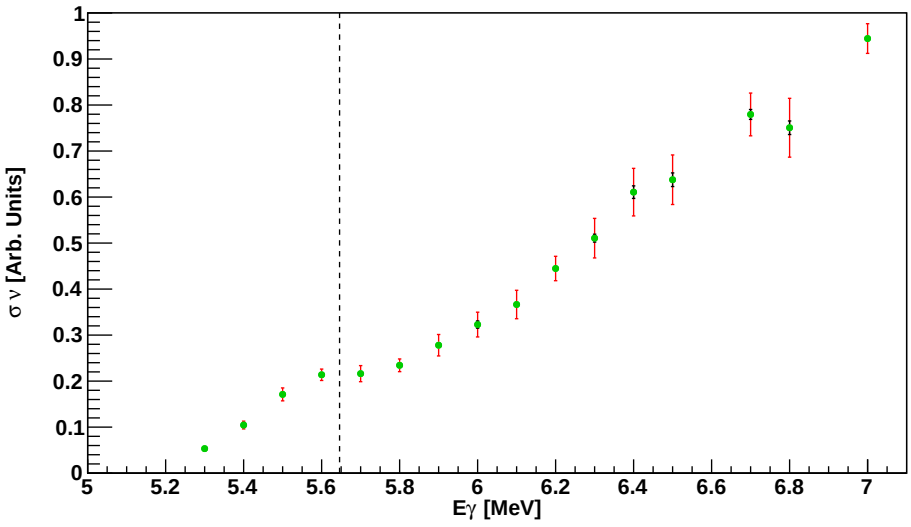

FIGURE 7.12: The relative prompt neutron yield from ^{239}Pu is shown as a function of beam energy. The black error bars show the statistical uncertainties and the red error bars show the systematic uncertainties. Uncertainties not shown are smaller than the size of the data points. The vertical dashed line indicates the (γ,n) threshold for ^{239}Pu which is 5.65 MeV.

the approximate location of the resonance as measured in [48], and would seem to establish the existence of the photofission resonance. However, it is possible that this peak instead is a Wigner cusp [103] and not a resonance.

A Wigner cusp is a feature in a cross section, here the (γ,f) reaction cross section, that occurs near the threshold of another reaction, which in this case is the (γ,n) reaction with a threshold of 5.6 MeV in ^{239}Pu. The cross section just above the threshold of the newly opened reaction - (γ,n) - may be large, and due to unitarity, the cross section of the other open reactions - including (γ,f) - may decrease. Wigner expects the cross section of the already open reactions to follow the form [103]:

$$\sigma(E) = c_1 + c_2|E - \epsilon_n|^{1/2} \tag{7.5}$$

where c_1 and c_2 are parameters and ϵ_n is the threshold of the recently opened reaction. We did not measure enough data points near the (γ,n) threshold to reasonably model

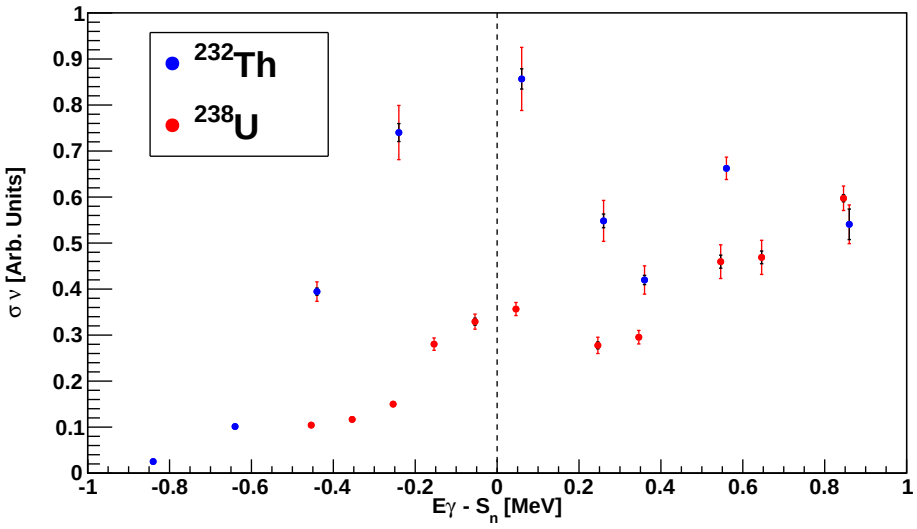

FIGURE 7.13: The relative prompt neutron yields from ^{232}Th and ^{238}U are shown as a function of the beam energy minus their neutron separation energy. The black error bars show the statistical uncertainties and the red error bars show the systematic uncertainties. Uncertainties not shown are smaller than the size of the data points. The vertical dashed line indicates the (γ,n) threshold. ^{232}Th and ^{238}U have been scaled vertically by different amounts.

c_1 and c_2, but it is possible that the small increase seen at 5.6 MeV actually occurs because the next points from 5.7 to 5.9 MeV are abnormally low due to the presence of this Wigner cusp.

For comparison, Figure 7.13 shows the relative prompt neutron yield as a function of beam energy for ^{232}Th and ^{238}U. In both of these cases, a cusp effect is observed just above the location of the (γ,n) threshold (located at 6.4 MeV in ^{232}Th and 6.2 MeV in ^{238}U). These cusp effects look similar to the one seen in ^{239}Pu.

At this time, we cannot make a definitive statement as to the existence of the photofission resonance in ^{239}Pu. We did not observe two sign changes in the angular distribution coefficient b, though we cannot rule out this possibility. The cross section behavior could be attributed to a Wigner cusp instead of a resonance. This is supported by the presence of Wigner cusps in ^{232}Th and ^{238}U. Therefore, the existence

of this resonance is highly uncertain.

7.6 Enrichment Determination

7.6.1 Prompt Neutron Polarization Ratio

Our results provide the framework for a potential new technique to determine the enrichment of special nuclear material. The prompt neutron polarization ratio R will be used instead of Σ or the b coefficient in this analysis to better illustrate the significant differences between the prompt neutron polarization asymmetries of the even-even and even-odd actinides. R is defined as the ratio of prompt neutron yield in the plane of beam polarization to the prompt neutron yield perpendicular to the plane of beam polarization:

$$R(E_\gamma, \theta, E_n) = \frac{\sum_{\phi=0,180^\circ} \frac{Y^L(E_\gamma,\theta,E_n,\phi)}{Y^C(E_{\gamma circ},\theta,E_n,\phi)}}{\sum_{\phi=90,270^\circ} \frac{Y^L(E_\gamma,\theta,E_n,\phi)}{Y^C(E_{\gamma circ},\theta,E_n,\phi)}} \tag{7.6}$$

Integrating the yields over E_n and using the a, b, and c coefficients gives:

$$R(E_\gamma, \theta) = 1 + \frac{2b}{a}\sin^2(\theta) + \frac{2c}{a}\sin^2(2\theta) \tag{7.7}$$

The c coefficient is sufficiently small that it can be neglected (Figure 7.6) and the normalization $a = 1 - b$ can be used, yielding:

$$R(E_\gamma, \theta) = 1 + \frac{2b}{1-b}\sin^2(\theta) \tag{7.8}$$

The advantage of using R over b or Σ is that it more easily demonstrates the large polarization asymmetries seen in the even-even actinides. R is also more physically intuitive, since it represents a direct ratio of yields in different detectors. $R(90^\circ)$ in particular is calculated since it is larger than R at other angles. The values of $R(90^\circ)$ are shown in Figure 7.14. The even-odd actinides have values of $R(90^\circ)$ close to 1, while the even-even actinides have values of $R(90^\circ)$ as large as 3.

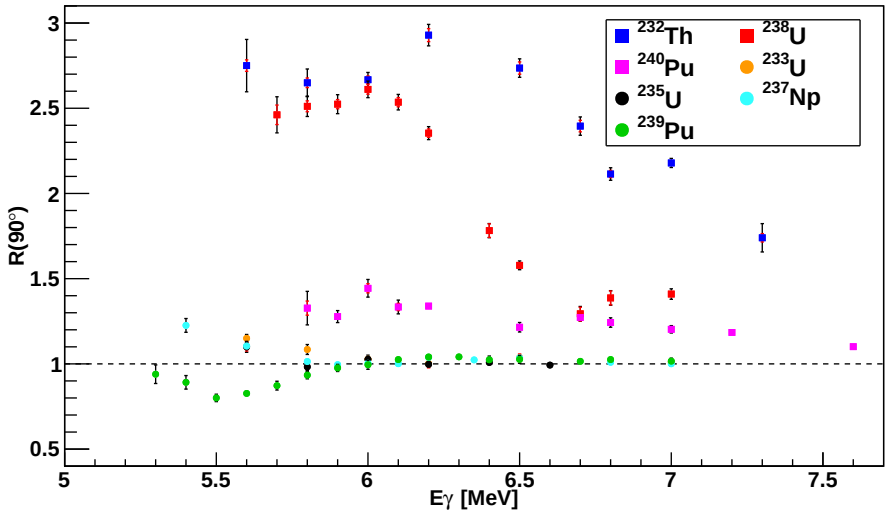

FIGURE 7.14: The values of $R(90°)$ are shown as a function of the beam energy. Yields were integrated over all neutron energies above 1.5 MeV. The black error bars show the statistical uncertainties and the red error bars show the systematic uncertainties. Uncertainties not shown are smaller than the size of the data points. The values of $R(90°)$ were calculated from Equation 7.8 and Figure 7.4.

7.6.2 Enrichment Measurement Technique

One potential application of our measurements is a novel way to measure the enrichment of special nuclear materials. Figure 7.14 shows $R(90°)$ for different isotopes at different beam energies. As previously mentioned, the even-even and even-odd actinides exhibit strikingly different behavior: the even-even actinides have large values of $R(90°)$ at low beam energies, while the even-odd actinides have small values of $R(90°)$ at low beam energies. Therefore, if given a target of unknown enrichment, the enrichment may be deduced by measuring $R(90°)$.

In reality, this technique also depends on the specific actinides involved, because the values of $R(90°)$ for ^{232}Th, ^{238}U, and ^{240}Pu are different. Also, it depends on the photofission cross section and average prompt neutron multiplicity for the actinides involved, since that will determine the relative proportion of prompt neutrons from the different contaminants in the target. In addition, the selected beam energy

will affect the technique, because $R(90^\circ)$ and the cross sections are functions of the beam energy. As the beam energy increases, the photofission cross sections generally increase, but the even-even and even-odd values of $R(90^\circ)$ become more similar. Equation 5.8 was used with our measured values of $\sigma\nu$ and $R(90^\circ)$ (in place of b in Equation 5.8) to predict $R(90^\circ)$ as a function of enrichment of the target. The beam energy found to minimize the uncertainty in determining the enrichment depended on the target composition, but was typically around 6.1 MeV. In all cases, a 5% systematic uncertainty in the $\sigma\nu$ products was assumed to account for the uncertainty in the mass thickness of each target.

The measured values of $R(90^\circ)$ and $\sigma\nu$ for the seven nuclei studied were used to calculate $R(90^\circ)$ for mixed targets of ^{235}U/^{238}U, ^{239}Pu/^{240}Pu, and ^{233}U/^{232}Th. These target combinations were chosen because, for each of these even-odd targets, the enrichment is commonly measured relative to the specified even-even target. For example, a 90% enriched target of ^{235}U generally means that the remaining 10% is ^{238}U.

Figure 7.15 shows the expected $R(90^\circ)$ as a function of enrichment of a ^{235}U/^{238}U target. Based on this figure, it is expected that a measurement of $R(90^\circ)$ can easily distinguish weapons-grade uranium from reactor-grade or depleted uranium. Figure 7.16 is the same plot for a target composed of ^{239}Pu and ^{240}Pu. Here it appears to be much more difficult to distinguish reactor-grade from weapons-grade plutonium.

7.6.3 ^{233}U Enrichment Measurement

The enrichment of the ^{233}U target has not been accurately determined, as discussed in Section 4.4. Therefore, we attempted to use our measurements to determine the enrichment of our ^{233}U sample. We assumed that the value of b for ^{233}U was similar to the value of b for ^{235}U, which is approximately 0 for beam energies above 6.0 MeV.

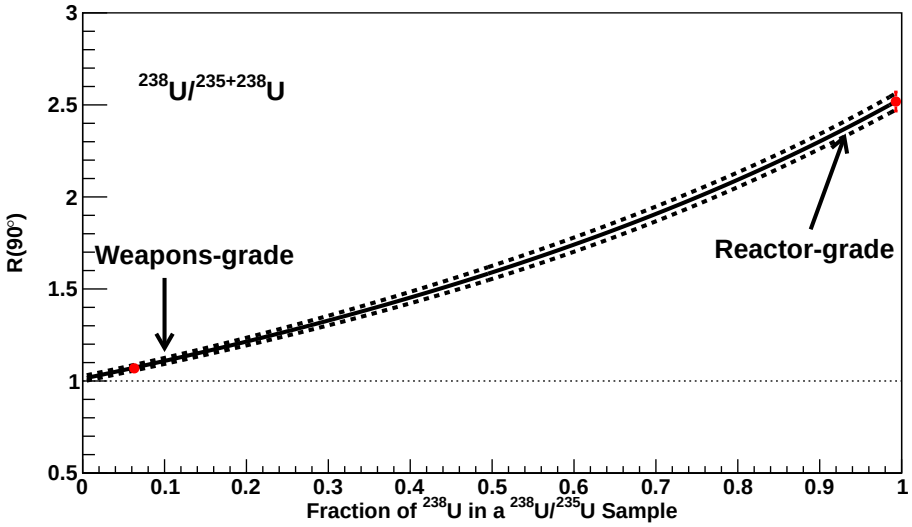

FIGURE 7.15: The expected $R(90°)$ versus enrichment of a ^{235}U/^{238}U target is shown. The dotted lines indicate our current combined statistical and systematic uncertainties, and the red points indicate our current measurements.

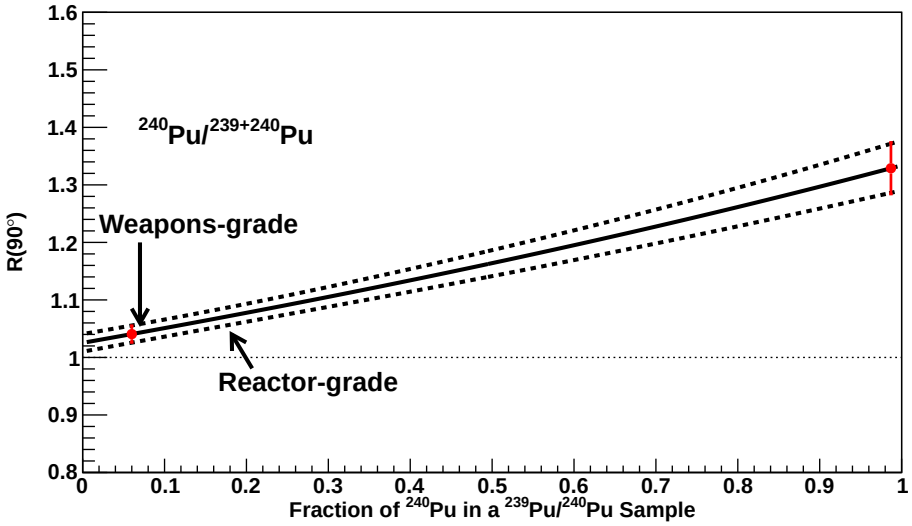

FIGURE 7.16: The expected $R(90°)$ versus enrichment of a ^{239}Pu/^{240}Pu target is shown. The dotted lines indicate our current combined statistical and systematic uncertainties, and the red points indicate our current measurements.

The expected enrichment of the target was varied and the χ^2 values were calculated between the extracted b values and 0 for three energy points above 6 MeV: 6.2, 6.5, and 7.0 MeV. The smallest χ^2 was found at an enrichment of 94.6% with a 1σ confidence interval of $[91.6\%, 97.4\%]$. This is reasonably close to the estimate of 97.5% provided by a scientist at Pacific Northwest National Laboratory. Therefore, an enrichment of the quoted value of 97.5% was used to generate the figures and data appendices in this dissertation.

The systematic uncertainties of the ^{233}U results were increased to account for the uncertainty in the enrichment of the target. The b and c coefficients were calculated using enrichments of 97.5% and 94.6%, and the difference between the coefficients for these two enrichments was taken as an additional systematic uncertainty. This additional systematic uncertainty was generally smaller than the other systematic uncertainties. The systematic uncertainties were added in quadrature to give the total systematic uncertainty, as presented in the figures and appendices in this dissertation.

Figure 7.17 shows the expected $R(90^\circ)$ as a function of enrichment of a ^{233}U/^{232}Th target. This demonstrates that $R(90^\circ)$ can be used to measure the enrichment of ^{233}U targets that were generated by neutron irradiation of ^{232}Th.

7.7 Concluding Remarks

In summary, we used the HIγS facility to perform the first ever measurements of prompt neutron polarization asymmetries in photofission. 100% polarized, quasi-monoenergetic γ-ray beams with energies between 5.3 and 7.6 MeV were used to induce fission of each of the seven actinide targets. Prompt neutron polarization asymmetries from photofission of ^{232}Th, ^{233}U, ^{235}U, ^{238}U, ^{237}Np, ^{239}Pu, and ^{240}Pu were measured at various scattering angles using 12-18 liquid scintillator neutron detectors. Systematic uncertainties were kept minimal by using circularly polar-

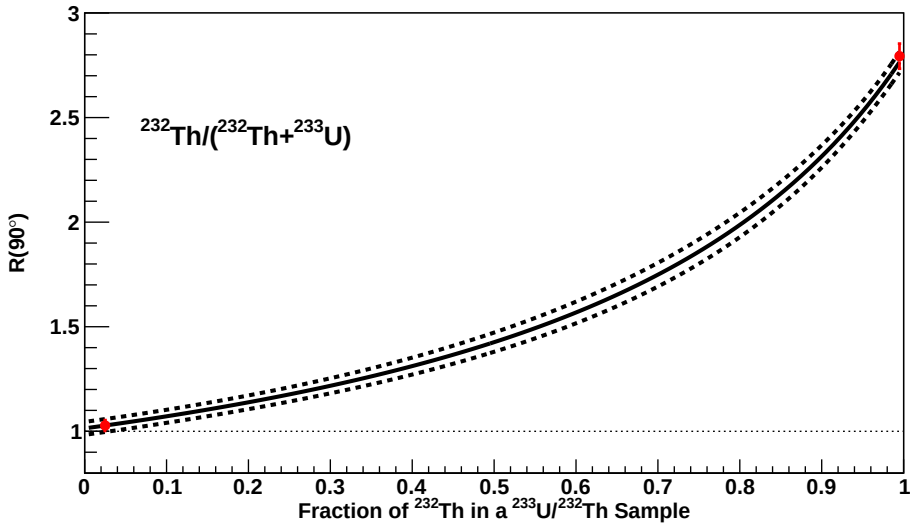

FIGURE 7.17: The expected $R(90^\circ)$ versus enrichment of a $^{233}U/^{232}Th$ target is shown. The dotted lines indicate our current combined statistical and systematic uncertainties, and the red points indicate our current measurements.

ized γ-ray beams to correct for differences in efficiency between the detectors. The quasi-monoenergetic nature of the γ-ray beams used in our experiments adds additional information to our understanding of photofission, since the majority of previous unpolarized angular distribution measurements were performed using unfolded bremsstrahlung beams. In addition, our polarization asymmetry measurements were able to achieve a much higher level of precision than previous angular distribution measurements.

Our polarization asymmetry measurements indicate a significant difference between the prompt neutron angular distributions from photofission of even-even actinides and even-odd actinides. The even-odd actinides show prompt neutron polarization asymmetries generally close to zero, while the even-even actinides have large polarization asymmetries. Our measurements are in good agreement with predictions of prompt neutron polarization asymmetries, which are based on previously measured fragment angular distributions coupled with a photofission calculation which simu-

lates prompt neutron emission. This agreement suggests that we have developed a model capable of predicting prompt neutron angular distributions and polarization asymmetries, given previously measured fragment angular distributions. This model also may make it possible to predict fragment angular distribution coefficients given prompt neutron angular distribution coefficients. In addition to developing this model, we have investigated a previously reported photofission resonance in ^{239}Pu and cast its existence into question. Finally, our work may have a significant impact in the field of applied nuclear physics, as we have discovered a new technique to determine the enrichment of special nuclear material. This technique may have applications in active interrogation of transportation containers for special nuclear material, or it may be used to quickly and precisely measure the enrichment of a given sample of special nuclear material in a laboratory setting.

Future measurements related to our work fall into two categories: basic nuclear physics and applied nuclear physics. In the context of basic science, new measurements of other actinides could be used to further test our predictive model of prompt neutron angular distributions. High precision measurements of fission fragment polarization asymmetries may also help in this regard. In addition, high precision measurements of fragment polarization asymmetries from photofission of an ultrapure ^{239}Pu target could more definitively prove or disprove of the existence of the photofission resonance and refine our understanding of the origin of angular distributions in photofission. If these measurements were to be applied in the field, extensive testing and simulation would have to be performed to model the effects of extended targets and shielding. If this technique were to be used in a more controlled environment to measure the enrichment of special nuclear material, tests with samples of unknown enrichments would be desirable to ensure the efficiency and accuracy of this technique.

Appendix A

Full Expansion of the Photonuclear Interaction Hamiltonian

In this appendix, the full expansion of the photonuclear interaction Hamiltonian into electric and magnetic multipoles will be derived. This appendix is intended to serve as a complement to the simplified derivation of the three dominant interaction modes (E1, M1, and E2) given in Section 2.2. Sections 1A-8 and 3C-2 of [104] were used in this derivation.

As in Section 2.2, we will start with the photonuclear interaction Hamiltonian:

$$H_{int} = -\frac{1}{c}\int \vec{j}\cdot\vec{A}(\vec{r})\mathrm{d}\vec{r} \tag{A.1}$$

where $\vec{j}$ is the total nuclear current, $\vec{r}$ is the integration variable over the nuclear coordinates, and $\vec{A}$ is the electromagnetic vector potential for the photon in the radiation gauge, $\nabla\cdot\vec{A}=0$ [104]. As before, Fermi's Golden Rule will be used to calculate transition rates, and final state spin densities will be neglected, so only the matrix element of H_{int} is needed. The vector field $\vec{A}(\vec{r})$ can be expanded in the form:

$$\vec{A}(\vec{r}) = \sum_{\kappa,\lambda\mu} A^{\dagger}_{\kappa,\lambda\mu}(r)\vec{\Phi}_{\kappa,\lambda\mu}(\hat{r}) \tag{A.2}$$

where $\vec{\Phi}$ is a vector spherical harmonic of rank λ and component μ which was generated by coupling the tensor Y_κ with the first rank tensor $\vec{e}$. The tensor $\vec{e}$ is given by:

$$\vec{e}_{\nu=\pm1} = \mp\frac{1}{\sqrt{2}}(\vec{e}_x \pm i\vec{e}_y)$$

$$\vec{e}_0 = \vec{e}_z$$

Using this expansion, Equation A.1 becomes:

$$H_{int} = -\frac{1}{c}\sum_{\kappa\lambda\mu}\int \vec{j}(\vec{r})\cdot\vec{\Phi}_{\kappa,\lambda\mu}(\hat{r})A^{\dagger}_{\kappa,\lambda\mu}(r)\mathrm{d}\vec{r} \tag{A.3}$$

The terms with $\kappa = \lambda \pm 1$ have parity $(-1)^\lambda$ and are called electric multipole terms. The terms with $\kappa = \lambda$ have parity $(-1)^{\lambda+1}$ and are called magnetic multipole terms. Separating these terms and inserting the appropriate $A_{\kappa,\lambda\mu}$ yields:

$$M(E\lambda,\mu) = \frac{-i(2\lambda+1)!!}{ck^{\lambda+1}(\lambda+1)}\int \vec{j}(\vec{r})\cdot\nabla\times(\vec{r}\times\nabla)(j_\lambda(kr)Y_{\lambda\mu}(\hat{r}))\mathrm{d}\vec{r} \tag{A.4}$$

$$M(M\lambda,\mu) = \frac{-(2\lambda+1)!!}{ck^{\lambda}(\lambda+1)}\int \vec{j}(\vec{r})\cdot(\vec{r}\times\nabla)(j_\lambda(kr)Y_{\lambda\mu}(\hat{r}))\mathrm{d}\vec{r} \tag{A.5}$$

where $M(E/M\lambda,\mu)$ is the matrix element for electric/magnetic transitions of multipolarity λ and projection μ, k is the photon momentum, j_λ is a Bessel function, and $Y_{\lambda\mu}$ is a spherical harmonic.

Let us now simplify the form of $M(E\lambda,\mu)$. The identity:

$$\nabla\times(\vec{r}\times\nabla)j_\lambda(kr)Y_{\lambda\mu}(\vec{r}) = -\nabla(\frac{\partial}{\partial r}(rj_\lambda(kr))Y_{\lambda\mu}(\hat{r})) - q^2\vec{r}j_\lambda(kr)Y_{\lambda\mu} \tag{A.6}$$

can be used to split $M(E\lambda,\mu)$ into two terms:

$$M(E\lambda,\mu) = \frac{i(2\lambda+1)!!}{ck^{\lambda+1}(\lambda+1)}\int \vec{j}(\vec{r})\cdot\nabla(\frac{\partial}{\partial r}(rj_\lambda(kr))Y_{\lambda\mu}(\hat{r}))\mathrm{d}\vec{r}$$

$$+\frac{i(2\lambda+1)!!}{ck^{\lambda+1}(\lambda+1)}\int(\vec{j}(\vec{r})\cdot\vec{r})k^2j_\lambda(kr)Y_{\lambda\mu}\mathrm{d}\vec{r}$$

Integration by parts can be used to simplify the first term, yielding:

$$M(E\lambda,\mu) = -\frac{i(2\lambda+1)!!}{ck^{\lambda+1}(\lambda+1)}\int(\nabla\cdot\vec{j}(\vec{r}))\frac{\partial}{\partial r}(rj_\lambda(kr))Y_{\lambda\mu}(\hat{r})\mathrm{d}\vec{r}$$

$$+\frac{i(2\lambda+1)!!}{ck^{\lambda+1}(\lambda+1)}\int(\vec{j}(\vec{r})\cdot\vec{r})k^2j_\lambda(kr)Y_{\lambda\mu}\mathrm{d}\vec{r}$$

Here the surface term from integration by parts has been neglected. The continuity equation, $\nabla\cdot\vec{j}(\vec{r})+\frac{\partial\rho}{\partial t}=0$ can be used to give:

$$M(E\lambda,\mu) = \frac{i(2\lambda+1)!!}{ck^{\lambda+1}(\lambda+1)}\int(\frac{\partial\rho}{\partial t})\frac{\partial}{\partial r}(rj_\lambda(kr))Y_{\lambda\mu}(\hat{r})\mathrm{d}\vec{r}$$

$$+\frac{i(2\lambda+1)!!}{ck^{\lambda+1}(\lambda+1)}\int(\vec{j}(\vec{r})\cdot\vec{r})k^2j_\lambda(kr)Y_{\lambda\mu}\mathrm{d}\vec{r}$$

The quantity $\frac{\partial\rho}{\partial t}$ is equal to $i[H,\rho]$, where H is the total Hamiltonian. H can be evaluated on the left bra and the right ket, giving

$$\frac{\partial\rho}{\partial t} = ck\rho \tag{A.7}$$

This is a generalization of Siegert's theorem, and greatly simplifies the electric multipole terms. The resulting matrix element is:

$$M(E\lambda,\mu) = \frac{(2\lambda+1)!!}{k^\lambda(\lambda+1)}\left(\int\rho(\vec{r})\frac{\partial}{\partial r}(rj_\lambda(kr))Y_{\lambda\mu}(\hat{r})\mathrm{d}\vec{r}+\frac{i}{c}\int(\vec{j}(\vec{r})\cdot\vec{r})kj_\lambda(kr)Y_{\lambda\mu}\mathrm{d}\vec{r}\right) \tag{A.8}$$

Now we will use the long wavelength approximation ($kr \ll 1$) to approximate the Bessel function:

$$j_\lambda(kr) = \frac{(kr)^\lambda}{(2\lambda+1)!!}\left(1-\frac{(kr)^2}{2(2\lambda+3)}+...\right) \tag{A.9}$$

$$j_\lambda(kr) \approx \frac{(kr)^\lambda}{(2\lambda+1)!!} \tag{A.10}$$

For $M(E\lambda,\mu)$, this yields:

$$M(E\lambda,\mu) = \int\rho(\vec{r})r^\lambda Y_{\lambda\mu}(\hat{r})\mathrm{d}\vec{r}+\frac{i}{c(\lambda+1)}\int(\vec{j}(\vec{r})\cdot\vec{r})kr^\lambda Y_{\lambda\mu}\mathrm{d}\vec{r} \tag{A.11}$$

The second term is order kr larger than the first term, so it is neglected. The resulting electric multipole moment is then:

$$M(E\lambda,\mu) = \int \rho(\vec{r}) r^{\lambda} Y_{\lambda\mu}(\hat{r}) \mathrm{d}\vec{r} \tag{A.12}$$

This agrees with the results presented in Section 2.2 to first and second order.

To simplify $M(M\lambda,\mu)$, only the Bessel approximation needs to be inserted, leading to:

$$M(M\lambda,\mu) = \frac{-1}{c(\lambda+1)} \int \vec{j}(\vec{r}) \cdot (\vec{r} \times \nabla)(r^{\lambda} Y_{\lambda\mu}(\hat{r})) \mathrm{d}\vec{r} \tag{A.13}$$

This agrees with the results presented in Section 2.2 to first order.

Appendix B

Tabulated Prompt Neutron Polarization Asymmetries

Table B.1: Measured prompt neutron polarization asymmetries (Σ) are given for each target, at each beam energy E_γ, at each scattering angle θ, and for each neutron energy bin E_n. The units of E_γ and E_n are MeV, and the units of θ are degrees. Each neutron energy bin is 1 MeV wide, and the central value of each bin is indicated in parenthesis. The statistical and systematic uncertainties are indicated by the subscripts 1 and 2, respectively. Entries with a "-" were unphysical polarization asymmetries and are not shown.

Target	E_γ	θ	$\Sigma(2)$	$\Delta\Sigma_1(2)$	$\Delta\Sigma_2(2)$	$\Sigma(3)$	$\Delta\Sigma_1(3)$	$\Delta\Sigma_2(3)$	$\Sigma(4)$	$\Delta\Sigma_1(4)$	$\Delta\Sigma_2(4)$	$\Sigma(5)$	$\Delta\Sigma_1(5)$	$\Delta\Sigma_2(5)$	$\Sigma(6)$	$\Delta\Sigma_1(6)$	$\Delta\Sigma_2(6)$	$\Sigma(7)$	$\Delta\Sigma_1(7)$	$\Delta\Sigma_2(7)$	$\Sigma(8)$	$\Delta\Sigma_1(8)$	$\Delta\Sigma_2(8)$	$\Sigma(9)$	$\Delta\Sigma_1(9)$	$\Delta\Sigma_2(9)$
^{232}Th	5.60	54	0.25	0.04	0.03	0.20	0.06	0.03	0.40	0.07	0.02	0.69	0.11	0.02	0.36	0.16	0.04	0.54	0.21	0.06	-	-	-	0.29	0.12	0.09
^{232}Th	5.60	71	0.41	0.07	0.03	0.44	0.08	0.01	0.73	0.13	0.01	0.52	0.16	0.04	0.22	0.25	0.07	0.12	0.31	0.08	0.52	2.89	0.16	-	-	-
^{232}Th	5.60	90	0.40	0.04	0.01	0.49	0.04	0.01	0.53	0.06	0.01	0.43	0.09	0.02	0.59	0.14	0.03	0.45	0.14	0.04	0.34	0.31	0.08	-	-	-
^{232}Th	5.60	107	0.26	0.06	0.01	0.45	0.08	0.01	0.59	0.12	0.03	0.36	0.16	0.04	0.42	0.31	0.06	0.14	0.51	0.07	-	-	-	-	-	-
^{232}Th	5.60	126	0.25	0.04	0.01	0.41	0.05	0.01	0.39	0.07	0.02	0.30	0.12	0.03	0.48	0.15	0.03	0.21	0.22	0.06	0.63	0.51	0.06	-	-	-
^{232}Th	5.80	54	0.24	0.02	0.01	0.31	0.03	0.01	0.39	0.04	0.02	0.28	0.06	0.02	0.61	0.08	0.02	0.25	0.13	0.05	0.39	0.27	0.10	0.35	0.45	0.15
^{232}Th	5.80	71	0.29	0.03	0.01	0.37	0.04	0.01	0.52	0.05	0.02	0.62	0.06	0.02	0.40	0.12	0.05	0.56	0.19	0.05	0.37	0.46	0.32	0.14	0.41	0.18
^{232}Th	5.80	90	0.37	0.02	0.01	0.43	0.03	0.01	0.50	0.04	0.01	0.55	0.05	0.02	0.64	0.08	0.02	0.44	0.12	0.04	0.70	0.21	0.07	0.59	0.24	0.08
^{232}Th	5.80	107	0.37	0.03	0.01	0.44	0.04	0.01	0.44	0.05	0.02	0.46	0.08	0.02	0.62	0.14	0.03	0.55	0.26	0.06	0.38	0.26	0.11	-	-	-
^{232}Th	5.80	126	0.30	0.02	0.01	0.42	0.03	0.01	0.28	0.04	0.02	0.54	0.06	0.02	0.63	0.07	0.03	0.53	0.14	0.05	0.76	0.26	0.08	0.36	0.49	0.16
^{232}Th	6.00	54	0.25	0.01	0.01	0.41	0.02	0.01	0.43	0.02	0.01	0.42	0.04	0.02	0.47	0.05	0.02	0.41	0.09	0.05	0.53	0.12	0.07	0.44	0.16	0.11
^{232}Th	6.00	71	0.34	0.02	0.01	0.43	0.02	0.01	0.48	0.03	0.01	0.55	0.04	0.02	0.41	0.06	0.03	0.33	0.11	0.06	0.27	0.18	0.09	0.39	0.30	0.13
^{232}Th	6.00	90	0.38	0.01	0.01	0.44	0.01	0.01	0.54	0.02	0.01	0.52	0.03	0.01	0.52	0.04	0.02	0.58	0.06	0.03	0.63	0.11	0.04	0.02	0.19	0.12
^{232}Th	6.00	107	0.36	0.01	0.01	0.46	0.02	0.01	0.49	0.03	0.01	0.47	0.04	0.02	0.54	0.07	0.03	0.64	0.08	0.04	0.36	0.20	0.09	0.63	0.39	0.20
^{232}Th	6.00	126	0.30	0.01	0.01	0.41	0.01	0.01	0.39	0.02	0.01	0.43	0.03	0.02	0.47	0.05	0.03	0.60	0.07	0.04	0.46	0.13	0.08	0.30	0.27	0.13
^{232}Th	6.00	144	0.22	0.02	0.02	0.26	0.03	0.02	0.36	0.05	0.03	0.30	0.07	0.05	0.50	0.12	0.06	0.51	0.21	0.12	-	-	-	-0.61	5.74	7.28
^{232}Th	6.20	54	0.28	0.02	0.01	0.39	0.02	0.01	0.45	0.03	0.02	0.54	0.04	0.02	0.38	0.07	0.04	0.69	0.11	0.06	-	-	-	-	-	-
^{232}Th	6.20	71	0.38	0.02	0.01	0.46	0.03	0.02	0.57	0.04	0.02	0.42	0.07	0.05	0.74	0.07	0.04	0.77	0.10	0.07	0.90	0.42	0.06	-	-	-
^{232}Th	6.20	90	0.43	0.01	0.01	0.48	0.02	0.01	0.55	0.02	0.01	0.61	0.04	0.02	0.55	0.07	0.03	0.69	0.09	0.05	0.80	0.16	0.07	0.73	0.19	0.10
^{232}Th	6.20	107	0.40	0.02	0.01	0.47	0.02	0.02	0.51	0.03	0.02	0.48	0.05	0.03	0.56	0.08	0.05	0.63	0.10	0.07	0.00	0.35	0.26	-	-	-
^{232}Th	6.20	126	0.33	0.01	0.01	0.42	0.02	0.01	0.41	0.03	0.02	0.57	0.04	0.02	0.37	0.07	0.05	0.69	0.09	0.05	0.68	0.18	0.09	-	-	-
^{232}Th	6.20	144	0.25	0.02	0.02	0.24	0.03	0.02	0.33	0.04	0.03	0.46	0.06	0.04	0.56	0.09	0.06	0.21	0.16	0.13	0.60	0.19	0.37	-0.43	0.95	0.50
^{232}Th	6.50	54	0.25	0.01	0.01	0.40	0.02	0.01	0.44	0.03	0.02	0.48	0.04	0.03	0.36	0.07	0.04	0.56	0.11	0.07	-	-	-	0.29	0.13	0.16
^{232}Th	6.50	71	0.38	0.02	0.01	0.44	0.03	0.02	0.44	0.04	0.03	0.53	0.06	0.04	0.63	0.09	0.05	0.75	0.10	0.07	0.76	0.48	0.13	-	-	-
^{232}Th	6.50	90	0.40	0.01	0.01	0.47	0.02	0.01	0.52	0.02	0.01	0.57	0.04	0.02	0.55	0.06	0.03	0.59	0.08	0.07	0.56	0.30	0.11	0.76	0.24	0.10
^{232}Th	6.50	107	0.36	0.02	0.01	0.47	0.02	0.02	0.45	0.03	0.02	0.47	0.05	0.04	0.64	0.07	0.05	0.86	0.08	0.03	0.16	0.27	0.25	-	-	-
^{232}Th	6.50	126	0.32	0.01	0.01	0.42	0.02	0.01	0.40	0.03	0.02	0.54	0.04	0.02	0.53	0.06	0.04	0.70	0.10	0.04	0.47	0.25	0.12	-	-	-
^{232}Th	6.50	144	0.21	0.02	0.01	0.28	0.03	0.02	0.36	0.04	0.03	0.52	0.06	0.04	0.42	0.10	0.07	0.30	0.14	0.11	0.42	0.26	0.49	0.58	1.26	0.41
^{232}Th	6.70	54	0.23	0.02	0.01	0.33	0.02	0.01	0.33	0.03	0.02	0.51	0.05	0.02	0.26	0.08	0.05	0.49	0.12	0.08	-	-	-	-	-	-
^{232}Th	6.70	71	0.33	0.02	0.01	0.33	0.03	0.02	0.44	0.04	0.03	0.46	0.07	0.04	0.59	0.10	0.09	0.61	0.19	0.14	-0.65	1.10	0.26	-	-	-
^{232}Th	6.70	90	0.33	0.02	0.01	0.43	0.02	0.01	0.50	0.03	0.02	0.45	0.05	0.03	0.44	0.09	0.05	-	-	-	0.49	0.09	0.10	0.87	0.04	0.05
^{232}Th	6.70	107	0.32	0.02	0.01	0.39	0.03	0.02	0.46	0.04	0.02	0.56	0.06	0.03	0.68	0.10	0.04	0.69	0.12	0.07	0.17	0.50	0.25	-	-	-
^{232}Th	6.70	126	0.28	0.02	0.01	0.33	0.02	0.01	0.41	0.03	0.02	0.32	0.05	0.03	0.53	0.07	0.04	0.49	0.12	0.06	-	-	-	-	-	-
^{232}Th	6.70	144	0.18	0.02	0.01	0.19	0.03	0.02	0.33	0.05	0.03	0.41	0.07	0.05	0.23	0.11	0.08	0.25	0.19	0.11	0.40	0.28	0.47	0.40	0.54	0.56
^{232}Th	6.80	54	0.22	0.01	0.01	0.31	0.02	0.01	0.32	0.03	0.02	0.39	0.04	0.02	0.40	0.06	0.03	0.41	0.08	0.05	0.53	0.17	0.07	-0.09	0.25	0.17
^{232}Th	6.80	71	0.26	0.02	0.01	0.33	0.02	0.01	0.42	0.03	0.02	0.42	0.05	0.02	0.45	0.07	0.03	0.48	0.10	0.05	0.41	0.22	0.08	0.25	0.29	0.16

Continued on Next Page...

Table B.1 – Continued

Target	E_γ	θ	$\Sigma(2)$	$\Delta\Sigma_1(2)$	$\Delta\Sigma_2(2)$	$\Sigma(3)$	$\Delta\Sigma_1(3)$	$\Delta\Sigma_2(3)$	$\Sigma(4)$	$\Delta\Sigma_1(4)$	$\Delta\Sigma_2(4)$	$\Sigma(5)$	$\Delta\Sigma_1(5)$	$\Delta\Sigma_2(5)$	$\Sigma(6)$	$\Delta\Sigma_1(6)$	$\Delta\Sigma_2(6)$	$\Sigma(7)$	$\Delta\Sigma_1(7)$	$\Delta\Sigma_2(7)$	$\Sigma(8)$	$\Delta\Sigma_1(8)$	$\Delta\Sigma_2(8)$	$\Sigma(9)$	$\Delta\Sigma_1(9)$	$\Delta\Sigma_2(9)$
^{232}Th	6.80	90	0.31	0.01	0.01	0.33	0.02	0.01	0.38	0.02	0.01	0.46	0.03	0.02	0.37	0.05	0.03	0.45	0.08	0.04	0.60	0.10	0.05	0.46	0.18	0.11
^{232}Th	6.80	107	0.28	0.02	0.01	0.39	0.02	0.01	0.38	0.03	0.02	0.50	0.05	0.02	0.44	0.07	0.04	0.17	0.11	0.07	0.86	0.11	0.09	-	-	-
^{232}Th	6.80	126	0.26	0.01	0.01	0.32	0.02	0.01	0.34	0.03	0.01	0.34	0.04	0.02	0.41	0.05	0.03	0.60	0.07	0.04	0.54	0.12	0.07	0.54	0.28	0.12
^{232}Th	7.00	54	0.21	0.01	0.01	0.30	0.01	0.01	0.30	0.02	0.01	0.38	0.03	0.02	0.34	0.04	0.03	0.30	0.07	0.05	0.28	0.13	0.09	0.49	0.12	0.15
^{232}Th	7.00	71	0.26	0.01	0.01	0.32	0.02	0.01	0.34	0.02	0.02	0.46	0.03	0.02	0.45	0.05	0.03	0.36	0.08	0.05	0.35	0.18	0.09	0.87	0.38	0.05
^{232}Th	7.00	90	0.32	0.01	0.01	0.37	0.01	0.01	0.42	0.02	0.01	0.42	0.02	0.01	0.41	0.04	0.02	0.58	0.05	0.03	0.71	0.09	0.04	0.47	0.10	0.14
^{232}Th	7.00	107	0.27	0.01	0.01	0.37	0.02	0.01	0.42	0.02	0.01	0.40	0.03	0.02	0.51	0.05	0.03	0.42	0.08	0.05	0.41	0.15	0.08	-0.24	0.40	0.20
^{232}Th	7.00	126	0.23	0.01	0.01	0.32	0.01	0.01	0.29	0.02	0.01	0.36	0.03	0.02	0.41	0.04	0.03	0.45	0.06	0.04	0.59	0.11	0.05	0.17	0.22	0.13
^{232}Th	7.00	144	0.18	0.02	0.01	0.17	0.03	0.02	0.24	0.04	0.03	0.31	0.06	0.05	0.49	0.09	0.06	0.45	0.17	0.09	0.73	0.29	0.34	0.16	0.89	0.72
^{232}Th	7.30	54	0.16	0.04	0.01	0.24	0.05	0.02	0.33	0.08	0.02	0.26	0.12	0.03	0.39	0.20	0.05	-	-	-	-	-	-	-	-	-
^{232}Th	7.30	71	0.19	0.05	0.02	0.25	0.08	0.03	0.29	0.11	0.04	0.10	0.17	0.05	0.31	0.45	0.12	0.98	0.19	0.01	-	-	-	-	-	-
^{232}Th	7.30	90	0.23	0.04	0.01	0.23	0.05	0.02	0.29	0.07	0.02	0.53	0.11	0.04	0.22	0.19	0.09	-	-	-	0.03	0.24	0.11	-	-	-
^{232}Th	7.30	107	0.28	0.05	0.01	0.30	0.06	0.02	0.26	0.10	0.03	0.43	0.14	0.05	0.35	0.26	0.08	0.60	0.30	0.10	-	-	-	-	-	-
^{232}Th	7.30	126	0.16	0.03	0.01	0.18	0.05	0.01	0.26	0.07	0.02	0.40	0.10	0.03	0.33	0.19	0.05	-0.00	0.29	0.09	0.14	0.43	0.14	-	-	-
^{232}Th	7.30	144	0.19	0.05	0.02	0.18	0.07	0.02	0.11	0.10	0.03	0.30	0.15	0.05	0.20	0.19	0.08	-0.55	0.47	0.08	0.94	0.38	0.06	-	-	-
^{233}U	5.60	54	0.04	0.02	0.01	0.06	0.02	0.01	0.04	0.03	0.02	0.06	0.04	0.02	0.15	0.07	0.04	-0.14	0.12	0.07	0.15	0.33	0.16	-	-	-
^{233}U	5.60	71	0.04	0.03	0.02	0.12	0.03	0.02	0.05	0.04	0.02	0.02	0.07	0.03	-0.21	0.10	0.05	-0.29	0.18	0.09	0.79	1.34	0.08	-0.65	0.34	0.10
^{233}U	5.60	90	0.06	0.02	0.01	0.06	0.02	0.01	0.06	0.02	0.02	0.12	0.04	0.02	0.00	0.08	0.04	-0.23	0.14	0.09	-0.58	0.40	0.48	-0.12	0.24	0.48
^{233}U	5.60	107	-0.01	0.02	0.01	0.03	0.03	0.02	0.12	0.04	0.03	0.22	0.08	0.04	0.10	0.13	0.07	-0.30	0.38	0.24	-	-	-	0.63	0.21	0.11
^{233}U	5.60	126	0.04	0.02	0.01	0.07	0.02	0.01	0.13	0.04	0.02	0.08	0.05	0.03	-0.09	0.12	0.05	-0.33	0.21	0.09	-	-	-	0.14	0.84	0.51
^{233}U	5.60	144	0.00	0.03	0.02	0.06	0.03	0.02	0.05	0.05	0.03	-0.12	0.08	0.05	-0.06	0.12	0.09	0.98	2.98	0.01	-	-	-	-	-	-
^{233}U	5.80	54	0.07	0.03	0.01	0.04	0.03	0.01	-0.06	0.04	0.02	0.05	0.05	0.02	-0.10	0.09	0.04	-0.18	0.17	0.07	-	-	-	-	-	-
^{233}U	5.80	71	0.11	0.05	0.02	0.04	0.04	0.02	0.01	0.05	0.02	0.04	0.08	0.03	-0.05	0.12	0.05	0.24	0.17	0.08	0.09	0.39	0.17	-0.23	0.36	0.19
^{233}U	5.80	90	-0.01	0.03	0.01	0.07	0.02	0.01	0.05	0.03	0.02	0.09	0.05	0.03	-0.06	0.09	0.04	0.21	0.13	0.08	-0.04	0.56	0.20	-	-	-
^{233}U	5.80	107	-0.00	0.03	0.02	0.06	0.04	0.02	-0.00	0.06	0.03	0.00	0.09	0.04	0.03	0.18	0.08	0.08	0.55	0.22	-	-	-	-0.88	4.94	1.11
^{233}U	5.80	126	0.02	0.02	0.01	0.08	0.03	0.01	0.06	0.04	0.02	0.10	0.07	0.03	-0.07	0.12	0.06	0.11	0.18	0.10	-	-	-	-	-	-
^{233}U	5.80	144	-0.03	0.04	0.02	0.06	0.05	0.02	-0.03	0.07	0.03	0.02	0.10	0.05	0.19	0.16	0.09	0.61	0.63	0.64	-	-	-	-	-	-
^{233}U	6.00	54	0.01	0.03	0.01	-0.05	0.02	0.01	0.05	0.03	0.02	-0.07	0.05	0.02	0.00	0.08	0.04	0.03	0.14	0.06	0.04	0.25	0.15	-	-	-
^{233}U	6.00	71	0.07	0.04	0.02	0.02	0.03	0.02	0.00	0.04	0.02	0.02	0.07	0.03	-0.17	0.14	0.05	-0.18	0.16	0.08	0.04	0.37	0.16	-	-	-
^{233}U	6.00	90	0.00	0.02	0.01	0.06	0.02	0.01	-0.01	0.03	0.02	-0.01	0.05	0.03	-0.00	0.08	0.04	-0.01	0.12	0.07	-0.01	0.25	0.23	-0.03	0.31	1.08
^{233}U	6.00	107	-0.02	0.03	0.02	-0.00	0.03	0.02	0.06	0.05	0.03	-0.07	0.08	0.04	0.14	0.19	0.06	-	-	-	0.12	1.17	1.74	-	-	-
^{233}U	6.00	126	0.01	0.02	0.01	-0.04	0.03	0.01	0.05	0.04	0.02	-0.08	0.06	0.03	-0.01	0.10	0.06	-	-	-	-	-	-	0.42	0.36	0.29
^{233}U	6.00	144	0.03	0.03	0.02	-0.05	0.04	0.02	-0.04	0.06	0.03	-0.18	0.09	0.05	0.10	0.16	0.09	-0.13	0.28	0.23	-	-	-	-0.21	2.28	0.72
^{233}U	6.20	54	0.06	0.02	0.01	0.02	0.02	0.01	0.04	0.03	0.02	0.02	0.04	0.02	0.01	0.07	0.04	0.03	0.11	0.06	-0.21	0.18	0.14	-	-	-
^{233}U	6.20	71	0.05	0.03	0.02	-0.02	0.03	0.02	-0.04	0.04	0.02	0.01	0.06	0.03	0.09	0.07	0.05	-0.01	0.15	0.08	-0.67	0.55	0.12	-0.25	0.34	0.18
^{233}U	6.20	90	0.04	0.02	0.01	0.02	0.02	0.01	-0.04	0.03	0.02	-0.03	0.04	0.03	0.06	0.07	0.04	-0.22	0.13	0.07	0.34	0.37	0.14	-	-	-
^{233}U	6.20	107	0.00	0.03	0.02	-0.00	0.03	0.02	0.03	0.05	0.03	-0.03	0.07	0.04	0.22	0.15	0.06	-0.02	0.43	0.20	0.73	0.64	0.09	-0.59	0.59	0.45
^{233}U	6.20	126	0.02	0.02	0.01	0.05	0.02	0.01	0.03	0.04	0.02	-0.08	0.06	0.03	0.03	0.11	0.06	-0.18	0.19	0.08	-	-	-	-0.14	0.80	0.41
^{233}U	6.20	144	0.03	0.03	0.02	0.01	0.04	0.02	-0.06	0.05	0.03	-0.06	0.08	0.05	0.24	0.13	0.09	-0.03	0.41	0.27	-0.10	1.23	0.55	-	-	-
^{233}U	6.50	54	0.02	0.02	0.01	0.01	0.02	0.01	-0.02	0.02	0.02	-0.03	0.03	0.02	-0.10	0.05	0.04	0.05	0.08	0.07	0.11	0.14	0.14	-	-	-
^{233}U	6.50	71	0.05	0.03	0.02	0.02	0.02	0.02	-0.01	0.03	0.02	0.03	0.05	0.03	0.01	0.08	0.05	-0.04	0.14	0.08	-0.13	0.24	0.16	-0.01	0.26	0.19
^{233}U	6.50	90	-0.01	0.02	0.01	0.05	0.02	0.01	0.04	0.02	0.02	0.07	0.03	0.03	0.06	0.06	0.04	0.01	0.09	0.06	-0.26	0.27	0.27	0.36	0.40	0.83

Continued on Next Page...

Table B.1 – Continued

Target	E_γ	θ	$\Sigma(2)$	$\Delta\Sigma_1(2)$	$\Delta\Sigma_2(2)$	$\Sigma(3)$	$\Delta\Sigma_1(3)$	$\Delta\Sigma_2(3)$	$\Sigma(4)$	$\Delta\Sigma_1(4)$	$\Delta\Sigma_2(4)$	$\Sigma(5)$	$\Delta\Sigma_1(5)$	$\Delta\Sigma_2(5)$	$\Sigma(6)$	$\Delta\Sigma_1(6)$	$\Delta\Sigma_2(6)$	$\Sigma(7)$	$\Delta\Sigma_1(7)$	$\Delta\Sigma_2(7)$	$\Sigma(8)$	$\Delta\Sigma_1(8)$	$\Delta\Sigma_2(8)$	$\Sigma(9)$	$\Delta\Sigma_1(9)$	$\Delta\Sigma_2(9)$
^{233}U	6.50	107	-0.02	0.02	0.02	0.04	0.02	0.02	-0.05	0.04	0.03	-0.07	0.06	0.04	0.08	0.12	0.06	0.03	0.28	0.20	0.78	0.45	0.11	-0.13	2.24	0.27
^{233}U	6.50	126	-0.01	0.01	0.01	0.01	0.02	0.01	0.03	0.03	0.02	0.00	0.05	0.03	0.06	0.07	0.05	-0.02	0.14	0.08	-	-	-	0.21	0.47	0.45
^{233}U	6.50	144	-0.01	0.02	0.02	-0.02	0.03	0.02	0.03	0.04	0.03	-0.17	0.07	0.05	0.19	0.10	0.09	-0.30	0.19	0.22	0.08	0.64	0.54	-	-	-
^{233}U	7.00	54	0.08	0.02	0.01	-0.00	0.02	0.01	-0.04	0.03	0.02	0.01	0.04	0.02	-0.11	0.07	0.04	0.21	0.12	0.06	-0.42	0.20	0.14	-	-	-
^{233}U	7.00	71	0.00	0.03	0.02	-0.01	0.03	0.02	0.03	0.04	0.02	0.02	0.06	0.03	-0.03	0.09	0.05	0.03	0.12	0.08	-0.25	0.45	0.14	0.14	0.43	0.19
^{233}U	7.00	90	0.03	0.02	0.01	0.05	0.02	0.01	0.01	0.03	0.02	-0.05	0.04	0.03	-0.06	0.07	0.04	-0.05	0.12	0.07	0.14	0.30	0.19	0.34	0.31	0.95
^{233}U	7.00	107	-0.04	0.03	0.02	-0.05	0.03	0.02	-0.01	0.05	0.03	0.01	0.07	0.04	-0.04	0.12	0.06	0.25	0.25	0.19	-0.02	0.58	0.21	-0.62	0.63	0.30
^{233}U	7.00	126	0.01	0.02	0.01	0.02	0.02	0.01	-0.02	0.04	0.02	0.03	0.06	0.03	-0.12	0.10	0.05	-0.24	0.21	0.08	-0.52	0.73	0.18	-	-	-
^{233}U	7.00	144	-0.04	0.03	0.02	-0.00	0.04	0.02	-0.03	0.06	0.03	-0.16	0.08	0.05	0.36	0.16	0.11	0.23	0.31	0.22	0.46	0.39	0.42	-	-	-
^{235}U	5.60	54	0.02	0.02	0.01	0.04	0.03	0.02	0.16	0.05	0.02	0.04	0.07	0.03	0.03	0.13	0.04	-	-	-	-	-	-	-	-	-
^{235}U	5.60	71	0.06	0.04	0.02	-0.08	0.06	0.02	0.05	0.08	0.04	0.15	0.08	0.05	0.04	0.24	0.11	0.84	0.15	0.04	-	-	-	0.73	0.08	0.17
^{235}U	5.60	90	0.05	0.02	0.01	0.13	0.03	0.01	0.04	0.04	0.02	0.26	0.07	0.03	0.22	0.12	0.09	-0.22	0.21	0.23	-	-	-	-	-	-
^{235}U	5.60	107	0.06	0.02	0.01	0.08	0.03	0.02	-0.07	0.05	0.03	0.21	0.09	0.05	0.07	0.14	0.07	-0.30	0.42	0.12	-0.04	0.28	0.19	0.78	0.85	0.16
^{235}U	5.60	126	0.05	0.02	0.01	0.05	0.02	0.01	0.07	0.04	0.02	0.04	0.05	0.03	0.17	0.11	0.05	-0.14	0.21	0.08	-	-	-	0.26	0.20	0.13
^{235}U	5.60	144	0.06	0.02	0.02	0.14	0.03	0.02	-0.06	0.05	0.03	0.15	0.09	0.04	-0.03	0.11	0.07	-0.09	0.18	0.10	-	-	-	-0.06	2.01	1.51
^{235}U	5.80	54	-0.01	0.02	0.01	-0.02	0.02	0.01	-0.01	0.03	0.01	-0.01	0.05	0.02	-0.06	0.08	0.04	-0.14	0.13	0.06	-	-	-	-0.32	0.19	0.12
^{235}U	5.80	71	0.08	0.03	0.01	-0.03	0.04	0.01	-0.03	0.06	0.02	-0.17	0.09	0.04	0.01	0.20	0.07	-0.05	0.76	0.18	-	-	-	0.62	0.12	0.15
^{235}U	5.80	90	0.02	0.02	0.01	0.01	0.02	0.01	-0.05	0.03	0.01	-0.02	0.05	0.02	0.08	0.09	0.04	-0.29	0.13	0.06	0.16	0.32	0.16	-	-	-
^{235}U	5.80	107	0.04	0.02	0.01	0.04	0.03	0.01	-0.09	0.05	0.02	0.04	0.07	0.04	0.19	0.13	0.06	0.07	0.17	0.08	-0.07	0.49	0.17	0.65	0.26	0.20
^{235}U	5.80	126	0.01	0.02	0.01	0.04	0.02	0.01	0.02	0.03	0.01	0.01	0.05	0.02	0.09	0.07	0.03	0.10	0.14	0.07	0.27	0.28	0.11	0.20	0.33	0.22
^{235}U	5.80	144	0.01	0.02	0.01	0.03	0.03	0.01	-0.06	0.05	0.02	0.20	0.07	0.03	-0.03	0.11	0.05	-0.14	0.20	0.09	-0.26	0.30	0.13	-	-	-
^{235}U	6.00	54	0.01	0.01	0.01	0.02	0.01	0.01	-0.01	0.02	0.01	0.05	0.02	0.02	-0.00	0.04	0.03	-0.07	0.06	0.05	0.02	0.10	0.09	-0.26	0.14	0.15
^{235}U	6.00	71	0.06	0.01	0.01	0.03	0.02	0.02	0.10	0.03	0.02	0.03	0.04	0.03	-0.02	0.07	0.06	0.05	0.12	0.10	0.25	0.23	0.23	0.31	0.25	0.36
^{235}U	6.00	90	0.02	0.01	0.01	0.06	0.01	0.01	0.02	0.02	0.01	0.08	0.02	0.02	0.14	0.04	0.03	-0.01	0.07	0.06	-0.00	0.15	0.12	0.15	0.23	0.16
^{235}U	6.00	107	-0.00	0.01	0.01	0.03	0.02	0.01	0.00	0.02	0.02	-0.11	0.04	0.03	0.06	0.06	0.05	0.01	0.10	0.09	0.24	0.16	0.14	0.74	0.13	0.16
^{235}U	6.00	126	-0.01	0.01	0.01	0.00	0.01	0.01	0.04	0.02	0.01	0.04	0.03	0.02	-0.06	0.04	0.03	0.02	0.07	0.07	-0.01	0.13	0.13	-0.39	0.16	0.17
^{235}U	6.00	144	-0.00	0.01	0.01	0.04	0.02	0.01	-0.07	0.02	0.02	0.05	0.04	0.03	-0.08	0.06	0.05	-0.01	0.09	0.08	-0.42	0.14	0.11	-0.25	0.20	0.19
^{235}U	6.20	54	0.00	0.01	0.01	0.02	0.01	0.01	0.00	0.01	0.01	0.00	0.02	0.02	0.06	0.03	0.03	-0.07	0.05	0.05	-0.08	0.08	0.09	-0.41	0.19	0.10
^{235}U	6.20	71	0.03	0.01	0.01	0.02	0.02	0.02	0.06	0.02	0.02	0.05	0.03	0.03	0.14	0.05	0.06	0.07	0.08	0.09	0.02	0.22	0.33	0.35	0.16	0.20
^{235}U	6.20	90	-0.00	0.01	0.01	0.01	0.01	0.01	0.01	0.01	0.01	0.09	0.02	0.02	0.13	0.03	0.03	-0.04	0.05	0.06	-0.11	0.09	0.10	-0.05	0.15	0.18
^{235}U	6.20	107	0.03	0.01	0.01	0.06	0.01	0.01	0.02	0.02	0.02	0.00	0.03	0.03	0.14	0.05	0.05	0.12	0.07	0.08	0.02	0.15	0.13	0.73	0.10	0.30
^{235}U	6.20	126	-0.01	0.01	0.01	0.03	0.01	0.01	0.02	0.01	0.01	0.08	0.02	0.02	-0.01	0.03	0.03	-0.07	0.05	0.06	0.03	0.09	0.09	0.02	0.12	0.19
^{235}U	6.20	144	-0.01	0.01	0.01	0.03	0.01	0.01	-0.03	0.02	0.02	0.07	0.03	0.03	-0.13	0.04	0.05	-0.08	0.07	0.08	-0.24	0.10	0.12	-0.12	0.15	0.19
^{235}U	6.40	54	-0.00	0.01	0.01	0.00	0.01	0.01	-0.02	0.01	0.02	0.02	0.02	0.03	0.07	0.03	0.04	-0.20	0.04	0.07	-0.02	0.06	0.12	0.06	0.14	0.19
^{235}U	6.40	71	0.06	0.01	0.02	0.02	0.01	0.02	0.05	0.02	0.03	-0.07	0.03	0.05	0.07	0.05	0.07	0.02	0.07	0.12	0.10	0.16	0.31	0.65	0.13	0.23
^{235}U	6.40	90	0.00	0.01	0.01	0.02	0.01	0.01	0.01	0.01	0.02	0.07	0.02	0.03	0.14	0.03	0.04	-0.03	0.04	0.08	0.10	0.08	0.13	-0.14	0.11	0.23
^{235}U	6.40	107	-0.00	0.01	0.01	0.01	0.01	0.02	-0.02	0.02	0.03	-0.07	0.03	0.05	0.09	0.04	0.07	0.15	0.07	0.11	0.11	0.11	0.17	0.25	0.16	0.32
^{235}U	6.40	126	-0.01	0.01	0.01	0.02	0.01	0.01	0.02	0.01	0.02	0.03	0.02	0.03	-0.03	0.03	0.05	-0.00	0.05	0.08	-0.14	0.07	0.11	-0.22	0.11	0.18
^{235}U	6.40	144	0.01	0.01	0.01	0.03	0.01	0.02	-0.01	0.02	0.03	0.08	0.03	0.04	-0.05	0.04	0.07	-0.01	0.06	0.10	-0.13	0.09	0.15	-0.30	0.13	0.18
^{235}U	6.60	54	-0.01	0.01	0.01	0.01	0.01	0.01	-0.00	0.02	0.02	0.02	0.02	0.03	0.08	0.04	0.04	-0.02	0.06	0.07	0.06	0.10	0.12	-0.29	0.13	0.18
^{235}U	6.60	71	0.03	0.01	0.02	-0.00	0.02	0.02	0.08	0.03	0.03	-0.02	0.04	0.05	0.05	0.07	0.07	-0.13	0.10	0.12	0.61	0.13	0.20	0.29	0.22	0.36
^{235}U	6.60	90	-0.01	0.01	0.01	0.02	0.01	0.01	-0.05	0.02	0.02	0.06	0.02	0.03	0.13	0.04	0.04	-0.13	0.06	0.08	-0.03	0.11	0.13	0.13	0.19	0.18

Continued on Next Page...

Table B.1 – Continued

Target	E_γ	θ	$\Sigma(2)$	$\Delta\Sigma_1(2)$	$\Delta\Sigma_2(2)$	$\Sigma(3)$	$\Delta\Sigma_1(3)$	$\Delta\Sigma_2(3)$	$\Sigma(4)$	$\Delta\Sigma_1(4)$	$\Delta\Sigma_2(4)$	$\Sigma(5)$	$\Delta\Sigma_1(5)$	$\Delta\Sigma_2(5)$	$\Sigma(6)$	$\Delta\Sigma_1(6)$	$\Delta\Sigma_2(6)$	$\Sigma(7)$	$\Delta\Sigma_1(7)$	$\Delta\Sigma_2(7)$	$\Sigma(8)$	$\Delta\Sigma_1(8)$	$\Delta\Sigma_2(8)$	$\Sigma(9)$	$\Delta\Sigma_1(9)$	$\Delta\Sigma_2(9)$
^{235}U	6.60	107	-0.00	0.01	0.01	0.05	0.02	0.02	0.02	0.03	0.03	0.01	0.04	0.05	0.05	0.06	0.07	0.13	0.09	0.11	0.06	0.13	0.17	0.64	0.11	0.20
^{235}U	6.60	126	-0.01	0.01	0.01	-0.00	0.01	0.01	-0.04	0.02	0.02	-0.02	0.03	0.03	0.03	0.04	0.05	-0.08	0.07	0.08	-0.15	0.10	0.11	0.15	0.18	0.18
^{235}U	6.60	144	0.01	0.01	0.01	0.03	0.02	0.02	-0.00	0.03	0.03	0.16	0.04	0.04	-0.06	0.06	0.07	0.08	0.09	0.10	-0.06	0.15	0.15	-0.18	0.20	0.20
^{238}U	5.70	75	0.30	0.03	0.02	0.40	0.04	0.02	0.39	0.06	0.03	0.44	0.08	0.04	0.43	0.14	0.08	-	-	-	-	-	-	0.57	0.19	0.57
^{238}U	5.70	90	0.37	0.03	0.02	0.45	0.04	0.02	0.53	0.05	0.03	0.58	0.07	0.04	0.39	0.16	0.09	0.74	0.16	0.11	-	-	-	-	-	-
^{238}U	5.70	126	0.30	0.04	0.02	0.31	0.05	0.03	0.33	0.08	0.05	0.43	0.15	0.07	0.29	0.17	0.11	-0.65	0.30	0.14	-	-	-	-	-	-
^{238}U	5.80	54	0.25	0.02	0.01	0.33	0.03	0.01	0.47	0.04	0.02	0.50	0.07	0.03	0.60	0.15	0.04	0.03	0.16	0.10	-0.01	0.41	0.27	-	-	-
^{238}U	5.80	71	0.34	0.03	0.01	0.35	0.04	0.02	0.49	0.05	0.03	0.46	0.09	0.04	0.55	0.15	0.06	0.78	0.19	0.08	0.17	1.20	0.86	-0.19	1.83	0.75
^{238}U	5.80	90	0.39	0.02	0.01	0.40	0.02	0.01	0.43	0.03	0.02	0.52	0.05	0.02	0.47	0.09	0.04	0.37	0.13	0.07	-	-	-	-	-	-
^{238}U	5.80	107	0.31	0.02	0.01	0.43	0.03	0.01	0.40	0.04	0.02	0.46	0.07	0.03	0.59	0.10	0.05	0.57	0.14	0.09	0.74	0.20	0.39	-	-	-
^{238}U	5.80	126	0.26	0.02	0.01	0.28	0.02	0.01	0.36	0.03	0.02	0.37	0.05	0.02	0.44	0.07	0.04	0.32	0.12	0.06	0.39	0.18	0.09	-	-	-
^{238}U	5.80	144	0.17	0.03	0.01	0.19	0.03	0.02	0.15	0.05	0.03	0.30	0.07	0.04	0.35	0.14	0.06	0.42	0.18	0.18	0.63	0.27	0.42	0.89	0.41	0.10
^{238}U	5.90	54	0.25	0.02	0.01	0.32	0.03	0.01	0.36	0.04	0.02	0.42	0.08	0.03	0.31	0.13	0.06	0.47	0.22	0.07	-	-	-	-	-	-
^{238}U	5.90	71	0.40	0.03	0.01	0.37	0.04	0.02	0.33	0.06	0.03	0.50	0.10	0.04	0.57	0.14	0.07	0.87	0.15	0.04	-	-	-	-	-	-
^{238}U	5.90	90	0.36	0.02	0.01	0.40	0.02	0.01	0.43	0.03	0.01	0.51	0.04	0.02	0.47	0.08	0.03	0.69	0.22	0.09	0.40	0.55	0.23	0.08	0.35	0.34
^{238}U	5.90	107	0.34	0.02	0.01	0.46	0.03	0.01	0.41	0.05	0.02	0.57	0.06	0.03	0.65	0.11	0.04	0.83	0.15	0.04	0.44	0.19	0.16	0.50	0.67	0.36
^{238}U	5.90	126	0.29	0.02	0.01	0.36	0.02	0.01	0.40	0.03	0.02	0.36	0.05	0.02	0.49	0.08	0.04	0.36	0.13	0.06	0.26	0.30	0.11	-	-	-
^{238}U	5.90	144	0.11	0.03	0.01	0.21	0.04	0.02	0.22	0.06	0.03	0.47	0.08	0.03	0.27	0.14	0.07	0.25	0.20	0.10	-	-	-	0.46	0.90	0.47
^{238}U	6.00	54	0.24	0.02	0.01	0.35	0.02	0.01	0.35	0.03	0.02	0.41	0.05	0.03	0.34	0.09	0.05	0.38	0.12	0.08	-	-	-	-	-	-
^{238}U	6.00	71	0.33	0.02	0.01	0.41	0.03	0.02	0.48	0.04	0.02	0.47	0.07	0.04	0.49	0.12	0.07	0.70	0.16	0.08	-0.10	2.30	1.00	-	-	-
^{238}U	6.00	90	0.38	0.01	0.01	0.44	0.02	0.01	0.48	0.02	0.01	0.57	0.04	0.02	0.52	0.06	0.03	0.42	0.10	0.08	-	-	-	-	-	-
^{238}U	6.00	107	0.30	0.02	0.01	0.47	0.02	0.01	0.47	0.04	0.02	0.47	0.05	0.03	0.58	0.09	0.04	0.64	0.12	0.06	0.87	0.15	1.31	-	-	-
^{238}U	6.00	126	0.27	0.01	0.01	0.35	0.02	0.01	0.39	0.03	0.02	0.37	0.04	0.02	0.51	0.05	0.03	0.52	0.09	0.05	0.51	0.16	0.10	-	-	-
^{238}U	6.00	144	0.15	0.02	0.01	0.25	0.03	0.02	0.16	0.05	0.03	0.35	0.06	0.04	0.01	0.11	0.07	0.65	0.14	0.07	0.47	0.25	0.15	0.41	0.30	0.34
^{238}U	6.10	54	0.27	0.02	0.01	0.36	0.02	0.01	0.43	0.03	0.02	0.36	0.05	0.03	0.52	0.11	0.04	0.13	0.15	0.08	-	-	-	-	-	-
^{238}U	6.10	71	0.39	0.02	0.01	0.39	0.03	0.02	0.41	0.05	0.03	0.51	0.08	0.04	0.34	0.12	0.08	0.23	0.24	0.13	0.50	0.67	0.28	-0.45	1.17	0.41
^{238}U	6.10	90	0.37	0.01	0.01	0.42	0.02	0.01	0.43	0.02	0.01	0.56	0.03	0.02	0.56	0.05	0.03	0.45	0.09	0.06	0.40	0.21	0.13	-0.09	0.25	0.29
^{238}U	6.10	107	0.32	0.02	0.01	0.47	0.03	0.01	0.45	0.04	0.02	0.39	0.06	0.03	0.46	0.09	0.05	0.73	0.12	0.05	0.82	0.19	0.08	-	-	-
^{238}U	6.10	126	0.27	0.01	0.01	0.33	0.02	0.01	0.38	0.03	0.02	0.37	0.04	0.02	0.38	0.06	0.03	0.48	0.09	0.05	0.51	0.18	0.08	-	-	-
^{238}U	6.10	144	0.14	0.02	0.01	0.17	0.03	0.02	0.06	0.05	0.03	0.24	0.07	0.04	0.23	0.10	0.06	0.19	0.16	0.09	-0.17	0.35	0.17	0.57	0.40	0.24
^{238}U	6.20	54	0.24	0.02	0.01	0.31	0.02	0.01	0.36	0.03	0.02	0.32	0.05	0.03	0.30	0.10	0.05	0.22	0.14	0.08	0.59	0.42	0.14	-	-	-
^{238}U	6.20	71	0.35	0.02	0.01	0.28	0.03	0.02	0.40	0.05	0.03	0.46	0.07	0.04	0.56	0.10	0.06	0.71	0.22	0.09	-	-	-	-	-	-
^{238}U	6.20	90	0.35	0.01	0.01	0.39	0.02	0.01	0.43	0.02	0.01	0.51	0.03	0.02	0.46	0.06	0.03	0.51	0.09	0.05	-0.02	0.27	0.23	0.41	0.36	0.21
^{238}U	6.20	107	0.28	0.02	0.01	0.48	0.03	0.01	0.48	0.04	0.02	0.47	0.06	0.03	0.43	0.10	0.06	0.66	0.14	0.07	0.61	0.17	0.14	-	-	-
^{238}U	6.20	126	0.27	0.01	0.01	0.30	0.02	0.01	0.33	0.03	0.02	0.34	0.04	0.02	0.51	0.05	0.03	0.23	0.10	0.06	0.68	0.15	0.06	0.58	0.26	0.13
^{238}U	6.20	144	0.17	0.02	0.01	0.18	0.03	0.02	0.21	0.05	0.02	0.27	0.07	0.04	0.39	0.10	0.06	0.20	0.15	0.09	0.52	0.48	0.13	0.33	0.62	0.32
^{238}U	6.40	75	0.20	0.02	0.02	0.28	0.02	0.02	0.31	0.03	0.03	0.40	0.05	0.04	0.20	0.08	0.08	0.73	0.14	0.09	0.10	0.61	0.93	-	-	-
^{238}U	6.40	90	0.25	0.02	0.02	0.28	0.02	0.02	0.31	0.03	0.03	0.31	0.05	0.05	0.44	0.08	0.09	0.54	0.13	0.16	0.29	0.37	0.22	-	-	-
^{238}U	6.40	126	0.20	0.02	0.02	0.24	0.03	0.03	0.27	0.04	0.04	0.35	0.06	0.06	0.45	0.10	0.10	0.18	0.22	0.21	-	-	-	-	-	-
^{238}U	6.50	54	0.12	0.02	0.01	0.17	0.03	0.01	0.19	0.04	0.02	0.30	0.06	0.03	0.10	0.10	0.05	0.12	0.17	0.08	-	-	-	-	-	-
^{238}U	6.50	71	0.20	0.03	0.01	0.15	0.04	0.02	0.37	0.06	0.03	0.15	0.10	0.05	0.46	0.12	0.06	0.37	0.21	0.16	-	-	-	-0.15	0.53	0.37
^{238}U	6.50	90	0.19	0.01	0.01	0.21	0.02	0.01	0.23	0.03	0.02	0.28	0.04	0.02	0.37	0.06	0.04	0.49	0.09	0.06	0.11	0.30	0.19	-	-	-

Continued on Next Page...

Table B.1 – Continued

Target	E_γ	θ	$\Sigma(2)$	$\Delta\Sigma_1(2)$	$\Delta\Sigma_2(2)$	$\Sigma(3)$	$\Delta\Sigma_1(3)$	$\Delta\Sigma_2(3)$	$\Sigma(4)$	$\Delta\Sigma_1(4)$	$\Delta\Sigma_2(4)$	$\Sigma(5)$	$\Delta\Sigma_1(5)$	$\Delta\Sigma_2(5)$	$\Sigma(6)$	$\Delta\Sigma_1(6)$	$\Delta\Sigma_2(6)$	$\Sigma(7)$	$\Delta\Sigma_1(7)$	$\Delta\Sigma_2(7)$	$\Sigma(8)$	$\Delta\Sigma_1(8)$	$\Delta\Sigma_2(8)$	$\Sigma(9)$	$\Delta\Sigma_1(9)$	$\Delta\Sigma_2(9)$
^{238}U	6.50	107	0.14	0.02	0.01	0.26	0.03	0.02	0.30	0.05	0.02	0.34	0.07	0.04	0.20	0.12	0.07	0.51	0.19	0.11	0.41	0.24	0.18	0.85	1.02	0.13
^{238}U	6.50	126	0.15	0.01	0.01	0.16	0.02	0.01	0.21	0.03	0.02	0.17	0.04	0.03	0.20	0.06	0.04	0.14	0.11	0.06	0.12	0.20	0.12	-	-	-
^{238}U	6.50	144	0.11	0.02	0.01	0.09	0.03	0.02	0.08	0.05	0.03	0.14	0.07	0.04	0.09	0.10	0.07	-0.07	0.18	0.08	-0.25	0.23	0.14	0.07	0.58	0.39
^{238}U	6.70	54	0.08	0.03	0.02	-0.01	0.03	0.03	0.20	0.05	0.04	0.06	0.08	0.07	0.15	0.12	0.11	0.22	0.19	0.18	-0.46	0.42	0.46	0.62	0.53	0.71
^{238}U	6.70	71	0.18	0.04	0.03	0.12	0.05	0.04	-0.08	0.07	0.06	-0.14	0.11	0.08	0.21	0.21	0.16	-0.59	0.36	0.14	-0.07	0.43	0.60	-	-	-
^{238}U	6.70	90	0.13	0.03	0.02	0.14	0.03	0.03	0.21	0.05	0.04	0.29	0.07	0.06	-0.06	0.11	0.11	0.31	0.20	0.19	0.28	0.37	0.43	-	-	-
^{238}U	6.70	107	0.12	0.04	0.03	0.07	0.05	0.05	0.00	0.08	0.06	0.04	0.12	0.10	-0.00	0.16	0.17	-0.04	0.29	0.23	0.48	0.30	0.28	-0.26	0.79	1.01
^{238}U	6.70	126	0.08	0.03	0.02	0.13	0.03	0.03	0.04	0.05	0.05	-0.00	0.08	0.06	0.32	0.12	0.09	0.21	0.25	0.14	0.20	0.35	0.26	-0.75	0.29	0.25
^{238}U	6.70	144	0.20	0.04	0.04	0.11	0.06	0.05	0.02	0.09	0.07	0.14	0.14	0.13	-0.03	0.25	0.21	-0.16	0.71	0.59	0.56	0.96	0.36	-	-	-
^{238}U	6.80	54	0.07	0.03	0.02	-0.00	0.03	0.03	0.17	0.05	0.04	0.06	0.07	0.07	0.33	0.10	0.10	-0.08	0.17	0.18	0.49	0.19	0.51	-	-	-
^{238}U	6.80	71	0.14	0.03	0.03	0.16	0.04	0.04	0.02	0.06	0.06	0.17	0.11	0.08	-0.07	0.21	0.18	0.18	0.25	0.20	0.71	0.99	0.28	-0.53	0.34	0.46
^{238}U	6.80	90	0.16	0.02	0.02	0.07	0.03	0.03	0.29	0.05	0.04	0.33	0.06	0.06	0.03	0.13	0.11	0.56	0.18	0.16	-	-	-	-	-	-
^{238}U	6.80	107	0.14	0.04	0.03	0.17	0.05	0.04	0.06	0.07	0.06	0.46	0.11	0.07	0.25	0.16	0.16	-0.07	0.42	0.22	-0.09	0.40	0.40	-0.34	0.64	0.97
^{238}U	6.80	126	0.08	0.02	0.02	0.08	0.03	0.03	0.11	0.05	0.04	0.20	0.07	0.06	0.13	0.12	0.10	0.50	0.27	0.10	0.43	0.34	0.25	-	-	-
^{238}U	6.80	144	0.13	0.04	0.04	0.14	0.05	0.05	-0.01	0.08	0.07	0.13	0.13	0.13	-0.18	0.26	0.20	-0.21	0.88	0.57	-0.61	0.29	0.34	-	-	-
^{238}U	7.00	54	0.07	0.02	0.01	0.15	0.02	0.01	0.18	0.04	0.02	0.18	0.06	0.03	0.26	0.10	0.05	0.21	0.16	0.08	0.33	0.28	0.21	-	-	-
^{238}U	7.00	71	0.16	0.03	0.01	0.13	0.04	0.02	0.14	0.06	0.03	0.21	0.09	0.05	0.33	0.13	0.07	0.10	0.19	0.14	0.90	0.35	0.07	-0.57	0.72	0.37
^{238}U	7.00	90	0.15	0.02	0.01	0.14	0.02	0.01	0.12	0.03	0.02	0.29	0.05	0.03	0.24	0.08	0.05	0.27	0.15	0.07	0.04	0.24	0.24	-	-	-
^{238}U	7.00	107	0.12	0.02	0.01	0.17	0.03	0.02	0.14	0.05	0.03	0.26	0.07	0.04	-0.02	0.11	0.07	0.39	0.20	0.19	0.22	0.32	0.20	0.63	1.41	9.71
^{238}U	7.00	126	0.11	0.02	0.01	0.15	0.02	0.01	0.15	0.03	0.02	0.10	0.05	0.03	0.13	0.07	0.04	0.28	0.11	0.07	0.02	0.22	0.14	0.67	0.25	0.12
^{238}U	7.00	144	0.00	0.02	0.01	0.04	0.03	0.02	0.01	0.05	0.03	0.07	0.07	0.04	0.11	0.10	0.06	-0.45	0.17	0.07	0.58	0.48	0.12	0.62	0.38	0.22
^{237}Np	5.40	54	-0.02	0.05	0.02	0.07	0.04	0.01	-0.06	0.06	0.01	-0.14	0.07	0.02	-0.08	0.12	0.02	0.30	0.18	0.03	-	-	-	0.06	0.24	0.13
^{237}Np	5.40	71	0.03	0.07	0.02	0.10	0.04	0.01	0.11	0.06	0.01	0.05	0.09	0.02	0.08	0.14	0.03	-0.07	0.20	0.04	-0.00	0.76	0.29	0.37	0.37	0.11
^{237}Np	5.40	90	0.10	0.04	0.01	0.08	0.03	0.01	0.09	0.04	0.01	0.05	0.06	0.01	0.20	0.08	0.02	0.06	0.13	0.03	0.22	0.21	0.06	-0.16	0.38	0.10
^{237}Np	5.40	107	0.08	0.05	0.01	0.10	0.04	0.01	0.05	0.06	0.01	0.05	0.11	0.02	0.28	0.14	0.02	-0.67	0.32	0.03	-0.06	0.28	0.06	-	-	-
^{237}Np	5.40	126	-0.03	0.04	0.01	0.07	0.03	0.01	0.06	0.04	0.01	-0.07	0.07	0.01	-0.06	0.12	0.02	-0.01	0.15	0.03	-	-	-	-	-	-
^{237}Np	5.60	54	-0.01	0.03	0.01	0.01	0.02	0.01	-0.00	0.03	0.01	-0.08	0.04	0.01	-0.12	0.07	0.02	0.19	0.11	0.03	0.07	0.24	0.08	0.15	0.22	0.10
^{237}Np	5.60	71	0.06	0.03	0.02	0.03	0.03	0.01	0.07	0.03	0.01	0.07	0.05	0.02	0.01	0.07	0.02	-0.14	0.12	0.04	-0.10	0.18	0.06	-0.10	0.25	0.11
^{237}Np	5.60	90	0.03	0.02	0.01	0.05	0.02	0.01	0.08	0.02	0.01	0.04	0.04	0.01	0.12	0.05	0.02	-0.09	0.08	0.03	0.35	0.15	0.04	0.13	0.22	0.08
^{237}Np	5.60	107	0.04	0.03	0.01	0.01	0.02	0.01	0.03	0.03	0.01	0.06	0.05	0.02	0.06	0.07	0.02	-0.20	0.11	0.04	-0.07	0.17	0.05	0.24	0.52	0.11
^{237}Np	5.60	126	0.03	0.02	0.01	0.05	0.02	0.01	0.06	0.02	0.01	0.08	0.04	0.01	0.01	0.06	0.02	-0.04	0.08	0.03	0.02	0.22	0.05	0.11	0.43	0.09
^{237}Np	5.80	54	0.00	0.02	0.01	0.01	0.02	0.01	-0.02	0.02	0.01	0.01	0.03	0.01	0.07	0.05	0.02	0.12	0.09	0.03	-0.06	0.18	0.05	0.11	0.20	0.08
^{237}Np	5.80	71	-0.01	0.03	0.01	0.02	0.02	0.01	-0.03	0.03	0.01	0.02	0.04	0.02	-0.04	0.06	0.02	0.10	0.10	0.03	-0.02	0.17	0.06	-0.13	0.16	0.10
^{237}Np	5.80	90	0.02	0.02	0.01	0.01	0.02	0.01	0.03	0.02	0.01	0.00	0.03	0.01	-0.00	0.04	0.02	-0.04	0.07	0.03	0.10	0.12	0.04	0.16	0.16	0.07
^{237}Np	5.80	107	-0.00	0.02	0.01	-0.03	0.02	0.01	-0.00	0.03	0.01	0.05	0.04	0.02	0.09	0.06	0.02	-0.02	0.10	0.04	-0.22	0.12	0.05	-0.11	0.32	0.09
^{237}Np	5.80	126	0.02	0.02	0.01	0.02	0.02	0.01	0.02	0.02	0.01	0.03	0.03	0.01	0.02	0.05	0.02	0.05	0.08	0.03	0.18	0.14	0.05	-	-	-
^{237}Np	5.90	54	0.01	0.02	0.01	0.02	0.02	0.01	-0.02	0.02	0.01	0.00	0.03	0.01	0.02	0.05	0.02	0.02	0.07	0.03	0.04	0.17	0.05	0.32	0.16	0.07
^{237}Np	5.90	71	0.06	0.03	0.01	-0.01	0.02	0.01	-0.01	0.03	0.01	0.01	0.04	0.02	-0.08	0.05	0.02	-0.08	0.08	0.03	-0.10	0.13	0.06	-0.15	0.16	0.10
^{237}Np	5.90	90	-0.01	0.02	0.01	0.01	0.01	0.01	0.01	0.02	0.01	0.02	0.03	0.01	0.01	0.04	0.02	-0.04	0.06	0.03	-0.01	0.10	0.05	-0.00	0.21	0.07
^{237}Np	5.90	107	-0.00	0.02	0.01	-0.02	0.02	0.01	-0.00	0.03	0.01	-0.07	0.04	0.02	-0.03	0.06	0.02	-0.18	0.08	0.04	-0.29	0.12	0.05	0.56	0.31	0.08
^{237}Np	5.90	126	-0.01	0.02	0.01	0.00	0.01	0.01	-0.01	0.02	0.01	-0.03	0.03	0.01	0.05	0.04	0.02	0.04	0.07	0.03	-0.23	0.14	0.04	-0.08	0.27	0.09
^{237}Np	6.00	54	0.02	0.02	0.01	0.00	0.02	0.01	0.01	0.02	0.01	0.01	0.03	0.01	-0.03	0.05	0.02	0.11	0.09	0.03	-0.03	0.15	0.05	0.42	0.15	0.07

Continued on Next Page...

Table B.1 – Continued

Target	E_γ	θ	$\Sigma(2)$	$\Delta\Sigma_1(2)$	$\Delta\Sigma_2(2)$	$\Sigma(3)$	$\Delta\Sigma_1(3)$	$\Delta\Sigma_2(3)$	$\Sigma(4)$	$\Delta\Sigma_1(4)$	$\Delta\Sigma_2(4)$	$\Sigma(5)$	$\Delta\Sigma_1(5)$	$\Delta\Sigma_2(5)$	$\Sigma(6)$	$\Delta\Sigma_1(6)$	$\Delta\Sigma_2(6)$	$\Sigma(7)$	$\Delta\Sigma_1(7)$	$\Delta\Sigma_2(7)$	$\Sigma(8)$	$\Delta\Sigma_1(8)$	$\Delta\Sigma_2(8)$	$\Sigma(9)$	$\Delta\Sigma_1(9)$	$\Delta\Sigma_2(9)$
^{237}Np	6.00	71	-0.01	0.03	0.01	0.01	0.02	0.01	-0.01	0.03	0.01	0.04	0.04	0.02	-0.07	0.07	0.02	-0.12	0.09	0.03	-0.03	0.15	0.06	-0.03	0.20	0.11
^{237}Np	6.00	90	0.04	0.02	0.01	0.00	0.02	0.01	-0.02	0.02	0.01	0.01	0.03	0.01	-0.00	0.05	0.02	-0.10	0.07	0.03	0.12	0.11	0.04	0.16	0.16	0.07
^{237}Np	6.00	107	-0.01	0.03	0.01	-0.04	0.02	0.01	0.03	0.03	0.01	0.03	0.05	0.02	0.03	0.06	0.02	-0.12	0.11	0.04	-0.10	0.15	0.05	-0.01	0.30	0.11
^{237}Np	6.00	126	-0.04	0.02	0.01	0.00	0.02	0.01	-0.01	0.02	0.01	-0.02	0.03	0.01	0.12	0.05	0.02	0.11	0.08	0.03	0.10	0.14	0.05	0.36	0.24	0.08
^{237}Np	6.10	54	0.01	0.02	0.01	-0.02	0.02	0.01	0.01	0.02	0.01	0.03	0.03	0.01	-0.06	0.05	0.02	-0.05	0.07	0.03	-0.06	0.16	0.06	0.16	0.18	0.07
^{237}Np	6.10	71	-0.02	0.02	0.01	0.05	0.02	0.01	-0.04	0.03	0.01	-0.00	0.04	0.02	-0.05	0.05	0.02	-0.17	0.08	0.03	-0.03	0.12	0.06	0.12	0.17	0.11
^{237}Np	6.10	90	0.00	0.02	0.01	-0.01	0.02	0.01	0.00	0.02	0.01	0.02	0.03	0.01	0.07	0.04	0.02	-0.09	0.06	0.03	-0.03	0.09	0.04	0.14	0.20	0.07
^{237}Np	6.10	107	0.02	0.02	0.01	0.00	0.02	0.01	0.01	0.03	0.01	-0.04	0.04	0.02	-0.07	0.06	0.02	0.05	0.10	0.04	-0.09	0.13	0.05	-0.21	0.20	0.10
^{237}Np	6.10	126	-0.01	0.02	0.01	0.01	0.01	0.01	0.01	0.02	0.01	0.00	0.03	0.01	0.14	0.04	0.02	-0.05	0.06	0.03	-0.10	0.10	0.04	-	-	-
^{237}Np	6.20	54	-0.01	0.01	0.01	-0.01	0.01	0.01	-0.02	0.01	0.01	-0.06	0.02	0.01	0.01	0.03	0.02	0.04	0.05	0.03	0.18	0.11	0.05	0.07	0.12	0.07
^{237}Np	6.20	71	0.01	0.02	0.01	0.03	0.01	0.01	0.05	0.02	0.01	0.05	0.03	0.02	0.00	0.04	0.02	0.01	0.05	0.03	-0.07	0.09	0.06	0.01	0.13	0.11
^{237}Np	6.20	90	0.02	0.01	0.01	0.02	0.01	0.01	0.01	0.01	0.01	0.01	0.02	0.01	0.00	0.03	0.02	-0.10	0.04	0.03	0.02	0.07	0.04	-0.03	0.11	0.07
^{237}Np	6.20	107	-0.01	0.02	0.01	0.02	0.01	0.01	0.00	0.02	0.01	0.07	0.03	0.02	0.03	0.04	0.02	-0.11	0.06	0.04	-0.16	0.09	0.05	0.00	0.19	0.10
^{237}Np	6.20	126	-0.02	0.01	0.01	0.02	0.01	0.01	-0.01	0.01	0.01	0.03	0.02	0.01	0.01	0.03	0.02	-0.06	0.05	0.03	-0.05	0.08	0.04	-0.17	0.17	0.08
^{237}Np	6.35	54	0.02	0.02	0.01	-0.01	0.01	0.01	0.00	0.02	0.01	0.02	0.03	0.01	0.06	0.04	0.02	0.04	0.06	0.03	0.23	0.11	0.05	0.00	0.16	0.08
^{237}Np	6.35	71	0.02	0.02	0.01	0.03	0.02	0.01	0.02	0.02	0.01	0.03	0.03	0.02	0.02	0.05	0.02	-0.08	0.07	0.03	0.19	0.11	0.06	-0.17	0.14	0.10
^{237}Np	6.35	90	-0.01	0.01	0.01	0.03	0.01	0.01	0.02	0.02	0.01	0.02	0.02	0.01	0.05	0.04	0.02	-0.14	0.05	0.03	0.16	0.09	0.04	0.06	0.11	0.07
^{237}Np	6.35	107	0.03	0.02	0.01	-0.01	0.02	0.01	-0.01	0.02	0.01	0.02	0.03	0.02	0.01	0.05	0.02	-0.05	0.08	0.04	0.01	0.11	0.05	-0.14	0.23	0.10
^{237}Np	6.35	126	0.01	0.01	0.01	0.02	0.01	0.01	0.00	0.02	0.01	0.04	0.02	0.01	0.07	0.04	0.02	-0.01	0.06	0.03	-0.18	0.09	0.04	-0.11	0.21	0.10
^{237}Np	6.50	54	0.01	0.01	0.01	-0.02	0.01	0.01	0.04	0.02	0.01	0.04	0.02	0.01	-0.05	0.04	0.02	0.08	0.06	0.03	0.09	0.10	0.05	0.13	0.14	0.07
^{237}Np	6.50	71	0.03	0.02	0.01	0.04	0.02	0.01	0.01	0.02	0.01	0.03	0.03	0.02	0.07	0.04	0.02	0.12	0.07	0.03	-0.10	0.10	0.06	0.05	0.17	0.11
^{237}Np	6.50	90	0.01	0.01	0.01	0.02	0.01	0.01	0.01	0.02	0.01	0.01	0.02	0.01	0.01	0.03	0.02	-0.00	0.05	0.03	0.05	0.08	0.04	-0.01	0.14	0.07
^{237}Np	6.50	107	0.03	0.02	0.01	-0.00	0.02	0.01	0.00	0.02	0.01	-0.02	0.03	0.02	0.01	0.05	0.02	-0.10	0.07	0.04	0.01	0.10	0.05	0.36	0.25	0.09
^{237}Np	6.50	126	0.00	0.01	0.01	0.02	0.01	0.01	-0.04	0.02	0.01	0.02	0.02	0.01	0.03	0.04	0.02	-0.01	0.05	0.03	-0.25	0.08	0.04	-0.11	0.20	0.08
^{237}Np	6.80	54	0.00	0.01	0.01	-0.01	0.01	0.01	-0.00	0.01	0.01	0.01	0.02	0.01	0.06	0.03	0.02	-0.01	0.04	0.03	0.13	0.07	0.05	0.08	0.11	0.08
^{237}Np	6.80	71	0.04	0.01	0.01	-0.01	0.01	0.01	-0.00	0.02	0.01	0.02	0.02	0.02	0.01	0.03	0.02	0.02	0.05	0.03	-0.02	0.07	0.06	0.09	0.11	0.10
^{237}Np	6.80	90	0.01	0.01	0.01	0.00	0.01	0.01	-0.01	0.01	0.01	0.01	0.02	0.01	0.01	0.03	0.02	-0.01	0.04	0.03	-0.01	0.06	0.04	0.17	0.09	0.07
^{237}Np	6.80	107	-0.00	0.01	0.01	-0.01	0.01	0.01	0.01	0.02	0.01	-0.01	0.02	0.02	0.07	0.03	0.02	-0.11	0.05	0.04	-0.11	0.07	0.05	-0.11	0.13	0.10
^{237}Np	6.80	126	0.00	0.01	0.01	-0.00	0.01	0.01	-0.03	0.01	0.01	-0.01	0.02	0.01	0.06	0.02	0.02	0.03	0.04	0.03	0.02	0.07	0.04	0.17	0.11	0.09
^{237}Np	7.00	54	-0.01	0.01	0.01	-0.01	0.01	0.01	-0.02	0.01	0.01	-0.00	0.02	0.01	0.04	0.03	0.02	0.01	0.04	0.03	0.07	0.07	0.05	0.23	0.10	0.07
^{237}Np	7.00	71	0.01	0.01	0.01	0.02	0.01	0.01	0.00	0.02	0.01	0.02	0.02	0.02	-0.01	0.03	0.02	0.03	0.05	0.03	-0.18	0.09	0.06	0.08	0.13	0.11
^{237}Np	7.00	90	-0.01	0.01	0.01	-0.01	0.01	0.01	0.01	0.01	0.01	0.00	0.02	0.01	0.01	0.02	0.02	-0.02	0.04	0.03	-0.01	0.06	0.04	-0.13	0.10	0.07
^{237}Np	7.00	107	-0.01	0.01	0.01	0.02	0.01	0.01	0.02	0.02	0.01	0.04	0.02	0.02	0.02	0.03	0.02	-0.08	0.05	0.04	0.10	0.08	0.05	-0.13	0.15	0.10
^{237}Np	7.00	126	-0.00	0.01	0.01	0.01	0.01	0.01	-0.01	0.01	0.01	0.01	0.02	0.01	0.03	0.03	0.02	-0.01	0.04	0.03	-0.09	0.06	0.04	0.04	0.11	0.09
^{239}Pu	5.30	54	-0.01	0.04	0.02	-0.05	0.05	0.04	0.07	0.08	0.04	-0.16	0.12	0.04	0.20	0.16	0.05	-0.12	0.56	0.10	-0.17	0.42	0.07	-	-	-
^{239}Pu	5.30	71	-0.06	0.08	0.01	-0.07	0.10	0.02	0.03	0.19	0.02	0.16	0.19	0.03	-0.36	0.71	0.10	0.42	0.49	0.06	0.07	0.27	0.06	-	-	-
^{239}Pu	5.30	90	-0.02	0.04	0.01	0.02	0.06	0.01	0.07	0.07	0.01	0.04	0.13	0.02	-0.02	0.22	0.04	0.18	0.29	0.06	-	-	-	-	-	-
^{239}Pu	5.30	107	-0.20	0.07	0.02	0.08	0.10	0.01	-0.08	0.11	0.02	-0.28	0.17	0.04	-0.11	0.41	0.05	-0.18	0.45	0.13	-0.39	0.68	0.10	-	-	-
^{239}Pu	5.30	126	-0.05	0.04	0.01	0.04	0.05	0.02	0.00	0.08	0.03	-0.10	0.13	0.03	0.02	0.22	0.04	-	-	-	-	-	-	-	-	-
^{239}Pu	5.30	144	-0.01	0.07	0.01	0.08	0.10	0.03	-0.12	0.14	0.02	0.62	0.39	0.04	0.25	0.38	0.04	-	-	-	0.79	0.09	0.02	-	-	-
^{239}Pu	5.40	54	0.01	0.03	0.02	-0.02	0.04	0.01	-0.09	0.06	0.02	-0.20	0.09	0.03	0.15	0.15	0.04	-0.01	0.26	0.08	-	-	-	-	-	-
^{239}Pu	5.40	71	-0.06	0.05	0.01	-0.11	0.06	0.02	-0.18	0.11	0.02	-0.19	0.14	0.03	0.05	0.27	0.08	-0.22	0.32	0.15	-0.77	0.79	0.60	-0.25	1.01	0.19

Continued on Next Page...

Table B.1 – Continued

Target	E_γ	θ	$\Sigma(2)$	$\Delta\Sigma_1(2)$	$\Delta\Sigma_2(2)$	$\Sigma(3)$	$\Delta\Sigma_1(3)$	$\Delta\Sigma_2(3)$	$\Sigma(4)$	$\Delta\Sigma_1(4)$	$\Delta\Sigma_2(4)$	$\Sigma(5)$	$\Delta\Sigma_1(5)$	$\Delta\Sigma_2(5)$	$\Sigma(6)$	$\Delta\Sigma_1(6)$	$\Delta\Sigma_2(6)$	$\Sigma(7)$	$\Delta\Sigma_1(7)$	$\Delta\Sigma_2(7)$	$\Sigma(8)$	$\Delta\Sigma_1(8)$	$\Delta\Sigma_2(8)$	$\Sigma(9)$	$\Delta\Sigma_1(9)$	$\Delta\Sigma_2(9)$
^{239}Pu	5.40	90	-0.03	0.03	0.01	-0.05	0.04	0.01	-0.06	0.06	0.01	-0.04	0.10	0.02	0.18	0.14	0.03	0.10	0.22	0.05	-	-	-	-	-	-
^{239}Pu	5.40	107	-0.00	0.06	0.01	-0.02	0.08	0.01	0.10	0.13	0.03	-0.43	0.12	0.03	-0.02	0.34	0.07	0.01	0.75	0.25	-	-	-	-	-	-
^{239}Pu	5.40	126	-0.04	0.03	0.01	-0.01	0.05	0.01	-0.12	0.06	0.01	-0.05	0.12	0.02	-0.01	0.20	0.04	0.04	0.32	0.14	-	-	-	0.06	0.40	0.13
^{239}Pu	5.40	144	-0.04	0.05	0.01	-0.08	0.07	0.01	-0.16	0.10	0.02	-0.04	0.21	0.03	0.05	0.22	0.04	-0.36	0.58	0.11	-	-	-	-	-	-
^{239}Pu	5.50	54	-0.06	0.02	0.01	-0.08	0.03	0.01	-0.11	0.04	0.01	-0.17	0.05	0.03	-0.13	0.08	0.02	-0.12	0.13	0.03	-0.29	0.24	0.05	-0.36	0.31	0.08
^{239}Pu	5.50	71	-0.10	0.03	0.01	-0.04	0.04	0.01	-0.05	0.06	0.01	-0.20	0.09	0.02	-0.03	0.14	0.05	-0.23	0.20	0.10	-0.38	0.26	0.12	-	-	-
^{239}Pu	5.50	90	-0.06	0.02	0.01	-0.12	0.03	0.01	-0.13	0.04	0.01	-0.22	0.06	0.01	-0.17	0.09	0.02	-0.08	0.13	0.04	-0.11	0.22	0.06	-	-	-
^{239}Pu	5.50	107	-0.03	0.03	0.01	-0.10	0.04	0.02	-0.12	0.06	0.02	-0.17	0.09	0.03	-0.23	0.12	0.03	-0.20	0.27	0.06	-0.76	0.27	0.14	-	-	-
^{239}Pu	5.50	126	-0.07	0.02	0.01	-0.04	0.03	0.01	-0.11	0.04	0.01	-0.12	0.06	0.02	-0.16	0.12	0.04	-0.05	0.13	0.05	-	-	-	-	-	-
^{239}Pu	5.50	144	-0.04	0.03	0.01	-0.10	0.04	0.01	-0.09	0.06	0.02	-0.01	0.10	0.02	0.39	0.18	0.04	-0.07	0.29	0.06	-0.34	0.30	0.11	-	-	-
^{239}Pu	5.60	54	-0.04	0.02	0.00	-0.02	0.02	0.01	-0.08	0.03	0.01	-0.05	0.04	0.01	-0.09	0.06	0.02	-0.23	0.10	0.03	-0.16	0.19	0.05	0.13	0.27	0.09
^{239}Pu	5.60	71	-0.01	0.02	0.01	-0.08	0.03	0.01	-0.11	0.05	0.01	-0.27	0.08	0.02	-0.06	0.10	0.03	-0.21	0.22	0.05	0.08	0.24	0.08	0.07	0.33	0.19
^{239}Pu	5.60	90	-0.11	0.02	0.00	-0.07	0.02	0.01	-0.14	0.03	0.01	-0.09	0.05	0.01	-0.10	0.08	0.02	-0.13	0.11	0.03	0.03	0.37	0.07	-	-	-
^{239}Pu	5.60	107	-0.04	0.02	0.01	-0.05	0.03	0.01	-0.15	0.05	0.01	-0.03	0.07	0.02	-0.14	0.14	0.03	0.04	0.24	0.06	0.01	0.33	0.07	-0.34	0.59	0.52
^{239}Pu	5.60	126	-0.07	0.02	0.00	-0.05	0.02	0.01	-0.04	0.03	0.01	-0.09	0.05	0.01	-0.06	0.08	0.02	-0.04	0.14	0.03	-0.16	0.33	0.21	0.09	0.35	0.09
^{239}Pu	5.60	144	-0.03	0.02	0.01	-0.08	0.03	0.01	0.03	0.04	0.01	-0.03	0.06	0.02	0.14	0.11	0.03	-0.12	0.16	0.05	0.39	0.35	0.07	-0.16	1.01	0.15
^{239}Pu	5.70	54	-0.01	0.02	0.01	0.01	0.03	0.01	0.01	0.04	0.01	0.08	0.06	0.02	-0.08	0.09	0.03	0.08	0.16	0.06	0.32	0.28	0.06	0.06	0.40	0.13
^{239}Pu	5.70	71	-0.04	0.03	0.01	-0.09	0.04	0.01	-0.03	0.06	0.02	-0.27	0.11	0.04	-0.06	0.13	0.05	0.00	0.21	0.07	-0.45	0.61	0.16	0.49	1.39	0.17
^{239}Pu	5.70	90	-0.03	0.02	0.01	-0.05	0.03	0.01	-0.02	0.04	0.01	-0.08	0.07	0.02	-0.16	0.10	0.03	-0.03	0.19	0.05	0.42	0.33	0.08	0.54	0.48	0.11
^{239}Pu	5.70	107	-0.04	0.03	0.01	0.01	0.04	0.01	-0.16	0.06	0.02	-0.11	0.08	0.03	-0.20	0.14	0.04	-0.10	0.20	0.06	0.12	0.45	0.11	-	-	-
^{239}Pu	5.70	126	-0.02	0.02	0.01	-0.04	0.03	0.01	0.10	0.04	0.01	0.01	0.07	0.02	-0.04	0.11	0.04	-0.15	0.18	0.05	-0.16	0.52	0.09	-0.19	0.45	0.15
^{239}Pu	5.70	144	0.02	0.03	0.01	0.03	0.04	0.03	0.09	0.05	0.04	0.07	0.07	0.04	-0.16	0.12	0.04	-0.03	0.19	0.09	0.33	0.43	0.11	0.69	2.00	0.08
^{239}Pu	5.80	54	-0.03	0.02	0.00	-0.01	0.02	0.01	-0.03	0.03	0.01	-0.01	0.04	0.01	-0.06	0.07	0.02	0.03	0.12	0.03	-0.28	0.23	0.05	-0.36	0.27	0.08
^{239}Pu	5.80	71	-0.01	0.02	0.01	-0.03	0.03	0.01	0.01	0.05	0.01	0.05	0.07	0.02	-0.04	0.16	0.04	0.07	0.23	0.08	-0.43	0.36	0.06	-0.61	0.75	0.18
^{239}Pu	5.80	90	-0.04	0.02	0.00	-0.08	0.02	0.01	0.02	0.04	0.01	-0.10	0.05	0.01	-0.01	0.09	0.02	-0.02	0.11	0.03	0.43	0.23	0.05	-	-	-
^{239}Pu	5.80	107	0.02	0.03	0.01	-0.06	0.03	0.01	-0.10	0.05	0.02	0.16	0.09	0.02	-0.01	0.13	0.03	-0.41	0.19	0.09	-0.52	0.29	0.30	0.53	1.50	0.12
^{239}Pu	5.80	126	-0.03	0.02	0.00	-0.04	0.02	0.01	-0.06	0.03	0.01	-0.07	0.05	0.01	-0.02	0.08	0.02	-0.29	0.13	0.04	0.31	0.51	0.08	0.10	0.28	0.08
^{239}Pu	5.80	144	-0.00	0.02	0.01	-0.01	0.03	0.01	-0.08	0.05	0.01	-0.03	0.07	0.02	0.11	0.13	0.04	-0.32	0.19	0.05	-0.39	0.27	0.11	-0.42	0.46	0.20
^{239}Pu	5.90	54	-0.01	0.02	0.01	0.01	0.02	0.01	-0.05	0.03	0.01	-0.04	0.04	0.01	0.01	0.06	0.02	-0.06	0.09	0.03	-0.14	0.15	0.05	0.07	0.24	0.11
^{239}Pu	5.90	71	0.03	0.02	0.01	0.03	0.03	0.01	-0.03	0.04	0.01	-0.15	0.06	0.02	-0.04	0.12	0.03	-0.06	0.16	0.05	0.10	0.20	0.08	-	-	-
^{239}Pu	5.90	90	-0.01	0.02	0.01	0.03	0.02	0.01	0.02	0.03	0.01	-0.09	0.04	0.01	0.04	0.07	0.02	-0.28	0.09	0.03	0.29	0.18	0.06	0.37	0.53	0.10
^{239}Pu	5.90	107	-0.01	0.02	0.01	-0.03	0.03	0.01	-0.04	0.05	0.02	-0.02	0.07	0.02	-0.05	0.12	0.04	0.06	0.16	0.05	-0.29	0.25	0.11	-	-	-
^{239}Pu	5.90	126	0.01	0.02	0.01	0.02	0.02	0.01	0.02	0.03	0.01	0.00	0.05	0.02	0.04	0.07	0.02	-0.01	0.13	0.04	-0.17	0.16	0.06	-0.37	0.45	0.10
^{239}Pu	5.90	144	0.00	0.02	0.01	0.01	0.03	0.01	0.02	0.05	0.02	0.05	0.08	0.02	-0.02	0.11	0.04	0.04	0.21	0.05	-0.22	0.25	0.09	-	-	-
^{239}Pu	6.00	54	-0.03	0.02	0.01	0.01	0.03	0.01	0.01	0.03	0.01	0.04	0.05	0.02	-0.05	0.08	0.03	0.02	0.11	0.04	-0.00	0.22	0.06	-	-	-
^{239}Pu	6.00	71	0.05	0.03	0.01	0.00	0.04	0.01	-0.01	0.06	0.02	-0.06	0.09	0.03	-0.05	0.11	0.04	0.03	0.20	0.07	0.41	0.41	0.38	0.42	0.42	0.22
^{239}Pu	6.00	90	0.02	0.02	0.01	-0.03	0.03	0.01	0.00	0.04	0.01	0.01	0.06	0.02	-0.06	0.09	0.03	-0.14	0.15	0.04	-	-	-	0.13	0.29	0.09
^{239}Pu	6.00	107	0.05	0.03	0.01	0.05	0.04	0.01	-0.09	0.06	0.02	-0.05	0.09	0.03	0.06	0.13	0.05	-0.20	0.23	0.07	-	-	-	-0.28	1.57	0.51
^{239}Pu	6.00	126	-0.04	0.02	0.01	-0.00	0.03	0.01	-0.07	0.04	0.01	-0.07	0.06	0.02	-0.01	0.09	0.03	-0.12	0.14	0.04	0.05	0.29	0.09	0.13	0.38	0.22
^{239}Pu	6.00	144	-0.00	0.02	0.01	0.04	0.03	0.01	0.02	0.05	0.02	0.09	0.08	0.04	-0.04	0.10	0.03	-0.01	0.16	0.06	-0.43	0.29	0.15	0.49	0.44	0.13
^{239}Pu	6.10	54	0.01	0.01	0.01	0.00	0.01	0.01	0.04	0.02	0.01	0.04	0.03	0.02	-0.01	0.04	0.02	-0.05	0.06	0.03	-0.01	0.10	0.05	0.00	0.12	0.08
^{239}Pu	6.10	71	0.01	0.01	0.01	0.02	0.02	0.01	0.02	0.03	0.01	0.07	0.04	0.02	-0.01	0.06	0.03	-0.09	0.09	0.04	0.04	0.12	0.07	-0.44	0.42	0.12

Continued on Next Page...

Table B.1 – Continued

Target	E_γ	θ	$\Sigma(2)$	$\Delta\Sigma_1(2)$	$\Delta\Sigma_2(2)$	$\Sigma(3)$	$\Delta\Sigma_1(3)$	$\Delta\Sigma_2(3)$	$\Sigma(4)$	$\Delta\Sigma_1(4)$	$\Delta\Sigma_2(4)$	$\Sigma(5)$	$\Delta\Sigma_1(5)$	$\Delta\Sigma_2(5)$	$\Sigma(6)$	$\Delta\Sigma_1(6)$	$\Delta\Sigma_2(6)$	$\Sigma(7)$	$\Delta\Sigma_1(7)$	$\Delta\Sigma_2(7)$	$\Sigma(8)$	$\Delta\Sigma_1(8)$	$\Delta\Sigma_2(8)$	$\Sigma(9)$	$\Delta\Sigma_1(9)$	$\Delta\Sigma_2(9)$
^{239}Pu	6.10	90	0.01	0.01	0.01	0.02	0.01	0.01	0.01	0.02	0.01	0.02	0.03	0.01	0.10	0.04	0.02	0.07	0.06	0.04	0.04	0.12	0.05	-0.01	0.20	0.10
^{239}Pu	6.10	107	0.01	0.01	0.01	0.01	0.02	0.01	0.05	0.03	0.02	-0.02	0.04	0.02	0.04	0.07	0.03	0.09	0.11	0.06	-0.14	0.14	0.07	0.33	0.39	0.12
^{239}Pu	6.10	126	0.01	0.01	0.01	0.04	0.01	0.01	0.01	0.02	0.01	-0.02	0.03	0.02	-0.02	0.05	0.02	-0.08	0.07	0.04	0.32	0.13	0.06	0.35	0.18	0.07
^{239}Pu	6.10	144	0.01	0.01	0.01	0.00	0.02	0.01	0.00	0.03	0.02	0.00	0.04	0.02	0.09	0.06	0.03	-0.22	0.11	0.05	0.20	0.25	0.09	0.36	0.24	0.13
^{239}Pu	6.20	54	0.02	0.01	0.00	0.02	0.01	0.01	0.03	0.02	0.01	0.02	0.03	0.01	-0.00	0.04	0.02	0.06	0.07	0.03	0.06	0.11	0.05	0.13	0.17	0.07
^{239}Pu	6.20	71	0.03	0.01	0.01	0.02	0.02	0.01	-0.05	0.03	0.01	0.02	0.04	0.02	-0.00	0.07	0.03	0.24	0.11	0.04	0.33	0.14	0.05	-0.73	0.95	0.08
^{239}Pu	6.20	90	0.02	0.01	0.00	0.04	0.01	0.01	0.03	0.02	0.01	0.06	0.03	0.01	0.10	0.04	0.02	-0.06	0.07	0.03	-0.16	0.10	0.04	0.42	0.19	0.08
^{239}Pu	6.20	107	0.04	0.01	0.01	0.04	0.02	0.01	-0.02	0.03	0.01	-0.01	0.04	0.02	0.04	0.07	0.03	-0.02	0.09	0.04	-0.07	0.17	0.06	-0.25	0.53	0.18
^{239}Pu	6.20	126	0.01	0.01	0.00	0.03	0.01	0.01	0.03	0.02	0.01	-0.01	0.03	0.01	-0.05	0.05	0.02	-0.00	0.08	0.03	-0.18	0.12	0.05	-0.37	0.25	0.07
^{239}Pu	6.20	144	0.03	0.01	0.01	-0.00	0.02	0.01	0.03	0.03	0.01	0.08	0.04	0.02	0.02	0.07	0.02	-0.16	0.10	0.04	0.01	0.20	0.13	-0.05	0.29	0.12
^{239}Pu	6.30	54	0.04	0.01	0.01	0.01	0.01	0.01	0.03	0.02	0.01	0.06	0.02	0.01	0.05	0.03	0.02	0.01	0.05	0.03	-0.06	0.09	0.05	0.02	0.12	0.08
^{239}Pu	6.30	71	0.03	0.01	0.01	0.03	0.02	0.01	0.02	0.02	0.01	0.08	0.03	0.02	0.12	0.05	0.03	0.08	0.09	0.05	0.05	0.11	0.06	0.18	0.31	0.13
^{239}Pu	6.30	90	0.02	0.01	0.01	0.02	0.01	0.01	0.02	0.02	0.01	0.05	0.02	0.01	0.06	0.04	0.02	-0.05	0.05	0.03	0.03	0.09	0.05	0.18	0.14	0.10
^{239}Pu	6.30	107	0.02	0.01	0.01	0.04	0.02	0.01	0.03	0.03	0.02	0.06	0.04	0.02	0.12	0.06	0.03	0.08	0.10	0.06	0.03	0.15	0.07	0.03	0.28	0.14
^{239}Pu	6.30	126	0.03	0.01	0.01	0.05	0.01	0.01	0.01	0.02	0.01	0.00	0.03	0.02	0.03	0.04	0.02	-0.08	0.07	0.04	-0.17	0.10	0.05	0.03	0.16	0.08
^{239}Pu	6.30	144	0.03	0.01	0.01	-0.01	0.02	0.01	0.00	0.02	0.01	0.02	0.04	0.02	0.05	0.05	0.03	-0.07	0.10	0.05	0.39	0.22	0.07	-0.24	0.19	0.13
^{239}Pu	6.40	54	-0.00	0.02	0.01	0.04	0.02	0.01	0.01	0.03	0.01	-0.02	0.04	0.01	0.03	0.06	0.02	0.06	0.10	0.03	-0.28	0.15	0.05	0.34	0.24	0.07
^{239}Pu	6.40	71	0.03	0.02	0.01	0.01	0.03	0.01	-0.03	0.05	0.01	-0.06	0.06	0.02	-0.03	0.11	0.03	-0.01	0.14	0.05	0.43	0.22	0.06	0.69	0.35	0.08
^{239}Pu	6.40	90	0.01	0.02	0.01	0.03	0.02	0.01	0.02	0.03	0.01	0.01	0.05	0.01	0.08	0.06	0.02	0.04	0.11	0.03	0.11	0.15	0.05	0.07	0.25	0.09
^{239}Pu	6.40	107	0.02	0.02	0.01	0.03	0.03	0.01	0.02	0.05	0.02	-0.07	0.07	0.02	0.08	0.12	0.04	0.13	0.16	0.08	0.29	0.36	0.09	-0.01	0.52	0.26
^{239}Pu	6.40	126	0.02	0.02	0.01	0.07	0.02	0.01	-0.06	0.03	0.01	0.04	0.05	0.02	0.04	0.08	0.02	-0.11	0.14	0.04	-0.23	0.22	0.06	0.28	0.38	0.08
^{239}Pu	6.40	144	0.04	0.02	0.01	0.06	0.03	0.01	-0.05	0.05	0.02	0.06	0.07	0.02	0.25	0.11	0.03	0.10	0.16	0.06	0.52	0.54	0.08	-0.37	0.41	0.14
^{239}Pu	6.50	54	0.03	0.02	0.01	-0.00	0.02	0.01	0.01	0.03	0.01	0.12	0.04	0.02	-0.02	0.07	0.02	-0.20	0.09	0.03	-0.19	0.17	0.07	-0.23	0.37	0.12
^{239}Pu	6.50	71	0.02	0.02	0.01	0.03	0.03	0.01	0.07	0.05	0.02	0.01	0.07	0.03	0.20	0.10	0.04	0.06	0.15	0.08	-0.01	0.32	0.15	-0.02	0.49	0.44
^{239}Pu	6.50	90	0.03	0.02	0.01	0.01	0.02	0.01	-0.00	0.03	0.01	0.04	0.05	0.02	0.16	0.08	0.03	-0.12	0.12	0.04	0.19	0.20	0.07	-	-	-
^{239}Pu	6.50	107	-0.01	0.02	0.01	0.08	0.03	0.01	-0.08	0.05	0.02	0.06	0.07	0.02	-0.01	0.11	0.04	-0.04	0.18	0.06	0.23	0.42	0.11	-0.24	0.31	0.16
^{239}Pu	6.50	126	-0.03	0.02	0.01	-0.04	0.02	0.01	-0.00	0.03	0.01	0.02	0.05	0.02	-0.02	0.07	0.03	0.08	0.11	0.04	0.19	0.26	0.15	-0.39	0.26	0.16
^{239}Pu	6.50	144	0.04	0.02	0.01	-0.01	0.03	0.01	0.10	0.04	0.02	0.04	0.06	0.02	0.18	0.09	0.03	0.14	0.14	0.06	0.26	0.27	0.13	-	-	-
^{239}Pu	6.70	54	0.01	0.01	0.01	0.03	0.02	0.02	0.05	0.02	0.02	0.02	0.04	0.03	0.02	0.05	0.05	-0.07	0.09	0.08	-0.32	0.14	0.18	0.23	0.24	0.30
^{239}Pu	6.70	71	-0.01	0.02	0.02	-0.03	0.02	0.02	0.01	0.03	0.03	-0.13	0.05	0.04	-0.09	0.08	0.07	0.06	0.14	0.12	-0.13	0.23	0.21	-	-	-
^{239}Pu	6.70	90	0.01	0.01	0.01	0.06	0.02	0.02	0.07	0.03	0.02	0.08	0.04	0.03	-0.02	0.06	0.05	-0.09	0.09	0.09	-0.39	0.15	0.13	-	-	-
^{239}Pu	6.70	107	-0.02	0.02	0.02	0.06	0.03	0.02	-0.03	0.04	0.03	-0.02	0.06	0.05	-0.03	0.08	0.08	-0.35	0.12	0.12	0.56	0.17	0.21	0.62	0.74	0.23
^{239}Pu	6.70	126	0.06	0.01	0.01	0.03	0.02	0.02	0.07	0.03	0.02	0.04	0.04	0.04	0.03	0.06	0.06	0.02	0.09	0.08	0.28	0.15	0.15	0.64	0.20	0.33
^{239}Pu	6.70	144	0.01	0.02	0.02	-0.05	0.03	0.03	0.05	0.04	0.04	0.11	0.06	0.06	0.17	0.09	0.09	0.13	0.16	0.13	-0.19	0.22	0.28	0.79	0.33	0.25
^{239}Pu	6.80	54	0.02	0.01	0.01	0.03	0.02	0.02	0.03	0.02	0.02	-0.01	0.03	0.03	0.07	0.05	0.05	0.08	0.09	0.08	-0.25	0.15	0.13	0.14	0.27	0.28
^{239}Pu	6.80	71	0.01	0.02	0.02	-0.03	0.02	0.02	0.02	0.03	0.03	-0.04	0.05	0.04	-0.15	0.07	0.07	-0.04	0.13	0.12	-0.48	0.30	0.17	-	-	-
^{239}Pu	6.80	90	0.02	0.01	0.01	0.04	0.02	0.02	0.07	0.02	0.02	0.05	0.04	0.04	-0.05	0.05	0.05	-0.03	0.09	0.10	-0.20	0.14	0.18	-	-	-
^{239}Pu	6.80	107	0.02	0.02	0.02	0.01	0.02	0.02	-0.02	0.03	0.03	0.13	0.06	0.05	-0.16	0.08	0.08	0.05	0.15	0.13	0.38	0.16	0.15	0.31	0.47	1.74
^{239}Pu	6.80	126	0.05	0.01	0.01	0.00	0.02	0.02	0.02	0.03	0.02	0.02	0.04	0.04	-0.19	0.06	0.06	-0.08	0.08	0.07	0.06	0.15	0.15	0.50	0.19	0.43
^{239}Pu	6.80	144	-0.05	0.02	0.02	-0.05	0.03	0.03	0.09	0.04	0.04	0.10	0.06	0.06	0.30	0.08	0.08	-0.12	0.14	0.14	-0.05	0.23	0.28	0.27	0.31	0.54
^{239}Pu	7.00	54	0.01	0.01	0.00	0.01	0.01	0.01	0.02	0.01	0.01	0.00	0.02	0.01	0.02	0.02	0.02	0.02	0.04	0.02	0.08	0.07	0.04	-0.07	0.13	0.08
^{239}Pu	7.00	71	0.02	0.01	0.01	0.01	0.01	0.01	-0.02	0.02	0.01	0.05	0.03	0.02	0.02	0.04	0.02	0.15	0.06	0.04	0.05	0.11	0.06	-0.12	0.22	0.13

Continued on Next Page...

Table B.1 – Continued

Target	E_γ	θ	$\Sigma(2)$	$\Delta\Sigma_1(2)$	$\Delta\Sigma_2(2)$	$\Sigma(3)$	$\Delta\Sigma_1(3)$	$\Delta\Sigma_2(3)$	$\Sigma(4)$	$\Delta\Sigma_1(4)$	$\Delta\Sigma_2(4)$	$\Sigma(5)$	$\Delta\Sigma_1(5)$	$\Delta\Sigma_2(5)$	$\Sigma(6)$	$\Delta\Sigma_1(6)$	$\Delta\Sigma_2(6)$	$\Sigma(7)$	$\Delta\Sigma_1(7)$	$\Delta\Sigma_2(7)$	$\Sigma(8)$	$\Delta\Sigma_1(8)$	$\Delta\Sigma_2(8)$	$\Sigma(9)$	$\Delta\Sigma_1(9)$	$\Delta\Sigma_2(9)$
^{239}Pu	7.00	90	0.01	0.01	0.00	0.00	0.01	0.01	0.03	0.01	0.01	0.00	0.02	0.01	0.02	0.03	0.02	-0.03	0.04	0.03	0.03	0.07	0.04	-0.15	0.11	0.07
^{239}Pu	7.00	107	0.03	0.01	0.01	0.01	0.01	0.01	-0.00	0.02	0.01	-0.02	0.03	0.02	-0.08	0.04	0.03	-0.01	0.06	0.04	-0.11	0.10	0.06	-0.12	0.19	0.10
^{239}Pu	7.00	126	0.01	0.01	0.00	0.01	0.01	0.01	-0.00	0.01	0.01	0.03	0.02	0.01	0.00	0.03	0.02	-0.05	0.04	0.03	-0.15	0.08	0.05	-0.40	0.12	0.08
^{239}Pu	7.00	144	0.01	0.01	0.01	-0.01	0.01	0.01	0.01	0.02	0.01	0.05	0.02	0.02	0.03	0.04	0.02	-0.06	0.06	0.04	-0.14	0.10	0.06	0.05	0.16	0.11
^{240}Pu	5.80	54	-0.00	0.07	0.02	0.08	0.07	0.02	0.09	0.13	0.04	-	-	-	-	-	-	-	-	-	-	-	-	-	-	-
^{240}Pu	5.80	71	-0.10	0.08	0.02	0.31	0.11	0.02	0.09	0.15	0.04	0.87	0.30	0.03	0.49	0.19	0.05	-	-	-	-	-	-	-	-	-
^{240}Pu	5.80	90	0.13	0.06	0.02	0.17	0.07	0.02	-0.06	0.09	0.02	-	-	-	-	-	-	-0.32	0.18	0.05	-	-	-	-0.51	4304.11	10729.26
^{240}Pu	5.80	107	0.01	0.08	0.02	0.38	0.11	0.02	-0.46	0.26	0.04	0.23	0.20	0.04	-0.40	0.49	0.09	-	-	-	-	-	-	0.29	4544.07	1136.47
^{240}Pu	5.80	126	-0.15	0.06	0.01	0.15	0.07	0.01	0.25	0.10	0.03	-	-	-	-	-	-	0.16	0.27	0.28	-	-	-	-	-	-
^{240}Pu	5.80	144	-0.18	0.15	0.03	0.31	0.29	0.05	0.71	0.81	0.06	-	-	-	-	-	-	-0.38	0.67	0.54	-	-	-	-0.56	5050.40	11109.82
^{240}Pu	5.90	54	0.03	0.02	0.01	0.11	0.03	0.01	0.19	0.05	0.01	0.02	0.06	0.01	-	-	-	-	-	-	-	-	-	-	-	-
^{240}Pu	5.90	71	0.03	0.03	0.01	0.08	0.04	0.01	0.38	0.06	0.01	-0.27	0.11	0.02	0.34	0.12	0.05	0.18	0.12	0.05	-	-	-	0.46	0.14	0.08
^{240}Pu	5.90	90	0.11	0.02	0.00	0.11	0.02	0.01	0.15	0.04	0.01	0.17	0.06	0.01	-0.15	0.11	0.03	-	-	-	-	-	-	-	-	-
^{240}Pu	5.90	107	0.07	0.03	0.01	0.39	0.04	0.01	-0.12	0.08	0.02	0.23	0.09	0.02	0.27	0.21	0.04	0.42	0.25	0.05	-	-	-	0.53	0.35	0.13
^{240}Pu	5.90	126	0.05	0.02	0.00	0.12	0.03	0.01	0.30	0.06	0.01	-0.19	0.06	0.01	0.02	0.14	0.06	-0.40	0.13	0.05	-	-	-	-	-	-
^{240}Pu	6.00	54	0.03	0.03	0.01	0.04	0.04	0.01	0.05	0.07	0.03	0.17	0.10	0.03	-	-	-	-	-	-	-	-	-	-	-	-
^{240}Pu	6.00	71	0.01	0.04	0.02	0.21	0.05	0.02	0.05	0.06	0.03	0.58	0.12	0.03	0.35	0.15	0.05	-	-	-	-	-	-	-	-	-
^{240}Pu	6.00	90	0.13	0.03	0.01	0.20	0.03	0.01	0.06	0.04	0.02	0.49	0.11	0.03	-	-	-	0.03	0.18	0.10	-	-	-	-0.59	0.51	1.47
^{240}Pu	6.00	107	0.05	0.04	0.01	0.24	0.05	0.02	0.11	0.09	0.03	0.29	0.10	0.04	0.83	0.84	0.05	-	-	-	-	-	-	0.73	0.19	0.40
^{240}Pu	6.00	126	-0.01	0.03	0.01	0.16	0.04	0.01	0.05	0.06	0.02	-	-	-	-	-	-	0.10	0.25	0.23	-	-	-	-0.38	0.72	0.49
^{240}Pu	6.00	144	0.00	0.07	0.03	-0.02	0.11	0.04	-0.11	0.27	0.10	-	-	-	-	-	-	0.17	0.65	0.68	-	-	-	-0.71	1.14	1.66
^{240}Pu	6.10	54	0.08	0.03	0.01	0.03	0.03	0.01	0.02	0.05	0.02	0.25	0.07	0.03	0.22	0.21	0.05	-	-	-	-	-	-	-	-	-
^{240}Pu	6.10	71	0.02	0.03	0.02	0.15	0.04	0.02	-0.03	0.06	0.03	0.33	0.11	0.04	0.78	0.15	0.05	-	-	-	-	-	-	-	-	-
^{240}Pu	6.10	90	0.10	0.02	0.01	0.13	0.03	0.01	0.10	0.04	0.02	0.32	0.08	0.03	0.40	0.17	0.06	-0.03	0.12	0.08	-	-	-	-0.31	0.11	0.10
^{240}Pu	6.10	107	0.09	0.03	0.01	0.33	0.04	0.02	0.19	0.06	0.03	0.19	0.10	0.04	0.60	0.36	0.08	-	-	-	-	-	-	-	-	-
^{240}Pu	6.10	126	0.01	0.02	0.01	0.08	0.03	0.01	0.08	0.05	0.02	0.17	0.13	0.05	-	-	-	0.10	0.34	0.19	-	-	-	-0.52	0.30	0.11
^{240}Pu	6.10	144	0.10	0.06	0.03	0.03	0.08	0.04	-0.09	0.19	0.08	-0.61	0.43	0.11	-	-	-	-0.59	0.66	0.21	-	-	-	0.02	0.32	0.46
^{240}Pu	6.20	54	0.05	0.01	0.00	0.11	0.01	0.01	0.10	0.02	0.01	0.07	0.03	0.01	0.54	0.10	0.03	-	-	-	-	-	-	-	-	-
^{240}Pu	6.20	71	0.05	0.01	0.01	0.13	0.02	0.01	0.26	0.03	0.01	-0.04	0.04	0.02	0.27	0.07	0.03	0.33	0.08	0.03	-	-	-	0.24	0.08	0.06
^{240}Pu	6.20	90	0.12	0.01	0.00	0.15	0.01	0.01	0.17	0.02	0.01	0.24	0.03	0.01	0.02	0.05	0.02	-	-	-	-	-	-	-	-	-
^{240}Pu	6.20	107	0.09	0.01	0.01	0.21	0.02	0.01	0.06	0.03	0.01	0.19	0.04	0.02	0.21	0.09	0.03	0.22	0.10	0.05	-	-	-	0.88	0.03	0.02
^{240}Pu	6.20	126	0.07	0.01	0.00	0.12	0.01	0.01	0.19	0.02	0.01	0.03	0.03	0.02	0.14	0.07	0.03	-0.18	0.09	0.04	-	-	-	-	-	-
^{240}Pu	6.50	54	0.03	0.02	0.01	0.01	0.02	0.01	0.09	0.04	0.02	0.17	0.06	0.03	0.18	0.11	0.06	-	-	-	-	-	-	-	-	-
^{240}Pu	6.50	71	0.08	0.03	0.01	0.10	0.03	0.02	0.09	0.04	0.03	0.16	0.08	0.04	0.25	0.11	0.05	-	-	-	-	-	-	-	-	-
^{240}Pu	6.50	90	0.03	0.02	0.01	0.09	0.02	0.01	0.17	0.03	0.02	0.18	0.06	0.03	0.19	0.10	0.07	0.12	0.10	0.07	-	-	-	-	-	-
^{240}Pu	6.50	107	0.07	0.02	0.01	0.18	0.03	0.02	0.15	0.05	0.03	0.22	0.08	0.04	0.11	0.16	0.08	-	-	-	-	-	-	-0.11	0.21	0.16
^{240}Pu	6.50	126	0.06	0.02	0.01	0.04	0.03	0.01	0.09	0.04	0.02	0.04	0.08	0.05	-	-	-	0.50	0.16	0.19	-	-	-	-0.61	0.50	0.11
^{240}Pu	6.50	144	-0.05	0.05	0.03	0.14	0.06	0.04	0.30	0.12	0.07	-0.17	0.28	0.11	-	-	-	0.39	0.28	0.21	-	-	-	-0.21	0.24	0.21
^{240}Pu	6.70	54	0.05	0.01	0.01	0.07	0.01	0.02	0.13	0.01	0.03	0.06	0.02	0.05	0.05	0.03	0.08	-	-	-	-	-	-	-	-	-
^{240}Pu	6.70	71	0.08	0.01	0.02	0.13	0.01	0.02	0.10	0.02	0.03	0.11	0.02	0.05	0.02	0.05	0.10	-	-	-	-	-	-	-	-	-
^{240}Pu	6.70	90	0.10	0.01	0.01	0.12	0.01	0.01	0.16	0.01	0.02	0.14	0.02	0.04	0.29	0.04	0.08	0.06	0.04	0.16	-	-	-	-	-	-
^{240}Pu	6.70	107	0.08	0.01	0.02	0.12	0.01	0.02	0.12	0.02	0.03	0.11	0.03	0.06	0.27	0.06	0.12	-	-	-	-0.15	0.03	0.08	0.01	0.10	0.28

Continued on Next Page...

Table B.1 – Continued

Target	E_γ	θ	$\Sigma(2)$	$\Delta\Sigma_1(2)$	$\Delta\Sigma_2(2)$	$\Sigma(3)$	$\Delta\Sigma_1(3)$	$\Delta\Sigma_2(3)$	$\Sigma(4)$	$\Delta\Sigma_1(4)$	$\Delta\Sigma_2(4)$	$\Sigma(5)$	$\Delta\Sigma_1(5)$	$\Delta\Sigma_2(5)$	$\Sigma(6)$	$\Delta\Sigma_1(6)$	$\Delta\Sigma_2(6)$	$\Sigma(7)$	$\Delta\Sigma_1(7)$	$\Delta\Sigma_2(7)$	$\Sigma(8)$	$\Delta\Sigma_1(8)$	$\Delta\Sigma_2(8)$	$\Sigma(9)$	$\Delta\Sigma_1(9)$	$\Delta\Sigma_2(9)$
^{240}Pu	6.70	126	0.07	0.01	0.01	0.08	0.01	0.02	0.08	0.01	0.03	0.01	0.03	0.09	0.11	0.04	0.08	-	-	-	-	-	-	-	-	-
^{240}Pu	6.80	54	0.07	0.02	0.01	0.04	0.02	0.01	0.09	0.04	0.02	0.11	0.06	0.03	0.08	0.11	0.06	-	-	-	-	-	-	-	-	-
^{240}Pu	6.80	71	0.07	0.03	0.01	0.09	0.03	0.02	0.02	0.04	0.03	0.16	0.07	0.04	0.34	0.10	0.05	-	-	-	-	-	-	-	-	-
^{240}Pu	6.80	90	0.08	0.02	0.01	0.13	0.02	0.01	0.12	0.03	0.02	0.12	0.05	0.03	0.13	0.10	0.06	0.19	0.10	0.07	-	-	-	-0.41	0.17	0.11
^{240}Pu	6.80	107	0.09	0.02	0.01	0.08	0.03	0.02	0.12	0.05	0.03	0.25	0.07	0.04	0.13	0.15	0.08	-	-	-	-	-	-	-	-	-
^{240}Pu	6.80	126	0.08	0.02	0.01	0.12	0.02	0.01	0.07	0.04	0.02	0.20	0.08	0.05	0.28	0.32	0.10	0.30	0.17	0.24	-	-	-	-	-	-
^{240}Pu	6.80	144	0.08	0.05	0.03	0.00	0.06	0.04	-0.11	0.11	0.08	0.17	0.17	0.11	-	-	-	-	-	-	-	-	-	-0.42	0.27	0.16
^{240}Pu	7.00	54	0.07	0.02	0.01	0.01	0.02	0.01	0.06	0.03	0.02	0.08	0.04	0.03	-0.01	0.09	0.06	-	-	-	-	-	-	-	-	-
^{240}Pu	7.00	71	0.03	0.02	0.01	0.11	0.03	0.02	0.07	0.04	0.03	0.16	0.06	0.04	0.32	0.09	0.05	-	-	-	-0.12	0.12	0.13	-	-	-
^{240}Pu	7.00	90	0.08	0.01	0.01	0.08	0.02	0.01	0.08	0.02	0.02	0.14	0.04	0.03	0.01	0.09	0.06	-0.08	0.09	0.07	-	-	-	-0.44	0.12	0.09
^{240}Pu	7.00	107	0.10	0.02	0.01	0.12	0.02	0.02	0.15	0.04	0.03	0.17	0.07	0.04	0.26	0.17	0.08	-	-	-	-	-	-	0.22	0.20	0.19
^{240}Pu	7.00	126	0.02	0.01	0.01	0.08	0.02	0.01	0.07	0.03	0.02	0.05	0.06	0.05	-0.13	0.14	0.14	-	-	-	-	-	-	-0.11	0.22	0.17
^{240}Pu	7.00	144	0.03	0.04	0.03	-0.00	0.06	0.04	0.05	0.11	0.08	0.19	0.16	0.11	-	-	-	0.23	0.33	0.25	-	-	-	0.28	0.34	0.37
^{240}Pu	7.20	54	0.04	0.01	0.00	0.05	0.01	0.01	0.04	0.01	0.01	0.06	0.02	0.01	0.12	0.05	0.03	-0.03	0.07	0.04	-	-	-	-	-	-
^{240}Pu	7.20	71	0.05	0.01	0.01	0.08	0.01	0.01	0.10	0.02	0.01	0.08	0.03	0.02	0.11	0.04	0.03	0.11	0.06	0.04	0.53	0.55	0.08	0.32	0.14	0.08
^{240}Pu	7.20	90	0.07	0.01	0.00	0.09	0.01	0.01	0.07	0.01	0.01	0.10	0.02	0.01	0.10	0.04	0.02	0.23	0.08	0.04	-	-	-	-	-	-
^{240}Pu	7.20	107	0.04	0.01	0.01	0.09	0.01	0.01	0.05	0.02	0.01	0.07	0.03	0.02	0.08	0.06	0.03	0.19	0.09	0.05	-	-	-	0.39	0.37	0.15
^{240}Pu	7.20	126	0.04	0.01	0.00	0.05	0.01	0.01	0.03	0.02	0.01	0.07	0.02	0.01	-0.04	0.04	0.02	0.08	0.06	0.04	-	-	-	-	-	-
^{240}Pu	7.60	54	0.01	0.01	0.00	0.03	0.01	0.01	0.02	0.01	0.01	0.03	0.02	0.01	-0.00	0.04	0.03	-0.02	0.05	0.04	0.25	0.26	0.14	-	-	-
^{240}Pu	7.60	71	0.03	0.01	0.01	0.07	0.01	0.01	0.05	0.02	0.01	0.02	0.02	0.02	0.04	0.04	0.03	0.13	0.06	0.04	0.59	0.31	0.07	0.24	0.14	0.08
^{240}Pu	7.60	90	0.03	0.01	0.00	0.04	0.01	0.01	0.08	0.01	0.01	0.04	0.02	0.01	0.01	0.03	0.02	0.06	0.06	0.05	-	-	-	-	-	-
^{240}Pu	7.60	107	0.03	0.01	0.01	0.04	0.01	0.01	0.05	0.02	0.01	0.01	0.03	0.02	0.07	0.05	0.03	0.03	0.10	0.05	-	-	-	0.14	0.28	0.15
^{240}Pu	7.60	126	0.02	0.01	0.00	0.02	0.01	0.01	0.02	0.01	0.01	0.09	0.02	0.01	-0.05	0.04	0.02	0.10	0.05	0.04	-	-	-	-0.30	0.25	0.11

Appendix C

Tabulated Prompt Neutron Polarization Asymmetries Integrated Over Neutron Energy

Table C.1: Measured prompt neutron polarization asymmetries are given for each target, beam energy E_γ, and scattering angle θ. Yields have been integrated over detected neutron energies. Statistical (stat) and systematic (sys) uncertainties are also given.

Target	E_γ (MeV)	θ (deg)	Σ	$\Delta\Sigma$ (stat)	$\Delta\Sigma$ (sys)
^{232}Th	5.60	54	0.335	0.029	0.014
^{232}Th	5.60	90	0.453	0.024	0.005
^{232}Th	5.60	126	0.330	0.027	0.006
^{232}Th	5.60	71	0.458	0.048	0.015
^{232}Th	5.60	107	0.406	0.043	0.012
^{232}Th	5.80	54	0.309	0.017	0.007
^{232}Th	5.80	90	0.440	0.014	0.005
^{232}Th	5.80	126	0.369	0.015	0.006
^{232}Th	5.80	71	0.394	0.021	0.008
^{232}Th	5.80	107	0.427	0.021	0.007
^{232}Th	6.00	54	0.357	0.014	0.008
^{232}Th	6.00	90	0.443	0.013	0.007

Continued on Next Page...

Table C.1 – Continued

Target	E_γ (MeV)	θ (deg)	Σ	$\Delta\Sigma$ (stat)	$\Delta\Sigma$ (sys)
^{232}Th	6.00	126	0.370	0.011	0.007
^{232}Th	6.00	71	0.412	0.020	0.013
^{232}Th	6.00	107	0.431	0.014	0.008
^{232}Th	6.00	144	0.266	0.018	0.011
^{232}Th	6.20	54	0.371	0.011	0.007
^{232}Th	6.20	90	0.485	0.010	0.006
^{232}Th	6.20	126	0.391	0.010	0.006
^{232}Th	6.20	71	0.454	0.015	0.009
^{232}Th	6.20	107	0.451	0.013	0.008
^{232}Th	6.20	144	0.282	0.016	0.011
^{232}Th	6.50	54	0.346	0.010	0.007
^{232}Th	6.50	90	0.460	0.009	0.006
^{232}Th	6.50	126	0.385	0.010	0.006
^{232}Th	6.50	71	0.430	0.014	0.009
^{232}Th	6.50	107	0.425	0.012	0.009
^{232}Th	6.50	144	0.278	0.015	0.010
^{232}Th	6.70	54	0.298	0.012	0.008
^{232}Th	6.70	90	0.403	0.012	0.007
^{232}Th	6.70	126	0.322	0.011	0.008
^{232}Th	6.70	71	0.364	0.017	0.011
^{232}Th	6.70	107	0.388	0.015	0.009
^{232}Th	6.70	144	0.220	0.017	0.011
^{232}Th	6.80	54	0.284	0.010	0.006
^{232}Th	6.80	90	0.346	0.009	0.005
^{232}Th	6.80	126	0.308	0.009	0.006
^{232}Th	6.80	71	0.328	0.012	0.007
^{232}Th	6.80	107	0.349	0.012	0.007
^{232}Th	7.00	54	0.273	0.010	0.007
^{232}Th	7.00	90	0.369	0.010	0.007
^{232}Th	7.00	126	0.284	0.010	0.007
^{232}Th	7.00	71	0.315	0.015	0.012

Continued on Next Page...

Table C.1 – Continued

Target	E_γ (MeV)	θ (deg)	Σ	$\Delta\Sigma$ (stat)	$\Delta\Sigma$ (sys)
^{232}Th	7.00	107	0.343	0.013	0.009
^{232}Th	7.00	144	0.207	0.014	0.011
^{232}Th	7.30	54	0.229	0.026	0.009
^{232}Th	7.30	90	0.259	0.027	0.008
^{232}Th	7.30	126	0.195	0.025	0.007
^{232}Th	7.30	71	0.231	0.039	0.013
^{232}Th	7.30	107	0.303	0.034	0.010
^{232}Th	7.30	144	0.182	0.037	0.012
^{233}U	5.60	54	0.057	0.016	0.008
^{233}U	5.60	90	0.064	0.015	0.007
^{233}U	5.60	126	0.058	0.018	0.008
^{233}U	5.60	71	0.061	0.023	0.012
^{233}U	5.60	107	0.042	0.022	0.011
^{233}U	5.60	144	0.011	0.027	0.013
^{233}U	5.80	54	0.033	0.017	0.008
^{233}U	5.80	90	0.040	0.015	0.007
^{233}U	5.80	126	0.055	0.017	0.008
^{233}U	5.80	71	0.058	0.024	0.010
^{233}U	5.80	107	0.023	0.023	0.011
^{233}U	5.80	144	0.007	0.028	0.013
^{233}U	6.00	54	-0.003	0.015	0.008
^{233}U	6.00	90	0.018	0.013	0.007
^{233}U	6.00	126	-0.009	0.015	0.008
^{233}U	6.00	71	0.028	0.020	0.011
^{233}U	6.00	107	-0.009	0.020	0.011
^{233}U	6.00	144	-0.022	0.023	0.012
^{233}U	6.20	54	0.035	0.013	0.007
^{233}U	6.20	90	0.012	0.012	0.007
^{233}U	6.20	126	0.025	0.013	0.008
^{233}U	6.20	71	0.008	0.018	0.011
^{233}U	6.20	107	0.009	0.018	0.010

Continued on Next Page...

Table C.1 – Continued

Target	E_γ (MeV)	θ (deg)	Σ	$\Delta\Sigma$ (stat)	$\Delta\Sigma$ (sys)
^{233}U	6.20	144	0.010	0.021	0.012
^{233}U	6.50	54	0.004	0.010	0.008
^{233}U	6.50	90	0.028	0.010	0.007
^{233}U	6.50	126	0.006	0.010	0.008
^{233}U	6.50	71	0.024	0.014	0.011
^{233}U	6.50	107	-0.003	0.014	0.010
^{233}U	6.50	144	-0.012	0.016	0.012
^{233}U	7.00	54	0.023	0.013	0.007
^{233}U	7.00	90	0.024	0.013	0.007
^{233}U	7.00	126	0.006	0.014	0.008
^{233}U	7.00	71	0.003	0.018	0.011
^{233}U	7.00	107	-0.033	0.018	0.010
^{233}U	7.00	144	-0.014	0.022	0.012
^{235}U	5.60	54	0.055	0.018	0.009
^{235}U	5.60	90	0.097	0.016	0.012
^{235}U	5.60	126	0.058	0.013	0.007
^{235}U	5.60	71	0.075	0.028	0.020
^{235}U	5.60	107	0.056	0.018	0.011
^{235}U	5.60	144	0.069	0.019	0.011
^{235}U	5.80	54	-0.018	0.024	0.015
^{235}U	5.80	90	0.012	0.025	0.007
^{235}U	5.80	126	0.026	0.022	0.007
^{235}U	5.80	71	0.028	0.038	0.013
^{235}U	5.80	107	0.030	0.029	0.009
^{235}U	5.80	144	0.023	0.032	0.010
^{235}U	6.00	54	0.013	0.014	0.006
^{235}U	6.00	90	0.040	0.016	0.007
^{235}U	6.00	126	0.002	0.015	0.007
^{235}U	6.00	71	0.054	0.024	0.011
^{235}U	6.00	107	0.007	0.020	0.009
^{235}U	6.00	144	-0.003	0.021	0.010

Continued on Next Page...

Table C.1 – Continued

Target	E_γ (MeV)	θ (deg)	Σ	$\Delta\Sigma$ (stat)	$\Delta\Sigma$ (sys)
^{235}U	6.20	54	0.008	0.013	0.006
^{235}U	6.20	90	0.013	0.014	0.007
^{235}U	6.20	126	0.008	0.014	0.007
^{235}U	6.20	71	0.042	0.022	0.016
^{235}U	6.20	107	0.042	0.018	0.009
^{235}U	6.20	144	-0.003	0.021	0.011
^{235}U	6.40	54	-0.003	0.004	0.007
^{235}U	6.40	90	0.016	0.004	0.007
^{235}U	6.40	126	0.003	0.004	0.007
^{235}U	6.40	71	0.038	0.007	0.012
^{235}U	6.40	107	0.003	0.006	0.010
^{235}U	6.40	144	0.010	0.006	0.010
^{235}U	6.60	54	0.001	0.006	0.007
^{235}U	6.60	90	-0.000	0.006	0.007
^{235}U	6.60	126	-0.014	0.006	0.007
^{235}U	6.60	71	0.027	0.010	0.012
^{235}U	6.60	107	0.021	0.009	0.010
^{235}U	6.60	144	0.018	0.009	0.010
^{238}U	5.70	75	0.358	0.021	0.012
^{238}U	5.70	90	0.439	0.021	0.011
^{238}U	5.70	126	0.297	0.030	0.019
^{238}U	5.80	54	0.325	0.016	0.007
^{238}U	5.80	90	0.413	0.015	0.008
^{238}U	5.80	126	0.303	0.012	0.006
^{238}U	5.80	71	0.385	0.021	0.012
^{238}U	5.80	107	0.388	0.016	0.008
^{238}U	5.80	144	0.196	0.019	0.010
^{238}U	5.90	54	0.308	0.016	0.008
^{238}U	5.90	90	0.408	0.015	0.006
^{238}U	5.90	126	0.341	0.013	0.006
^{238}U	5.90	71	0.401	0.022	0.010

Continued on Next Page...

Table C.1 – Continued

Target	E_γ (MeV)	θ (deg)	Σ	$\Delta\Sigma$ (stat)	$\Delta\Sigma$ (sys)
^{238}U	5.90	107	0.419	0.017	0.008
^{238}U	5.90	144	0.188	0.020	0.010
^{238}U	6.00	54	0.304	0.012	0.007
^{238}U	6.00	90	0.436	0.011	0.006
^{238}U	6.00	126	0.338	0.011	0.006
^{238}U	6.00	71	0.390	0.017	0.009
^{238}U	6.00	107	0.407	0.014	0.008
^{238}U	6.00	144	0.199	0.016	0.010
^{238}U	6.10	54	0.329	0.012	0.007
^{238}U	6.10	90	0.415	0.011	0.006
^{238}U	6.10	126	0.321	0.011	0.006
^{238}U	6.10	71	0.393	0.017	0.010
^{238}U	6.10	107	0.401	0.014	0.008
^{238}U	6.10	144	0.150	0.017	0.010
^{238}U	6.20	54	0.286	0.012	0.007
^{238}U	6.20	90	0.392	0.012	0.006
^{238}U	6.20	126	0.305	0.011	0.006
^{238}U	6.20	71	0.351	0.018	0.010
^{238}U	6.20	107	0.387	0.015	0.008
^{238}U	6.20	144	0.196	0.017	0.010
^{238}U	6.40	75	0.257	0.012	0.012
^{238}U	6.40	90	0.279	0.013	0.013
^{238}U	6.40	126	0.244	0.016	0.017
^{238}U	6.50	54	0.159	0.014	0.007
^{238}U	6.50	90	0.222	0.013	0.007
^{238}U	6.50	126	0.170	0.012	0.007
^{238}U	6.50	71	0.215	0.021	0.011
^{238}U	6.50	107	0.218	0.017	0.009
^{238}U	6.50	144	0.099	0.018	0.010
^{238}U	6.70	54	0.071	0.019	0.017
^{238}U	6.70	90	0.155	0.018	0.016

Continued on Next Page...

Table C.1 – Continued

Target	E_γ (MeV)	θ (deg)	Σ	$\Delta\Sigma$ (stat)	$\Delta\Sigma$ (sys)
^{238}U	6.70	126	0.089	0.018	0.016
^{238}U	6.70	71	0.091	0.026	0.022
^{238}U	6.70	107	0.083	0.026	0.025
^{238}U	6.70	144	0.148	0.031	0.027
^{238}U	6.80	54	0.072	0.017	0.017
^{238}U	6.80	90	0.163	0.017	0.016
^{238}U	6.80	126	0.106	0.018	0.016
^{238}U	6.80	71	0.122	0.024	0.022
^{238}U	6.80	107	0.157	0.025	0.023
^{238}U	6.80	144	0.101	0.029	0.028
^{238}U	7.00	54	0.123	0.013	0.007
^{238}U	7.00	90	0.156	0.013	0.007
^{238}U	7.00	126	0.130	0.012	0.007
^{238}U	7.00	71	0.156	0.020	0.011
^{238}U	7.00	107	0.143	0.017	0.009
^{238}U	7.00	144	0.021	0.018	0.010
^{237}Np	5.40	54	0.011	0.026	0.009
^{237}Np	5.40	90	0.092	0.018	0.005
^{237}Np	5.40	126	0.015	0.021	0.004
^{237}Np	5.40	71	0.081	0.030	0.005
^{237}Np	5.40	107	0.087	0.028	0.007
^{237}Np	5.60	54	-0.005	0.013	0.005
^{237}Np	5.60	90	0.052	0.011	0.004
^{237}Np	5.60	126	0.046	0.012	0.004
^{237}Np	5.60	71	0.043	0.016	0.005
^{237}Np	5.60	107	0.026	0.015	0.005
^{237}Np	5.80	54	0.006	0.011	0.004
^{237}Np	5.80	90	0.015	0.010	0.004
^{237}Np	5.80	126	0.024	0.010	0.004
^{237}Np	5.80	71	0.004	0.014	0.005
^{237}Np	5.80	107	-0.007	0.013	0.005

Continued on Next Page...

Table C.1 – Continued

Target	E_γ (MeV)	θ (deg)	Σ	$\Delta\Sigma$ (stat)	$\Delta\Sigma$ (sys)
^{237}Np	5.90	54	0.012	0.010	0.005
^{237}Np	5.90	90	0.004	0.009	0.004
^{237}Np	5.90	126	-0.007	0.009	0.004
^{237}Np	5.90	71	0.007	0.013	0.005
^{237}Np	5.90	107	-0.022	0.012	0.005
^{237}Np	6.00	54	0.016	0.011	0.004
^{237}Np	6.00	90	0.009	0.010	0.004
^{237}Np	6.00	126	-0.003	0.010	0.004
^{237}Np	6.00	71	-0.001	0.014	0.005
^{237}Np	6.00	107	-0.013	0.014	0.005
^{237}Np	6.10	54	-0.004	0.010	0.004
^{237}Np	6.10	90	0.003	0.009	0.004
^{237}Np	6.10	126	0.006	0.009	0.004
^{237}Np	6.10	71	-0.003	0.012	0.005
^{237}Np	6.10	107	-0.000	0.012	0.005
^{237}Np	6.20	54	-0.010	0.007	0.004
^{237}Np	6.20	90	0.014	0.006	0.004
^{237}Np	6.20	126	0.002	0.006	0.004
^{237}Np	6.20	71	0.030	0.009	0.005
^{237}Np	6.20	107	0.009	0.009	0.005
^{237}Np	6.35	54	0.013	0.008	0.004
^{237}Np	6.35	90	0.011	0.008	0.004
^{237}Np	6.35	126	0.016	0.008	0.004
^{237}Np	6.35	71	0.026	0.011	0.005
^{237}Np	6.35	107	0.004	0.010	0.005
^{237}Np	6.50	54	0.010	0.008	0.004
^{237}Np	6.50	90	0.014	0.007	0.004
^{237}Np	6.50	126	0.001	0.007	0.004
^{237}Np	6.50	71	0.033	0.010	0.005
^{237}Np	6.50	107	0.006	0.010	0.005
^{237}Np	6.80	54	0.003	0.006	0.004

Continued on Next Page...

Table C.1 – Continued

Target	E_γ (MeV)	θ (deg)	Σ	$\Delta\Sigma$ (stat)	$\Delta\Sigma$ (sys)
^{237}Np	6.80	90	0.005	0.005	0.004
^{237}Np	6.80	126	-0.001	0.005	0.004
^{237}Np	6.80	71	0.012	0.007	0.005
^{237}Np	6.80	107	-0.003	0.007	0.005
^{237}Np	7.00	54	-0.005	0.006	0.004
^{237}Np	7.00	90	-0.005	0.006	0.004
^{237}Np	7.00	126	0.004	0.005	0.004
^{237}Np	7.00	71	0.012	0.007	0.005
^{237}Np	7.00	107	0.007	0.007	0.005
^{239}Pu	5.30	54	-0.013	0.031	0.036
^{239}Pu	5.30	90	0.017	0.030	0.005
^{239}Pu	5.30	126	-0.006	0.030	0.011
^{239}Pu	5.30	71	-0.047	0.057	0.009
^{239}Pu	5.30	107	-0.116	0.051	0.015
^{239}Pu	5.30	144	0.024	0.056	0.007
^{239}Pu	5.40	54	-0.025	0.024	0.018
^{239}Pu	5.40	90	-0.033	0.024	0.005
^{239}Pu	5.40	126	-0.041	0.025	0.008
^{239}Pu	5.40	71	-0.111	0.037	0.012
^{239}Pu	5.40	107	-0.060	0.043	0.012
^{239}Pu	5.40	144	-0.069	0.038	0.008
^{239}Pu	5.50	54	-0.092	0.014	0.010
^{239}Pu	5.50	90	-0.106	0.015	0.004
^{239}Pu	5.50	126	-0.082	0.015	0.006
^{239}Pu	5.50	71	-0.090	0.022	0.007
^{239}Pu	5.50	107	-0.087	0.023	0.009
^{239}Pu	5.50	144	-0.050	0.021	0.006
^{239}Pu	5.60	54	-0.046	0.015	0.004
^{239}Pu	5.60	90	-0.099	0.018	0.006
^{239}Pu	5.60	126	-0.063	0.016	0.005
^{239}Pu	5.60	71	-0.065	0.027	0.010

Continued on Next Page...

Table C.1 – Continued

Target	E_γ (MeV)	θ (deg)	Σ	$\Delta\Sigma$ (stat)	$\Delta\Sigma$ (sys)
^{239}Pu	5.60	107	-0.052	0.022	0.007
^{239}Pu	5.60	144	-0.025	0.021	0.021
^{239}Pu	5.70	54	0.010	0.015	0.004
^{239}Pu	5.70	90	-0.039	0.016	0.005
^{239}Pu	5.70	126	-0.013	0.015	0.005
^{239}Pu	5.70	71	-0.070	0.023	0.006
^{239}Pu	5.70	107	-0.047	0.021	0.007
^{239}Pu	5.70	144	0.029	0.019	0.020
^{239}Pu	5.80	54	-0.021	0.015	0.005
^{239}Pu	5.80	90	-0.036	0.018	0.005
^{239}Pu	5.80	126	-0.038	0.017	0.005
^{239}Pu	5.80	71	-0.007	0.025	0.008
^{239}Pu	5.80	107	-0.017	0.024	0.007
^{239}Pu	5.80	144	-0.013	0.022	0.017
^{239}Pu	5.90	54	-0.014	0.011	0.004
^{239}Pu	5.90	90	-0.001	0.012	0.004
^{239}Pu	5.90	126	0.009	0.012	0.004
^{239}Pu	5.90	71	0.002	0.016	0.006
^{239}Pu	5.90	107	-0.020	0.018	0.006
^{239}Pu	5.90	144	0.012	0.017	0.006
^{239}Pu	6.00	54	-0.006	0.013	0.004
^{239}Pu	6.00	90	0.002	0.015	0.005
^{239}Pu	6.00	126	-0.035	0.014	0.005
^{239}Pu	6.00	71	0.019	0.021	0.008
^{239}Pu	6.00	107	0.015	0.020	0.007
^{239}Pu	6.00	144	0.014	0.018	0.010
^{239}Pu	6.10	54	0.014	0.007	0.004
^{239}Pu	6.10	90	0.021	0.007	0.004
^{239}Pu	6.10	126	0.015	0.007	0.004
^{239}Pu	6.10	71	0.016	0.010	0.005
^{239}Pu	6.10	107	0.018	0.011	0.006

Continued on Next Page...

Table C.1 – Continued

Target	E_γ (MeV)	θ (deg)	Σ	$\Delta\Sigma$ (stat)	$\Delta\Sigma$ (sys)
^{239}Pu	6.10	144	0.009	0.010	0.005
^{239}Pu	6.20	54	0.022	0.012	0.004
^{239}Pu	6.20	90	0.031	0.014	0.005
^{239}Pu	6.20	126	0.017	0.014	0.005
^{239}Pu	6.20	71	0.021	0.019	0.007
^{239}Pu	6.20	107	0.032	0.019	0.006
^{239}Pu	6.20	144	0.027	0.018	0.010
^{239}Pu	6.30	54	0.034	0.006	0.004
^{239}Pu	6.30	90	0.021	0.006	0.004
^{239}Pu	6.30	126	0.026	0.006	0.004
^{239}Pu	6.30	71	0.036	0.009	0.005
^{239}Pu	6.30	107	0.033	0.009	0.006
^{239}Pu	6.30	144	0.017	0.009	0.005
^{239}Pu	6.40	54	0.010	0.011	0.004
^{239}Pu	6.40	90	0.021	0.012	0.004
^{239}Pu	6.40	126	0.020	0.012	0.004
^{239}Pu	6.40	71	0.016	0.016	0.006
^{239}Pu	6.40	107	0.022	0.017	0.006
^{239}Pu	6.40	144	0.041	0.017	0.006
^{239}Pu	6.50	54	0.013	0.011	0.004
^{239}Pu	6.50	90	0.022	0.012	0.005
^{239}Pu	6.50	126	-0.023	0.012	0.004
^{239}Pu	6.50	71	0.036	0.017	0.006
^{239}Pu	6.50	107	0.009	0.017	0.006
^{239}Pu	6.50	144	0.044	0.015	0.009
^{239}Pu	6.70	54	0.018	0.009	0.009
^{239}Pu	6.70	90	0.034	0.010	0.009
^{239}Pu	6.70	126	0.052	0.010	0.009
^{239}Pu	6.70	71	-0.020	0.013	0.012
^{239}Pu	6.70	107	0.004	0.014	0.013
^{239}Pu	6.70	144	0.016	0.016	0.014

Continued on Next Page...

Table C.1 – Continued

Target	E_γ (MeV)	θ (deg)	Σ	$\Delta\Sigma$ (stat)	$\Delta\Sigma$ (sys)
^{239}Pu	6.80	54	0.026	0.009	0.009
^{239}Pu	6.80	90	0.028	0.009	0.009
^{239}Pu	6.80	126	0.023	0.009	0.010
^{239}Pu	6.80	71	-0.009	0.012	0.012
^{239}Pu	6.80	107	0.014	0.013	0.013
^{239}Pu	6.80	144	-0.005	0.015	0.015
^{239}Pu	7.00	54	0.011	0.005	0.004
^{239}Pu	7.00	90	0.009	0.006	0.004
^{239}Pu	7.00	126	0.006	0.005	0.004
^{239}Pu	7.00	71	0.018	0.008	0.006
^{239}Pu	7.00	107	0.013	0.008	0.006
^{239}Pu	7.00	144	0.007	0.007	0.006
^{240}Pu	5.80	54	0.041	0.052	0.028
^{240}Pu	5.80	90	0.111	0.041	0.018
^{240}Pu	5.80	126	0.024	0.045	0.010
^{240}Pu	5.80	71	0.179	0.065	0.031
^{240}Pu	5.80	107	0.119	0.067	0.012
^{240}Pu	5.80	144	-0.090	0.141	0.029
^{240}Pu	5.90	54	0.061	0.018	0.011
^{240}Pu	5.90	90	0.108	0.015	0.004
^{240}Pu	5.90	126	0.075	0.016	0.004
^{240}Pu	5.90	71	0.099	0.021	0.006
^{240}Pu	5.90	107	0.141	0.024	0.006
^{240}Pu	6.00	54	0.029	0.024	0.012
^{240}Pu	6.00	90	0.158	0.020	0.011
^{240}Pu	6.00	126	0.052	0.023	0.008
^{240}Pu	6.00	71	0.142	0.027	0.015
^{240}Pu	6.00	107	0.171	0.032	0.011
^{240}Pu	6.00	144	-0.045	0.061	0.029
^{240}Pu	6.10	54	0.065	0.020	0.010
^{240}Pu	6.10	90	0.125	0.017	0.008

Continued on Next Page...

Table C.1 – Continued

Target	E_γ (MeV)	θ (deg)	Σ	$\Delta\Sigma$ (stat)	$\Delta\Sigma$ (sys)
^{240}Pu	6.10	126	0.056	0.020	0.008
^{240}Pu	6.10	71	0.098	0.025	0.013
^{240}Pu	6.10	107	0.192	0.026	0.011
^{240}Pu	6.10	144	0.033	0.053	0.027
^{240}Pu	6.20	54	0.085	0.008	0.005
^{240}Pu	6.20	90	0.143	0.007	0.003
^{240}Pu	6.20	126	0.097	0.008	0.004
^{240}Pu	6.20	71	0.116	0.010	0.005
^{240}Pu	6.20	107	0.121	0.010	0.004
^{240}Pu	6.50	54	0.063	0.015	0.008
^{240}Pu	6.50	90	0.083	0.013	0.007
^{240}Pu	6.50	126	0.059	0.015	0.008
^{240}Pu	6.50	71	0.087	0.019	0.011
^{240}Pu	6.50	107	0.124	0.019	0.011
^{240}Pu	6.50	144	0.054	0.041	0.028
^{240}Pu	6.70	54	0.071	0.005	0.010
^{240}Pu	6.70	90	0.116	0.004	0.009
^{240}Pu	6.70	126	0.081	0.005	0.010
^{240}Pu	6.70	71	0.109	0.006	0.013
^{240}Pu	6.70	107	0.094	0.006	0.013
^{240}Pu	6.80	54	0.074	0.014	0.009
^{240}Pu	6.80	90	0.098	0.012	0.007
^{240}Pu	6.80	126	0.091	0.014	0.008
^{240}Pu	6.80	71	0.095	0.018	0.011
^{240}Pu	6.80	107	0.116	0.019	0.011
^{240}Pu	6.80	144	0.000	0.040	0.027
^{240}Pu	7.00	54	0.064	0.011	0.009
^{240}Pu	7.00	90	0.073	0.010	0.008
^{240}Pu	7.00	126	0.039	0.011	0.008
^{240}Pu	7.00	71	0.090	0.015	0.010
^{240}Pu	7.00	107	0.129	0.015	0.011

Continued on Next Page...

Table C.1 – Continued

Target	E_γ (MeV)	θ (deg)	Σ	$\Delta\Sigma$ (stat)	$\Delta\Sigma$ (sys)
^{240}Pu	7.00	144	0.042	0.036	0.027
^{240}Pu	7.20	54	0.047	0.005	0.003
^{240}Pu	7.20	90	0.084	0.005	0.003
^{240}Pu	7.20	126	0.042	0.005	0.003
^{240}Pu	7.20	71	0.074	0.007	0.004
^{240}Pu	7.20	107	0.057	0.007	0.004
^{240}Pu	7.60	54	0.021	0.005	0.003
^{240}Pu	7.60	90	0.044	0.004	0.003
^{240}Pu	7.60	126	0.025	0.004	0.003
^{240}Pu	7.60	71	0.048	0.006	0.004
^{240}Pu	7.60	107	0.038	0.006	0.004

Appendix D

Tabulated Prompt Neutron Angular Distribution Coefficients

Table D.1: Measured prompt neutron angular distribution coefficients b and c are given for each target and beam energy E_γ combination. The coefficients are as used in Equation 5.4 and the normalization $a + b = 1$ is taken. The finite size and target contamination corrections discussed in Section 5.9.2 have been applied. The χ^2 value per degree of freedom η is given for each fit. Statistical (stat) and systematic (sys) uncertainties are also given.

Target	E_γ (MeV)	b	Δb (stat)	Δb (sys)	c	Δc (stat)	Δc (sys)	χ^2/η
^{232}Th	5.60	0.467	0.022	0.005	-0.029	0.041	0.012	0.26
^{232}Th	5.80	0.452	0.012	0.004	-0.003	0.024	0.009	1.95
^{232}Th	6.00	0.455	0.006	0.003	0.035	0.013	0.007	0.46
^{232}Th	6.20	0.491	0.008	0.005	0.020	0.015	0.009	0.79
^{232}Th	6.50	0.465	0.008	0.005	0.032	0.014	0.010	1.84
^{232}Th	6.70	0.411	0.009	0.006	0.016	0.015	0.010	0.69
^{232}Th	6.80	0.358	0.008	0.004	0.054	0.015	0.009	0.86
^{232}Th	7.00	0.371	0.005	0.003	0.012	0.009	0.006	0.29
^{232}Th	7.30	0.270	0.022	0.007	0.042	0.032	0.010	0.97
^{233}U	5.60	0.070	0.010	0.006	0.010	0.013	0.007	0.17
^{233}U	5.80	0.041	0.013	0.006	0.013	0.017	0.008	0.53

Continued on Next Page...

Table D.1 – Continued

Target	E_γ (MeV)	b	Δb (stat)	Δb (sys)	c	Δc (stat)	Δc (sys)	χ^2/η
^{233}U	6.00	0.013	0.012	0.008	-0.024	0.014	0.007	0.42
^{233}U	6.20	0.001	0.010	0.012	0.022	0.013	0.008	0.26
^{233}U	6.50	0.018	0.008	0.011	-0.018	0.010	0.008	0.49
^{233}U	7.00	0.005	0.011	0.008	-0.001	0.013	0.008	1.75
^{235}U	5.60	0.048	0.015	0.011	0.013	0.017	0.011	0.97
^{235}U	5.80	-0.009	0.011	0.005	-0.001	0.012	0.006	0.37
^{235}U	6.00	0.013	0.006	0.005	-0.023	0.006	0.005	0.36
^{235}U	6.20	-0.001	0.005	0.005	-0.006	0.005	0.005	0.29
^{235}U	6.40	0.004	0.004	0.007	-0.013	0.005	0.008	1.46
^{235}U	6.60	-0.004	0.006	0.007	-0.007	0.007	0.007	2.07
^{238}U	5.70	0.422	0.018	0.010	-0.040	0.049	0.030	3.11
^{238}U	5.80	0.430	0.010	0.005	-0.012	0.017	0.008	0.30
^{238}U	5.90	0.432	0.009	0.004	0.000	0.017	0.008	0.60
^{238}U	6.00	0.446	0.007	0.004	-0.013	0.013	0.008	0.38
^{238}U	6.10	0.434	0.007	0.004	-0.015	0.013	0.007	0.97
^{238}U	6.20	0.404	0.007	0.004	0.003	0.013	0.008	0.39
^{238}U	6.40	0.281	0.011	0.010	0.061	0.028	0.029	0.60
^{238}U	6.50	0.224	0.008	0.005	0.016	0.013	0.007	0.76
^{238}U	6.70	0.128	0.016	0.015	0.003	0.021	0.018	1.91
^{238}U	6.80	0.162	0.015	0.014	-0.015	0.019	0.018	0.83
^{238}U	7.00	0.170	0.011	0.006	-0.003	0.013	0.007	1.75
^{237}Np	5.40	0.101	0.016	0.004	-0.059	0.022	0.006	0.16
^{237}Np	5.60	0.050	0.010	0.003	-0.015	0.013	0.005	2.73
^{237}Np	5.80	0.007	0.009	0.003	0.008	0.011	0.004	1.09
^{237}Np	5.90	-0.002	0.008	0.003	0.000	0.010	0.004	1.62
^{237}Np	6.00	0.002	0.009	0.003	0.001	0.011	0.004	1.03
^{237}Np	6.10	0.001	0.008	0.003	-0.001	0.010	0.004	0.22
^{237}Np	6.20	0.019	0.005	0.003	-0.018	0.007	0.004	1.74
^{237}Np	6.35	0.012	0.007	0.003	0.007	0.009	0.004	0.57
^{237}Np	6.50	0.017	0.006	0.003	-0.007	0.008	0.004	1.44
^{237}Np	6.80	0.005	0.005	0.003	-0.004	0.006	0.004	0.58

Continued on Next Page...

Table D.1 – Continued

Target	E_γ (MeV)	b	Δb (stat)	Δb (sys)	c	Δc (stat)	Δc (sys)	χ^2/η
^{237}Np	7.00	0.000	0.005	0.003	-0.000	0.006	0.004	1.21
^{239}Pu	5.30	-0.031	0.029	0.006	0.006	0.032	0.020	1.47
^{239}Pu	5.40	-0.057	0.022	0.005	-0.016	0.024	0.010	1.15
^{239}Pu	5.50	-0.111	0.013	0.004	-0.022	0.014	0.006	0.18
^{239}Pu	5.60	-0.095	0.011	0.003	0.003	0.011	0.004	0.24
^{239}Pu	5.70	-0.068	0.015	0.005	0.045	0.016	0.009	1.21
^{239}Pu	5.80	-0.034	0.012	0.004	-0.013	0.012	0.004	0.20
^{239}Pu	5.90	-0.012	0.011	0.004	0.001	0.012	0.004	0.82
^{239}Pu	6.00	-0.003	0.013	0.005	-0.015	0.014	0.005	1.48
^{239}Pu	6.10	0.013	0.007	0.004	0.002	0.007	0.004	0.02
^{239}Pu	6.20	0.020	0.007	0.003	0.004	0.008	0.003	0.13
^{239}Pu	6.30	0.020	0.006	0.004	0.015	0.007	0.004	0.49
^{239}Pu	6.40	0.012	0.011	0.004	0.010	0.012	0.004	0.72
^{239}Pu	6.50	0.013	0.011	0.004	-0.008	0.012	0.005	3.32
^{239}Pu	6.70	0.007	0.009	0.008	0.020	0.011	0.010	3.05
^{239}Pu	6.80	0.013	0.008	0.008	0.005	0.010	0.009	1.12
^{239}Pu	7.00	0.008	0.004	0.003	0.002	0.004	0.003	0.20
^{240}Pu	5.80	0.141	0.036	0.015	-0.069	0.046	0.018	0.43
^{240}Pu	5.90	0.122	0.014	0.003	-0.011	0.019	0.007	0.86
^{240}Pu	6.00	0.182	0.017	0.009	-0.090	0.022	0.010	0.49
^{240}Pu	6.10	0.143	0.015	0.008	-0.036	0.020	0.010	1.74
^{240}Pu	6.20	0.145	0.006	0.003	-0.008	0.009	0.005	0.57
^{240}Pu	6.50	0.097	0.011	0.007	0.002	0.016	0.009	0.89
^{240}Pu	6.70	0.120	0.004	0.008	-0.004	0.005	0.011	0.39
^{240}Pu	6.80	0.108	0.011	0.007	0.010	0.016	0.009	0.60
^{240}Pu	7.00	0.092	0.009	0.007	-0.004	0.012	0.009	2.62
^{240}Pu	7.20	0.084	0.004	0.003	-0.014	0.006	0.004	1.39
^{240}Pu	7.60	0.048	0.004	0.003	-0.009	0.005	0.004	0.75

Bibliography

[1] R. Vandenbosch and J. R. Huizenga, *Nuclear Fission* (Academic Press, New York, 1973).

[2] A. DeShalit and H. Feshbach, *Theoretical Nuclear Physics Volume I* (John Wiley and Sons, New York, 1990).

[3] C. Wagemans (editor), *The Nuclear Fission Process* (CRC Press, Inc., Boca Raton, 1991).

[4] D. L. Hill and J. A. Wheeler, Phys. Rev. **89**, 1102 (1953).

[5] E. Hayward, Nat. Bur. Stand. U.S. Monogr. **118**, 1 (1970).

[6] P. Möller, D. G. Madland, A. J. Sierk, and A. Iwamoto, Nature **409**, 785 (2001).

[7] P. Möller, J. R. Nix, W. D. Myers, and W. J. Swiatecki, At. Data and Nucl. Data Tables **59**, 185 (1995).

[8] J. Randrup, P. Möller, and A. J. Sierk, EPJ Web of Conferences **21**, 08006 (2012).

[9] F. J. Hambsch, H. H. Knitter, C. Budtz-Jørgensen, and J. P. Theobald, Nuc. Phys. **A491**, 56 (1989).

[10] R. Vogt and J. Randrup, Phys. Rev. C **84**, 044621 (2011).

[11] H. J. Krappe and K. Pomorski, *Theory of Nuclear Fission* (Springer-Verlag, New York, 2012).

[12] U. Brosa, S. Grossman, and A. Müller, Phys. Rep. **197**, 167 (1990).

[13] A. Bohr, Proc. U.N. Int. Conf. Peaceful Uses At. Energy **2**, 151 (1956).

[14] S. G. Kadmensky, Phys. At. Nuc. **65**, 1390 (2002).

[15] S. G. Kadmensky and L. V. Rodionova, Phys. At. Nuc. **66**, 1219 (2003).

[16] S. G. Kadmensky and L. V. Titova, Phys. At. Nuc. **72**, 324 (2009).

[17] J. B. Marion and J. L. Fowler (editors), *Fast Neutron Physics Part II: Experiments and Theory* (John Wiley and Sons, New York, 1963).

[18] J. J. Sakurai, *Modern Quantum Mechanics* (Addison-Wesley Publishing Company, Inc., New York, 1994).

[19] L. W. Fagg and S. S. Hanna, Rev. Mod. Phys. **31**, 711 (1959).

[20] V. Weisskopf, Phys. Rev. **52**, 295 (1937).

[21] A. P. Baerg, R. M. Bartholomew, F. Brown, L. Katz, and S. B. Kowalski, Can. J. Nucl. Phys. **37**, 1418 (1959).

[22] A. I. Baz, N. M. Kulikova, L. E. Lazareva, N. V. Nikitina, and V. A. Semenov, Proc. Second UN Int. Conf. Peaceful Uses At. Energy **15**, 184 (1958).

[23] I. E. Bocharova, V. G. Zolotukhin, S. P. Kapitza, G. N. Smirenkin, A. S. Soldatov, and Yu. M. Tsipenyuk, Sov. Phys. JETP **22**, 335 (1966).

[24] I. E. Bocharova *et al.*, USSR Report to the INDC **279**, 47 (1987).

[25] H. G. de Carvalho and A. G. da Silva, Il Nuovo Cimento **19**, 1131 (1961).

[26] E. J. Dowdy and T. L. Krysinski, Nucl. Phys. **A175**, 501 (1971).

[27] B. Forkman and S. A. E. Johansson, Nucl. Phys. **20**, 136 (1960).

[28] L. P. Geraldo, J. Phys. G **12**, 1423 (1986).

[29] A. V. Ignatyuk, N. S. Rabotnov, G. N. Smirenkin, A. S. Soldatov, and Yu. M. Tsipenyuk, Sov. Phys. JETP **34**, 684 (1971).

[30] K. N. Ivanov, Yu. A. Solov'ev, and K. A. Petrzak, JETP Lett. **17**, 429 (1973).

[31] S. P. Kapitza, N. S. Rabotnov, G. N. Smirenkin, A. S. Soldatov, L. N. Usachev, and Yu. M. Tsipenyuk, JETP Lett. **9**, 73 (1969).

[32] L. Katz, A. P. Baerg, and F. Brown, Proc. Second UN Int. Conf. Peaceful Uses At. Energy **15**, 188 (1958).

[33] V. M. Khvastunov *et al.*, Phys. At. Nucl. **57**, 1858 (1994).

[34] V. M. Khvastunov and V. V. Denyak, Phys. At. Nucl. **64**, 1269 (2001).

[35] L. J. Lindgren, A. Alm, and A. Sandell, Nucl. Phys. **A298**, 43 (1978).

[36] A. Manfredini, L. Fiore, C. Ramorino, H. G. de Carvalho, and W. Wölfli, Nucl. Phys. **A123**, 664 (1969).

[37] S. Nair, D. B. Gayther, B. H. Patrick, and E. M. Bowey, J. Phys. G **3**, 965 (1977).

[38] N. S. Rabotnov *et al.*, Proc. Phys. Chem. Fission Conference, Salzburg **1**, 135 (1965).

[39] N. S. Rabotnov, G. N. Smirenkin, A. S. Soldatov, L. N. Usachov, S. P. Kapitza, and Yu. M. Tsipenyuk, Nucl. Phys. **77**, 92 (1966).

[40] N. S. Rabotnov, G. N. Smirenkin, A. S. Soldatov, L. N. Ysachev, S. P. Kapitza, and Yu. M. Tsipenyuk, Phys Lett. B **26**, 218 (1968).

[41] N. S. Rabotnov, G. N. Smirenkin, A. S. Soldatov, L. N. Usachev, S. P. Kapitza, and Yu. M. Tsipenyuk, Sov. J. Nucl. Phys. **11**, 285 (1970).

[42] H. G. R. Prakash, G. Sanjeev, K. B. V. Kumar, K. Siddappa, B. K. Nayak, and A. Saxena, Ann. Nucl. En. **38**, 757 (2011).

[43] H. G. Rajaprakash, G. Sanjeev, K. B. V. Kumar, K. Siddappa, B. K. Nayak, and A. Saxena, Rad. Meas. **46**, 413 (2011).

[44] R. Ratzek *et al.*, Z. Phys. A **308**, 63 (1982).

[45] V. E. Rudnikov, G. N. Smirenkin, A. S. Soldatov, and S. Juhasz, Sov. J. Nucl. Phys. **48**, 414 (1988).

[46] A. S. Soldatov, Z. A. Aleksandrova, L. D. Gordeeva, and G. N. Smirenkin, Sov. J. Nucl. Phys. **1**, 335 (1965).

[47] A. S. Soldatov, G. N. Smirenkin, S. P. Kapitza, and Y. M. Tsipeniuk, Phys. Lett. **14**, 217 (1965).

[48] A. S. Soldatov, Yu. M. Tsipenyuk, and G. N. Smirenkin, Sov. J. Nucl. Phys. **11**, 552 (1970).

[49] F. Steiper, T. Frommhold, W. Henkel, A. Jung, U. Kneissl, and R. Stock, Nucl. Phys. **A563**, 282 (1993).

[50] J. R. Tompkins, Ph.D. thesis, University of North Carolina at Chapel Hill (2012).

[51] E. J. Winhold, P. T. Demos, and I. Halpern, Phys. Rev. **87**, 1139 (1952).

[52] E. J. Winhold and I. Halpern, Phys. Rev. **103**, 990 (1956).

[53] V. E. Zhuchko, A. V. Ignatyuk, Yu. B. Ostapenko, G. N. Smirenkin, A. S. Soldatov, and Yu. M. Tsipenyuk, JETP Lett. **24**, 277 (1976).

[54] V. E. Zhuchko, A. V. Ignatyuk, Yu. B. Ostapenko, G. N. Smirenkin, A. S. Soldatov, and Yu. M. Tsipenyuk, Phys. Lett. B **68**, 323 (1977).

[55] V. E. Zhuchko, Yu. B. Ostapenko, G. N. Smirenkin, A. S. Soldatov, and Yu. M. Tsipenyuk, Sov. J. Nucl. Phys. **27**, 746 (1978).

[56] V. E. Zhuchko, Yu. B. Ostapenko, G. N. Smirenkin, A. S. Soldatov, and Yu. M. Tsipenyuk, Sov. J. Nucl. Phys. **30**, 326 (1979).

[57] H. R. Bowman, S. G. Thompson, J. C. D. Milton, and W. J. Swiatecki, Phys. Rev. **126**, 2120 (1962).

[58] E. A. Seregina, Ph.D. thesis, Obninsk Institue for Nuclear Power Engineering (1985).

[59] C. Budtz-Jørgensen and H. H. Knitter, Nuc. Phys. **A490**, 307 (1988).

[60] D. Seeliger, H. Kalka, H. Märten, A. Ruben, K. Arnold, and I. Düring, IEAE Report INDC(GDR)-056/L (1989).

[61] N. V. Kornilov, A. B. Kagalenko, S. V. Poupko, P. A. Androsenko, and F. J. Hambsch, Nuc. Phys. **686**, 187 (2001).

[62] A. S. Vorobyev *et al.*, Nucl. Instrum. Methods **A598**, 795 (2009).

[63] H. R. Weller *et al.*, Prog. Part. Nucl. Phys. **62**, 257 (2009).

[64] Y. K. Wu, Private communication (2012).

[65] V. N. Litvinenko, B. Burnham, J. M. J. Madey, S. H. Park, and Y. Wu, Nucl. Instrum. Methods **A375**, 46 (1996).

[66] M. A. Blackston, Ph.D. thesis, Duke University (2007).

[67] C. W. Roberson and P. Sprangle, *A review of free electron lasers* (Naval Research Laboratory, Washington, D. C., 1989).

[68] V. B. Berestetskii, E. M. Lifshitz, and L. P. Pitaevskii, *Relativistic Quantum Theory* (Pergamon Press, 1971).

[69] D. J. Griffiths, *Introduction to Electrondynamics* (Prentice Hall, New Jersey, 1999).

[70] V. N. Litvinenko *et al.*, Phys. Rev. Lett. **78**, 4569 (1997).

[71] S. S. Henshaw, Ph.D. thesis, Duke University (2010).

[72] R. E. Pywell, O. Mavrichi, W. A. Wurtz, and R. Wilson, Nucl. Instrum. Methods **A606**, 517 (2009).

[73] B. A. Perdue, Ph.D. thesis, Duke University (2010).

[74] G. F. Knoll, *Radiation detection and measurement* (John Wiley and Sons, Inc., 2010).

[75] G. A. Warren, Private communication (2012).

[76] J. M. Mueller *et al.*, Phys. Rev. C **85**, 014605 (2012).

[77] D. E. G. Trotter *et al.*, Nucl. Instrum. Methods **A599**, 234 (2009).

[78] A. Ruben *et al.*, IEEE Nuclear Science Symposium Conference Record N15-273 681 (2007).

[79] J. T. Caldwell, E. J. Dowdy, R. A. Alvarez, B. L. Berman, and P. Meyer, Nucl. Sci. Eng. **73**, 153 (1980).

[80] V. V. Varlamov and N. N. Peskov, Report: Moscow State Univ. Inst. of Nucl. Phys. Reports 8 (2007).

[81] S. Lemaire, P. Talou, T. Kawano, M. B. Chadwick, and D. G. Madland, Phys. Rev. C **72**, 024601 (2005).

[82] P. Talou, B. Becker, T. Kawano, M. B. Chadwick, and Y. Danon, Phys. Rev. C **83**, 064612 (2011).

[83] B. Becker, P. Talou, T. Kawano, Y. Danon, and I. Stetcu, Phys. Rev. C **87**, 014617 (2013).

[84] O. Litaize and O. Serot, Phys. Rev. C **82**, 054616 (2010).

[85] J. Randrup and R. Vogt, Phys. Rev. C **80**, 024601 (2009).

[86] R. Vogt, J. Randrup, J. Pruet, and W. Younes, Phys. Rev. C **80**, 044611 (2009).

[87] R. Vogt, J. Randrup, D. A. Brown, M. A. Descalle, and W. E. Ormand, Phys. Rev. C **85**, 024608 (2012).

[88] R. Vogt and J. Randrup, Phys. Rev. C **87**, 044602 (2013).

[89] T. England and B. Rider, Evaluation and compilation of fission yields (1992), ENDF-349, LA-UR-94-3106, Extracted from ENDF.

[90] W. Reisdorf, J. Unik, H. Griffin, and L. Glendenin, Nucl. Phys. **A177**, 337 (1971).

[91] G. Audi and A. Wapstra, Nucl. Phys. **A595**, 409 (1995).

[92] C. Wagemans, E. Allaert, A. Deruytter, R. Barthélémy, and P. Schillebeeckx, Phys. Rev. C **30**, 218 (1984).

[93] C. Tsuchiya *et al.*, J. Nucl. Sci. Technol. **37**, 941 (2000).

[94] K. Nishio, Y. Nakagome, I. Kanno, and I. Kimura, J. Nucl. Sci. Technol. **32**, 404 (1995).

[95] F. Vivès, F.-J. Hambsch, H. Bax, and S. Oberstedt, Nucl. Phys. **A662**, 63 (2000).

[96] M. Chadwick *et al.*, Nucl. Data Sheets **112**, 2887 (2011).

[97] H. Baba, Nucl. Phys. **A159**, 625 (1970).

[98] T. Kawano, S. Chiba, and H. Koura, J. Nucl. Sci. Technol. **43**, 1 (2006).

[99] H. Koura, M. Uno, T. Tachibana, and M. Yamada, Nucl. Phys. **A674**, 47 (2000).

[100] W. R. Leo, *Techniques for Nuclear and Particle Physics Experiments* (Springer-Verlag, New York, 1994).

[101] G. Cowen, *Statistical Data Analysis* (Clarendon Press, Oxford, 1998).

[102] B. L. Berman, J. T. Caldwell, E. J. Dowdy, S. S. Dietrich, P. Meyer, and R. A. Alvarez, Phys. Rev. C **34**, 2201 (1986).

[103] E. P. Wigner, Phys. Rev. **73**, 1002 (1948).

[104] A. Bohr and B. R. Mottelson, *Nuclear Structure Volume I: Single Particle Motion* (World Scientific Publishing Co., Singapore, 1998).

[105] A. Kafkarkou *et al.*, Nucl. Instrum. Methods **B316**, 48 (2013).

[106] G. Laskaris *et al.*, Phys. Rev. Lett. **110**, 202501 (2013).

[107] W. R. Zimmerman *et al.*, Phys. Rev. Lett. **110**, 152502 (2013).

[108] L. S. Myers *et al.*, Phys. Rev. C **86**, 044614 (2012).

[109] J. M. Mueller *et al.*, Phys. Rev. C **83**, 064605 (2011).

[110] R. J. Charity, J. M. Mueller, L. G. Sobotka, and W. H. Dickhoff, Phys. Rev. C **76**, 044314 (2007).

Biography

Jonathan Michael Mueller

Personal

- Born on April 27, 1987 in Abington, PA

Degrees Awarded

- B.S. in Physics, Mathematics, and Economics from Washington University in St. Louis (2009)
- A.M. in Physics from Duke University (2013)

Publications

[**76**] J. M. Mueller et al., *Measurement of prompt neutron polarization asymmetries in photofission of* $^{235,238}U$, ^{239}Pu, *and* ^{232}Th. Phys. Rev. C **85**, 014605 (2012).

[**105**] A. Kafkarkou et al., *Study of the* $^{10}B(p,\alpha)$ *reaction between 2.1 and 6.0 MeV.* Nucl. Instrum. Methods **B316**, 48 (2013).

[**106**] G. Laskaris et al., *First Measurements of Spin-Dependent Double-Differential Cross Sections and the GDH Integrand from* $^{3}He(\vec{\gamma},n)pp$ *at Incident Photon Energies of 12.8 and 14.7 MeV.* Phys. Rev. Lett. **110**, 202501 (2013).

[**107**] W. R. Zimmerman et al., *Unambiguous Identification of the Second* 2^+ *State in* ^{12}C *and the Structure of the Hoyle State.* Phys. Rev. Lett. **110**, 152502 (2013).

[**108**] L. S. Myers et al., *Compton scattering from ^{6}Li at 60 MeV*. Phys. Rev. C **86**, 044614 (2012).

[**109**] J. M. Mueller et al., *Asymmetry dependence of nucleon correlations in spherical nuclei extracted from a dispersive-optical-model analysis*. Phys. Rev. C **83**, 064605 (2011).

[**110**] R. J. Charity, J. M. Mueller, L. G. Sobotka, and W. H. Dickhoff, *Dispersive-optical-model analysis of the asymmetry dependence of correlations in Ca isotopes*. Phys. Rev. C **76**, 044314 (2007).

Oral Presentations Given

- DNDO ARI Meeting, 2013
- APS April Meeting, 2013
- DNDO ARI Meeting, 2012
- APS DNP Fall Meeting, 2011
- DNDO ARI Meeting, 2011
- APS April Meeting, 2011
- Co-author on 5 other oral presentations

Poster Presentations Given

- DNDO ARI Meeting, 2013
- DNDO ARI Meeting, 2012
- DOE SCGF Meeting, 2012
- DNDO ARI Meeting, 2011
- DOE SCGF Meeting, 2011
- DNDO ARI Meeting, 2010
- Co-author on 12 other poster presentations

Fellowships and Awards

- Henry W. Newson Award (2013)
- Best Student Oral Presentation, DNDO ARI Meeting (2012)
- Best Student Oral Presentation, DNDO ARI Meeting (2011)
- DOE Office of Science Graduate Fellowship (2010-2013)
- James B. Duke Graduate Fellowship (2009-2013)
- Valedictorian, Washington University School of Engineering (2009)
- Senior Prize in Physics, Washington University (2009)
- Member, $\Sigma\Pi\Sigma$
- Greg Delos Summer Fellowship, Washington University (2008)
- Antoinette Frances Dames Award, Washington University (2007)